Institut National Polytechnique de Lorraine
Ecole Doctorale Informatique-Automatique - Electronique - Mathématiques
Département de formation doctorale Electrotechnique - Electronique

THESE

Présentée en vue de l'obtention du titre de

Docteur de l'Institut National Polytechnique de Lorraine

Spécialité : Génie Electrique

Par

Arnaud MADUR
Ingénieur ENSEM

Contribution à la métrologie magnétique des multipôles d'accélérateurs : les quadrupôles du Synchrotron SOLEIL

Contribution to the magnetic metrology of accelerator multipole magnets : Synchrotron SOLEIL Storage Ring Quadrupoles

Directeur de Thèse :
Professeur Alain MAILFERT

Jury :

Président :	*D. RAOUX*
Rapporteurs :	*L. FARVACQUE*
	P. PUZO
	L. WALCKIERS
Membres :	*A. DAEL*
	B. MULTON
	A. NADJI
	F.M. SARGOS

Date de soutenance :
26 octobre 2006

Remerciements

Je remercie le Synchrotron SOLEIL et plus particulièrement son directeur, Denis Raoux, pour m'avoir accueilli, permis de mener mes travaux dans un environnement de qualité et enfin pour avoir accepté que ma soutenance ait lieu au sein de SOLEIL. Je le remercie par ailleurs d'avoir présider le jury de ma thèse. Je remercie aussi Patrick Puzo et Laurent Farvacque pour leur analyse approfondie du mémoire et d'avoir accepté de confondre leur expertise afin de le rapporter conjointement. Je souhaite témoigner à Louis Walckiers toute ma reconnaissance pour l'attention apportée à son rôle de rapporteur, son expertise des mesures magnétiques m'a été très précieuse. Je remercie chaleureusement Bernard Multon pour l'intéret qu'il a témoigné à mes travaux de thèse.

Mes sincères remerciements vont au professeur Alain Mailfert qui m'a permis de découvrir le monde de la recherche lors de mon DEA et qui a accepté de diriger cette thèse malgré la distance. Par ailleurs, aucun de ces travaux n'aurait pu être effectué sans la confiance initiale d'Antoine Daël qui m'a d'une part proposé un travail de thèse et qui a d'autre part accepté de participer activement à mon encadrement au sein du Synchrotron SOLEIL. Je le remercie également d'avoir préparé l'encadrement de la seconde partie de ma thèse avec attention. Dans un second temps, j'ai eu la chance d'être encadré par Amor Nadji. Grâce à sa patience, j'ai été en mesure de finir mes travaux de recherches sur un thème de la physique des accèlèrateurs. Je remercie également Jean-Michel Rifflet d'avoir accepté de suivre à nouveau mes travaux en participant activement au comité de suivi de ma thèse.

L'épisode du banc de mesures magnétiques a été une formidable aventure au sein du groupe magnétisme et insertions. Je remercie chaleureusement Michel Massal pour sa bienveillance quotidienne et ses conseils avisés. Merci a l'équipe BMS pour tous ces moments inoubliables que nous avons passés ensemble. Je remercie Fabrice d'avoir partagé avec moi sans retenue ses connaissances et de m'avoir soutenu tout au long de ma thèse, et particulièrement dans les moments difficiles. Merci à Chams' que nous avons fait frissoner plus d'une fois : tes quadrupoles sont parfaits Chams'. Merci à Philippe pour sa bonne humeur malgré la pression quotidienne lors de la mise en route du banc et à François pour nos longues discussions philosophiques. Je remercie Olivier pour ses conseils et son soutien lors de la derniere ligne droite. Fabien, je te remercie pour tous ces moments que nous avons passé ensemble. Je remercie aussi Oleg, José pour sa bonne humeur quotidienne et Mathieu pour ses précieux conseils informatiques. Un grand merci à Mathieu Valleau pour ses blagues...

Même si mon passage au sein du groupe physique machine fut plus court, il fut aussi riche en émotions avec notamment la mise en route de l'anneau de stockage. Pascale, merci pour ton excellente humeur quotidienne et ton soutien de tous les instants. Marie-Agnès, travailler avec toi fut un plaisir, le sérieux dans la bonne humeur. Merci à Laurent pour ses conseils pertinents et Alex pour son aide pendant les "run". Je remercie également l'équipe commissioning, travailler avec vous a été très formateur. Cette thèse doit beaucoup à la disponibilité du personnel de SOLEIL, je pense notamment au groupe alimentations, au groupe alignement, au groupe diagnostique et

au groupe fonctionnement. Je souhaite d'ailleurs remercier particulièrement François Bouvet pour sa disponibilité, notamment lors de nos expériences sur les sextupôles. Je remercie sincèrement Jean-Marc Filhol pour sa confiance et ses suggestions de dernière minute, Marie-Paule Level et Marie-Emmanuelle Couprie pour leurs conseils avisés, et Jean-Claude Besson pour son intérêt concernant ma thèse.

Je souhaite aussi remercier vivement Sabine Podgorny pour son aide précieuse et Pierre Lebasque pour son écoute attentive. Un grand merci aussi à Hélène Rozelot pour l'attention et le soutien qu'elle m'a témoigné.

Enfin, merci à mes parents pour leur confiance totale et à Hélène pour son soutien incommensurable.

Table des matières

Remerciements **3**

Introduction **9**

1 Cadre général **13**
1.1 Accélérateurs d'hier et d'aujourd'hui . . . 13
1.1.1 Accélérateurs linéaires . . . 14
1.1.2 Accélérateurs circulaires . . . 16
1.2 Les sources de lumière synchrotron . . . 20
1.2.1 Histoires de rayonnements . . . 20
1.2.2 Le synchrotron SOLEIL . . . 21
1.2.2.1 Applications . . . 22
1.2.2.2 Introduction au formalisme des accélérateurs . . . 22
1.2.3 Optimisation de l'Anneau de Stockage . . . 25
1.2.3.1 Grandeurs fondamentales de la physique des accélérateurs . . . 25
1.2.3.2 Optimisation de la brillance . . . 28
1.3 Problématique de l'alignement . . . 29
1.3.1 Dispositifs de mesures magnétiques . . . 30
1.3.1.1 Les procédés utilisés . . . 30
1.3.1.2 Mesures magnétiques d'aimants d'accélérateur . . . 34

2 Theoretical studies and Developments **39**
2.1 Harmonic coils theory . . . 39
2.1.1 Theory for rotating coils . . . 40
2.1.1.1 Solution of Laplace equation . . . 40
2.1.1.2 Complex Formalism . . . 41
2.1.1.3 Magnetic flux calculation . . . 43
2.1.2 Error sources studies . . . 44
2.1.2.1 Calculation of the magnetic axis location offset . . . 44
2.1.2.2 Angular error . . . 45
2.1.2.3 Effect of sag . . . 46
2.1.2.4 Bucking coils . . . 46
2.2 Contribution to theoretical experiments . . . 46
2.2.1 Development of the method . . . 46
2.2.2 2D model . . . 48
2.2.3 Analytical 3D model . . . 50
2.2.4 Application of the 3D model . . . 52
2.3 Reference measurements . . . 54

2.3.1 Principle . . . 54
2.3.1.1 Ideal case . . . 55
2.3.1.2 Positioning error of the sensor measuring coils . . . 55
2.3.1.3 Errors from the tool machining . . . 56
2.3.1.4 Advanced reference tools theory . . . 58
2.3.1.5 Angular errors . . . 60
2.3.2 Final design and new approach proposition . . . 62
2.3.2.1 Mechanical Measurements . . . 62
2.3.2.2 Improvement of the reference tool design . . . 63

3 Magnetic-Based Alignment 65
3.1 State of art of rotating coil benches . . . 65
3.1.1 General concept . . . 66
3.1.1.1 Mechanical Stands . . . 66
3.1.1.2 Mechanical Links . . . 67
3.1.1.3 Electronic Equipments . . . 68
3.1.1.4 Sensor Mechanical Design . . . 68
3.1.2 SOLEIL harmonic bench: initial design . . . 70
3.1.2.1 General concept . . . 70
3.1.2.2 Technological choices . . . 73
3.1.2.3 Performances . . . 75
3.2 The SOLEIL Multipolar Magnetic Measurement Bench . . . 78
3.2.1 Improvements of the mechanics . . . 79
3.2.1.1 Kinetic chain . . . 79
3.2.1.2 Sag effect minimization . . . 80
3.2.1.3 Torsion minimization . . . 81
3.2.2 Alignment during the sensor assembly . . . 82
3.2.2.1 Fiberglass structure assembly . . . 83
3.2.2.2 Aluminum Tips . . . 84
3.3 Commissioning of the SMB . . . 86
3.3.1 Measurement Protocol . . . 86
3.3.2 Tests . . . 89
3.3.2.1 Equipments . . . 90
3.3.2.2 Reproducibility . . . 90
3.3.3 Bench defect measurements . . . 92
3.3.3.1 Sag of the sensor . . . 92
3.3.3.2 Magnetic misalignment . . . 93
3.4 Magnetic Data Study . . . 95
3.4.1 Special Measurements . . . 95
3.4.1.1 Optimization of the 12-pole . . . 95
3.4.1.2 Magnetic Forces . . . 96
3.4.1.3 Hysteresis . . . 97
3.4.1.4 Cross-Talk . . . 100
3.4.1.5 Magnetic length . . . 100
3.4.2 Series Measurements . . . 101
3.4.2.1 Magnetic field harmonics . . . 101
3.4.2.2 Centering . . . 107
3.4.3 First SR electron beam results . . . 109

4 Beam-Based Alignment **113**
4.1 Introduction to tools and methods for BBA . . . 114
4.1.1 Methods for quadrupole magnets . . . 114
4.1.1.1 Methods using correctors . . . 116
4.1.1.2 K-modulation . . . 118
4.1.2 Methods for sextupole magnets . . . 119
4.1.2.1 Methods with Correctors . . . 120
4.1.2.2 Method with Movers . . . 120
4.1.3 Environment . . . 121
4.1.3.1 Element description . . . 121
4.1.3.2 Control and command organisation . . . 123
4.2 Application of the BBA to the SOLEIL SR quadrupoles . . . 124
4.2.1 Development of a Matlab Graphical User Interface . . . 124
4.2.2 Beam-Based Measurements . . . 126
4.3 BBA for sextupole magnets . . . 130
4.3.1 Proposition of a new method: The Magnetic Axis Moving method . . . 131
4.3.2 First application of the MAM method at SOLEIL . . . 133

Conclusion **137**

Bibliography **139**

Notations **143**

List of Figures **151**

A Reference measurement **153**
A.1 Measurements relations . . . 153
A.2 Mechanical defects relations . . . 154
A.3 Integrated Magnetic flux density components . . . 155
A.4 Feed-down formula demonstration . . . 156
A.5 Some Machine Physics formulas . . . 157

B Sensor Assembly **159**

C Wedges Calculation **161**
C.1 Effect on the rectangular wedge . . . 162
C.2 Effect on cylindrical wedges . . . 163
C.3 Example of wedges calculation . . . 164
C.4 Wedges calculation in the SMB measuring program . . . 165

D 160 Magnetic Flowers **167**

E Corrector bumps **169**
E.1 π bump . . . 169
E.2 Three corrector bump . . . 169

F **171**

Introduction

Parmi les grands instruments dédiés à la physique, les accélérateurs suscitent actuellement beaucoup d'engouement. Ceux optimisés pour la production de rayonnement dit "synchrotron" sont notamment en plein essor. Phénomène parasite à son origine, ce type de rayonnement est rapidement devenu un outil de recherche incontournable si l'on se réfère à la demande toujours croissante des utilisateurs. La Source Optimisée de Lumière d'Energie Intermédiaire du LURE[1] (SOLEIL) est un ensemble d'accélérateurs d'électrons mettant à la disposition de la communauté utilisatrice un rayonnement synchrotron de haute performance. Cette communauté s'est considérablement développée pendant vingt cinq ans grâce au LURE (arrêté maintenant) qui après les anneaux de stockage ACO[2], DCI[3] et SUPERACO a atteint le nombre de 2000 utilisateurs par an.

Pour atteindre les performances visées, SOLEIL, source de rayonnement synchrotron de 3ème génération, est équipé d'éléments d'insertion qui délivreront les faisceaux de photons. La brillance, la stabilité des photons dans l'espace et le temps sont les principaux critères de qualité recherchés pour les utilisateurs. Comme ces paramètres sont directement liés à la qualité du faisceau d'électrons circulant dans la machine, les performances attendues pour les différents éléments la constituant sont très pointues. C'est le cas notamment des éléments focalisants de l'anneau de stockage : les quadrupôles. Par analogie avec l'optique, les quadrupôles exercent sur le faisceau d'électrons un effet qui est similaire à celui d'une lentille mince focalisant un faisceau de lumière. Pour un faisceau d'électrons, cet effet de focalisation est assuré par le champ magnétique produit par ces quadrupôles qui a une symétrie quadrupolaire. Afin de ne pas perturber la dynamique des électrons, il est important que le champ magnétique fourni soit le plus pur possible. Cela veut dire que les harmoniques, qui sont des composantes du champ magnétique produit, autres que quadrupolaires, doivent être minimisés. C'est pourquoi une campagne de mesures magnétiques doit être menée afin de s'assurer que chacun des 160 quadrupôles ait un taux d'harmoniques en dessous des tolérances fixées. Du fait de certains défauts de fabrication, un décalage de la position et de l'orientation de l'axe magnétique des quadrupôles détériore la qualité du champ. Cela perturbe la trajectoire des électrons, ce qui implique que ces quantités doivent non seulement être mesurées mais aussi corrigées. La minimisation de ces défauts permet de réduire sensiblement les perturbations du premier ordre subies par le faisceau.

Pour cela, SOLEIL a décidé de développer un banc de mesures magnétiques multipolaires dans le but d'effectuer ces mesures magnétiques et ces corrections. Les tolérances concernant les axes magnétiques des multipôles sont très strictes étant données les perturbations que ce genre de défaut peut introduire. Ces perturbations proviennent de l'extrême sensibilité du faisceau d'électrons qui est fortement focalisé pour obtenir une grande brillance des photons. Il est nécessaire que les électrons traversent les quadrupôles suivant leur axe dont la position transverse par rapport

[1] LURE : Laboratoire d'Utilisation du Rayonnement Electromagnétique
[2] ACO : Accélérateurs Circulaire d'Orsay
[3] DCI : Dispositif de Collision dans l'Igloo

à l'axe longitudinal doit être limitée à 25 μm au sens des moindes carrés. De plus, si l'angle du plan médian du champ quadrupolaire par rapport au plan horizontal est important, il apparaît un phénomène de couplage entre le plan vertical et le plan horizontal. Pour limiter ce couplage, l'erreur d'orientation du plan médian magnétique doit être inférieure à $0.1 mrad$ autour de l'axe longitudinal, au sens des moindres carrés. Le premier capteur, dédié à ces mesures, n'a pas permis d'atteindre ces spécifications. C'est dans ce contexte que nous avons amorcé notre recherche en étudiant les causes des problèmes rencontrés, afin de développer un nouveau capteur plus performant. Les travaux de W.G. Davies [1] concernant la mesure des quadrupôles ont constitué le point de départ de notre étude pour atteindre la précision de mesure nécessaire. De plus, un quadrupôle de référence a été fabriqué dans le but de l'identifier et de quantifier les défauts du banc de mesure et notamment du capteur. Ces mesures sont indispensables lors de la mise en route du banc pour definir si il a les qualités requises pour commencer les mesures de séries des 160 quadrupôles de l'anneau de stockage.

Une fois mesurés, les quadrupôles sont installés dans l'anneau de stockage. Cette installation introduit inévitablement des défauts de positionnement, pouvant encore une fois perturber le faisceau s'ils ne sont pas pris en compte. Lors des premières phases de mise en route de l'anneau de stockage, le faisceau doit circuler convenablement malgré ces décalages. Pour les mesurer, on cherche à connaître la position du faisceau par rapport aux axes magnétiques des quadrupôles. La première étape consiste à prendre la référence des BPM[4], et non celle des quadrupôles, pour définir cette position. Les BPM ont quatre électrodes situées à un rayon fixe et decalées entre elles d'un angle de 90°dans le plan transverse (plan perpendiculaire à l'axe du faisceau). En combinant les signaux fournis par ces électrodes à chaque passage du faisceau, il est possible de déterminer sa position. Ensuite, afin de déterminer la position du faisceau par rapport aux axes magnétiques des quadrupôles, les décalages entre ces axes et les références des BPM sont alors mesurés au moyen de méthodes utilisant le faisceau. C'est l'étape de la mise en route de la machine qui constitue l'alignement des quadrupôles basé sur le faisceau ("Beam-Based Alignment"). Outre les aimants quadrupolaires, les éléments corrigeant des effets de second ordre sur la dynamique du faisceau (sextupôles) peuvent être choisis comme référence. A ce titre, nous proposerons une nouvelle méthode d'alignement basée sur le faisceau.

Dans le cadre de notre travail, nous proposons une étude préliminaire qui permet de situer le point de départ de notre travail. Ainsi, un bref rappel historique sur l'évolution des accélérateurs définit la place du synchrotron SOLEIL parmi les autres accélérateurs. SOLEIL étant dédié à une communauté d'utilisateurs, les tolérances fixées pour les quadrupôles seront définies à partir de leurs besoins. Puis, notre travail portant essentiellement sur la mesure magnétique d'aimants d'accélérateurs, une étude des procédés existants est effectuée.

Ensuite, les outils mathématiques permettant de traiter les mesures magnétiques effectuées au moyen de bobines tournantes sont explicités. A partir des travaux de W.G. Davies, nous étudierons les problèmes que peuvent susciter certains défauts. Par ailleurs, nous proposerons une méthode qui permet d'effectuer des expériences théoriques sur ces défauts pour les étudier qualitativement. La mise en évidence des défauts du banc étant un aspect important de sa conception, il est nécessaire de définir une méthode de mesure au moyen d'un quadrupôle de référence.

Ces études nous permettent de rassembler toutes les informations nécessaires à la conception du banc de mesure et notamment du capteur. C'est pourquoi après avoir abordé la conception générale des bancs de mesures harmoniques, nous nous attarderons sur les différents aspects de la conception de celui de SOLEIL. Enfin, les différentes étapes de la mise en route du banc et les résultats de la mesure de série des 160 quadrupôles sont présentées. Pour finir, diverses méthodes

[4]BPM : Beam Position Monitor

d'alignements des quadrupôles basées sur le faisceau sont exposées avec notamment les résultats obtenus lors de la mise en route de l'anneau de stockage de SOLEIL.

Chapitre 1

Cadre général

Objectifs du chapitre
L'objectif de ce chapitre est de présenter au lecteur un ensemble de connaissances générales concernant les accélérateurs de particules. Dans ce cadre là, l'évolution des accélérateurs des particules est traitée. De même la physique des particules dans un accélérateur est explicitée afin de donner quelques éléments de base pouvant aider à déterminer l'origine des tolérances fixées pour les quadrupôles de l'anneau de stockage du synchrotron SOLEIL. La thèse traitant de la métrologie magnétique des multipôles d'accélérateurs, un parcours succinct des méthodes de mesures existantes est effectué en fin de chapitre.

Dans un premier temps ce chapitre a pour but d'étudier l'évolution technologique des accélérateurs de particules. Tout en permettant de recenser les différents types de machine existantes, évoquer l'histoire des accélérateurs permet de faire ressortir les principaux problèmes qui ont été progressivement résolus. Cette démarche est d'autant plus justifiée que le synchrotron SOLEIL est doté de trois types d'accélérateurs différents : un accélérateur linéaire (ou LINAC), un booster (ou synchrotron) et un anneau de stockage. SOLEIL est un accélérateur d'électrons entièrement dédié à la production de rayonnement dit "synchrotron". Initialement perçu comme une perte d'énergie parasite, ce type de rayonnement est rapidement devenu indispensable dans divers domaines de recherche en physique. Etant donnée l'exigence exprimée par les physicens en matière de qualité du rayonnement, tous les éléments de la machine doivent être optimisés. C'est notamment le cas des éléments focalisant le faisceau d'électrons. Ces derniers produisent un champ magnétique de géométrie quadrupolaire agissant sur le faisceau électronique comme une lentille mince agirait sur un faisceau lumineux en optique. La qualité de ces éléments dépend tout d'abord de leur fabrication. Ensuite seules des mesures magnétiques caractérisant avec précision leurs propriétés magnétiques permettent de maîtriser le comportement du faisceau d'électrons. La métrologie magnétique des quadrupôles intervenant avant leur installation sur l'anneau de stockage, il est nécessaire de mesurer à nouveau la position de leur axe magnétique. Cette dernière étape est d'autant plus nécessaire qu'il est primordial que les électrons traversent les quadrupôles suivant leur axe.

1.1 Accélérateurs d'hier et d'aujourd'hui

Les machines désignées aujourd'hui comme synchrotrons sont des accélérateurs de particules circulaires dédiés à la production de rayonnements électromagnétiques au spectre large appelés

"lumière synchrotron". SOLEIL, source de lumière synchrotron de 3ème génération, est le résultat d'optimisations multiples à compter du jour où le premier accélérateur a été conçu. Initialement dédiés à la recherche sur la physique nucléaire, les applications des accélérateurs sont maintenant nombreuses et variées. Après un rappel sur l'histoire de l'évolution des accélérateurs de particules, on s'attardera un peu sur l'histoire du rayonnement synchrotron pour ensuite présenter brièvement le fonctionnement d'une source de lumière synchrotron telle que SOLEIL.

1.1.1 Accélérateurs linéaires

Dans les années 1920, la recherche sur la physique nucléaire ne pouvait plus se contenter d'utiliser les accélérateurs naturels que constituaient les sources radioactives. En effet ces dernières laissaient échapper les particules α franchissant la barrière de Coulomb, ce qui permettait d'effectuer des collisions. Cependant l'énergie des collisions était limitée par celle des particules alpha. Il est alors devenu nécessaire d'avoir recours à des particules ayant des énergies et des intensités plus grandes et donc de les accélérer. C'est ainsi que les accélérateurs électrostatiques ont vu le jour.

Le premier accélérateur
En 1932, J.D. Cockroft et E.T.S. Walton réussissent à casser un atome de lithium avec des protons à 500 kV, pour cela il recevront le prix Nobel en 1951 [2], [3]. Ils ont tout simplement soumis des protons à une différence de potentiel suffisamment grande (500kV) qui a permis de les accélérer à l'intérieur d'un tube à décharge. Après un premier essai non concluant avec un transformateur de 200 kV, ils eurent l'idée de concevoir un multiplicateur de tension au moyen d'un montage complexe contenant des condensateurs qui a permis d'atteindre la tension permettant d'accélérer des protons (500 kV).

Le générateur de Van De Graaf
En 1931, R.J. Van de Graaf inventa un générateur électrostatique qui atteignit un potentiel de 1.5 MV [4]. Le principe de ce générateur consiste à charger une cloche métallique au moyen d'une courroie qui transporte ces charges de la source vers la cloche (voir figure 1.1). Cependant ce type de machine n'a été que peu utilisée et bien après la performance de J.D. Cockroft et E.T.S. Walton et peu. Même si la machine de Van De Graaf permet d'obtenir un faisceau de particules ayant une énergie stable et de faible dispersion, elle n'est pas en mesure de fournir autant de courant que le générateur de Cockroft-Walton.

Accélération avec des champs radiofréquence
L'invention des cavités accélératrices utilisant une source alternative est un des principaux tournants de l'évolution des modes d'accélération. Rolf Wideröe, un étudiant norvégien fut tout d'abord à l'origine de ce qu'il a appelé le transformateur de faisceau d'électrons qui est devenu le bétatron (développé dans la partie 1.1.2). Alors qu'il était en quête d'une nouvelle idée pour obtenir son doctorat, une publication de G. Ising traitant de l'accélération linéaire d'ions lourds en utilisant différentes tensions a retenu son attention. R. Wideröe prouva expérimentalement la faisabilité du concept énoncé dans cette publication. En effet, il construisit le premier accélérateur linéaire composé de tubes de longueur croissante, alimentés par un champ radiofréquence (RF) alternatif.

Afin que les particules soient toujours accélérées lors des transitions entre chaque tube, elles doivent subir un champ électrique ayant toujours la même orientation. La période de la radiofréquence restant fixe, la longueur des tubes doit varier selon la loi suivante :

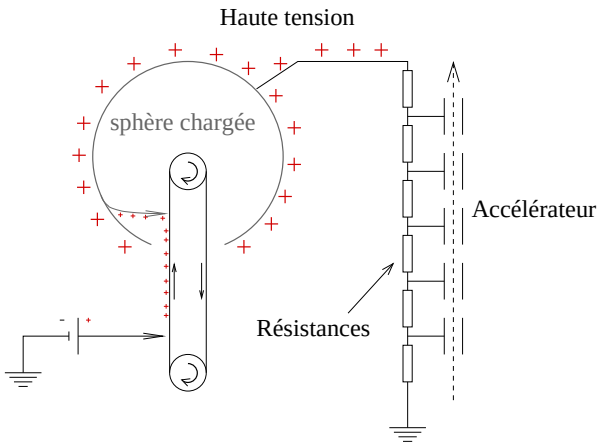

FIG. 1.1 – Générateur Van de Graaf

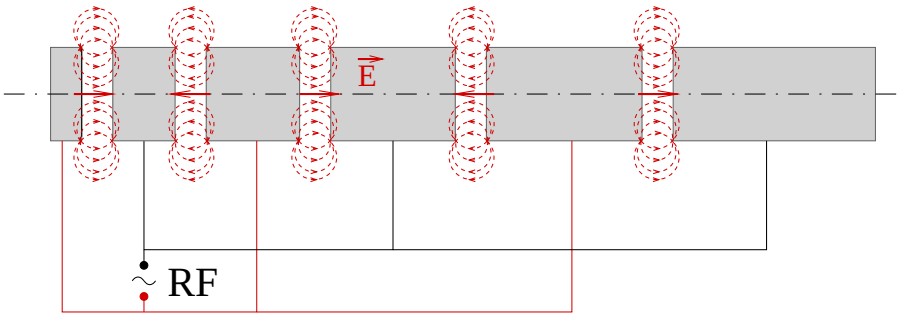

FIG. 1.2 – Structure accélératrice de Wideröe

La longueur L_i du $i^{ème}$ tube doit être égale à la distance parcourue par les particules à la vitesse v_i pendant une demi période de la radiofréquence (équation 1.1).

$$L_i \approx \frac{1}{2}\, v_i\, T_{RF} \tag{1.1}$$

Bien que cette idée soit révolutionnaire, les accélérateurs linéaires ne furent que très peu développés lors des années 30 du fait de leur coût, de la difficulté de mise en oeuvre et surtout à cause de l'engouement de la communauté des accélérateurs pour les cyclotrons. De plus ces premiers linacs furent vite limités par la fréquence RF disponible (30MHz maximum).

Ce n'est qu'après les développements sur les technologies radar et radio effectués pendant la seconde guerre mondiale que l'évolution des accélérateurs linéaires put reprendre. On notera tout de même l'invention du klystron en 1937 par Hansen et les frères Varian.

En 1946, L.W. Alvarez et W.K.H. Panofsky ont construit le premier LINAC (LINear ACcelerator) qui a permis d'atteindre une énergie de 32 MeV. La structure de Wideröe générant beaucoup de pertes à haute fréquence du fait de sa structure capacitive, L.W. Alvarez mit en court-circuit tous les tubes de manière à rendre la structure inductive. Ainsi il obtient une cavité dont la fréquence de résonance dépend directement de l'inductance et de la capacité de la structure. A partir de ce moment là, l'accélération des particules n'est pas seulement due à un champ électrique mais à un champ électromagnétique entrant en résonance à l'intérieur de la cavité.

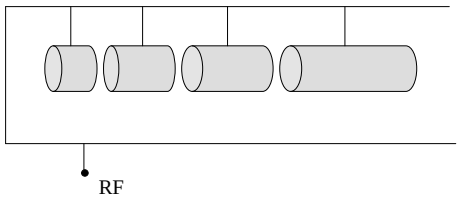

FIG. 1.3 – structure d'Alvarez

Depuis les accélérateurs ont été beaucoup développés jusqu'à atteindre des dimensions gigantesques comme celles du SLAC (Stanford Linear Accelererator). C'est le plus grand accélérateur linéaire du monde avec ses 3.2 km de long et une énergie de 50 GeV. Son fonctionnement a débuté dans les années 60 et il est toujours utilisé du fait des nombreuses modifications qui ont permis d'améliorer ses performances.

1.1.2 Accélérateurs circulaires

Bétatron

R. Wideröe proposa d'utiliser le principe du transformateur électrique pour concevoir le premier accélérateur circulaire d'électrons. Il faut tout d'abord que le dispositif crée un champ dipolaire uniforme qui permet de courber la trajectoire des électrons. Ensuite si à ce champ dipolaire s'ajoute un champ magnétique variable en fonction du temps, selon la loi de Faraday sur l'induction électromagnétique, il y a naissance d'une force électromotrice qui permet d'accélérer les électrons (1.2).

$$\nabla\times \vec{E} = -\frac{\partial}{\partial t}\,\vec{B} \tag{1.2}$$

De plus en 1923, Wideröe formula une condition nécessaire mais non suffisante pour que le faisceau d'électron conserve un rayon de courbure constant afin qu'il puisse circuler dans une

chambre à vide aux dimensions raisonnables. C'est la condition 1/2 de Wideröe :

$$B(R) = \frac{1}{2} B_{moy}(R) \tag{1.3}$$

Le champ magnétique au rayon de circulation des électrons $B(R)$ doit être la moitié du champ magnétique moyen $B_{moy}(R)$ vu par ces derniers le long de leur trajectoire sur un tour.

Bien que Wideröe ait développé tout le dispositif théorique nécessaire pour concevoir un bétatron , il n'a jamais réussi à obtenir une machine fonctionnelle (dernier essai en 1927 à Aachen). Il changea de voie et travailla désormais pour le compte des accélérateurs linéaires (voir partie 1.1.1).

C'est seulement en 1940, que D.W. Kerst construisit le premier bétatron qui fonctionna à 2.2 MeV à l'université de l'Illinois (USA)[5]. En 1950, le plus grand bétatron du monde (300 Mev) voyait le jour, toujours grâce à D. W. Kerst.

Cyclotron

Dès lors, les champs magnétiques variables ne sont plus utilisés (1.2) pour accélérer les particules. Tous les nouveaux types d'accélérateurs circulaires travaillent directement avec des champs électriques pour accélérer les particules. En 1930, Lawrence et Edlefsen établissent le principe de fonctionnement d'un cyclotron. Puis deux ans plus tard, Lawrence et un des ses étudiants, Livingston, mettent sur pied le premier cyclotron. Tout comme le bétatron, un champ magnétique dipolaire uniforme est nécessaire mais il n'est pas utilisé pour accélérer les particules : il reste constant. L'intérêt de ce concept est de découpler la fonction guidage de la fonction accélération en produisant localement le champ électrique nécessaire à l'accélération des particules. Le champ dipolaire est produit par un dipôle très volumineux car son entrefer doit contenir les deux "D" dans lesquels circulent les particules. Ces "D" sont alimentés par un oscillateur radiofréquence permettant de créer la différence de potentiel adéquat pour l'accélération des particules lors de leurs passages entre les "D" (figure 1.4).

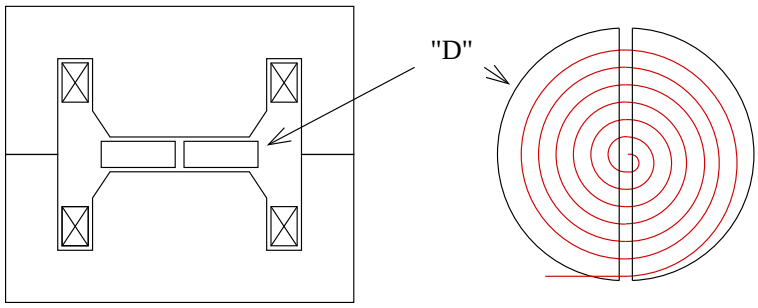

FIG. 1.4 – Principe du cyclotron

L'utilisation des cyclotrons est limitée par le fait qu'ils ne peuvent accélérer des particules relativistes. En effet, dans ce cas la fréquence de révolution devient plus petite ce qui fait perdre la synchronisation entre la fréquence de la radiofréquence et la fréquence de révolution des particules.

Les accélérateurs développés précédemment sont très vite limités par des phénomènes physiques insurmontables pour l'époque :

- Les accélérateurs dit électrostatiques sont limités par la tension de claquage,
- les cyclotrons ne peuvent accélérer que des particules non relativistes,
- quant aux bétatrons qui arrivent tout de même à atteindre 300 MeV, ils sont limités par les pertes d'énergie dues au rayonnement synchrotron.

L'idée d'utiliser une seule cavité RF (pour des raisons de coût) pour accélérer plusieurs fois le même faisceau fait son chemin. C'est alors qu'en 1945 V. Veksler (URSS) et E. McMillan (USA) établissent de manière indépendante la relation de synchronisation entre les particules à accélérer et le champ électrique variable fourni par la RF :

$$\omega = \frac{q\,B}{\gamma_r\,m_0} \tag{1.4}$$

où "q" est la charge de la particule, B l'induction, γ_r est une grandeur relativiste exprimant l'énergie réduite de la particule, m_0 est la masse au repos de la particule.

Synchrotron à électrons
Suite à ces avancées, les physiciens ont cherché à obtenir des particules ne circulant que sur une seule orbite de rayon de courbure ρ.

$$B\,\rho = \frac{p}{q} \tag{1.5}$$

Étant donnée l'équation 1.5, il est nécessaire de synchroniser l'induction magnétique B avec la quantité de mouvement p de manière à conserver ρ. Bien que McMillan fut le premier à lancer la construction (fin en 1949) d'un "electron synchrotron", la première machine de ce type à fonctionner fut celle de F. Goward et D. Barnes (Angleterre) en 1946, suivie par celle de General Electric (70 Mev) dans laquelle le premier rayonnement synchrotron issu d'un accélérateur de particules fut observé expérimentalement.

Synchrocyclotron
Des chercheurs de Berkeley (USA) ont appliqué le résultat trouvé par E. McMillan et V. Veksler aux cyclotrons avant qu'il ne soit utilisé pour les synchrotrons. Après des tests concluants, ils utilisèrent ce nouveau principe pour leur nouveau cyclotron et c'est alors qu'ils ont constaté que la tension au bornes des "D" était bien inférieure à celle qu'ils appliquaient pour un fonctionnement en mode cyclotron classique : le synchrocyclotron était né.

Synchrotron à protons
Les électrons atteignent une vitesse proche de celle de la lumière pour une énergie relativement basse et ont par conséquence une fréquence de révolution quasi constante durant la montée en énergie. Par contre les protons ont besoin d'une énergie de l'ordre du Gev pour devenir relativistes. Par conséquent, la fréquence RF doit pouvoir avoir une large plage de variation tout comme le champ magnétique afin de respecter le critère de stabilité énoncé précédemment. Des années de recherche et de développements technologiques ont été nécessaires pour rendre enfin possible l'accélération des protons. En 1953, le premier synchrotron à protons fonctionnait à une énergie de 1 GeV à Birmingham et un an plus tard le Cosmotron de Brookhaven accélérait des protons à 3 GeV.

Synchrotron
Jusqu'aux années 30 seuls des champs magnétiques dipolaires et champs électromagnétiques à radiofréquence ont été utilisés. Lors de leurs travaux sur les cyclotrons, E.O. Lawrence et S.M. Livingston ont découvert expérimentalement qu'en modifiant le circuit magnétique du cyclotron, ils arrivaient à créer une force focalisante verticale qui empêchait les particules d'aller rencontrer les pôles supérieur et inférieur. Dès lors, la condition pour obtenir une focalisation verticale suffisante fut la suivante :

$$0 < n = -\frac{r}{B}\frac{\partial B_z}{\partial r} < 1 \tag{1.6}$$

Ce principe a été utilisé pour le Cosmotron, ce dernier utilisant des dipôles dit en "C" (ouverture dirigée vers l'extérieur voir figure 1.5) permettant de fournir un gradient de champ magnétique relativement faible du fait des champs de fuites. C'est ce que l'on appelle la focalisation faible. N'étant focalisées que dans le plan vertical, les particules avaient des excursions relativement grandes dans le plan horizontal.

Afin d'optimiser les performances du Cosmotron, E.D. Courant, S. Livingston et H.S. Snyder ont décidé d'alterner la position de l'ouverture des dipôles. En d'autres termes d'alterner les effets de la focalisation et c'est alors qu'ils ont constaté une amélioration de la focalisation : ils allaient être capable de maîtriser la trajectoire des particules. Ainsi en approfondissant ce résultat, ils proposèrent de concevoir un synchrotron à focalisation forte utilisant des dipôles en "E" (figure 1.6) dont les pôles ont été optimisés pour fournir des forces focalisantes importantes [6] : c'est la naissance de la focalisation forte.



FIG. 1.5 – Dipôle en C

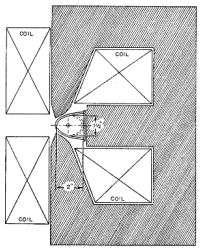

FIG. 1.6 – Dipôle er

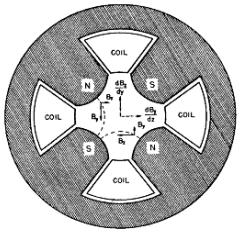

FIG. 1.7 – Quadrupôle

Afin d'obtenir une focalisation dans les deux plans (vertical et horizontal), les gradients sont alternés. En effet, lorsqu'une une configuration magnétique focalise dans un plan, elle défocalise dans l'autre. Par analogie à l'optique géométrique, les quadrupôles peuvent être assimilés à des lentilles minces. L'utilisation de deux lentilles, de longueurs focales f_1 et f_2 en valeur algébrique, séparées par une distance d conduit à la longueur focale globale f_{Tot} vérifiant la relation 1.7 :

$$\frac{1}{f_{Tot}} = \frac{1}{f_1} + \frac{1}{f_2} - \frac{d}{f_1\, f_2} = \frac{f_2 + f_1 - d}{f_1\, f_2} \tag{1.7}$$

De plus si $f_1 = -f_2$ avec $|f_1| = |f_2| = f$,

$$f_{Tot} = \frac{f^2}{d} > 0 \tag{1.8}$$

En utilisant seulement deux fois plus de matériaux que le Cosmotron initial, ce nouveau synchrotron travaillait à une énergie 10 fois plus grande, et avec une ouverture réduite d'un ordre de grandeur (de plusieurs dizaines de cm à quelques centimètres).

De plus, à la fin de leur publication [6], Courant, Livingston et Snyder évoquent pour la première fois la possibilité d'utiliser un élément magnétique ayant 4 pôles de forme hyperbolique dédié à la focalisation d'ions dans les accélérateurs linéaires (figure 1.7) : le quadrupôle était né.

Le principe de la focalisation forte ou du gradient alterné a révolutionné la conception des accélérateurs de particules, c'est devenu la base même de l'architecture d'un accélérateur circulaire de particules. Cette découverte a permis la construction de synchrotrons à gradients alternés atteignant de grandes énergies : 1959 CERN Proton Synchrotron (CPS) travaillant à 28 GeV (Genève) ; 1960, Alternating Gradient Synchrotron (AGS) travaillant à 33 GeV (Brookhaven).

Anneaux de stockage

R. Wideroe réalisa que deux particules non relativistes de même énergie entrant en collision

dégageaient 4 fois plus d'énergie qu'une seule particule terminant son voyage sur une cible fixe.

Pour des particules relativistes, ce constat est bien plus avantageux. C'est ce que démontra D.W. Kerst en 1956 [7].

L'énergie disponible au centre de masse est :

$$\begin{array}{rcll} \mathcal{E}_{cm}^{fixe} & = & \sqrt{2\,\mathcal{E}\,\mathcal{E}_0} & \text{pour une collision particule/cible fixe} \\ \mathcal{E}_{cm}^{coll.} & = & 2\,\mathcal{E} & \text{pour une collision particule / particule} \end{array} \tag{1.9}$$

Ainsi, à partir des équations 1.9, pour disposer d'une énergie au centre de masse de 2 GeV, il faut travailler avec deux faisceaux de 1 GeV dans le cas de la collision ou avec un faisceau de 4000 GeV dans le cas de la cible fixe.

Il n'en fallait pas plus pour entrer dans l'ère des anneaux de stockage dédiés à la collision des particules. C'est ainsi que des anneaux de stockage ont commencé à être construits dans les années 60. A cette époque, malgré les récentes avancées sur la focalisation forte, les premiers anneaux de stockage sont à focalisation faible et permettent des collisions électrons/positrons.

C'est alors qu'a commencé à apparaître l'importance de l'alignement des éléments magnétiques. Comme nous le montrerons dans la prochaine partie, un défaut d'alignement des éléments magnétiques, en particulier des quadrupôles, introduit des perturbations en ce qui concerne la dynamique du faisceau. Comme ces perturbations sont proportionnelles aux défauts d'alignement et à la force du champ magnétique produit, la maîtrise de l'alignement devient un enjeu majeur.

1.2 Les sources de lumière synchrotron

1.2.1 Histoires de rayonnements

Toute particule relativiste dont la trajectoire est courbée par un champ magnétique émet un rayonnement électromagnétique dit « synchrotron ». Il n'est pas possible de connaître la date exacte du premier rayonnement émis. En effet, les particules chargées relativistes voyageant le long des lignes de champ magnétique générées par diverses étoiles et planètes émettent ce type de rayonnement de manière naturelle (sans intervention humaine). Quant à la découverte du phénomène, elle remonte au 24 avril 1947. Ce jour-là, les chercheurs du laboratoire de recherche de General Electric, situé au Etats-Unis, ont observé visuellement le rayonnement synchrotron produit par leur synchrotron à électrons. Cependant, cette observation ne fut que la vérification expérimentale d'un phénomène pressenti par les scientifiques depuis plusieurs années. Tout commença en 1897 lorsque Larmor exprima, à partir de l'électrodynamique classique, la puissance totale émise par une particule chargée [8]. L'année suivante, le physicien français Liénard utilisa ce résultat pour l'étendre au cas d'une particule subissant une accélération centripète sur une trajectoire circulaire [9]. Ses travaux furent confirmés par les résultats de Wiechert qui obtint les mêmes résultats de manière indépendante. Cela a donné naissance aux potentiels de Liénard-Wiechert, formalisme couramment utilisé lors de l'étude du rayonnement synchrotron.
Jusqu'aux années 50, d'un point de vue expérimental, le rayonnement synchrotron a été considéré comme une perte d'énergie des faisceaux de particules évoluant dans les accélérateurs. Cependant, lorsque ce faisceau lumineux fut expérimentalement observé, il a été étudié et son grand intérêt scientifique a été mis en évidence.

En effet, le rayonnement émis a :
- une grande étendue spectrale,
- une brillance exceptionnelle qui permet la réalisation d'expériences à très hautes résolutions spectrale ou spatiale,

- une polarisation qui est totalement contrôlable (linéaire, circulaire, elliptique),
- une structure pulsée qui permet des expériences résolues en temps,
- une grande stabilité, très intéressante pour l'imagerie.

A ses débuts, l'utilisation du rayonnement synchrotron était considérée comme une activité exotique. Par conséquent, les physiciens des hautes énergies pour lesquels étaient construits les accélérateurs, n'accordaient que peu de temps de faisceau aux utilisateurs de rayonnement synchrotron pour leur permettre de mettre en place leurs expériences. Dès lors que les anneaux de stockage commencèrent à se développer, l'utilisation d'un faisceau d'électrons comme source de rayonnement synchrotron est rapidement devenue avantageuse en terme de puissance rayonnée. Dans les années 1970, de nombreux anneaux de stockage ont été construits, ces derniers partageant leurs activités entre la physique des hautes énergies et l'utilisation du rayonnement synchrotron. Cela constituait les sources de lumière synchrotron de première génération.

La deuxième génération regroupe les accélérateurs construits uniquement pour produire du rayonnement synchrotron. Le premier fut celui de Daresbury (1970) appelé Synchrotron Radiation Source (SRS). Devant une demande de plus en plus importante, de nombreuses sources de rayonnement synchrotron ont été construites dans le monde. On notera la naissance à Orsay du premier anneau de stockage français dédié à la lumière synchrotron : Super-ACO en 1984. Avant Super-ACO, il existait déjà deux accélérateurs de particules : le Dispositif de Collisions dans l'Igloo (DCI) et l'Accélérateur Circulaire d'Orsay sur lesquels des expériences sur le fameux rayonnement ont été menées. Quelque soit le pays où est construite la source de lumière, le phénomène observé est le même : la demande est toujours plus croissante.

Parmi les nombreux paramètres caractérisant la lumière synchrotron, la brillance est la seule grandeur que les utilisateurs ne peuvent pas optimiser. La brillance représente le flux de photons de la lumière synchrotron. La brillance est un invariant en mécanique statistique, ce qui explique l'impossibilité de l'optimiser une fois le faisceau de lumière produit. Seule une optimisation de la source, c'est-à-dire le faisceau d'électrons, permet d'augmenter la brillance. Les sources de lumière synchrotron de troisième génération sont optimisées pour fournir des faisceaux de photons ayant une grande brillance. En plus de l'optimisation de l'optique de l'anneau de stockage, ce dernier doit accueillir de nouveaux éléments qui permettent d'augmenter la brillance : les onduleurs. Ces éléments d'insertions font "onduler" le faisceau, pour qu'à chaque changement de trajectoire, les électrons produisent du rayonnement synchrotron. L'introduction de ces onduleurs requiert une optimisation de l'optique afin de dégager de l'espace au sein de l'anneau de stockage.

1.2.2 Le synchrotron SOLEIL

Le synchrotron SOLEIL n'est pas un synchrotron au sens originel du terme comme beaucoup de sources de rayonnement synchrotron de 3ème génération mais un ensemble de trois types de machines.

- Un accélérateur linéaire (LINAC) qui fournit un faisceau d'électrons d'une énergie de 100 MeV,
- un booster qui, lui est un synchrotron : il amène les électrons à leur énergie nominale de fonctionnement à savoir 2.75 GeV.
- un anneau de stockage dont le rôle est de conserver un faisceau d'électrons stable et de petite taille afin de produire le rayonnement synchrotron.

Le but de cette source est de fournir une lumière dont le spectre commence dans l'infrarouge (10^{-2} eV) jusqu'à atteindre le début des rayons X-durs (1 keV) afin de satisfaire toute la communauté des utilisateurs. La stabilité et la brillance des faisceaux de photons feront de

SOLEIL une des sources les plus performantes au monde.

1.2.2.1 Applications

Un accélérateur d'électrons dédié à la production de rayonnement synchrotron est une machine conçue pour une communauté d'utilisateurs. SOLEIL sera équipé de 24 lignes de lumière dans lesquelles diverses expériences seront menées à partir de la lumière synchrotron (voir figure 1.8).

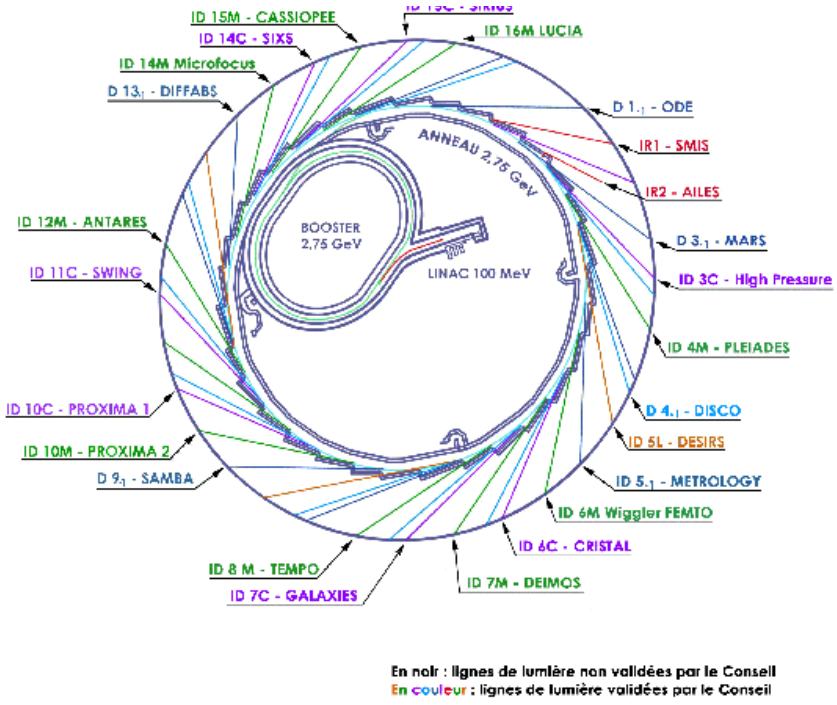

FIG. 1.8 – Lignes de lumières de SOLEIL

Dans les laboratoire situés dans les lignes de lumière, le faisceau de photons pourra avoir des applications :

- médicales (radiothérapie, pharmacie),
- technologiques (caractérisation de matériaux, micro-technologie),
- environnement (détection de polluants)
- patrimoine (restauration).

Il est important de noter que cette présentation des applications utilisant la lumière synchrotron est très succincte. Cependant, elle permet tout de même de rendre compte de la diversité des domaines de recherches pouvant avoir recours à ce type de rayonnement.

1.2.2.2 Introduction au formalisme des accélérateurs

Pour produire le rayonnement synchrotron, les électrons circulent dans un anneau dit de stockage. Cet anneau est composé de divers éléments produisant des champs magnétiques permettant de définir la trajectoire et les caractéristiques du faisceau d'électrons. Les électrons voyageant à la vitesse v, subissent la force de Lorentz ($\overrightarrow{F_l}$) en présence de l'induction magnétique ($\overrightarrow{B}$) et électrique ($\overrightarrow{E}$).

$$\overrightarrow{F_l} = q\left(\overrightarrow{E} + \overrightarrow{v} \times \overrightarrow{B}\right) \tag{1.10}$$

Tout accélérateur circulaire est une succession de mailles comportant des éléments de courbure (dipôles) qui permettent au faisceau de suivre une trajectoire circulaire, des éléments de focalisation (quadrupôles) empêchant le faisceau de diverger et des espaces libres entre chaque élément. Il existe d'autres éléments mais nous ne les détaillerons pas dans cette partie.

En matière de modélisation, chaque élément cité précédemment intervenant dans la dynamique du faisceau de particules peut être associé à une matrice de transfert (M) qui permet de lier la position (y) et l'angle (y') des particules avant $(s = s_0)$ et après sa traversée $(s = s_1)$ par rapport à une référence théorique.

$$\begin{pmatrix} y(s_1) \\ y'(s_1) \end{pmatrix} = \begin{pmatrix} a & b \\ c & d \end{pmatrix} \begin{pmatrix} y(s_0) \\ y'(s_0) \end{pmatrix} = M \cdot \begin{pmatrix} y(s_0) \\ y'(s_0) \end{pmatrix} \tag{1.11}$$

Espace libre

L'exemple le plus simple en matière de matrice de transfert est l'espace vide. Lorsque le faisceau traverse un espace vide de champ électromagnétique de longueur l, il le traverse en ligne droite comme le montre la figure 1.9. Ce qui donne la matrice de transfert suivante :

$$\begin{pmatrix} y(s_1) \\ y'(s_1) \end{pmatrix} = \begin{pmatrix} 1 & l \\ 0 & 1 \end{pmatrix} \begin{pmatrix} y(s_0) \\ y'(s_0) \end{pmatrix} \tag{1.12}$$

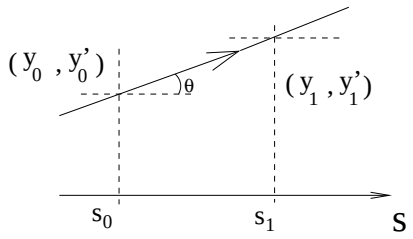

FIG. 1.9 – Espace libre

Élément de courbure

Pour courber la trajectoire des particules dans le plan horizontal, un champ magnétique purement vertical est appliqué. Ce champ magnétique est produit par les éléments appelés dipôles. La figure 1.10 montre le schéma d'un dipôle en "H" sur lequel est tracée la force de Laplace vue par les électrons. La traversée d'un dipôle peut s'exprimer par une matrice de transfert exprimée par 1.13 pour le cas des dipôles dit "secteur" ayant un rayon de courbure ρ et un angle de déflexion θ (voir 1.11).

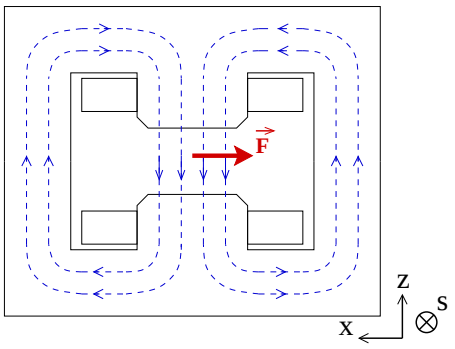

FIG. 1.10 – Dipôle : vue de face

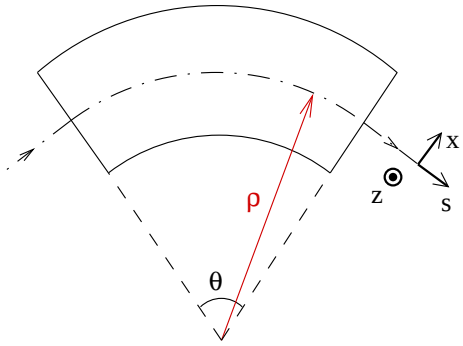

FIG. 1.11 – Dipôle : vue de dessus

$$M^H_{Sect} = \begin{pmatrix} cos\,\theta & \rho\, sin\,\theta \\ -(1/\rho)\, sin\,\theta & cos\,\theta \end{pmatrix} \qquad M^V_{Sect} = \begin{pmatrix} 1 & \rho\,\theta \\ 0 & 1 \end{pmatrix} \tag{1.13}$$

La plupart des machines sont équipées de dipôles dits rectangulaires, ces derniers étant beaucoup plus faciles à fabriquer. La terminaison rectangulaire ajoute un effet focalisant dans le plan vertical et défocalisant dans le plan horizontal. La matrice de transfert d'un tel élément est obtenue en multipliant la matrice dipôle secteur par une matrice tenant compte de cet effet.

$$M_{Rect} = \begin{pmatrix} 1 & 0 \\ \frac{1}{\rho}\, tan(\frac{\theta}{2}) & 1 \end{pmatrix} \cdot M_{Sect} \cdot \begin{pmatrix} 1 & 0 \\ \frac{1}{\rho}\, tan(\frac{\theta}{2}) & 1 \end{pmatrix} \tag{1.14}$$

Lentille Focalisante

La focalisation du faisceau d'électrons est assurée par des champs magnétiques quadrupolaires, comme le montre la figure 1.12

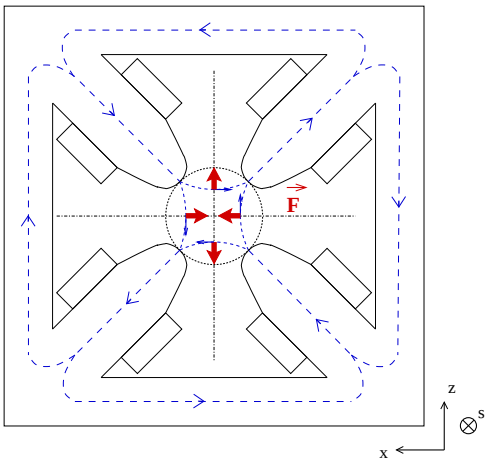

FIG. 1.12 – Quadrupôle focalisant dans le plan horizontal pour un faisceau d'électrons

Comme nous l'avons vu précédemment, les quadrupôles peuvent être assimilés en première approximation à des lentilles minces de longueur focale f (analogie avec l'optique géométrique). Ainsi l'action des quadrupôles sur le faisceau peut être traduit par la relation suivante :

$$\begin{pmatrix} y(s_1) \\ y'(s_1) \end{pmatrix} = \begin{pmatrix} 1 & 0 \\ -1/f & 1 \end{pmatrix} \begin{pmatrix} y(s_0) \\ y'(s_0) \end{pmatrix} \tag{1.15}$$

Si k est la force de focalisation du quadrupôle ($k = \frac{g}{B\rho}$, g en T.m), alors $k.l = 1/f$ avec l représentant la longueur magnétique du quadrupôle. Comme le montre la figure 1.13, l'angle de déflection imposé par la lentille est :

$$\theta = \frac{1}{f}\, y \tag{1.16}$$

Dès lors que la distance focale est courte devant la longueur du quadrupôle, ce qui est souvent le cas, il faut utiliser les matrices de transfert d'une lentille épaisse (voir A.5).

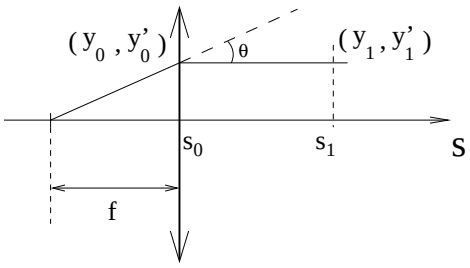

FIG. 1.13 – Lentille mince

1.2.3 Optimisation de l'Anneau de Stockage

Avant d'étudier l'optimisation de l'Anneau de Stockage, nous nous proposons d'effectuer un bref rappel des grandeurs fondamentales de la physique des accélérateurs.

1.2.3.1 Grandeurs fondamentales de la physique des accélérateurs

Le but de cette partie est d'introduire quelques éléments fondamentaux concernant la physique des accélérateurs. Après un bref rappel de quelques résultats de la relativité, nous nous attarderons sur l'étude du mouvement d'une particule chargée. Par cette étude, nous allons faire apparaître un certain nombre de paramètres clés souvent utilisés pour définir les propriétés du faisceau d'électrons.

Rappel des équations de la relativité
Une particule de charge q et de quantité de mouvement $\overrightarrow{p}$ voyageant à la vitesse $\overrightarrow{v}$ dans un environnement soumis à un champ électromagnétique subit la force de Lorentz ($\overrightarrow{F_l}$) définie par l'équation 1.10.

$$\frac{d\overrightarrow{p}}{dt} = \overrightarrow{F_l} \tag{1.17}$$

La relativité nous permet d'exprimer la relation entre la quantité de mouvement $p = ||\overrightarrow{p}||$, l'énergie totale $\mathcal{E}$, l'énergie cinétique $\mathcal{E}_k$ et l'énergie au repos $\mathcal{E}_0$ de la particule.

$$\mathcal{E} = \mathcal{E}_0 + \mathcal{E}_k \tag{1.18}$$

$$\mathcal{E}^2 = \mathcal{E}_0^2 + p^2c^2 = (m_{p0}\,c^2)^2 + p^2c^2 \tag{1.19}$$

c étant la vitesse de la lumière et m_{p0} étant la masse de la particule au repos, liée à sa masse m_p par la relation :

$$m_p = m_{p0}\gamma_r \tag{1.20}$$

γ_r est l'énergie réduite de la particule :

$$\frac{\mathcal{E}}{\mathcal{E}_0} = \frac{m_{p0}\gamma_r\,c^2}{m_{p0}\,c^2} = \gamma_r \tag{1.21}$$

γ_r peut s'exprimer en fonction de la vitesse réduite de la particule $\beta_r = v/c$.
En divisant l'équation 1.17 par $(m_pc^2)^2$, on obtient la relation suivante :

$$\gamma_r^2 = 1 + (\beta_r)^2 \tag{1.22}$$

Cela nous permet de définir la quantité de mouvement réduite :

$$\frac{pc}{\mathcal{E}_0} = \sqrt{\gamma_r^2 - 1} \tag{1.23}$$

Equations du mouvement quand $\Delta p/p_0 = 0$

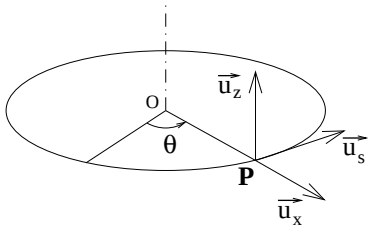

FIG. 1.14 – Coordonnées cylindriques

A partir de l'équation 1.17, on obtient l'équation du mouvement d'une particule chargée dans le cadre de l'approximation linéaire [10]. Cette équation est exprimée dans le repère (P,$\vec{u_x}$,$\vec{u_z}$,$\vec{u_s}$) lié à la particule.

$$x'' + k_x(s)x = 0\,; \qquad x'' = \frac{d^2x}{ds^2} \tag{1.24a}$$

$$z'' + k_z(s)z = 0 \tag{1.24b}$$

Ces équations sont sans second membre pour l'instant car toutes les particules ont à la même énergie ($\Delta p/p_0 = 0$). Les équations 1.24 sont linéaires et sont de la forme de l'équation de Hill. Elles sont aussi découplées par rapport à x et z, ce qui permet de regrouper l'étude sur une seule équation (1.25) dont la variable est y :

$$y'' + K(s)\, y = 0 \tag{1.25}$$

La fonction K doit vérifier la condition de périodicité : $K(s + L) = K(s)$, L étant soit la circonférence de l'anneau, soit la longueur d'une superpériode. Les anneaux sont constitués de cellules regroupées en superpériodes, ces dernières se répétant un certain nombre de fois dans l'anneau, $K(s)$ vérifie une condition de périodicité.

L'équation de Hill est une équation différentielle du second ordre ressemblant à celle d'un oscillateur harmonique à la différence près que $K(s)$ n'est pas constant. On montre que la solution de l'équation 1.25 est de la forme :

$$y(s) = \sqrt{\beta_y(s)\,\epsilon}\, cos(\varphi(s) + \varphi_0)\,;\ \text{avec}\ \varphi' = \frac{1}{\beta_y} \tag{1.26}$$

$$y'(s) = -\sqrt{\frac{\epsilon}{\beta_y(s)}}\, cos(\varphi(s) + \varphi_0) + \frac{\beta_y'(s)}{2}\sqrt{\frac{\epsilon}{\beta_y(s)}} sin(\varphi(s) + \varphi_0) \tag{1.27}$$

$\beta_y(s)$ est la fonction bétatron , ϵ l'émittance définie dans un prochain paragraphe, $\varphi(s)$ la phase de la particule ($\varphi(s) = \int ds/\beta(s)$) et φ_0 représente la phase initiale de la particule.

Le nombre d'onde ν

Le nombre d'onde représente le nombre d'oscillations de la fonction bétatron sur 1 tour du faisceau.

$$\nu_y = \frac{1}{2\pi} \oint \frac{ds}{\beta_y(s)} \tag{1.28}$$

L'émittance
Dans l'espace des phases (y,y'), les équations 1.26 et 1.27 représentent l'équation d'une ellipse (voir figure 1.15). Le point noir représente un électron pour une position longitudinale donnée (s) pour laquelle ses coordonnées dans l'espace des phases sont y et y'. Lorsque $\beta'_y(s) = 0$, les demi-axes de l'ellipses sont $\sqrt{\beta(s)\,\epsilon}$ pour la direction y et $\sqrt{\epsilon/\beta(s)}$ suivant y'.

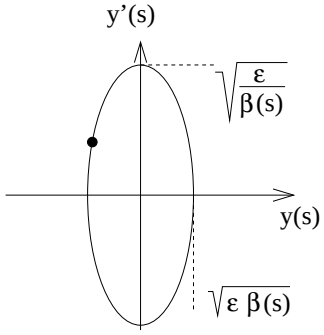

FIG. 1.15 – Emittance

Cette ellipse a une aire $\mathbf{A} = \pi\,\epsilon$ où ϵ représente l'émittance du faisceau d'électrons exprimée en mm.mrad.

Matrice de transfert
A partir des équations 1.26 et 1.27, on montre que la matrice de transfert peut s'exprimer de manière générale en fonction des paramètres dits "paramètres de Twiss", α, β, γ.

$$M_{s_0/s_1} = \begin{pmatrix} \frac{\sqrt{\beta_1}}{\sqrt{\beta_0}}(cos(\Delta\varphi) + \alpha_0 sin(\Delta\varphi)) & \sqrt{\beta_1\,\beta_0}\,sin\,(\Delta\varphi) \\ \frac{1}{\sqrt{\beta_1\,\beta_0}}\left((\alpha_0 - \alpha_1)cos(\Delta\varphi) - (\alpha_1\,\alpha_0 + 1)sin\Delta\varphi\right) & \frac{\sqrt{\beta_0}}{\sqrt{\beta_1}}(cos\Delta\varphi - \alpha_1 sin\Delta\varphi) \end{pmatrix} \tag{1.29}$$

avec $\beta_0 = \beta(s_0)$, $\beta_1 = \beta(s_1)$, $\Delta\varphi = \varphi(s_1) - \varphi(s_0)$ et $\alpha(s) = -\beta(s)'/2$.

Équation du mouvement quand $\Delta p/p_0 \neq 0$
Lorsque l'on traite le cas où toutes les particules ne sont pas à la même énergie $\Delta p/p_0 \neq 0$, on dit qu'il y a de la dispersion et elle est définie par la fonction de dispersion $\eta(s)$. Dans le cas où $\Delta p/p_0 \neq 0$, l'équation 1.24a devient :

$$x'' + k_x(s)x = \frac{1}{\rho(s)}\frac{\Delta p}{p_0} \quad ; \quad \text{avec } \rho(s) \text{ le rayon de courbure} \tag{1.30}$$

La solution de cette équation différentielle est de la forme suivante :

$$x(s) = x_\beta(s) + x_\eta(s) \tag{1.31}$$

- Avec $x_\eta(s) = \eta(s)\Delta p/p_0$ décrivant la deviation de l'orbite fermée pour les particules ayant un Δp donné par rapport à l'orbite de référence,
- et $x_\beta(s)$ est la solution de l'équation homogène et représente les oscillations de la fonction bétatron autour de l'orbite fermée dispersive.

Ainsi la solution s'exprime de la manière suivante :

$$x(s) = \eta(s)\frac{\Delta p}{p_0} + \sqrt{\epsilon\beta_x(s)}\, cos(\varphi(s) + \varphi_0) \tag{1.32}$$

$$x'(s) = \eta'(s)\frac{\Delta p}{p_0} + (1 - \alpha(s))\sqrt{\frac{\epsilon}{\beta_x(s)}}[-sin(\varphi(s) + \varphi_0) + cos(\varphi(s) + \varphi_0)] \tag{1.33}$$

1.2.3.2 Optimisation de la brillance

Comme nous l'avons dit précédemment, pour optimiser la brillance, il faut travailler sur la source du rayonnement. Cela commence par le choix du type de particule à accélérer. La puissance rayonnée P_{ray} par une particule d'énergie $\mathcal{E}$, suivant une trajectoire de rayon de courbure ρ est la suivante :

$$P_{ray} = \frac{e^2\, c}{6\pi\epsilon_0 (m^2_{0pc})^4}\frac{\mathcal{E}^4}{\rho^2} \tag{1.34}$$

Plus l'énergie au repos ($m_{p0}c^2$) de la particule sera petite, plus la puissance de rayonnement synchrotron rayonnée sera grande. C'est pourquoi les sources de lumière synchrotron utilisent des électrons comme source de rayonnement. En calculant le rapport entre la puissance rayonnée par un électron P^e_{ray} et la puissance rayonnée par un proton P^p_{ray} de même énergie, nous constatons que :

$$\frac{P^e_{ray}}{P^p_{ray}} = \left(\frac{m_{pr}\, c^2}{m_e\, c^2}\right)^4 = 1.13.10^{13} \tag{1.35}$$

La brillance $\mathcal{B}$ est le flux de photons (dN_{ph}/dt) par unité de surface de la source ($d\mathcal{A}$), par unité d'angle solide du cône de rayonnement ($d\Omega$), par unité de bande passante du spectre ($d\lambda/\lambda$). Cette brillance est proportionnelle au courant du faisceau $I_{faisceau}$ et inversement proportionnelle à son émittance.

$$\mathcal{B} = \frac{dN_{ph}/dt}{d\mathcal{A}\, d\Omega\, d\lambda/\lambda} \propto \frac{I_{faisceau}}{\epsilon_x\, \epsilon_z} \tag{1.36}$$

La brillance est donc optimisée en travaillant sur deux paramètres propres au faisceau d'électrons :

- son courant ($I_{faisceau}$),
- son émittance ($\epsilon_x\, \epsilon_z$).

Il n'est pas possible d'augmenter de manière significative la brillance en augmentant le courant car ce dernier sera vite limité par la pression résiduelle du vide (durée de vie), par les instabilités dues aux courants images circulant dans la chambre à vide et au refroidissement des éléments qui doivent absorber l'énergie dissipée par la partie du faisceau de photons qui n'est pas utilisée.

Par conséquent, il faut diminuer l'émittance. On montre que l'émittance horizontale dépend du nombre d'aimants de courbure N_a comme le montre la relation 1.37.

$$\epsilon_x \propto \theta^3 = \left(\frac{2\pi}{N_a}\right)^3 \tag{1.37}$$

Cependant plus le nombre de dipôles sera grand, plus la circonférence de la machine sera grande. Il y a donc un compromis à trouver entre les performances désirées pour l'émittance et les moyens financiers disponibles pour construire la machine.

De plus la fonction bétatron et la fonction de dispersion doivent être minimisées au centre des dipôles.

La limitation de la taille de la machine par le budget et la limitation en fonction béta et de dispersion nous amènent à concevoir des cellules très courtes. Un ensemble de cellules différentes composent une super-période, qui est une structure symétrique répétée le long de la machine. Une cellule est un ensemble d'éléments magnétiques qui est répété dans chaque super-période. En prenant pour exemple le cas de l'anneau de stockage de SOLEIL, il est composé de 4 super-périodes, elles-mêmes composées de 4 cellules.

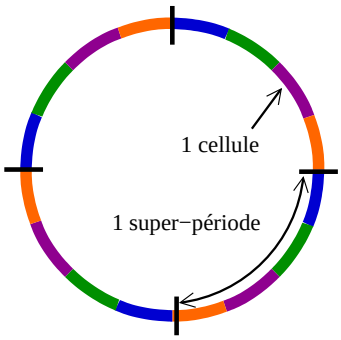

FIG. 1.16 – Décomposition de l'anneau de stockage

Le besoin en cellules courtes nécessite d'avoir recours à une focalisation forte. Plus la force des quadrupôles est grande plus le faisceau va être sensible aux défauts de positionnement de leur axe magnétique. Du fait de la grande sensibilité de la machine à cause de la forte focalisation des quadrupôles, il faut que le faisceau passe au plus proche de l'axe magnétique. C'est l'objet de notre travail.

Pour atteindre une brillance de 10^{20} photons/s/mm^2/mrad^2/0.1% de bande passante, toutes les précautions doivent être prises concernant les éléments de l'anneau de stockage. En ce qui concerne les quadrupôles, le faisceau doit traverser les quadrupôles à l'intérieur d'une zone limitée à 25 μm r.m.s. dans le plan transverse autour de l'axe magnétique.

1.3 Problématique de l'alignement

Comme on a pu le voir, les premiers développements des accélérateurs exigeaient d'importants progrès technologiques mais ne nécessitaient pas encore une maîtrise approfondie des différents éléments des machines. Ce n'est qu'une fois que les concepts généraux furent établis que s'est mise en place l'optimisation des éléments. Les effets des optimisations devenant de plus en plus pointus, les moyens utilisés pour les mesurer ont dû à leur tour être optimisés. La métrologie est rapidement devenue une discipline spécialisée dont les différentes applications sont aussi très ciblées.

Une fois l'élément réalisé, la chaîne de la conception est vérifiée en effectuant des mesures. Dès lors qu'un écart est constaté entre le modèle de la machine et la réalité délivrée par les mesures, il est ré-introduit dans le modèle pour affiner la conception (voir figure 1.17). La métrologie est le point clé de la chaîne d'optimisation, c'est l'étape qui permet d'en déterminer la qualité.

Ainsi la métrologie peut permettre de prédire d'autant plus fidèlement qu'elle peut être précise le comportement réel des particules traversant ces éléments. Étant données les performances visées par le Synchrotron SOLEIL et la constitution de la maille de l'anneau de stockage du point de vue de la physique de la machine, les quadrupôles sont les éléments les plus sensibles (voir partie 1.2.3.2). Par conséquent, SOLEIL a décidé d'assurer un suivi approfondi de la qualité

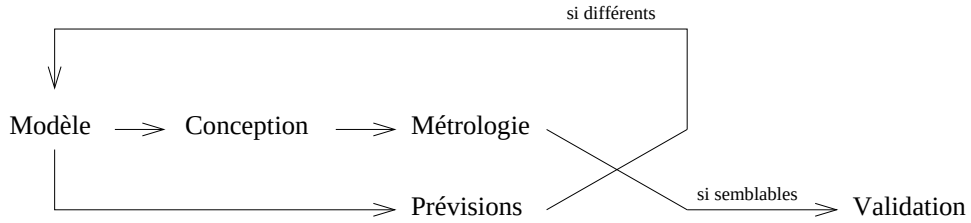

FIG. 1.17 – Rôle de la métrologie

des 160 quadrupôles de l'anneau de stockage. Ce suivi commence par la caractérisation de leurs propriétés magnétiques au moyen d'un banc de mesures harmoniques que SOLEIL a souhaité développer. Une caractérisation de quadrupôle ne signifie pas seulement une mesure précise de ses caractéristiques magnétiques. Il faut aussi, à partir de la mesure initiale, ramener son axe magnétique sur l'axe théorique ($\pm$ 25μm) et annuler le moindre angle ($\pm$0.1 $mrad$) autour de l'axe longitudinal par rapport au plan horizontal. Bien que minimisée par ce travail, la dispersion du positionnement et de l'orientation de l'axe magnétique des quadrupôles par rapport à une référence unique risque de s'accroître lors de l'installation de ces derniers sur la machine et ce, malgré le soin que l'on peut apporter à cette tâche.

C'est alors, que l'on aura recours à des mesures traduisant le comportement du faisceau vis à vis des défauts d'alignement finaux des quadrupôles. Du fait de la grande résolution des outils que l'on va utiliser pour ces mesures, il sera possible de connaître avec précision les défauts d'alignement des quadrupôles par rapport aux références des outils de mesures. Suite à ces mesures une correction sera effectuée, cela peut être une modification de la prise en compte des défauts d'alignement initiaux dans le modèle qui permet de piloter la machine ou alors un nouvel alignement mécanique des quadrupôles.

Le but de cette partie est de recenser les outils qui pourraient être utilisés pour effectuer les tâches mentionnées précédemment. C'est pourquoi dans un premier temps, on s'intéressera aux dispositifs de mesures magnétiques de façon générale pour ensuite travailler sur les outils que l'on est amené à utiliser lors des mesures faisant intervenir le faisceau d'électrons.

1.3.1 Dispositifs de mesures magnétiques

Il existe de nombreux procédés permettant de mesurer le champ magnétique, le choix dépendant du type de champ à mesurer (fixe ou variable dans le temps), du type d'information désirée (ponctuel/global, 1D/.../ 3D), de son ordre de grandeur (quelques μT, quelques T), de la précision souhaitée et du type de mesure (absolu ou relatif)[11].

Sur la figure (1.18), apparaissent plusieurs procédés de mesures dont la précision a été tracée en fonction des niveaux de champ à mesurer.

Comme cela a été dit précédemment, malgré sa pertinence la figure 1.18 ne suffit pas pour choisir le dispositif de mesure. En plus des paramètres évoqués, il faut aussi ajouter l'encombrement, la mise en oeuvre et surtout le coût.

1.3.1.1 Les procédés utilisés

La résonance magnétique nucléaire (RMN)
En 1938, la résonance magnétique nucléaire était utilisée pour la première fois. De nos jours

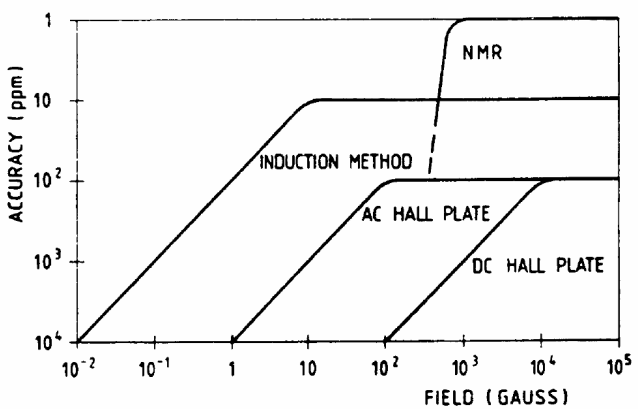

FIG. 1.18 – Plage d'utilisation des capteurs ($1\,Gauss = 1 \cdot 10^{-4}\,T$) [11]

cette méthode de mesure est très répandue et ce, dans des domaines divers comme la chimie, la physique et l'imagerie médicale.

La RMN permet de mesurer le champ magnétique avec une très grande précision car elle repose sur un phénomène physique bien maîtrisé. Dès qu'une particule a un spin non nul, elle a intrinsèquement un moment magnétique non nul $\overrightarrow{\mu}$. Par conséquent, si cette particule est placée dans une induction magnétique B, elle entre en précession à la fréquence de Larmor (f_L) [12] :

$$f_L = \frac{\omega_L}{2\pi} = \frac{\gamma}{2\pi} B \tag{1.38}$$

où γ est le coefficient gyromagnétique qui est propre à la particule utilisée.

Ainsi à partir de 1.38, connaissant γ et en mesurant la fréquence de précession, on obtient la valeur de l'induction magnétique B. Les particules sont des protons ou des deutérons du matériau utilisé pour la mesure. Ces derniers étant présent dans les molécules d'eau, c'est l'eau qui sert généralement d'échantillon de test. Cet échantillon est excité au moyen d'un bobinage connecté à un oscillateur radiofréquence et la fréquence de résonance mesurée est directement proportionnelle à l'induction magnétique. Le coefficient de proportionnalité étant de 42.5764 MHz/T pour les protons et de 6.53569 MHz/T pour les deuterons.

Les sondes RMN peuvent mesurer une plage d'induction magnétique allant de 11 mT à 13T avec une précision de 10 ppm [11]. Les avantages de ce type de mesure sont nombreux, on notera principalement sa grande précision de mesure, la linéarité en fonction du niveau de champ, et son utilisation relativement simple. Les inconvénients que l'on peut trouver à la sonde RMN est qu'elle ne peut mesurer que des champs homogènes et stables dans le temps et ne délivre aucune information quant à leur direction.

Du fait de la grande précision du champ magnétique délivré par ces sondes, elles servent à étalonner grand nombre de dispositifs de mesures magnétiques et notamment les sondes de Hall.

Générateur de Hall

En 1856 W. Thomson a découvert qu'un conducteur électrique placé dans un champ magnétique voyait sa résistance augmenter. Puis en 1879, E.H. Hall a trouvé une explication à ce phénomène. Par ailleurs, il a mesuré une différence de potentiel de part et d'autre du sens de circulation d'un courant appliqué à un matériau conducteur (figure 1.19).

L'effet Hall est une réaction à la force magnétique ($\overrightarrow{F_B}$) subie par les électrons se déplaçant à

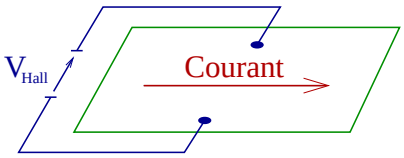

FIG. 1.19 – Effet Hall

la vitesse $\overrightarrow{v}$ dans un matériau soumis à une induction magnétique $\overrightarrow{B}$.

$$\overrightarrow{F_B} = q\overrightarrow{v} \times \overrightarrow{B} \tag{1.39}$$

$\overrightarrow{F_B}$ dévie les électrons de leur trajectoire initiale. Lorsque l'équilibre s'établit, les forces agissant sur les électrons se neutralisent selon l'expression la force de Lorentz :

$$\overrightarrow{F_l} = \overrightarrow{F_E} + \overrightarrow{F_B} = q\left(\overrightarrow{E} + \overrightarrow{v} \times \overrightarrow{B}\right) = \overrightarrow{0} \tag{1.40}$$

Il y a donc apparition d'une force électrostatique qui se traduit par un champ électrique $\overrightarrow{E}$. Cependant, ces particules évoluant dans un matériau (supposé homogène et isotrope) ne vont pas subir l'effet de ce champ magnétique aussi librement que dans le vide. Elles seront vite freinées par les collisions avec les atomes environnants mais d'un point de vue macroscopique, on observe un mouvement global linéaire des particules. La direction du mouvement est déviée d'un angle θ par rapport au cas sans champ magnétique. θ est l'angle de Hall [13].

En effet, sous l'effet d'une induction magnétique, une composante transverse de champ électrique (E_x) apparait :

$$\overrightarrow{E} = E_s\,\overrightarrow{e_s} + E_x\,\overrightarrow{e_x} \tag{1.41}$$

Avec

$$tan(\theta) = \frac{E_s}{E_x} = \mu_H\,B \tag{1.42}$$

μ_H est la mobilité de Hall.

On montre que pour optimiser l'effet Hall, il faut utiliser un matériau peu conducteur mais dont les porteurs de charges ont une grande mobilité. Certains semi-conducteurs sont utilisés pour exploiter l'effet Hall car ils ont ces propriétés contrairement aux métaux conducteurs.

Afin que ce phénomène soit applicable à la mesure de champs magnétiques, il est nécessaire que la sonde de Hall soit peu encombrante.

De plus même en l'absence de champ magnétique, certains défauts de fabrication induisent l'apparition d'une tension de Hall. Même si l'effet de ces défauts peut être maîtrisé, il n'existe pas de fonction mathématique liant la tension de Hall au champ magnétique. C'est pourquoi dans le cadre de mesures magnétiques de haute précision, un étalonnage de la réponse de la sonde de Hall est nécessaire. Cela est effectué au moyen d'une source de champ dipolaire dans laquelle est placée une sonde RMN servant de référence pour la mesure de champ. Pour différentes valeurs de champ mesurées par la sonde RMN, la tension délivrée par la sonde de Hall est relevée. Ainsi, une courbe réponse décrivant l'évolution de la tension de Hall en fonction du champ magnétique mesuré à une température de travail donnée est obtenue.

Toutefois, un tracé précis de la courbe réponse nécessite la maîtrise de plusieurs éléments :

- homogénéité du champ magnétique d'étalonnage,
- stabilité de la source de courant permettant de produire le champ magnétique,
- stabilité de la température de travail,

– niveau de bruit.

Dès lors qu'il est nécessaire de mesurer des champs magnétiques non homogènes, de nouveaux effets sont à prendre en compte comme l'effet Hall gradient, et l'effet Hall plan. Ces derniers sont explicités notamment par les travaux de B. Berkes [13].

Du fait de leur petite taille, les sondes de Hall permettent d'effectuer des mesures de champ magnétiques quasi ponctuelles (taille de l'élément sensible : $0.2 * 0.2 * 0.2\, mm^3$) que ce soit en mode continu ou variable. Elles permettent de tracer des cartes de champs magnétiques délivrant des informations à la fois globale et locale. Malgré un nombre conséquent de paramètres à prendre en compte, l'utilisation des sondes Hall est très répandue car relativement simple. En effet, ces dernières sont souvent livrées avec une électronique qui gère de manière satisfaisante l'effet des défauts. Mais dans le cadre de mesures magnétiques très précises, de nombreux tests doivent tout de même être effectués afin de vérifier la qualité de la gestion électronique fournie. Leur coût est relativement réduit pour une gamme d'utilisation assez large que ce soit soit en terme de mesure de champ magnétique ou en terme de température d'utilisation (ambiante, cryogénique).

Le SQUID

Le SQUID (Superconducting Quantum Interference Device) est un dispositif permettant de mesurer des champs magnétiques très faibles en utilisant un phénomène propre aux matériaux supraconducteurs : l'effet Josephson. Les matériaux supraconducteurs ont la propriété d'atteindre une résistance nulle à très basse température. La possibilité de travailler à des courants très élevés en a fait des matériaux très utilisés pour les aimants d'accélérateurs devant fournir des inductions magnétiques élevées (8.3 T pour les dipôles du LHC) L'état supraconducteur est caractérisé par l'assemblage des électrons par paires (paires de Cooper) dès lors que la température, la densité de courant et le champ magnétique du matériau sont inférieurs à leur valeur critique. Ce couplage par paires intervient dans la définition du quantum de flux ψ_0 qui est une grandeur fondamentale permettant de caractériser l'effet Josephson :

$$\psi_0 = \frac{h}{2\,e} \approx 2.07 \cdot 10^{-15}\, T \cdot m^2 \tag{1.43}$$

où h est la constante de Planck et e la charge de l'électron.

L'effet Josephson apparaît lorsque deux matériaux supraconducteurs sont séparés par un isolant électrique de faible épaisseur (quelques nm).

En l'absence de tension appliquée aux bornes de la jonction, un courant continu ou courant de paires de Cooper, peut circuler dans la jonction : c'est l'effet Josephson continu.

Quant à l'effet Josephson alternatif, il apparaît dès lors que la tension appliquée est non nulle. Si la tension est continue, le courant de jonction oscille à une fréquence dépendant directement de cette tension et du quantum de flux. Le principe du SQUID repose sur sa capacité à compter les quanta de flux ψ_0.

Mesures par induction

Le principe utilise la loi de Faraday-Lenz sur l'induction électromagnétique :

$$u = -\frac{d\psi}{dt} \tag{1.44}$$

Dès lors qu'un fil conducteur subit une variation de flux, une force électromotrice e apparaît à ses bornes. C'est un procédé très utilisé car simple à appliquer mais surtout parce qu'il permet d'atteindre une très grande précision de mesure. Les aimants d'accélérateurs sont souvent mesurés

au moyen de bobines, la géométrie de ces dernières dépendant directement du type d'information à extraire. Ce procédé est très flexible car il permet de mesurer des champs magnétiques fixes ou variables, une grande plage de valeur de champ et ce, quelle que soit la température de travail (ambiante, cryogénique). Cette méthode est développée dans la prochaine partie traitant de la mesure d'aimants d'accélérateurs car elle y a été très exploitée du fait des qualités précédemment citées mais aussi de part sa capacité d'adaptation.

1.3.1.2 Mesures magnétiques d'aimants d'accélérateur

Les performances des accélérateurs dépendent de beaucoup de facteurs. En matière de qualité du faisceau de particules, les aimants sont parmi les éléments qu'il convient de maîtriser le mieux. Cela passe par une connaissance pointue de leurs caractéristiques magnétiques qui ne sont obtenues que par métrologie. L'idée d'effectuer une cartographie ponctuelle du champ magnétique produit par les aimants peut séduire dans un premier temps. Cependant, les accélérateurs devenant de plus en plus gourmands en nombre d'éléments magnétiques, il est nécessaire d'effectuer des mesures dites "de série". Les cartographies sont en général incompatibles avec ce mode de mesure qui doit allier rapidité d'exécution et précision. C'est pourquoi un grand nombre de méthodes utilisant des bobines mesurant des variations de flux ont été développées. Ces dernières permettent en effet une mesure rapide, précise et adaptée des propriétés magnétiques des aimants. L'homogénéité du champ, sa force, son axe magnétique, son intégrale, ses champs de fuite, ses harmoniques représentent l'ensemble des paramètres qui doivent être connus voire corrigés lorsque l'aimant est installé dans la machine. Ces paramètres sont mesurés par des méthodes différentes qui peuvent délivrer une information soit ponctuelle, soit intégrale.

Les aimants d'accélérateurs ne répondant pas tous aux mêmes critères de qualité, il est nécessaire de développer des outils de mesures bien spécifiques. Après avoir présenté l'intérêt des cartographies d'aimant, les nombreuses méthodes utilisant la loi de Faraday-Lenz seront développées.

Cartographie d'aimant

Ce type de mesure est en général effectué par des sondes de Hall étalonnées au moyen d'une sonde RMN. Une ou plusieurs sondes de Hall sont placées au bout d'un bras mécanique possédant N axes de liberté. Ainsi, en quadrillant l'espace à mesurer avec le capteur, une cartographie du champ magnétique est obtenue. A SOLEIL, la cartographie a été utilisée pour la caractérisation des dipôles. En effet, un boîtier contenant 15 sondes de Hall (figure 1.20) mono-dimensionnelles a permis de mesurer les propriétés du champ magnétique dans le plan médian de l'aimant (figure 1.21).

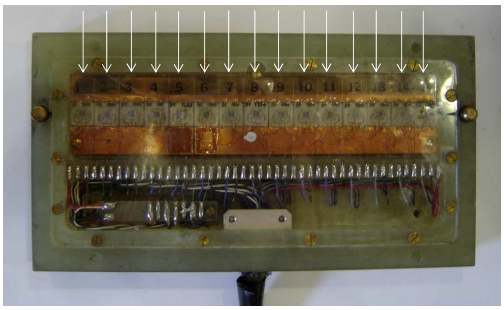

FIG. 1.20 – Boîtier 15 sondes de Hall

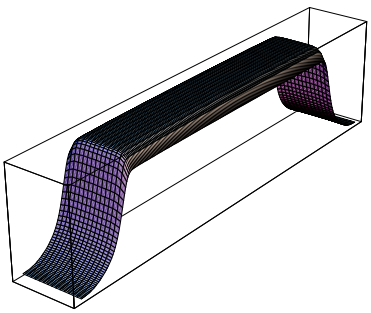

FIG. 1.21 – Exemple de cartographie

Plus la carte de champ doit être détaillée, plus la mesure est longue. A titre indicatif, la cartographie d'un dipôle de SOLEIL durait 2h (installation + mesures), et représentent 4110 mesures sur 1.4 mètres. Comme cela a été mentionné précédemment, ce type de mesure n'est pas compatible avec des mesures de série dans le contexte de SOLEIL. Néanmoins, il permet de caractériser quelques aimants, et pour déterminer l'identité magnétique des aimants, les méthodes par comparaison ont été développées.

Fil Tendu

Afin de minimiser le nombre de cartographies, la mesure consiste à comparer un aimant de référence cartographié à un aimant inconnu. Pour cela, une mesure de l'intégrale de champ des deux aimants est effectuée au moyen d'un fil conducteur tendu ("Stretched Wire") dans les deux entrefers. Les deux aimants sont alimentés en sens inverse de sorte que si les champs magnétiques sont identiques, les intégrales de champs s'annulent et la différence de potentiel mesurée aux bornes du fil est nulle. Si la tension mesurée est en dehors d'une tolérance fixée au préalable, alors l'aimant inconnu est cartographié afin de connaître l'origine de la dissemblance. A SOLEIL, sur 38 dipôles à mesurer, seulement 11 ont été cartographiés, ce qui a permis un gain de temps de 40 heures.

Plus généralement, la mesure magnétique au fil tendu est très intéressante car elle permet de déterminer directement l'intégrale de champ vue par le faisceau. Elle est très utilisée pour la mesure de l'intégrale de champ résiduelle des onduleurs, qui doit être corrigée pour que ces derniers aient un fonctionnement transparent du point de vue de la physique de la machine.

Fil Pulsé

Le fil tendu peut être utilisé pour déterminer des caractéristiques plus pointues mais cela nécessite des études et des équipements plus complexes.

Lorsqu'un fil tendu de tension T, de longueur l, soumis à une induction magnétique $B(s)$ indépendante du temps est parcouru par un courant alternatif $I(t)$ de fréquence $f = \omega/2\pi$, il peut entrer en résonance et se mettre à vibrer. Ainsi, en liant la fréquence du courant appliqué à la fréquence et l'amplitude de la vibration mesurée, les caractéristiques magnétiques de l'aimant mesuré peuvent être déterminées avec précision [14].

En effet, le principe fondamental de la dynamique permet de déterminer une telle relation pour les déplacements $\mathcal{D}_z(s,t)$ dans le plan vertical. Les forces subies par un tel fil de masse m dans le plan vertical sont :

- sa tension $\overrightarrow{T}$,
- les frottements avec l'air $\overrightarrow{Fr}$,
- la gravité $\overrightarrow{G}$,
- la force découlant de la loi de Laplace $\overrightarrow{F_{Mag}} = I(t)\overrightarrow{dl} \times \overrightarrow{B}$.

$$m\overrightarrow{a} = \overrightarrow{T} + \overrightarrow{Fr} + \overrightarrow{G} + \overrightarrow{F_{Mag}} = \sum \overrightarrow{F} \tag{1.45}$$

$$m\frac{\partial^2 \mathcal{D}_z(s,t)}{\partial t^2} = T\frac{\partial^2 \mathcal{D}_z(s,t)}{\partial s^2} - \gamma\frac{\partial^2 \mathcal{D}_z(s,t)}{\partial t} - m\,g + B_x(s) * I_0 e^{i\,\omega t} \tag{1.46}$$

La résolution de cette équation différentielle est détaillée dans les travaux de A. Temnykh [14] et permet de définir une fonction très utile. Cette fonction $\mathcal{H}(\omega)$ permet de calculer la moyenne

du produit de la position du fil ($\mathcal{D}_z(s,t)$) et du courant appliqué (I(t)).

$$\mathcal{H}(\omega) = \frac{1}{T}\int_0^T \mathcal{D}_z(s,t)\cdot I(t)\,dt = \sum_{n=0}^{\infty}\mathcal{H}_n(\omega) \tag{1.47}$$

$$\text{Avec } \mathcal{H}_n(\omega) = \frac{B_n\, I_0^2}{2m} sin\left(\frac{\pi n}{l}s\right)\frac{\omega-\omega_n}{4\omega(\omega-\omega_n)^2+\omega\gamma^2} \tag{1.48}$$

$$\text{et } B_x(s) = \sum_{n=0}^{\infty} B_n\, sin\left(\frac{\pi n}{l}s\right) \tag{1.49}$$

Lorsque les frottements sont faibles et la fréquence du courant appliqué est proche de la fréquence de résonance (ω_n), la fonction $\mathcal{H}_n$ est expérimentalement mesurable et permet d'identifier les coefficients de la fonction 1.50.

$$\mathcal{H}_n^{mes}(\omega) = \vartheta_n \frac{\omega-\tau_n}{4\omega(\omega-\tau_n)^2+\omega\, \upsilon_n^2} \tag{1.50}$$

Ainsi à partir de l'identification de ϑ_n, B_n peut être déduit,

$$B_n = \vartheta_n \frac{1}{sin\left(\frac{\pi n}{l}s\right)}\frac{2m}{I_0^2} \tag{1.51}$$

Cette méthode est très utilisée pour la caractérisation d'onduleurs mais aussi pour mesurer les quadrupôles. Le principal défaut de cette méthode réside dans le temps de mesure. En effet, l'identification de chaque harmonique prend du temps (30 harmoniques en 25 minutes [14]) et à cette durée, il faut ajouter le temps nécessaire à la caractérisation et à l'ajustement de l'axe magnétique.

Bobine Tendue

Afin de recueillir d'autres types d'information, il est nécessaire d'avoir recours aux bobines tendues appelées aussi "bodyless coil". Ce type de mesure permet d'avoir une mesure directionnelle de l'intégrale de champ mesurée. En effet seule la composante du champ magnétique perpendiculaire à la surface de la bobine est mesurée.

D'autre part, l'utilisation de bobines tendues dont la position est fixe dans le temps et l'espace donne la possibilité de caractériser des aimants permanents. En effets ces derniers étant positionnés sur un plateau mobile traversant la surface de la bobine tendue, le courant induit par leur passage est l'image de leurs caractéristiques magnétiques.

Bobine Tournante

Les mesures au moyen d'une bobine tournante permettent de déterminer les harmoniques de champ magnétique des multipoles de la machine. Le principe est faire tourner une bobine à un rayon fixe et de mesurer le flux produit par l'aimant. Ce type de mesure est en général intégral, c'est à dire que la bobine mesure l'intégrale de la projection des vecteurs induction par rapport à la surface définie par la bobine. Parfois pour certaines applications nécessitant une approche cartographique, il peut y avoir plusieurs bobinages juxtaposés longitudinalement, ce qui permet d'obtenir plus d'informations concernant l'intégrale de champ en fonction de la position longitudinale [15].

Il existe trois types de bobines tournantes :

- radiales : le plan du bobinage est radial (figure 1.22). Ce type de bobine n'est sensible qu'à la composante tangentielle du champ magnétique mesuré.

- tangentielles : le plan de la bobine est orthogonal au plan radial. Seule la composante tangentielle est mesurée (figure 1.23).
- multipolaires : ce type de bobine permet de ne mesurer qu'un ensemble d'harmoniques de champ bien définis [16] (figure 1.24).

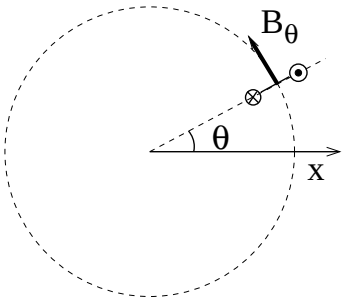

FIG. 1.22 – Radiale

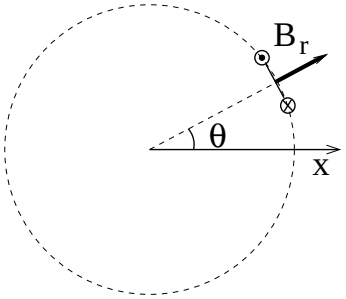

FIG. 1.23 – Tangentielle

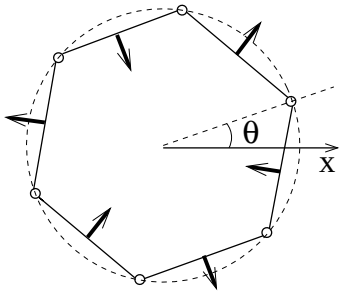

FIG. 1.24 – Multipolaire

A partir des harmoniques de champ magnétique mesurés, d'autres propriétés magnétiques telles que la position et l'orientation de l'axe magnétique peuvent être définies. Le traitement théorique concernant les bobines tournantes radiales est développé dans le chapitre 2.

Les mesures magnétiques des quadrupôles de SOLEIL ont été effectuées à l'aide de bobines radiales. Même si ces dernières sont plus simples à mettre en oeuvre, il est indispensable de maîtriser toute source de défauts car les performances visées sont très pointues. L'objectif de notre travail est d'obtenir une sensibilité suffisante pour mesurer et régler la position des axes magnétiques des quadrupôles à 25 μm près et leur orientation autour de l'axe longitudinal à 0.1 $mrad$ près.

Résumé du chapitre 1

Ce chapitre a montré que les méthodes utilisées pour la caractérisation des aimants d'accélérateurs sont bien connues. C'est l'augmentation des performances des accélérateurs qui a donné naissance à un travail de recherche visant à toujours améliorer la qualité des outils dédiés à la métrologie des aimants d'acélérateurs. Ce chapitre a également permis de mettre en évidence l'origine des contraintes sur la conception des quadrupôles du synchrotron SOLEIL. La dernière partie de ce chapitre, dédiée au recensement des méthodes de mesures, a permis de présenter celle utilisée pour caractériser les aimants multipolaires de SOLEIL : la méthode des bobines tournantes.

NOTE IMPORTANTE

Avec l'autorisation du président de l'Institut National Polytechnique de Lorraine, la suite du mémoire est écrite en anglais. Ce choix a pour but de faciliter la diffusion du travail de thèse au sein la communauté internationale des sources de lumière synchrotron. Chaque chapitre comprendra néanmoins deux encadrés en français : le premier en début de chapitre présentera son objectif et le deuxième en fin de chapitre résumera son contenu.

Chapter 2

Theoretical studies and Developments

Objectifs du chapitre
L'objectif de ce chapitre est de présenter les outils théoriques nécessaires à la mise en oeuvre des mesures magnétiques par bobines tournantes. Après avoir étudié la répartition du champ magnétique dans l'ouverture d'un aimant, nous proposerons un inventaire des erreurs de mesure qui peuvent conduire à de mauvaises interprétations. Il existe déjà dans la littérature de nombreux travaux portant sur des sources d'erreurs de mesure. Nous développerons ici une approche innovante de cette problématique par ce que nous appelons les expériences théoriques. Enfin, comme il est nécessaire de mesurer ces phénomènes pour pouvoir les corriger, une méthode appliquée au Banc de Mesures Magnétiques multipolaires de SOLEIL (BMS) est exposée.

The purpose of this chapter is to present the theoretical developments related to magnetic measurements performed by means of a rotating coil. In this context, the magnetic field in the aperture of a multipole magnet is first calculated to prepare the study of measuring errors effects. Several works have already treated this problem but a new approach is proposed here with the theoretical experiments. Then a method to determine and correct measuring errors of the SOLEIL Multipolar Magnetic Measurement Bench (SMB) is presented.

2.1 Harmonic coils theory

As introduced in section 1.3, specifications on quadrupole magnet magnetic field quality are tight. Magnetic field quality is defined in this part and is mostly determined by the magnetic design of the studied magnet. Moreover SOLEIL decided to fix challenging objectives concerning the alignment quality of the quadrupole magnets. Their axis location must have a gaussian distribution of 25 μm r.m.s. (root mean square) and the tilt angles within 0.1 $mrad$ r.m.s.. To reach such tolerances, being confident in the quadrupole magnet design and fabrication is not sufficient since alignment parameters are very sensitive. The challenge of that work has two aspects. First the quadrupole magnet alignment properties must be accurately measured by means of the SOLEIL Multipolar Magnetic Measurement Bench (SMB). The quadrupole magnets must be tuned with respect to the measurements to make their alignment properties fit the specification fixed by SOLEIL machine physicist. This part first deals with a three dimensional calculation of the magnetic field in the aperture of a magnet. Then the study of the flux seen by a rotating coil can be reduced to a two dimensional calculation. This development is the basis needed to start the study of alignment quantities and error sources.

2.1.1 Theory for rotating coils

Here are recalled the Maxwell's equations (2.1) in their classical analytical vectorial form. They are needed to calculate the three dimensional magnetic field in the aperture of a magnet.

$$\nabla \times \overrightarrow{H} = \overrightarrow{J} + \frac{\partial}{\partial t}\overrightarrow{D} \tag{2.1a}$$

$$\nabla \times \overrightarrow{E} = -\frac{\partial}{\partial t}\overrightarrow{B} \tag{2.1b}$$

$$\nabla \cdot \overrightarrow{B} = 0 \tag{2.1c}$$

$$\nabla \cdot \overrightarrow{D} = \rho \tag{2.1d}$$

2.1.1.1 Solution of Laplace equation

The main purpose of this section is to determine the general expression of the magnetic field in the aperture of a quadrupole magnet. In a region free of charges and current sources like in the aperture of a quadrupole, Maxwell's equations lead to:

$$\overrightarrow{\nabla} \times \overrightarrow{B} = \overrightarrow{0} \tag{2.2a}$$

$$\Rightarrow \overrightarrow{B} = -\overrightarrow{\nabla}\phi(r,\theta,s) \tag{2.2b}$$

According to the equation 2.2b, the magnetic flux density, $\overrightarrow{B}$, stems from the scalar potential ϕ. Introducing 2.2b in 2.1c, Laplace equation can be deduced:

$$\nabla \cdot (-\nabla\phi(r,\theta,s)) = -\nabla^2\phi(r,\theta,s) = 0 \tag{2.3}$$

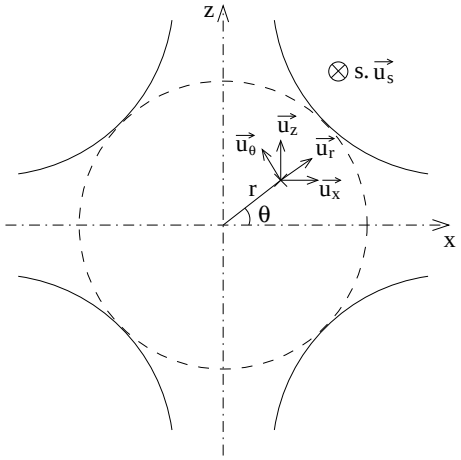

Figure 2.1: Frame

Equation 2.5 expresses the Laplace equation in cylindrical coordinates (r,θ,s) defined by the figure 2.1.

$$\frac{1}{r}\frac{\partial}{\partial r}\left(r\frac{\partial\phi(r,\theta,s)}{\partial r}\right) + \frac{1}{r^2}\frac{\partial^2\phi(r,\theta,s)}{\partial\theta^2} + \frac{\partial^2\phi(r,\theta,s)}{\partial s^2} = 0 \tag{2.4}$$

Laplace equation can be solved using the separate variable method [1] or the "Frobenius method" [15].

Both give the following solution :

$$\phi(r,\theta,s) = \sum_{n=0}^{\infty}\sum_{m=0}^{\infty} \frac{(-1)^m n!}{2^{2m} m!(n+m)!}\, r_0^{2m} \left(\frac{r}{r_0}\right)^{n+2m} \left(\frac{d^{2m}k_{n0}^{S}(s)}{ds^{2m}} cos(n\theta) - \frac{d^{2m}k_{n0}^{N}(s)}{ds^{2m}} sin(n\theta)\right) \tag{2.5}$$

This general solution describes the magnetic field evolution, whatever its sources are, in a region free of charge and current sources. The solution reported in 2.5 begins with a sum over "n" which is the harmonic order of the magnetic field. This sum over n is a function of the radius "r" and the reference radius r_0. The reference radius is arbitrary chosen and defines the magnetic field harmonics which make it a fundamental parameter for accelerator magnets. Each expression of n harmonic is made of two orthogonal components: a "Normal" and a "Skew" one, respectively distinguished by a "N" and a "S" subscript. Then each component of the n harmonic can then be developed in a sum of the variable m. This sum gives the dependence of the scalar potential n harmonic versus the longitudinal variable s. For a given harmonic order (n), its expression is completely determined once its longitudinal dependence, expressed by the function $k_{n0}(s)$, is known for m=0 [15]. There are 2n longitudinal functions for each harmonic. These functions depend on the magnetic field source characteristics, they are continuous over s, cancel at $\pm\infty$ and do not have general analytical known form [17].

Introducing equation 2.5 in 2.2b lead to the cylindrical components of the magnetic flux density expressed by the relation 2.6:

$$B_r(r,\theta,s) = \frac{1}{r_0}\sum_{n=0}^{\infty}\sum_{m=0}^{\infty}(n+2m)\left(\frac{r}{r_0}\right)^{n+2m-1}\left(k_{nm}^{N}(s)sin(n\theta) - k_{nm}^{S}(s)cos(n\theta)\right) \tag{2.6a}$$

$$B_\theta(r,\theta,s) = \frac{1}{r_0}\sum_{n=0}^{\infty}\sum_{m=0}^{\infty}(n)\left(\frac{r}{r_0}\right)^{n+2m-1}\left(k_{nm}^{N}(s)cos(n\theta) + k_{nm}^{S}(s)sin(n\theta)\right) \tag{2.6b}$$

$$B_s(r,\theta,s) = \sum_{n=0}^{\infty}\sum_{m=0}^{\infty}\left(\frac{r}{r_0}\right)^{n+2m}\left(\frac{dk_{nm}^{N}(s)}{ds}sin(n\theta) - \frac{dk_{nm}^{S}(s)}{ds}cos(n\theta)\right) \tag{2.6c}$$

$$\text{with } k_{nm}^{N/S}(s) = \frac{(-1)^m n!}{2^{2m} m!(n+m)!} r_0^{2m}\left(\frac{d^{2m}k_{n0}^{N/S}(s)}{ds^{2m}}\right) \tag{2.7}$$

2.1.1.2 Complex Formalism

When the beam goes through a magnet, it sees the magnet integrated magnetic field along the longitudinal direction : it is the quantity which has to be measured. This quantity is determined by means of coils with a rectangular geometry which enables to measure the magnet s-integrated magnetic field. The next calculation step is to integrate the solution (equation 2.5) along the s axis in order to get the flux seen by the measuring coil. It is assumed that the rectangular measuring coil has a sufficient length to measure all the magnetic field produced along the longitudinal direction. Consequently, the boundaries of the longitudinal integration can be set to $\pm\infty$.

From W. G. Davies's work [1], once the scalar potential $\phi(r,\theta,s)$ is integrated over s, all m>0 terms vanish and lead to this integrated expression.

$$\Phi(r,\theta) = \int_{-\infty}^{+\infty} \phi(r,\theta,s)\, ds = \sum_{n=0}^{\infty} \left(\frac{r}{r_0}\right)^n \left(K_n^S cos(n\theta) - K_n^N sin(n\theta)\right) \tag{2.8}$$

$$\text{with } K_n^{N/S} = \int_{-\infty}^{+\infty} k_{n0}^{N/S}(s) ds \tag{2.9}$$

Measurements with rectangular coils are not sensitive to m>0 terms and other coil shapes are necessary [18] to measure them. In our case we only need to measure the s-integrated magnetic field from $-\infty$ to $+\infty$ since it is only what the electron beam "sees". The calculation of the s-integrated magnetic flux density components (noted with the following letter B) by means of the s-integrated scalar potential ($\Phi(r,\theta)$) leads to a two dimensional problem which can be treated with the complex formalism tools. The calculations are now proceeded with the complex scalar potential defined by the equation 2.10.

$$\overline{V} = \Phi - i\,\mathsf{A}_s \tag{2.10}$$

Φ is the s-integrated scalar potential and A_s is the longitudinal component of the s-integrated vector potential defined by the equation 2.11 in which $\overrightarrow{A}$ is the vector potential.

$$\overrightarrow{\mathsf{A}}(r,\theta) = \int_{-\infty}^{+\infty} \overrightarrow{A}(r,\theta,s) ds = [\mathsf{A}_r, \mathsf{A}_\theta, \mathsf{A}_s] \tag{2.11}$$

Since vector potential $\overrightarrow{A}$ verifies Laplace's equation ($\nabla^2 \overrightarrow{A} = 0$), A_s is obtained using similar method to the one used to calculate the expression of the scalar potential ($\phi(r,\theta,s)$).

$$\mathsf{A}_s(r,\theta) = \sum_{n=0}^{\infty} \left(\frac{r}{r_0}\right)^n \left(-K_n^N cos(n\theta) - K_n^S sin(n\theta)\right) \tag{2.12}$$

Hence by introducing 2.8 and 2.12 in 2.10

$$\overline{V}(r,\theta) = \sum_{n=0}^{\infty} \left(\frac{r}{r_0}\right)^n (cos(n\theta) + isin(n\theta))(K_n^S + iK_n^N) \tag{2.13}$$

Equation 2.13 can be reduced to a more compact expression by introducing the complex variable $\overline{\zeta} = r\,e^{i\theta} = x + iz$ and the complex harmonic coefficient $\overline{C}_n = K_n^S + iK_n^N$, the coefficients $K_n^{N/S}$ being defined by the equation 2.9.

$$\overline{V}(\overline{\zeta}) = \sum_{n=0}^{\infty} \left(\frac{\overline{\zeta}}{r_0}\right)^n \overline{C}_n \tag{2.14}$$

$\overline{V}$ verifies Cauchy-Riemann conditions. It is thus analytic and it enables to derive the complex magnetic flux induction from the complex scalar potential.

$$-\frac{d\overline{V}}{d\overline{z}} = \mathsf{B}_x - i\mathsf{B}_z = \overline{\mathsf{B}}^* \tag{2.15}$$

However it is more practical to use $i\overline{\mathsf{B}}^*$ which is also analytic. This leads to $\overline{\mathbb{B}}$, a complex s-integrated magnetic flux variable defined by the relation 2.16.

$$\overline{\mathbb{B}}(\overline{\zeta}) = i\overline{\mathsf{B}}^{*} = \mathsf{B}_z + i\mathsf{B}_x = \sum_{n=0}^{\infty} \overline{\mathbb{C}}_n \left(\frac{\overline{\zeta}}{r_0}\right)^{n-1} \tag{2.16}$$

Equation 2.16 is the classic formalism used for accelerator magnet magnetic field analysis [19]. As shows the equation 2.16, $\overline{\mathbb{B}}$ can be developed in series of $\overline{\zeta}$, the complex variable and r_0, the so-called reference radius. Then there are the complex harmonic coefficient $\overline{\mathbb{C}}_n$ made of their normal and skew components, respectively $\mathcal{B}_n$ and $\mathcal{A}_n$ (see relation 2.17).

$$\overline{\mathbb{C}}_n = \frac{1}{n}(K_n^N - iK_n^S) = \mathcal{B}_n + i\mathcal{A}_n \tag{2.17}$$

2.1.1.3 Magnetic flux calculation

As introduced before, the calculations are aimed at determining the magnetic flux seen by the measuring coils during their rotation. Magnetic flux calculation with the complex formalism presented previously is detailed in [19]. The purpose of this section is to focus on its main steps to present the reasoning. The simple case of a one turn rectangular coil is studied. If this coil is cut by the transverse plane (x-z), its two filaments are thus located at $\overline{\zeta_1}$ and $\overline{\zeta_2}$ in the complex plane as shown on figure 2.2.

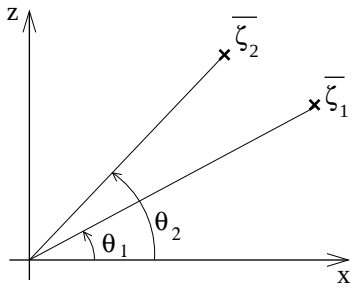

Figure 2.2: Rectangular coil filament location

The magnetic flux ψ seen through the surface defined by these two filaments is expressed in the equation 2.18.

$$\psi = \mathcal{R}e\left[\int_{\overline{\zeta_1}}^{\overline{\zeta_2}} \overline{\mathbb{B}}\, d\overline{\zeta}\right] \tag{2.18}$$

Then 2.16 is introduced in 2.18, its angular dependence being extracted.

$$\psi(\theta) = \mathcal{R}e\left[\sum_{n=1}^{\infty} \frac{\overline{\chi}_n}{n\, r_0^{n-1}} \overline{\mathbb{C}_n}\, e^{i\, n\theta}\right], \qquad \text{with } \overline{\chi}_n = \overline{\zeta_2}^{\,n} - \overline{\zeta_1}^{\,n} \tag{2.19}$$

Discrete flux measurements are performed over one turn of the sensor and a discrete Fourier analysis is executed to obtain the integrated magnetic flux harmonics $\overline{\Psi_n}$. Then after some calculations [19], these integrated magnetic flux harmonics are relied to magnetic flux density harmonics by means of the following relation.

$$\overline{\mathbb{C}_n} \approx \frac{2}{N} \frac{n\, r_0^{n-1}}{\overline{\chi_n}} \overline{\Psi_{n+1}} \tag{2.20}$$

Now all the basic tools to pursue deeper studies on the problems one could encounter are available. Indeed, three dimensional expression of the magnetic flux density is available if the $k_{n0}(s)$

function can be determined by means of a quadrupole for which real magnetic characteristics are well known. As it is possible to work in the 2D space, complex formalism has been developed since it provides simple and powerful mathematical tools for magnet characteristics calculations. The next parts are dedicated to real world phenomenon, effect of errors on measurements and the way they could be studied and determined occupied the major part of the work.

2.1.2 Error sources studies

Application of the theory developed previously to real measurement conditions has to cope with the influence of several defects of the measurement bench like bench misalignment or rotating sensor deformation. The consequence of a bench defect on magnetic measurements is the apparition of spurious harmonic component in the measured magnetic field harmonic content. If the measured harmonics are different from their real values, it leads to a bad knowledge of the magnet field quality. Then, this erroneous description of the magnetic field quality is unfortunately used for beam dynamics simulation ans leads to a misunderstood behaviour of the circulating beam during the commissioning. To minimize the occurrence of such a scenario, a defect study as exhaustive as possible has to be lead.

2.1.2.1 Calculation of the magnetic axis location offset

As mentioned previously, the magnetic axis of a quadrupole is defined as the axis where a beam with no angle is going through without being deflected by a dipolar magnetic field.

More generally :

The magnetic axis of a 2m-pole magnet is the axis parallel to the reference axis and along which the integrated m-1 components of the 2m-pole magnet harmonic content are zero.

The effect of the magnetic axis misalignment on harmonic content is detailed in A.4. Here are the main steps of the reasoning. The purpose is to find a relation between harmonics obtained in the case of a perfect magnet (no offset) and in the case of a misaligned magnet (offset). That is to say, to compare $\overline{\mathbb{B}}(\overline{\zeta})$ in the magnetic frame and in a frame displaced in the complex plane of $\overline{\zeta_{\mathtt{off}}}$.

If $\overline{\mathbb{C}}_n^{\mathtt{mag}}$ are the complex harmonics in the magnetic frame and $\overline{\mathbb{C}}_n^{\mathtt{meas}}$ in the displaced one which also represent the measured harmonics, the relation is expressed by equation 2.21 (see A.4 for calculation details).

$$\overline{\mathbb{C}}_n^{\mathtt{mag}} = \sum_{k=n}^{\infty} \overline{\mathbb{C}}_k^{\mathtt{meas}} \frac{(k-1)!}{(k-n)!(n-1)!} \left(\frac{\overline{\zeta_{\mathtt{off}}}}{r_0} \right)^{k-n} \tag{2.21}$$

It is almost impossible to measure $\overline{\mathbb{C}}_n^{\mathtt{mag}}$ directly after the first measurement since there are low probability for the sensor axis to be exactly located on the magnetic frame. The formula is therefore very useful since it enables to know the magnet characteristics without being disturbed by its misalignment versus the sensor. However the harmonic transformation of the equation 2.21 requires $\overline{\zeta_{\mathtt{off}}}$ to be known: it must be calculated.

Using the definition of the 2m-pole magnet magnetic axis and the feed-down formula, the relation between $\overline{\zeta_{\mathtt{off}}}$ and the $\overline{\mathbb{C}}_n^{\mathtt{meas}}$ can be deduced [19]. By canceling the m-1 component $\overline{\mathbb{C}}_{m-1}^{\mathtt{mag}}$ and limiting the sum to $k = m$ for a 2m-pole magnet, the magnetic axis location $\overline{\zeta_{\mathtt{off}}}$ is expressed in the following equation (2.22)

$$\overline{\zeta_{off}} = -\frac{r_0}{m-1}\frac{\overline{\mathbb{C}}_{m-1}^{meas}}{\overline{\mathbb{C}}_{m}^{meas}} \qquad \forall m > 1 \tag{2.22}$$

The main assumption to obtain the equation 2.22, is that k>m components (see equation 2.21) are neglected since they are very small versus the main component and misalignment effects are not visible on higher order harmonics. This assumption is verified for accelerator magnet where unwanted magnetic field harmonics are minimized to few 10^{-4} of the main component.

2.1.2.2 Angular error

Another important defect for which the electron is very sensitive is the magnet (and / or the sensor) angular positioning error (tilt angle). The angular error which could occur in a 2m-pole magnet is defined as the tilt angle between a purely normal component ($\mathcal{A}_m = 0$) and the real magnetic field vector ($\mathcal{A}_m \neq 0$).

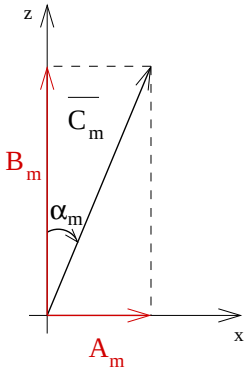

Figure 2.3: Magnetic tilt angle

The main component of a measured magnetic field being defined as $\overline{\mathbb{C}}_m^{mag} = \mathcal{B}_m + i\mathcal{A}_m$, the angle is:

$$\theta_m = -\frac{\alpha_m}{m} = -\frac{1}{m} ATan\left(\frac{\mathcal{A}_m}{\mathcal{B}_m}\right) \tag{2.23}$$

The 1/m factor is needed to convert the magnetic angle α_m into the mechanical angle θ_m. Indeed, $\frac{1}{m}$ is the ratio between the magnetic period of the 2m-pole magnet ($\frac{2\pi}{m}$) and the mechanical period (2π).For the particular case of the quadrupole:

$$\theta_2 = -\frac{1}{2} ATan\left(\frac{\mathcal{A}_2}{\mathcal{B}_2}\right) \tag{2.24}$$

Then knowing the θ_m, harmonic coefficients can be calculated in the main component frame with the formula of equation 2.25.

$$\overline{\mathbb{C}}_n^{mag} = \overline{\mathbb{C}}_n^{meas}\, e^{-i\, n\theta_m} \tag{2.25}$$

Magnetic axis location and angular errors determination are the main parameters which are calculated and corrected after the magnetic field harmonic measurements. Both the magnet and the rotating sensor can introduce these errors but their treatment are different depending on their origin. In the first case (magnet), these errors have to be corrected whereas in the second case (rotating sensor) they only have to be known in order to take them into account during the calculation of the magnet errors. Indeed, if errors from the rotating sensor are corrected on the measured magnet, it will increase the initial magnets defects.

2.1.2.3 Effect of sag

Any mechanical element laying on two points undergoes gravity effect by sagging. Measuring harmonics with a sensor which is sagging leads to spurious harmonics in the harmonic content. From Davies theory [1], sag effect generates harmonics $n \pm 1$ which are orthogonal to their sources. n is the order of natural harmonics which really exist. For example, in the quadrupole case, the main component ($\mathcal{B}_2$) generates a dipolar ($\mathcal{A}_1$) and a sextupolar($\mathcal{A}_3$) skew components. Moreover a real quadrupole has natural harmonics. One of them is the 12-pole component ($\mathcal{B}_6$), consequently there will be also spurious $\mathcal{A}_5$ and $\mathcal{A}_7$.

Bucking coils can cancel spurious harmonics. The principle is to eliminate the harmonic which is the source of the spurious one. That is why, $\mathcal{B}_2$ component is often removed with bucking coils. Moreover canceling the main component enables to measure more accurately other harmonics which are much smaller ($\approx$ $few\, 10^{-4}\, of\, \mathcal{B}_2$).

2.1.2.4 Bucking coils

As mentioned previously, additional coils are often used to get a better sensitivity for high order harmonics measurement. Moreover, these coils enable to cancel effects of the sensor defects which generate some spurious harmonics. The principle of bucking coil is to use the flux measured by one or more additional coil to remove the unwanted components. Principle of bucking coils is not developped here but for more information, it is detailed in [16].

2.2 Contribution to theoretical experiments

The purpose of this section is to propose a new approach to study effects of rotating coil 3D defects on the measured harmonic content even if s-integrated measurements give 2D magnetic characteristics. First, a mathematical model is developed to modelize a sensitivie coil with a general shape or contour. Then the work is aimed at defining an analytical magnetic model for the quadrupole magnetic field source which is easy to calculate without being so far from the behaviour a real quadrupole. Finally different case of rotating coil are studied by gathering both the rotating coil shape model and the magnetic field source model in order to understand the spurious harmonics apparitions.

2.2.1 Development of the method

The purpose is to simulate the effect of a modelized coil shape on the measurements of the flux seen by this coil during its rotation. This is performed by using basic geometrical analysis tools to calculate curvilinear integral since vector potential is used to calculate the magnetic flux.

If the coil shape ($\mathcal{C}$) is known, the flux seen by the measuring coils can be simulated as expressed by the equation 2.26.

$$\psi = \oint_{\mathcal{C}} \overrightarrow{A_{Qp}}(x, z, s) \cdot \overrightarrow{dl}, \qquad \mathcal{C} \text{ is the coil contour} \tag{2.26}$$

ψ is the flux seen by the modelized rotating coil and $\overrightarrow{A_{Qp}}$ the vector potential of the modelized quadrupole magnetic field source. Figure 2.4 shows an example of coil shape with geometrical defects which was initially rectangular. The contour $\mathcal{C}$ of this out of shape coil is separated in four part plotted with a different color (red, orange, yellow, brown). The figure 2.4 shows also one projection of each contour part on 2D planes (x-z and z-s).

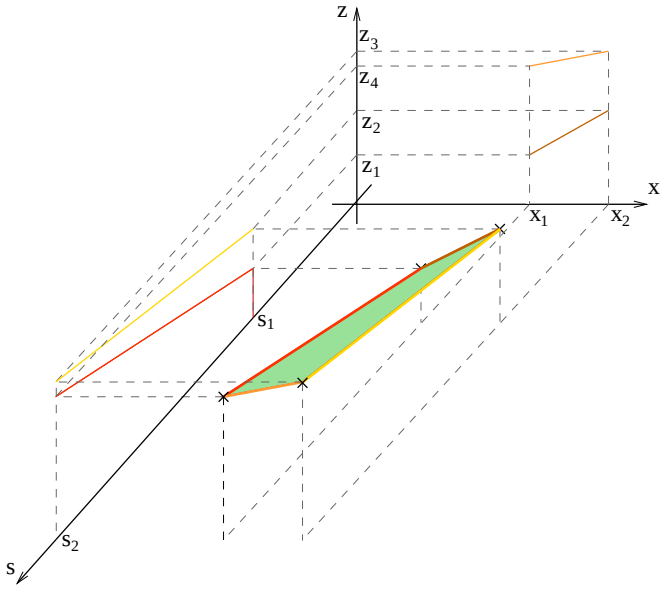

Figure 2.4: View of an out of shape coil and the four projected segments

As mentioned previously, the coil contour $\mathcal{C}$ can be divided in four segments $\mathcal{C}_i$, limited by l_1^i and l_2^i (integration bounds), which is useful for the magnetic flux calculation as expressed by the equation 2.27.

$$\psi = \sum_{i=1}^{4} \int_{l_1^i}^{l_2^i} \overrightarrow{A_{Qp}}(x,z,s) \cdot \overrightarrow{dl^i}\,; \qquad \text{over } \mathcal{C}_i \tag{2.27}$$

Since it is more convenient to integrate along the cartesian coordinates, a main direction of integration (s for example) has to be chosen. Then the contour "i" equation defined by $g^i(l^i)$ has to be projected to the related planes: x-s and z-s for our example which leads to two functions of s, respectively $g_x^i(s)$ and $g_z^i(s)$ for one contour "i".

From the previous explanations, the method to obtain the magnetic flux from a coil with a given shape is now detailed using basic geometrical analysis.

If $P_{\alpha_0}^i$ is a point belonging to the contour $\mathcal{C}_i$ of the coil at initial angular position α_0, that is to say the first position of the measuring coil during its rotation, $P_{\alpha_0}^i$ is located in the 3D cartesian space, having the point "O" as origin, by the equation 2.29:

$$\text{With } \overrightarrow{OP_{\alpha_0}^i} = x\overrightarrow{e_x} + z\overrightarrow{e_z} + s\overrightarrow{e_s} \tag{2.28}$$

$$= g_x^i(s)\overrightarrow{e_x} + g_z^i(s)\overrightarrow{e_z} + s\overrightarrow{e_s} \tag{2.29}$$

Thanks to the equation 2.29 in which the contour equation has been uncoupled among the three cartesian components, it is thus easy to find the cartesian components of $\overrightarrow{dl^i}$ defined by the equation 2.30:

$$\overrightarrow{dl^i} = \frac{\partial \overrightarrow{OP_{\alpha_0}^i}}{\partial s} = \frac{\partial g_x^i(s)}{\partial s}\overrightarrow{e_x} + \frac{\partial g_z^i(s)}{\partial s}\overrightarrow{e_z} + \overrightarrow{e_s} \tag{2.30}$$

And its norm is expressed by the equation 2.31:

$$dl^i = \sqrt{\left(\frac{\partial g_x^i(s)}{\partial s}\right)^2 + \left(\frac{\partial g_z^i(s)}{\partial s}\right)^2 + 1}\, ds \tag{2.31}$$

Relations 2.29 and 2.31 enable us to calculate the flux at the initial angular position of the sensor ($\alpha = \alpha_0 = 0$). However the flux evolution during one turn of the sensor must be numerically simulated. Therefore the new contour $\mathcal{C}^i(\alpha)$ on which the vector potential must be known have to be rotated by an angle alpha. Thus the contour $\mathcal{C}^i(\alpha)$ is defined by $\overrightarrow{OP^i_\alpha}$ obtained by applying the rotation matrix $\mathbb{R}(\alpha)$ on $\overrightarrow{OP^i_{\alpha_0}}$. These calculations are defined by equations 2.32 and 2.33.

$$\overrightarrow{OP}^i_\alpha = \mathbb{R}(\alpha) \cdot \overrightarrow{OP}^i_{\alpha_0} = \begin{bmatrix} x^i_\alpha(s) \\ z^i_\alpha(s) \\ s \end{bmatrix} = \begin{bmatrix} h^i_x(s,\alpha) \\ h^i_z(s,\alpha) \\ s \end{bmatrix} \tag{2.32}$$

$$\text{and also, } \overrightarrow{dl^i_\alpha} = \mathbb{R}(\alpha) \cdot \overrightarrow{dl^i_{\alpha_0}} \tag{2.33}$$

The rotation of $\overrightarrow{OP}^i_{\alpha_0}$ of an angle α leads to new contour functions $h^i_x(s,\alpha)$ and $h^i_z(s,\alpha)$. Hence the magnetic flux dependence on α can be computed using equation 2.34:

$$\psi(\alpha) = \sum_{i=1}^{4} \int_{l^i_1}^{l^i_2} \overrightarrow{A_{Qp}}(h^i_x(s,\alpha), h^i_z(s,\alpha), s) \cdot \overrightarrow{dl^i_\alpha} \tag{2.34}$$

Using the method developed previously and then equation 2.34, whatever the coil shape is, it is possible to simulate the magnetic flux it would measure if the coil shape can be properly modelized. The next step is to provide the coil model with an analytical magnetic field source in order to study the effect of 3D defects study.

2.2.2 2D model

To test the previous 3D model of the sensor, the simplest magnetic field source we could use is a perfect 2D quadrupole, i.e. an infinitely long and pure quadrupole. Thus relation 2.16 is used with only $\mathcal{B}_2$ component $\neq 0$

$$\overline{\mathbb{B}}(\overline{\zeta}) = \frac{1}{r_0}\, \mathcal{B}_2\, \overline{\zeta} \tag{2.35}$$

Then integrating $\overrightarrow{B} = \overrightarrow{\nabla} \times \overrightarrow{A}$ for this particular case lead to

$$\overrightarrow{A}(x,z,s) = -\frac{1}{2}\, \frac{\mathcal{B}_2}{r_0}\, (x^2 - z^2)\, \overrightarrow{e_s} \tag{2.36}$$

Perfect rectangular coil

This is a very simple case since it is easy to identify harmonic coefficient from flux calculations. Measurements of a perfect quadrupole magnetic field by means of perfect rectangular coil enables to check the general method mentioned previously.

The coil shape is a perfect rectangular coil delimited by (x_1, x_2 and s_1, s_2).

⋆ Everything is perfect

For this simple case, the flux obtained is:

$$\psi(\alpha) = (x_2 - x_1)(s_2 - s_1)\, \frac{\mathcal{B}_2}{r_0}\, cos(2\alpha) \tag{2.37}$$

⋆ Misalignment in x direction

The coil rotation axis is displaced of a quantity x_{off} along $\overrightarrow{e_x}$, the flux becomes:

$$\psi(\alpha) = (x_2 - x_1)(s_2 - s_1)\,\frac{\mathcal{B}_2}{r_0}\,(x_{\text{off}}\,cos(\alpha) + cos(2\alpha)) \tag{2.38}$$

⋆ Angular defect α_{off}

The coil starts its measurements with an offset angle α_{off}, thus the flux is

$$\psi(\alpha) = (x_2 - x_1)(s_2 - s_1)\,\frac{\mathcal{B}_2}{r_0}\,(cos(2\alpha_{\text{off}})cos(2\alpha) - sin(2\alpha_{\text{off}})sin(2\alpha)) \tag{2.39}$$

The results obtained enabled to illustrate the relations 2.22 and 2.24 and to apply the integration method detailed in section 2.2.1.

Mechanical torsion of the coil

It could be more interesting to apply our method to a more concrete case such as a torsional defect of the sensor (see figure 2.5). The sensor is defined by four points (P_1, P_2, P_3, P_4) representing the four ends of the coil and by the fixed distance between (P_1 and P_3, P_2 and P_4). It is assumed that since only small defects are treated, the contours are defined by straight lines which equations are easy to calculate from points P_i. A straight line equation in 3D cartesian space is defined by a couple of equation of the main variable.

$$\mathcal{C}^i : \begin{array}{l} x = a^i\,s + b^i = g_x^i(s) \\ z = c^i\,s + d^i = g_z^i(s) \end{array} \tag{2.40}$$

Each contour $\mathcal{C}^i$ is determined by two equations $g_x^i(s)$ and $g_z^i(s)$ which enable to apply the integration method developed in 2.2.1.

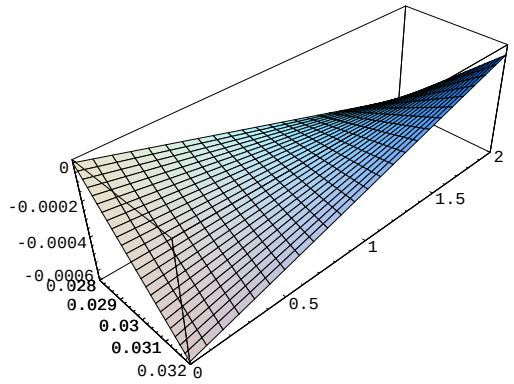

Figure 2.5: Mechanical torsion of coil

The flux calculation leads to 2.41:

$$\psi^i(\alpha) = \left[\int_{s_1}^{s_2} (g_x^i(s)^2 - g_z^i(s)^2)\,ds\right]\,cos(2\alpha) + \left[\int_{s_1}^{s_2} (g_x^i(s)\cdot g_z^i(s))\,ds\right]\,sin(2\alpha) \tag{2.41}$$

From the previous relation, if the torsion is symmetric, the skew quadrupole term vanishes. Then for any torsion defect, the angular error made on the flux measurement represents the mean angle of the sensor along the s axis.

Mechanical sag of the coil

A mechanical problem which is often encountered is sagging of the coil like shown on figure 2.6, units of the 3D plot are millimeters. To take it into account in the context of our theoretical experiments, the principle is to begin working with a perfect rectangular coil and then to apply a deformation along the z axis representing the sensor undergoing gravity forces. The equation of the mean fiber of a girder with a length L, laying on two stands located at $s = \pm L/2$ and sagging under its own weight (w) is formulated by the equation 2.42.

$$\mathcal{S}ag(s) = -\frac{ms}{24\,E_y\,I_{Gx}}\left(\frac{5}{16} - \frac{3}{2}\left(\frac{s}{L}\right)^2 + \left(\frac{s}{L}\right)^4\right) \tag{2.42}$$

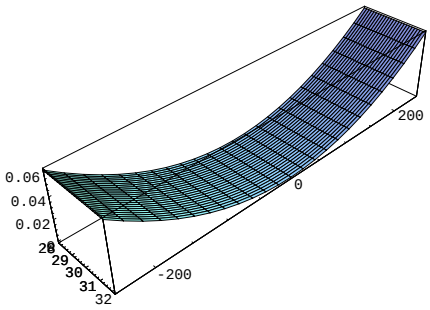

Figure 2.6: Mechanical sag of coil

Hence the effect of the coil sag is taken into account adding the effect described by the last formula to the z-component of $\overrightarrow{A_{Qp}}$.

$$\psi(\alpha) = \sum_{i=1}^{4}\int_{l_1^i}^{l_2^i} \overrightarrow{A_{Qp}}(h_x^i(s,\alpha), h_z^i(s,\alpha) + \mathcal{S}ag(s), s)\cdot\overrightarrow{dl_\alpha^i} \tag{2.43}$$

And 2.31 for s axis integration becomes the relation 2.44.

$$\overrightarrow{dl^i} = \frac{\partial g_x^i(s)}{\partial s}\overrightarrow{e_x} + \frac{\partial(g_z^i(s) + \mathcal{S}ag(s))}{\partial s}\overrightarrow{e_z} + \overrightarrow{e_s} \tag{2.44}$$

Since the vector potential has only the A_s component and the $\overrightarrow{dl^i}$ has always a unit component $\overrightarrow{e_s}$ in the present case of a perfect 2D quadrupole magnetic field source, there will be no visible effect of sag on $\overrightarrow{dl^i}$ direction. Even if the sag is taken into account in the vector potential calculation, we cannot expect to see a skew sextupolar component after the Fourier analysis of $\psi(\alpha)$. However, from the study of W.G. Davies' calculations, the signature of a coil sag is the apparition of a skew sextupolar component [1]. The conclusion of this short analysis is that the 2D model of the quadrupole does not enable to study 3D defect like coil sag. It has been checked by theoretical experiments implemented in a Mathematica code [20].

The simulations confirm that the 2D model is not accurate enough to produce skew sextupolar component when the sensor is undergoing a sag effect. The 2D model of the quadrupole magnetic field source is not as close to the reality as we would like, another model which takes into account 3D effects must be established.

2.2.3 Analytical 3D model

As mentioned previously, a more accurate model of a real quadrupole magnetic field source must be established to study complex defect of the measuring coil. The purpose is always to get an

analytical model in order to facilitate its computation. As the analytical expression of a punctual dipole vector potential is known in the 3D space thanks to the equation 2.45 [21], we propose to use four punctual magnetic dipoles to create a quadrupole magnetic field.

The three dimensional vector potential of a punctual magnetic dipole located on "Q" (figure 2.7) is expressed by the equation 2.45.

$$\overrightarrow{A}(r,\theta,s) = \frac{\mu_0}{4\pi}\frac{\overrightarrow{M}\times\overrightarrow{R}}{||\overrightarrow{R}||^3} \tag{2.45}$$

The figure 2.7 shows a punctual magnetic dipole and its related parameters. P is the point where the magnetic field needs to be known, "r" is the radius location of "P" and "a", the radius location of "Q".

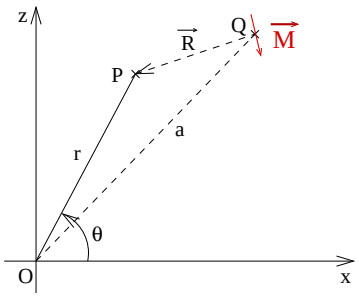

Figure 2.7: Punctual magnetic Dipole

Using the superposition principle, the three dimensional vector potential of a quadrupole magnet defined by four punctual magnetic dipoles ($\pm\overrightarrow{M}$) located at radius a and angles $\theta_i = \frac{\pi}{4} + (i-1)\frac{\pi}{2}$; i=1..4 is expressed in the equation 2.46.

$$\overrightarrow{A_{Qp}}(r,\theta,s) = \sum_{i=1}^{4} \frac{(-1)^i||\overrightarrow{M}||}{\sqrt[3]{r^2+2\cdot r\cdot a\cdot cos(\theta-\theta_i)+a^2+s^2}} \begin{bmatrix} s\cdot sin(\theta_i) \\ -s\cdot cos(\theta_i) \\ r\cdot sin(\theta-\theta_i) \end{bmatrix}_{A_x,\,A_z,\,A_s} \tag{2.46}$$

Implementation in scientific code

As analytical calculation of the flux is difficult to obtain by hand, the method developed in section 2.2.1 has been implemented in a Mathematica code. The figure 2.8 represents the process performed by the mathematica code. The aim of the code is to behave as the bench command and control program would work during a multipole magnet measurement. During the theoretical experiment, the magnetic field source is performed by a model calculated previously (equation 2.46 for example) and the rotating coil is given by the equation of the contour which is needed to be studied (torsion, sag). The code uses the analytical models calculated previously for both the magnetic field source and the measuring coil shape.

A theoretical experiment begins by a numerical integration of the flux seen by the coil rotating in the magnetic field produced by the four punctual magnetic dipoles is calculated by the code. Then after a Fourier analysis, harmonic content of the "theoretically measured" magnetic field gives the mean to quantify the effect of the introduced defect.

Moreover, to check the progress of the coil rotating in the magnetic field, the sensor shape is plotted during its rotation. It enables to see directly if the effect of the defect which have been

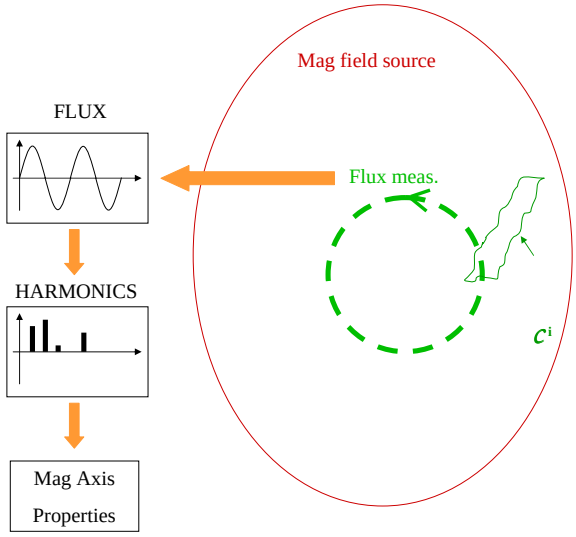

Figure 2.8: Mathematica code process

voluntarily introduced behaves as expected. As an example, the sensor shape evolution is plotted at its N angular positions in the case of a perfect rectangular coil on figure 2.9.

2.2.4 Application of the 3D model

First, the 3D model for magnetic field source is tested by computing the flux seen by a perfect rectangular coil. Once the model behaves as expected, it is used to study different defects of the sensor.

Case of a perfect rectangular coil
As mentioned before, the sensor evolution during its rotation is plotted (figure2.9) and the program delivers the plot of the flux measured for the N the angular positions (figure 2.10).

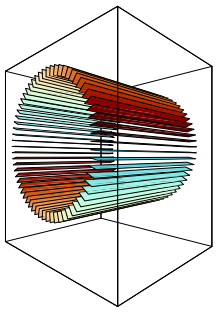

Figure 2.9: Coil rotation

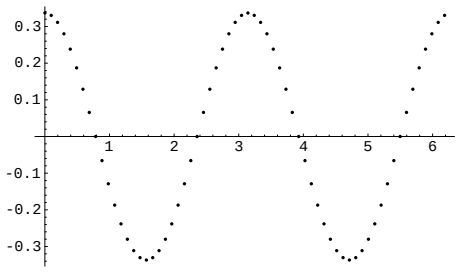

Figure 2.10: Measured flux

It seems useless to plot the sensor evolution but when complex defects need to be integrated in the program, it is important to get a view of the shape through which the flux is calculated. In the case of a perfect rectangular rotating coil, after a Fourier analysis of the measured flux (figure 2.10), only natural harmonics of a real quadrupole magnet are present.

- $\mathcal{B}_6$ which represents mostly the effect of the finite length of the quadrupole,

- $\mathcal{B}_{10}$ representing the cut of hyperbolas shape of real magnet magnetic circuit,

To get acquainted with the evaluation of the origin of harmonics in real quadrupole magnets, a big work has been done by J. Cobb and R. Cole in [22]. The figure 2.11 shows the harmonic content of the quadrupole performed by the 4 punctual magnetic dipoles model we have proposed, from which the main component ($\mathcal{B}_2$) has been removed. This quadrupole has a strong normal 12-pole ($\mathcal{B}_6$) component. In real quadrupole magnet this component is not so strong but what matters is the qualitative aspect of the studies which are led. This harmonic content is defined as the reference for the next studies. Indeed, any harmonic content from other configuration will subtracted from this reference in order to highlight the harmonics which are spuriously created.

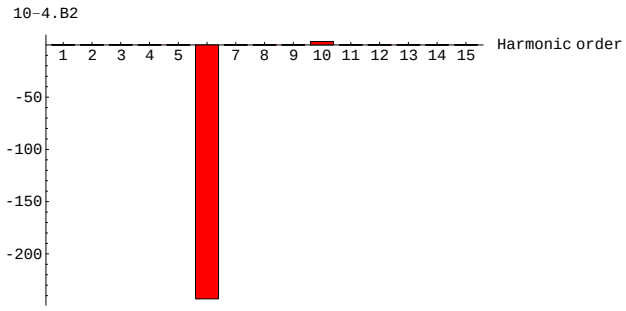

Figure 2.11: Natural Harmonics of the 3D model

We also checked that for any displacement of the sensor rotation axis $\overline{\zeta_{\text{off}}}$, the theoretical experiment calculations leads to the same positioning offset as the one entered as a rotating coil defect before the simulation. All these checking steps enable to study a more complex rotating coil defect like the sag effect.

Effect of mechanical sag

Here are only given the results about theoretical experiments for a coil undergoing a mechanical sag. Introducing a sag to the model of the coil generates the additional harmonics of the table 2.47. As mentioned previously, the harmonics in the table, are the result of the difference between the reference model (harmonic content plotted on the figure 2.11). For these simulations, the sag represented a $1.5\,10^{-4}$ of the total length of the sensor.

n	$\mathcal{B}_n$	$\mathcal{A}_n$
1	0	49
2	0.0	0
3	0	0.07
4	0.06	0
5	0	−5.9
6	0.0	0
7	0	0.0
8	−0.003	0
9	0	0.14
10	0.0	0
11	0	0.0

(2.47)

The previous table illustrates the W.G. Davies conclusion since harmonics of order $n \pm 1$ appeared. The results obtained shows also that these spurious harmonics depend on the magnitude

of their sources. Our reference 3D magnetic source model has a strong 12-pole ($\mathcal{B}_6$) component. Consequently, it generates a $\mathcal{A}_5$ and a $\mathcal{A}_7$ component with the $\mathcal{A}_5$ stronger than the expected $\mathcal{A}_3$ (skew sextupole). In a normal manufactured quadrupole, the natural harmonic are smaller and then the spurious harmonics obtained due to the sensor sagging are decreasing with the harmonic order.

The 3D model is now validated since it can describe various phenomena with a good fidelity. Until now only defects on the sensor have been introduced. It is also possible to study effects of errors on pole positioning, orientation or magnetic field strength. This possibility is used in part 3.4.2.1 where the origin of a measured spurious harmonic is studied. On one hand, understanding the origin of measured harmonic is an important step in the data analysis process. On the other hand, defects which lead to erroneous characterization of the magnetic axis must be determined. It is the subject of the next part.

2.3 Reference measurements

A tool has to be designed to quantify bench imperfections. Its handling and its data measurements analysis must be easy to perform. The tool is a small 2m-pole magnet with its intrinsic magnetic axis properties. The number of pole (m) is related to the 2m-pole magnets which have to be characterized on the bench.

There are two ways to use this tool:

- The tool magnetic axis properties are accurately known:
  This knowledge is used to standardize the bench by means of absolute measurements. It required a perfect confidence in the tool characterization which depends on the mastering of a consequent amount of error sources.

- The tool magnetic axis properties is not known:
  Relative measurements must be performed to get 2m-pole characteristics. Errors can be separated from quantities which need to be quantified by several measurements.

While bench defects are the only one to evolve, both methods are available. However, if for any reason, the tool get imperfections (shock, wearing,...) we have to be able to localize the error sources and remove them from measurements. As it is important to master any micrometer leakage to fit the specifications, the second method is chosen.

First, theoretical aspect is treated, the simulations performed wit RADIA software complete this work. Finally the SMB standardizing tool design is depicted.

2.3.1 Principle

The main idea is to use a tool which produces a 2m-pole magnetic field with a given magnetic axis ($\overline{\Delta\zeta_{Mp}}$ and $\overline{\theta_{Mp}}$). Then, as relative measurements are the aim of our experiments, let imagine a mechanical interface which enables to position the tool at any desired position. Before going further in explanation, some definitions must be mentioned.

Definitions

- The reference frame is the one defined at SOLEIL Synchrotron which uses x and z variables for transverse plane (x for horizontal axis and z for vertical axis) and s variable for longitudinal axis which follows the beam direction.

- Complex formalism is used for calculations of transverse plane magnetic axis displacements. So the variable $\overline{\zeta}$ represents a complex number with affix $x + i\,z$.
- Complex entities related to any displacements of entity named "Ent" are defined like $\overline{\Delta\zeta_{Ent}} = \Delta x_{Ent} + i\Delta z_{Ent}$.
- A magnetic measurement is defined as the magnetic axis location and orientation computed from magnetic field harmonics measured (see section 2.1).
- Magnetic axis of multipole measured is marked by "P" letter in any scheme.
- Any magnetic measurement ($\overline{\Delta\zeta_{Meas}}$) give the magnetic offset between the sensor magnetic frame ($Sensor_{Mag-Frame}$) and the 2m-pole magnet magnetic frame ($Mp_{Mag-Frame}$).

The purpose is to find the location of the 2m-pole magnet magnetic axis versus the sensor mechanical frame ($Sensor_{Mech-Frame}$): $\overline{\Delta\zeta_{Mp}}$

2.3.1.1 Ideal case

Let imagine a perfect bench. It means that the magnetic axis location measurement marked with ("P") gives the real magnetic offset of the 2m-pole magnet. To get such a result, sensor magnetic and mechanical fi

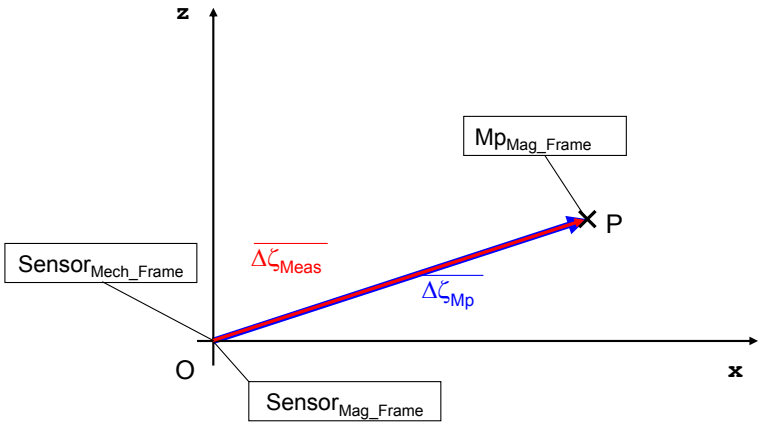

Figure 2.12: Vectorial representation of offset axis: Ideal case

So an ideal magnetic measurement leads to the following relation:

$$\overline{\Delta\zeta_{Meas}} = \overline{\Delta\zeta_{Mp}} \tag{2.48}$$

The equation (2.48) represented by the figure 2.12 is trivial. The previous graphic is such simple that it does not provide more information than equation (2.48). However its usefulness is highlighted in next sections since a whole view of cases studied is needed.

2.3.1.2 Positioning error of the sensor measuring coils

In spite of all cares brought to sensor assembling, its magnetic and mechanical frames are not merged as assumed in the ideal case. Consequently, a new quantity is defined to quantify the

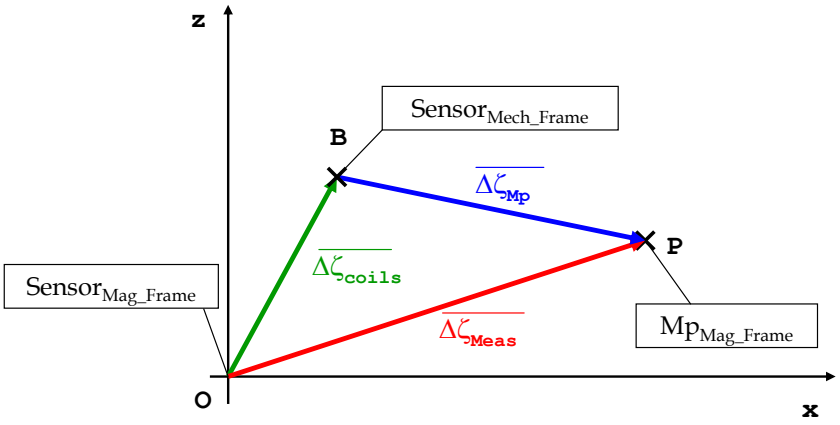

Figure 2.13: Vectorial representation of offset axis: sensor default

measurement coils positioning error: $\overline{\Delta\zeta_{coils}}$. It represents the offset between the sensor magnetic and mechanical frames due to machining and assembling defects.

Figure 2.13 represents how each frame interacts themselves and it leads to the equation (2.49).

$$\overline{\Delta\zeta_{Meas}} = \overline{\Delta\zeta_{Mp}} + \overline{\Delta\zeta_{coils}} \tag{2.49}$$

$\overline{\Delta\zeta_{coils}}$ is an intrinsic parameter of the sensor so wherever the magnetic centre is located, the value of $\overline{\Delta\zeta_{coils}}$ remains the same. At least two measurements are required to determine both unknowns of equation (2.49). A first one with the tool in any position, and a second one with the tool turned of 180 ° around the "s" axis from the last position.

For the measurement n ° 1, the equation 2.49 is available. Then measurement n ° 2 gives a similar relation as indicated in 2.50.

$$\overline{\Delta\zeta_{Meas1}} = \overline{\Delta\zeta_{Mp}} + \overline{\Delta\zeta_{coils}} \tag{2.50a}$$
$$\overline{\Delta\zeta_{Meas2}} = -\overline{\Delta\zeta_{Mp}} + \overline{\Delta\zeta_{coils}} \tag{2.50b}$$

Thanks to these measurements, $\overline{\Delta\zeta_{coils}}$ and $\overline{\Delta\zeta_{Mp}}$ can be quantified:

$$\overline{\Delta\zeta_{coils}} = \frac{\overline{\Delta\zeta_{Meas1}} + \overline{\Delta\zeta_{Meas2}}}{2} \tag{2.51}$$
$$\overline{\Delta\zeta_{Mp}} = \frac{\overline{\Delta\zeta_{Meas1}} - \overline{\Delta\zeta_{Meas2}}}{2} \tag{2.52}$$

Only swing measurements and half sums are required to determine bench defects, the reference tool could not be simpler to use. However the reference tool machining is not perfect, that is why offsets implied by this mechanical effect must be studied.

2.3.1.3 Errors from the tool machining

The protocol mentioned previously only works if the reference magnet is turning around the origin of the sensor mechanical frame ($Sensor_{Mech-Frame}$) marked ("B") on the figure 2.14. It means that the origin of the sensor and the 2m-pole magnet mechanical frames must be merged. It cannot be possible since the reference tool mechanical interface got defects from its machining.

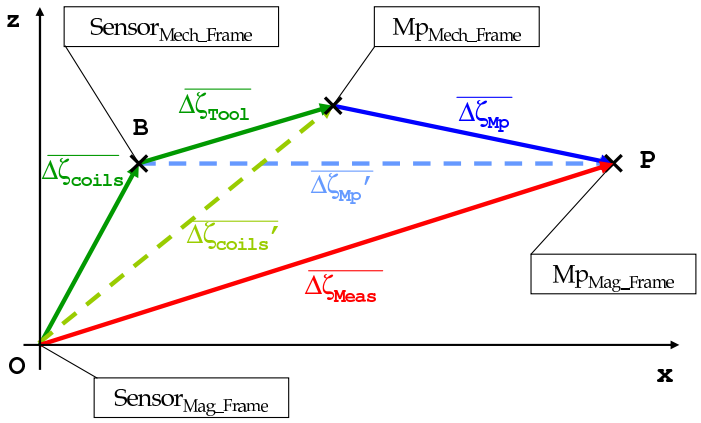

Figure 2.14: Vectorial representation of offset axis: Tool default

Such imperfections are taken into account by means of the complex variable $\overline{\Delta\zeta_{Tool}}$. Figure 2.14 shows how the machining quality can act on measurements.

On figure 2.14, $\overline{\Delta\zeta_{coils}}$ and $\overline{\Delta\zeta_{Mp}}$ have the same affixes as in previous schemes (figures 2.12 and 2.13) since in reality these entities remain constant.

$$\overline{\Delta\zeta_{Meas}} = \overline{\Delta\zeta_{coils}}' + \overline{\Delta\zeta_{Mp}} \tag{2.53}$$

$$= \overbrace{\overline{\Delta\zeta_{coils}} + \overline{\Delta\zeta_{Tool}}} + \overline{\Delta\zeta_{Mp}} \tag{2.54}$$

$\overline{\Delta\zeta_{Tool}}$ provides uncertainty in $\overline{\Delta\zeta_{coils}}$ and $\overline{\Delta\zeta_{Mp}}$ determination since it can be different for each position (1 & 2).

$$\overline{\Delta\zeta_{Meas1}} = \overline{\Delta\zeta_{Mp}} + \overline{\Delta\zeta_{coils}} + \overline{\Delta\zeta_{Tool\,1}} \tag{2.55a}$$

$$\overline{\Delta\zeta_{Meas2}} = -\overline{\Delta\zeta_{Mp}} + \overline{\Delta\zeta_{coils}} + \overline{\Delta\zeta_{Tool\,2}} \tag{2.55b}$$

If the relation 2.51 is used, the equivalent measurement coils positioning error obtained is:

$$\overline{\Delta\zeta_{coils\,Eq}} = \overline{\Delta\zeta_{coils}} + \frac{\overline{\Delta\zeta_{Tool\,1}} + \overline{\Delta\zeta_{Tool\,2}}}{2} = \frac{\overline{\Delta\zeta_{coils\,1}}' + \overline{\Delta\zeta_{coils\,2}}'}{2} \tag{2.56}$$

The use of $\overline{\Delta\zeta_{coils\,Eq}}$ during series measurement leads to erroneous value of $\overline{\Delta\zeta_{Mp}}$. That is why it is necessary to cancel the effect of $\overline{\Delta\zeta_{Tool}}$ by removing it mathematically. The only way to know this quantity for each position of the 2m-pole magnet tool is to perform 3D mechanical measurements. Then corrections are applied to measurements versus reference tool position and the swing measurements mentioned in section 2.3.1.2 can be operated. After corrections, it is like if the 2m-pole magnet tool is turning around the sensor mechanical frame origin (see equation 2.57).

$$\overline{\Delta\zeta_{Meas\,New}} = \overline{\Delta\zeta_{Meas}} - \overline{\Delta\zeta_{Tool}} = \overline{\Delta\zeta_{coils}} + \overline{\Delta\zeta_{Mp}} \tag{2.57}$$

$\overline{\Delta\zeta_{coils}}$ and $\overline{\Delta\zeta_{Mp}}$ can now be properly determined with the use of $\overline{\Delta\zeta_{Meas\,New}}$ in equations 2.51 and 2.52,

2.3.1.4 Advanced reference tools theory

This section is dedicated to measurement errors minimization by studying the reference tool practical use. Indeed, principles mentioned previously are applied to a 2m-pole magnet from which several magnetic configurations have to be available: normal, skew, positive and negative. To achieve these objectives the reference 2m-pole magnet is provided with a polygonal mechanical interface (see figure 2.15 for m=4, i.e. quadrupole magnet).

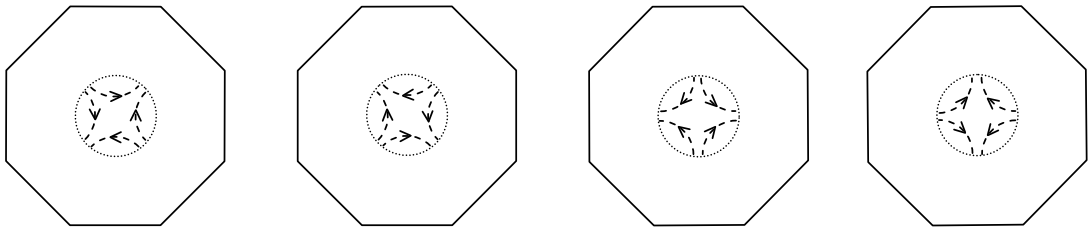

Figure 2.15: Octagonal mechanical interface

Notations

- Each side of the polygonal interface is marked with a number $k = 1..N$ with $N = 2\,m$,
- Letters "A" and "B" are used to distinguish each face.
- The side number "k" grows with the trigonometric sense if the face looked at is "A".
- Each magnetic axis location measurement is noted $\overline{\Delta\zeta_{Meas-kX}}$,
- In $\overline{\Delta\zeta_{Meas-kX}}$ expression:
  - "k" subscript is the number located on the upper side of the polygonal mechanical interface,
  - "X" stands for the face letter located at the entrance of the beam.
- "1A" position is defined as the reference position.
- The reference 2m-pole positioned on "1A" is a positive normal 2m-pole magnet and its magnetic axis is located at $\overline{\Delta\zeta_{Mp}}$.

2m-pole magnet without mechanical defaults

Like in 2.3.1.2 section, the rotation of the 2m-pole magnet around its mechanical frame origin is studied. Since the external interface has a particular geometry (regular polygon), relations between measurements can obviously be brought out. Indeed, measurements at all the 2m-pole magnet position (k=1..N) are given by the following formulas for both faces ("A" & "B"):

$$\overline{\Delta\zeta_{Meas-kA}} = \overline{\Delta\zeta_{Mp}}\, e^{i\frac{-2\pi}{N}(k-1)} + \overline{\Delta\zeta_{coils}} \text{ ; k=1..N} \tag{2.58a}$$

$$\overline{\Delta\zeta_{Meas-kB}} = -i\,\overline{\Delta\zeta_{Mp}}^{*}\, e^{i\frac{2\pi}{N}(k-1)} + \overline{\Delta\zeta_{coils}} \text{ ; k=1..N} \tag{2.58b}$$

$$\text{with } \overline{\Delta\zeta_{Mp}}^{*} = \Delta x - i\,\Delta z$$

Above relations are developed in appendix A as it enables to evaluate errors occurred during the standardizing campaign. Consequently, it is all the more better to operate more than two measurements for $\overline{\Delta\zeta_{coils}}$ determination.

Moreover, from equation 2.58a or 2.58b it can be deduced that the sum of all measurements over one face ("A" or "B") cancels magnetic axis contribution ($\overline{\Delta\zeta_{Mp}}$). Then the mean value of the N measurements performed enables to characterize $\overline{\Delta\zeta_{coils}}$.

$$\frac{1}{N}\sum_{k=1}^{N}\overline{\Delta\zeta_{Meas-kA}} = \frac{1}{N}\left[\overline{\Delta\zeta_{Mp}}\underbrace{\left(\sum_{k=1}^{N}e^{i\frac{-2\pi}{N}(k-1)}\right)}_{=0} + N\overline{\Delta\zeta_{coils}}\right] = \overline{\Delta\zeta_{coils}} \tag{2.59}$$

The mean value of the N measurements minimizes random errors as mean value of a random signal is all the more close to zero as N is high. Equations 2.58a, 2.58b and 2.59 show that all the magnetic axis are located on a circle of a radius $\left|\overline{\Delta\zeta_{Mp}}\right|$. Its centre is the sensor mechanical frame origin located at $\overline{\Delta\zeta_{coils}}$ from the sensor magnetic frame. By plotting the evolution of the magnetic axis location in the x-z plane, a regular polygon must be observed in the case of perfect measurements. This provides a useful graphical method to assess the quality of the reference tool measurements.

2m-pole magnet with mechanical defaults

Mechanical defects correction ($\overline{\Delta\zeta_{Tool}}$ see section 2.3.1.3) depends on how the reference magnet is installed on the bench girder. That is why a mechanical stand is required to position the 2m-pole magnet. x and z axis positioning of the 2m-pole magnet could be performed by means of a L-shaped interface (figure 2.16). This interface provides a direct measurements of the tool erroneous displacements due to its mechanical defects.

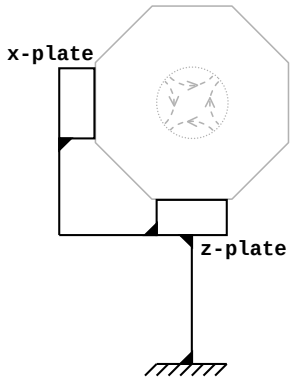

Figure 2.16: Stand of the reference tools

Two plates made of steel are used to ensure the 2m-pole magnet positioning: a vertical one for x-axis and an horizontal one for z-axis.

A 2m-pole magnet on "k" position undergo mechanical defects:

- along the x-axis from the facet $j = \left(k \pm (\frac{N}{4})\right)_{[N]}$ in contact with the "x" plate,
- along the z-axis from the facet $l = \left(k + (\frac{N}{2})\right)_{[N]}$ in contact with the "z" plate.

The subscript "[N]" stands for "modulo N" and the "±" sign (in "j") is used to take into account the face measured ; "+" sign for the "A" face and "−" sign for the other i.e. "B".

Consequently, the entity to subtract to $\overline{\Delta\zeta_{Meas-kA}}$ is:

$$\overline{\Delta\zeta_{Tool\,k}} = \overline{\Delta\zeta_{Mech-j\,l}} = \Delta Mech_j + i\,\Delta Mech_l \tag{2.60}$$

However the reference stand can be swung around z axis and the "X" plate can also be located on the right side of the beam (s axis). In that case,

- it reverses the "±" sign definition for "j" (− sign →"A", + sign →"B"),
- it changes the sign of $\Delta Mech_j$ and equation (2.60) becomes:

$$\overline{\Delta\zeta_{Mech-j\,l}} = -\Delta Mech_j + i\,\Delta Mech_l \tag{2.61}$$

In appendix A.2 all cases explained previously are developed. Mechanical defects of the reference tool can only be measured by mean of 3 dimensional mechanical measurements. Once all defects are known, they are introduced in the relation 2.60 or 2.61 which is subtracted to $\overline{\Delta\zeta_{Meas-kX}}$

If a magnetic measurement campaign of the N position of the reference tool is performed, their mean value can be calculated.

$$\frac{1}{N}\sum_{k=1}^{N}\overline{\Delta\zeta_{Mech-j\,l}} = \frac{1}{N}\sum_{k=1}^{N}\Delta Mech_{\left(k\pm\left(\frac{N}{4}\right)\right)_{[N]}} + i\,\frac{1}{N}\sum_{k=1}^{N}\Delta Mech_{\left(k+\left(\frac{N}{2}\right)\right)_{[N]}} \tag{2.62}$$

$$= \langle\Delta Mech\rangle\,(1+i) \tag{2.63}$$

$$= \left\langle\overline{\Delta\zeta_{Mech}}\right\rangle \tag{2.64}$$

If the mean value method of equation 2.59 is used, an interesting result is obtained:

$$\left\langle\overline{\Delta\zeta_{Meas}}\right\rangle = \frac{1}{N}\sum_{k=1}^{N}\overline{\Delta\zeta_{Meas-k}}$$

$$= \overline{\Delta\zeta_{Sensor}} + \left\langle\overline{\Delta\zeta_{Mech}}\right\rangle \tag{2.65}$$

One more advantage to use the mean value method is that it also smoothes statistical errors from mechanical measurement, reference tool handling and magnetic measurement. Once the mean value of mechanical errors are known, it must be subtracted to 2.65 to find $\overline{\Delta\zeta_{Sensor}}$.

2.3.1.5 Angular errors

Magnetic tilt angle is determined from theory mentioned in 2.1.2.2. There are several reasons which can lead to erroneous measurements of this quantity. The angular reference must be the printed circuit coils median plane which must be merged with the horizontal plane when the measurements start. It is never the case since manufacturing errors cannot be small enough to remain "transparent" in the magnetic tilt angle determination. There is an angular offset which must be removed to the measured magnetic tilt angle (θ_{Meas}) in order to get the real magnetic tilt angle (θ_{Mp}) of the measured 2m-pole magnet.

$$\theta_{Meas} = \theta_{Mp} + \theta_{Sensor} \tag{2.66}$$

The purpose of the next investigations is to show that similar swing measurements to those developed in part 2.3.1.2 can be performed to discriminate such a defect. The objective is to find two positions of the reference tool which provide opposite magnetic tilt angles.

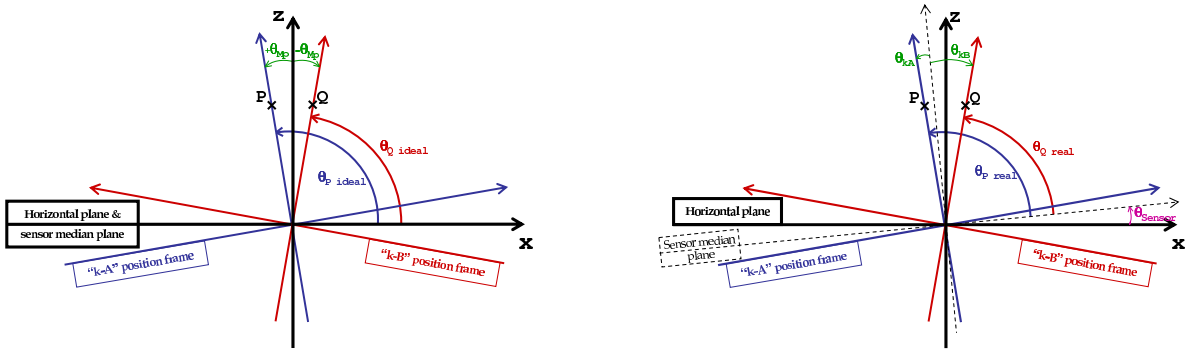

Figure 2.17: Influence of θ_{Sensor} value

Ideal case: $\theta_{Sensor} = 0$

When there is no angular defect as $\theta_{Sensor} = 0$, sensor median plane and the horizontal one are merged.

In the sensor frame, let's define an arbitrary point named "P" with affix $\overline{\zeta_P} = x_P + i\, z_P = \left|\overline{\zeta_P}\right| e^{i\theta_P}$ and belonging to the normal axis of the 2m-pole magnet defined as the axis of the magnetic field normal component. After a 180° z-axis rotation, "P" point becomes "Q" with affix $\overline{\zeta_Q} = \left|\overline{\zeta_Q}\right| e^{i\theta_Q}$.

From the definition of the magnetic tilt angle (see section 2.1.2.2), angles at the position "kA-ideal" and "kB-ideal" can be expressed versus $\overline{\zeta_P}$ and $\overline{\zeta_Q}$ arguments respectively.

$$\theta_{Meas-A} = \theta_P - \frac{\pi}{2} = \theta_{Mp} \tag{2.67}$$

$$\theta_{Meas-B} = \theta_Q - \frac{\pi}{2} \tag{2.68}$$

Moreover,

$$\overline{\zeta_Q} = x_Q + iz_Q = -x_P + iz_P = -(x_P + \imath z_P)^* = e^{i\pi}\overline{\zeta_P}^* \tag{2.69}$$

thus,

$$\theta_Q = \pi - \theta_P \tag{2.70}$$

$$\Rightarrow \quad \theta_{Meas-B} = \frac{\pi}{2} - \theta_P = -\theta_{Meas-A} = -\theta_{Mp} \tag{2.71}$$

These measurements are symmetric and can be used to determine θ_{Sensor}.

Case $\theta_{Sensor} \neq 0$

All magnetic tilt angles are defined from the horizontal plane whereas they are measured from the sensor median plane. When both planes are not merged, the angle got from the magnetic measurement does not represent the tilt angle to identify.

$$\theta_{Meas-A} = (\theta_P - \theta_{Sensor}) - \frac{\pi}{2} = \theta_{Mp} - \theta_{Sensor} \tag{2.72a}$$

$$\theta_{Meas-B} = (\theta_Q - \theta_{Sensor}) - \frac{\pi}{2} = -\theta_{Mp} - \theta_{Sensor} \tag{2.72b}$$

Swing measurements around the z-axis are suitable for θ_{Sensor} determination.

From 2.72 both unknown can be deduced.

$$\theta_{Sensor} = \frac{\theta_{Meas-1A} + \theta_{Meas-2A}}{2} \tag{2.73a}$$

$$\theta_{Mp} = \frac{\theta_{Meas-1A} - \theta_{Meas-2A}}{2} \tag{2.73b}$$

As in 2.3.1.4 section, the influence of the reference tool machining on magnetic tilt angle measurements has been studied but their effects are negligible. That is why it is not developed here. A complete theory about the use of a 2m-pole magnet reference tool is available and to fulfill the theory requirements, now is detailed how the design of the tool has been performed .

2.3.2 Final design and new approach proposition

Two multipolar permanent magnet reference tools have been manufactured: one quadrupole and one sextupole. The magnetic design was performed with the RADIA code [23]. The purpose of this part is to describe the multipolar reference. First their final design is depicted in order to emphasize on their defects. Then a new approach is proposed for the reference magnet design. It is a normal evolution after the first experiments performed.

2.3.2.1 Mechanical Measurements

Once the reference magnet are manufactured they must be mechanically measured. Indeed as developed in part 2.3.1.3, it is important to know the positioning defects due to machining error of the multigonal interface. That is why the mechanical data of the multipolar references are now reported.

Quadrupolar reference magnet

The design distance between one face of the octagon and its center is 110 mm. The figure 2.18 gives the difference between this value and the measured values. Then the angle between each faces were measured to quantify the quality of the manufacturer machining. The angles values are reported on the figure 2.19.

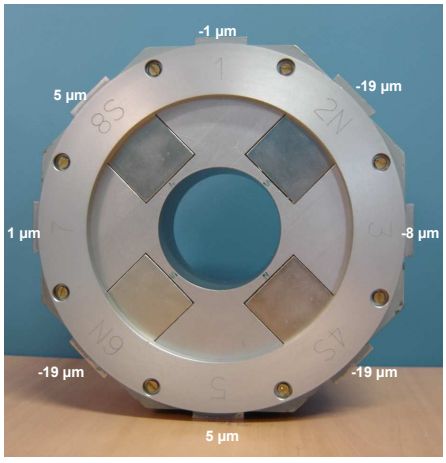

Figure 2.18: Machining defects

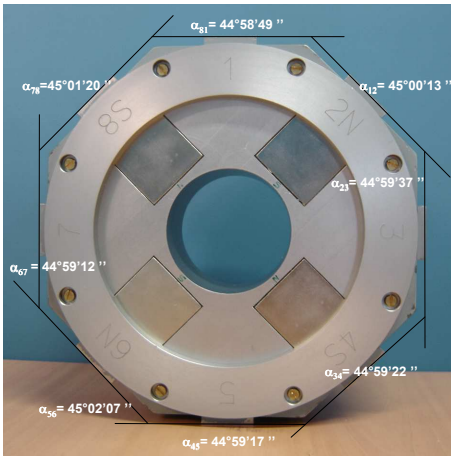

Figure 2.19: Angular defects

The mean value of the defects over one turn is -6.875 μm. As developed at the end of the part 2.3.1.3, this value is needed to calculate the rotating coil positioning defect.

Sextupolar reference magnet
Here are the real dimensions of the sextupolar reference magnet.

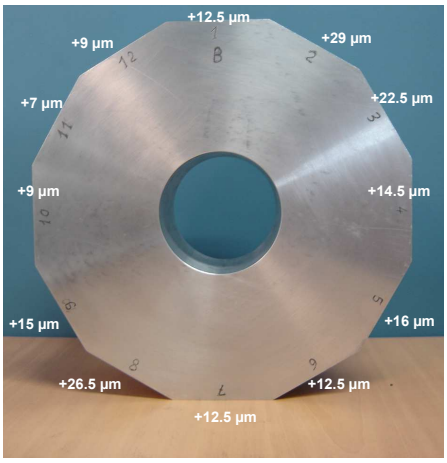

Figure 2.20: Machining defects

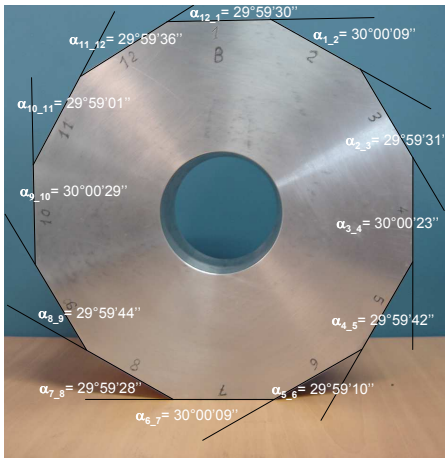

Figure 2.21: Angular defects

The mean value of the measured defects is 15.5 μm.

2.3.2.2 Improvement of the reference tool design

From the use we made of the multigonal reference tools, I can suggest an idea to improve the accuracy of the reference measurements made. As shown in the previous part, it is difficult to machine a multigonal interface and to install it on the bench without a few amount of errors.

The aim is to work with only 1 defect instead of 8 for the quadrupole (figure 2.18) or 12 for the sextupole (figure 2.20). The mechanical interface of the reference multipole must be a cylinder which is installed on stand with a "V" shaped interface. The only mechanical defect of this new mechanical reference (cylinder) is its radius. The advantage of this concept is that the machining of a cylinder is easier to master.

However the use of this new reference is a little different. The protocol is to put the cylindrical reference multipole on several angular position over one turn. The magnetic axis location is measured between each position. By plotting the measured data in the transverse plane, a circle must be obtained as shown on the figure 2.22.

With this new tool there is only one mechanical defect to measure, its positioning is easier to operate and much more accurate and reproducible. The calculation of the sensor magnetic offset requires to find the circle which best fit the data. The center location of this circle gives the coordinates of the researched offsets. The advantage of this tool has an infinite number of angular position which enables to choose the statistical quality of the measurements. At least three positions of the tool are required to find the center of circle. Then more positions can be measured but their number will be limited by time the spent for the measurement campaign.

However this new tool cannot measure the angular offset since there is no mechanical reference which enables a perfect swing of 180 ° around the vertical axis. Various solutions can be found to ensure this type of measurement, they are not detailed here.

The accuracy of the tool is improved by the good quality of the mechanical contacts between the "V" and the cylinder which is easy to get nowadays with the modern machining tools.

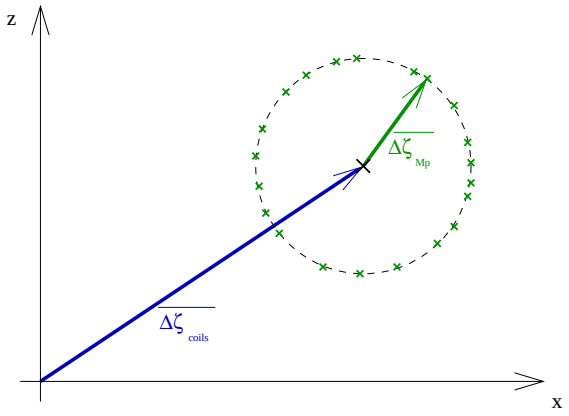

Figure 2.22: Offsets determination with the new method

Résumé du chapitre

La première partie de chapitre a permis de présenter la théorie des bobines tournantes qui repose sur des mesures de variation de flux. Dans un second temps, nous avons réalisé un modèle 3D des quadrupôles et des bobines tournantes qui permet de modéliser les conséquences des défauts des bobines tournantes, tels que leur flêche ou encore leur torsion, sur les harmoniques de champ. Dans le chapitre suivant, nous verrons comment cette méthode peut être appliquée à la compréhension de l'origine de certains harmoniques non attendus. Dans une troisième partie, nous avons présenté un quadrupôle de référence à aimants permanents visant à caractériser les défauts du banc de mesures de SOLEIL. Une méthode de détection des défauts a été mise en place. Sa mise en oeuvre sera exposée dans ce qui suit. Enfin, nous avons proposé un nouveau type d'aimant de référence cylindrique qui permettrait de réduire les incertitudes de positionnement.

Chapter 3

Magnetic-Based Alignment

Objectifs du chapitre
Ce chapitre est dédié aux résultats expérimentaux obtenus lors de la caractérisation des aimants 2m-polaires de l'anneau de stockage du synchrotron SOLEIL. Dans un premier temps, un état de l'art des dispositifs à bobines tournantes est réalisé dans lequel figure le dispositif de mesure disponible à SOLEIL lors du commencement de nos travaux de recherche. Notre travail a consisté à éprouver ce dispositif de mesure. Les problèmes rencontrés et les défauts mis en évidence lors de la mesure de quelques aimants sont exposés. Cette première étude expérimentale nous a conduit à proposer un nouveau dispositif de mesure dont la conception et la mise en oeuvre sont reportés ici. Les résultats obtenus sont également présentés.

This chapter is dedicated to the experimental work achieved on Synchrotron SOLEIL Storage Ring (SR) 2m-pole magnet characterization. First, the preliminary studies of existing rotating coil benches are detailed. Then the SOLEIL multipole magnetic measurement bench is depicted by laying emphasis on the main problems which had to be solved. Afterwards results obtained from experimental validation of the bench and from the 160 SR quadrupole series magnetic measurements are analysed. The objective is to deliver perfectly known SR quadrupole magnets to the machine physicist so that they can perform precise simulations for the beginning of the SR commissioning.

3.1 State of art of rotating coil benches

Before designing the bench, a non exhaustive study about the work performed on rotating coil bench developments is carried out. The aim of such a study is to gather the positive aspects of benches even if they do not have identical performances. Instead of studying each bench (Swiss Light Source (SLS), Centre Européen de Recherche Nucléaire (CERN), Sigmaphi, Danfisyk), the study turns around 5 aspects which cannot be ignored during the design of a rotating coil bench: the stand for the magnets, the mechanical links installed on this stand, the electronic equipments, the mechanical design of the magnetic sensor and finally the technology used for the sensitive coils. Then the first SOLEIL multipole magnetic measurement bench which needed to be modified is also depicted in this part.

3.1.1 General concept

Harmonic coil benches are firstly dedicated to measure magnetic field harmonics of 2m-pole magnets ($m \geq 2$). These harmonics enable to describe the effect of the quadrupole magnet imperfections on the electron beam dynamics. That is why it is very important to know them with a very good resolution. Even if nowadays, the design delivered by softwares is close to the final product, measurements are mandatory since specifications from machine physics are strict. Moreover only magnetic metrology can detect unpredicted defects which could be harmful for the beam behaviour. Afterwards the second reason which leads to magnetic characterization of the SR quadrupoles is the need for a very precise alignment of their magnetic axis. Misalignment of SR quadrupole implies orbit distortion which debases the electron beam quality. Magnetic axis properties (location and orientation) are calculated from harmonic measurements. Their correction directly depends on the mechanical design of the quadrupole magnets and on their stand on which they are installed in the machine. Since tolerances are small, each part of the bench is a critical point to master. That is why it is necessary to take time to study available solutions which could be adapted to the requirements. Quality for magnetic measurements is obtained if each element of the bench is properly designed and assembled.

3.1.1.1 Mechanical Stands

The first point to think about is how each element is positioned. As shows the kinematic scheme on the figure 3.1 the global mechanical design is simple.

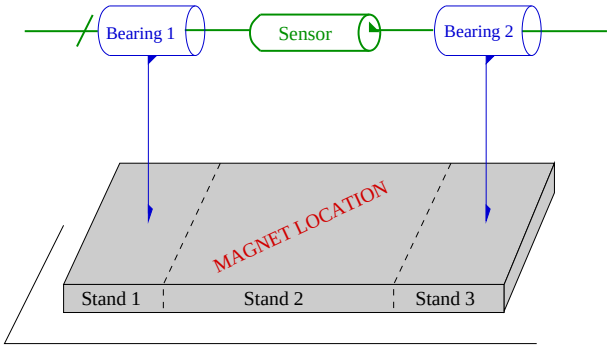

Figure 3.1: General kinematic scheme

To ensure the positioning of the bearings and the 2m-pole magnet, 3 stands may be manufactured. Nevertheless the number of stands can be reduced. It depends on the magnet which has to be measured on the bench. The less elements there are the more precise the bench will be. If there are only magnets of one machine to measure, only one stand is sufficient. All the magnets of a ring have the same general mechanical dimensions, that is to say the same location of their mechanical axis versus the bench local frame is the same for all. Consequently, there is no need to adapt the magnet stand for its magnetic measurements therefore only one stand for all the equipment is required. The advantage is that the design becomes simpler and the installation and alignment of each element is easier to master.

But from the magnet manufacturer point of view such a configuration does not allow to measure magnets of different dimensions without replacing the heavy(=waste of time) and onerous main stand. That is why, harmonic bench of magnet manufacturers are often made of three stands whereas particle accelerator magnetic measurement groups develop benches with only one. There are indeed two identical stands receiving the devices for pivot links and the magnetic sensor

driving, and a tunable one in the middle to adjust the vertical position of the multipole to measure. The tunable stand can be completely automated [24] or manually adjusted [25].

Then, once the number of stands is determined, the way how they receive the magnets and the measuring equipments have to be defined. Generally, fixed pins are inserted in stand and are used to position elements.

Then there are several mechanical parameters to adjust as

- the altitude of the magnet mechanical centre,
- the plane described by the surface of the stand which receives the magnet,
- the parallelism between the line made by the pivot link centres.

Perfect mechanical adjustment of the bench is not reachable and unavoidable defects can appear due to machining defects and assembly errors. That is why reference measurements (see section 2.3) are performed to characterize residual errors like the stands defaults.

3.1.1.2 Mechanical Links

The ideal way to get a high reproducibility bench would be to install 2m-pole magnet while the sensor is already installed on the bench and never dismantled. It would avoid all losses in accuracy due to sensor mounting and unmounting. But in this case, errors got from 2m-pole magnet dismantling would be greater. 2m-pole magnets cannot and must not be often dismantled, excepted for the vacuum chamber installation which is an unavoidable operation. That is why sliding contacts are preferred to pivot link at bearing locations to enable the sensor installation while the 2m-pole magnet is already on the bench. Up to now, we know a part of the 2m-pole magnet protocol of installation on the bench:

- Step 1: Installation of the magnet on the bench,
- Step 2: Insertion of the sensor through the 2m-pole magnet aperture.

Among the available solutions there are bronze bearings, ball bearings and also air bearings. The choice of the bearing technology is related to the sensor mechanical parameters as its weight, its length and more generally, its inertial geometry.

Air Bearings

Air bearing are based on mechanical lift due to high pressure which applies a force on the device to levitate. There is no metallic parts in contact therefore friction seen by the moving device is very close to zero. That is why it is often used for devices which need to reach very high rotating speed (300 000 turn/min). Air bearings require very clean air with a stabilized high pressure which are provided by an expensive pneumatic circuit installation. Such a technology can provide the stability required for the harmonic sensor. Indeed it eliminates friction between moving part and then release torsional constrain on the sensor mechanical structure. However air bearings are costly to set up, difficult to operate as they need very clean mechanical parts. Indeed the clearance between the moving parts is so small that any dirt can damage the system. As an example, initial Sigmaphi bench comes from a former magnetic measurement laboratory at CEA/ DAPNIA/ STCM using air bearings. As it was noisy to use and not really reliable, Sigmaphi replaced them by classical ball bearings easier, and cheaper to maintain.

Bronze Bearings

With bronze bearing, the moving part is directly in contact with the internal diameter of the bearing. The bearing is made with bronze material which has an intrinsic lubrication property. This property enables to reduce friction between parts in contact. Its use limits the rotation speed and the weight of the rotating device. Indeed if one of both is too large it will lead to a premature fatigue of the bearing and to a loss in the alignment accuracy. However, bronze bearings are easy to design since it does not require to apply many rules of mechanical construction.

Ball Bearings
In the case of the ball bearing, the friction between the fixed and the moving part is reduced by inserting balls between. The rolling friction is much smaller than the sliding friction. Indeed, there is much less friction between two moving shapes. This friction is replaced by the rolling friction which is much smaller. There are many types of ball bearing which are are available in various standard form. For many needs a ball bearing technology can be find. The use of ball bearings often implies an adaptation of the surrounding mechanical parts which is not always easy to design.

3.1.1.3 Electronic Equipments

To drive magnetic measurements, there is a minimum amount of electronic equipments to provide. A motor is required to rotate the sensor. It is generally a DC motor but it could be advantageous to master its rotation and then a step by step motor could fit. However step by step movement could induce vibrations that is why a more sophisticated DC motor provided with a programmable electronic command is preferred. The angular speed of the motor must be relatively constant but it is not a key point since measurements are integrated between several angular positions [19]. Then an integrator-voltmeter is needed to measure the induced signal coming from the rotating coils. It is often a Metrolab Precise Digital Integrator which is the reference for integrated voltage measurements. Then a rotary encoder delivers the signal to the voltmeter which starts the measurements. The choice of the encoder accuracy depends on the accuracy needed for the magnetic tilt angle.

To prevent from errors on harmonics due to external defects, bucking coils are used to cancel their effects. Bucking coil principle has been detailed in part 2.1.2.4. The choice of the measurement mode (normal or bucking) can be switched manually or automatically with an electronic box. The design of the electronic box is determined by the context of the magnetic measurements. That is to say the number of magnets to measure and the number of tasks to integrate.

To enable the communication between each element depicted previously, a user interface program must be developed. There is no privileged choice concerning the software. In the context of the collaboration with Sigmaphi, we used the same software as them which we adapted to our needs.

3.1.1.4 Sensor Mechanical Design

Even if the previous points are important, the magnetic sensor design is the most. As machines need always higher performances, tolerances on magnetic axis location and orientation are getting lower and lower. This implies stricter mechanical constraints, especially on the magnetic sensor.

Sensitive Coils
The choice of the sensitive coils technology is often the starting point of the sensor design. Indeed the geometry of the coil stand in the sensor mechanical structure depends on the technology chosen. The simplest is to use a bobbin of thin copper filaments (few hundred micrometers)

wound on a stand which is fixed on the sensor. In one hand, it is very difficult to machine a very precise groove where the filaments are placed. In another hand, the winding can move during the sensor rotation due to the clearance in the groove which can cause errors.

To minimize the previous defects Litz wire can be used instead of copper filaments. Litz wire looks like a classical copper filament but it is constituted N independent filaments inside. As N times less turn are required, the winding on the stand become easier. However the difficulty is that each thin filament must be manually welded compare to the two ends of a classical copper filament winding. Whatever the wire chosen (copper, Litz), the assembly remains difficult in the case of bucking coils. There are indeed several independent mechanical stands containing a winding to assemble with strict tolerances on the final sensor.

Then a more onerous solution is to use printed circuit coils. The advantage is that there is only a rectangular plate to fix on the mechanical structure. Moreover filament location can be exactly measured and remains stable during the measurements. It is the technology we chose for our sensor. This choice is more developed in 3.1.2.2.

Structure

The mechanical design of the sensor structure is probably the key point of the bench performance.

Machine physicists need to work with as reliable harmonics as possible. Therefore the sensitive coils have to catch the 2m-pole magnet magnetic field very close to the poles. The poles are the physical limit above which the sensor cannot rotate anymore. Consequently, the coil is often located on the edge of the mechanical structure which can reduce its rigidity. Indeed, if the rigidity is weakened, the sensor performs spurious movements which create spurious components in the harmonic content. The main goal of the sensor mechanical structure design is dedicated to the cancellation of spurious movements sources occurring during the rotation.

That is why two main topics must be treated:

- the unavoidable sag effect,
- the torsion from the motor to the encoder.

The objective is to minimize the coil sag. It is not possible to cancel this effect completely but the use of bucking coil can remove this effect from the magnetic harmonic content (see section 2.1.2.4). Indeed if the sensor undergoes a sag effect due to its weight and its mechanical structure, it would deliver an erroneous signal which would mainly be interpreted by the presence of a spurious skew sextupolar component in the harmonic content [1] (see section 2.2.4). Thus sag effect must be minimized. During the sensor rotation, it is also important that the residual sag is kept constant whatever the sensor angular position is. The sag angular dependence is directly linked to the one of the moment of inertia of the mechanical structure. That is why this entity must be kept constant versus the angular position. That is to say the sensor mechanical structure must have a high degree of symmetry around the rotation axis. It is important to note that getting constant moment of inertia implies constant coil sag but it does not limit sag effect.

Moreover, torsion increases with the length of the sensor. In addition to all the previous studies, the structure needs to be reinforced to limit errors on magnetic tilt angle (see section 2.1.2.2) measurements and unstable rotation. It must be performed without debasing the homogeneous sag optimization and at the same time this operation is limited the small aperture of the magnet where the sensor must go through.

Sensor mechanical structure optimization is one of the most important task to overcome during a magnetic measurement bench development. It is the main lesson we learned from the first magnetic sensor which has been manufactured at SOLEIL.

3.1.2 SOLEIL harmonic bench: initial design

The first design of the SOLEIL Multipolar Magnetic Measurement Bench (SMB) was not able to fit the specifications required for the series measurements of the 160 quadrupoles. We spent much time to commission it and to overcome difficulties. The works and studies which have been performed on this initial design are detailed here. The purpose is to study the problems encountered in order to get a satisfactory solution from the machine physicists point of view.

3.1.2.1 General concept

First it is important to remind the specifications required for the SOLEIL Storage Ring (SR) quadrupole magnets. Magnetic field harmonics must be known within $\pm 10^{-4}$ of the main component and magnetic axis properties must be measured and tuned to fit the following tolerances:

- Magnetic axis location: $\pm 25\,\mu m$,
- Magnetic axis orientation (tilt angle): $\pm 0.1\,mrad$

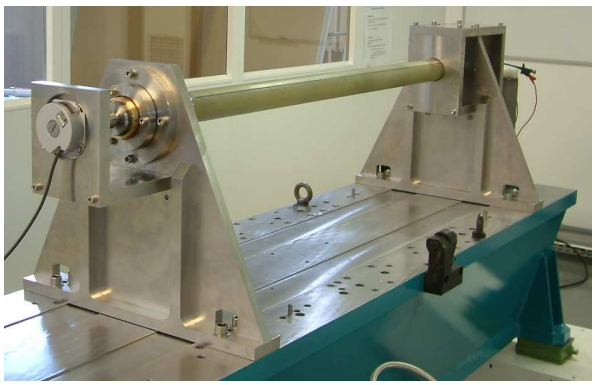

Figure 3.2: Initial Bench Design

The objective of SOLEIL Multipolar Magnetic Measurement Bench (SMB) was to attain measurement conditions close to those of the multipoles installed in the SR. That is why, they have been characterized in 21°C air conditioned room over a girder identical to those of the final installation. Since several types of experiment must be performed, the girder has been adapted to the needs. It was indeed necessary to measure long and short quadrupoles (320 mm and 460 mm) and sextupoles (160 mm) which require a dedicated mechanical positioning interface for each.

Even if the bench is mainly dedicated to measure the 160 SR quadrupoles, it must also perform some special measurements. Indeed, once each element is installed in the machine, it occurs that sextupoles and quadrupoles are only spaced of 120 mm. Such small space between these two types of magnet could induce cross talk of their magnetic field and then create additional spurious harmonics. Thus, measurements must be performed to check if this phenomenon exists. To get reliable measurements, it could be better to perform all these experiments with the same magnetic sensor. Consequently, a long sensor shown on the figure 3.2 has been designed ($1.2\,m$).

Electronic equipments

The sensor is equipped with several electronic devices driven by a program written in Testpoint, a data acquisition and analysis software developed by Capital Equipment Corporation (CEC) [26]. The graphical user interface dedicated to the SMB measurements is depicted on the figure 3.3.

The program commands

- a 24V brushless motor to rotate the sensor,
- a Keythley voltmeter to check the current value in multipoles and the room temperature,
- a current power supply by means of a dedicated Industrial Compact PC connected to the local network. The communication is based on TANGO object-oriented language [27] used at SOLEIL to command and control all the machine devices.
- a Metrolab Precise Digital Integrator (PDI) for flux measurements [28]. It takes signal from
  - measurement coils which deliver a voltage related to the flux induced by the sensor rotation inside the aperture of the magnet,
  - a Heidenhain rotary encoder which gives 720000 points per sensor turn for angular position measurements ($1point = 8.7\mu rad = 0.510^{-3} degrees$)[29]. It is able to measure angles 10 times smaller than the accuracy expected for magnetic angle determination.

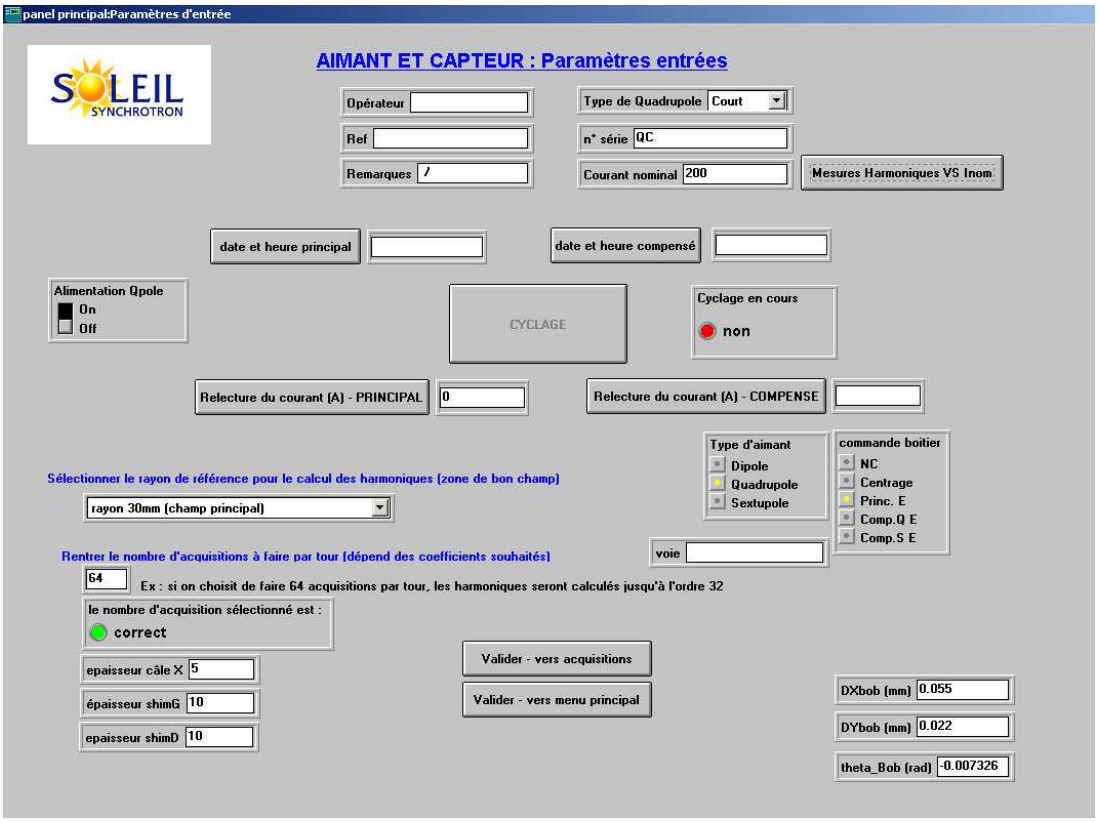

Figure 3.3: The TestPoint user interface for the SMB

All these elements are represented on the SMB synoptic scheme figure 3.4. It gives a global view of interconnections between each devices.

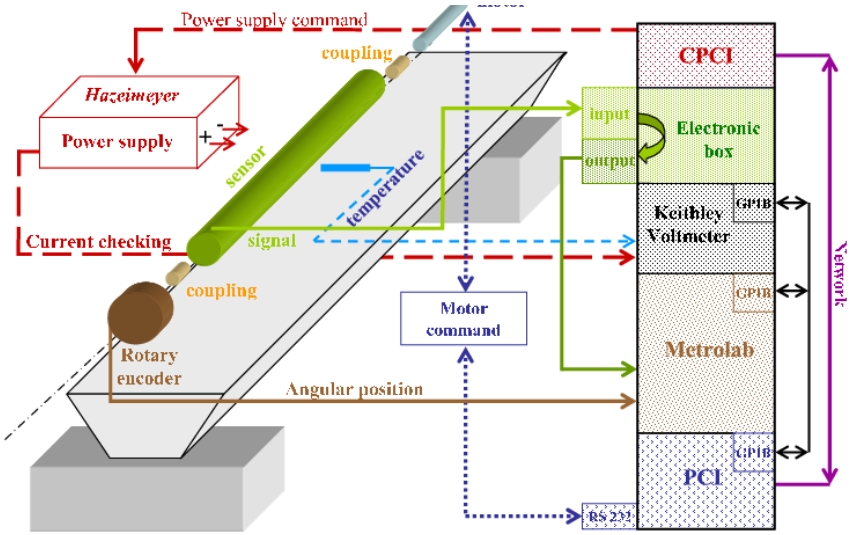

Figure 3.4: SMB synoptic scheme

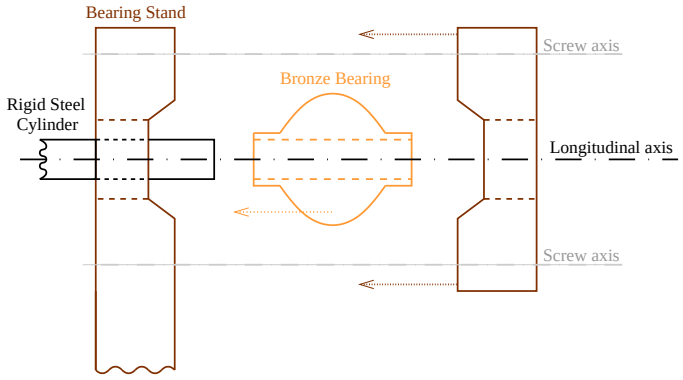

Figure 3.5: Bronze bearing alignment

Quadrupole magnet characterization protocol
A quadrupole characterization requires 3 steps:

- installation: the quadrupole must be installed on the bench and connected to fluids: electricity, water, security connections.

- magnetic measurements: during this step magnetic measurements are performed to characterize magnets and knowing its characteristics, the quadrupole is mechanically tuned to centre the magnetic axis and to cancel its magnetic angle.

- magnetic axis reference transportation (fiducialization): Once the quadrupole is properly tuned, a mechanical memorization of the tuning is performed. A mechanical device is installed on the quadrupole frame and it measures the sensor mechanical axis location. It gives the magnetic axis position versus the quadrupole mechanical frame. This data is very important for the quadrupole alignment in the machine.

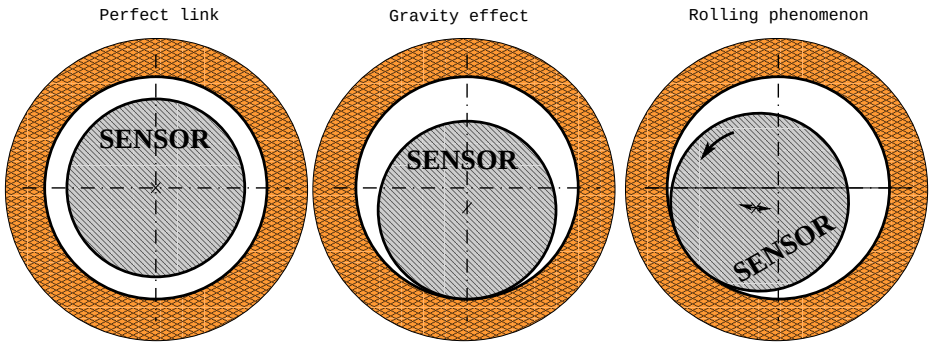

Figure 3.6: Rolling phenomenon

3.1.2.2 Technological choices

This part details the parts of the bench which had difficulties to work properly and then avoided the SMB to obtain the performances expected.

Sliding links

To enable the sensor rotation, the bench is provided with two pivot links. However to cope with assembly constraints before measurements, some freedom degrees must be released as shown on figure 3.1. Indeed, bearing positions are fixed and then the sensor must be introduced from the entrance of the 2m-pole magnet to its exit.

The entrance and the exit of a 2m-pole magnet are the sides which would see the e- beam entering and exiting if the 2m-pole magnet would be installed on the machine.

Bearing technology chosen for the bench is the one using bronze material (see part 3.1.1.2) since it is easy to conceive and it is well adapted for sliding links. Bronze cylindrical guideways are fixed on rigid stands installed on the bench girder.

The simplicity won during these bearing conception was lost in their alignment protocol. The positioning reference is given by two rigid "V" fixed on the bench girder. These "V" define an imaginary straight line which represents the longitudinal s-axis. A steel cylinder with the same dimensions as the sensor is installed on the two "V" in order to align the two bronze bearings versus the longitudinal reference. The bronze bearing assembly procedure is shown on figure 3.5.

The accuracy of such an alignment procedure mostly depends on the clearances between bearing internal diameter and the cylinder one. Moreover, since these clearances are the same for the sensor, a rolling phenomenon can appear during the sensor rotation between its external diameters located in bearings and their internal diameter (see figure 3.6). With such a phenomenon, the measurement uncertainty can get high values!

The larger the clearances are, the more important the phenomenon is. It implies spurious movements of the sensor which are frictions dependent and consequently not really reproducible.

Sensitive coils

Printed circuit technology was chosen for the sensitive coils. On a thin plate of fiberglass filled with epoxy resine (2 mm), it is possible to work with five radial coils made of forty turns each: ten layers of four turn coils connected in series as shown on figure 3.7. The filaments are 100 μm thick and spaced of 100 μm.

The main advantage of this technology is that filaments location can easily be measured



Figure 3.7: Sensitive coils

since for each printed circuit plate a spare one is manufactured. This spare is identical to the first one because it is manufactured by the same machine at the same time on the same stand. Consequently the spare printed circuit is used to check the quality of the coils. By performing a cut of this spare, the relative location of each filament can be measured. From these measurements illustrated by the figure 3.8, the maximum misalignment between two layers is 85 μm compared to 100 μm of the specifications.

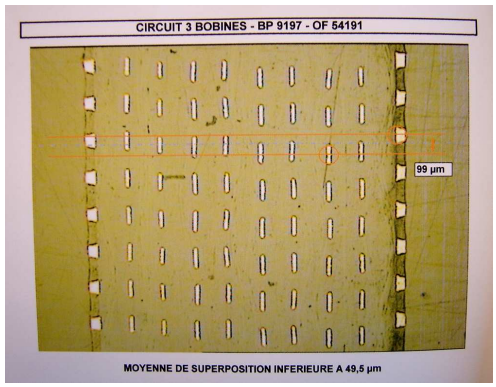

Figure 3.8: Cut view of printed circuit

Structure of the sensor

First, magnetic and conductive material cannot be used to design the sensor stand. Indeed, if these type of material are used, the flux produced by the multipole magnets is disturbed and its measurements leads to erroneous magnet characterization. Consequently composite materials were chosen since it provides good mechanical properties without debasing the surrounding magnetic field properties. An additional reason is that composite materials have a smaller mass density which makes the magnetic sensor lighter and then easier to handle during the measurements of the 160 quadrupoles.

Then it was an initial wish to design an evolutionary sensor so that it sensitive coil could be replaced. Indeed it could enable adapting the sensor sensitivity to the magnet which must be measured. Moreover, sensitive coils must skim magnet poles since it is important to get as information as possible from measurements. Consequently, the sensor stand must be half cut over its diameter as sensitive elements are printed circuit coils engraved on 10 layers of thin (200 μm) rectangular plates. It means that the printed circuit plate is such broad that it required the cylindrical stand to be half cut over its diameter to sandwich it. Separating the stand in two part weakens the sensor mechanical properties so it adds a constraint on the design. Made of

fibreglass composite material, both part of the sensor stand (halves cylinders) are sandwiching printed circuit coils by means of screws to enable coil replacement.

3.1.2.3 Performances

Preliminary measurements were performed to test the sensor detailed previously. The purpose was to measure 15 short quadrupoles by performing swing measurement in order to determine both quadrupole magnetic axis characteristics and sensor defects. For the sensor defects, only horizontal offset and tilt angle offset can deduced from these measurement. The vertical offset need the quadrupole to be swung of 180 ° around the longitudinal axis. The magnetic sensor detailed previously has some defects which have been brought out after some preliminary measurements.

Preliminary measurements
After the first measurements an important skew sextupolar component appeared in the harmonic content of quadrupoles (figure 3.9). The skew sextupole component is due to a sag of the sensor.

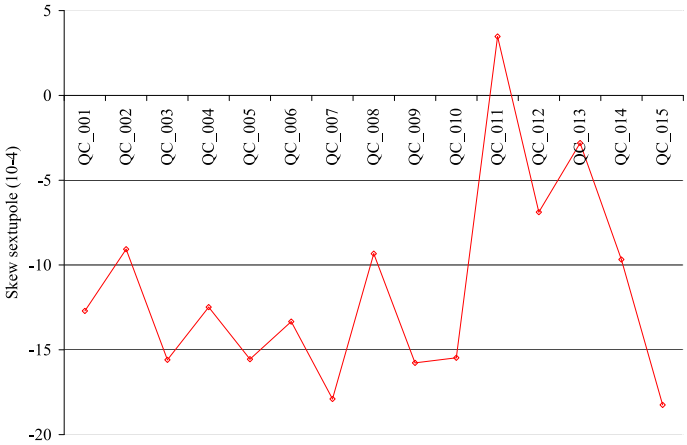

Figure 3.9: Skew sextupole component (10^{-4} of $\mathcal{B}_2$)

However, this sag do not seem to be reproducible. That is why deeper studies developed in the next part were necessary. On the figures 3.10 and 3.11 are reported respectively the evolution

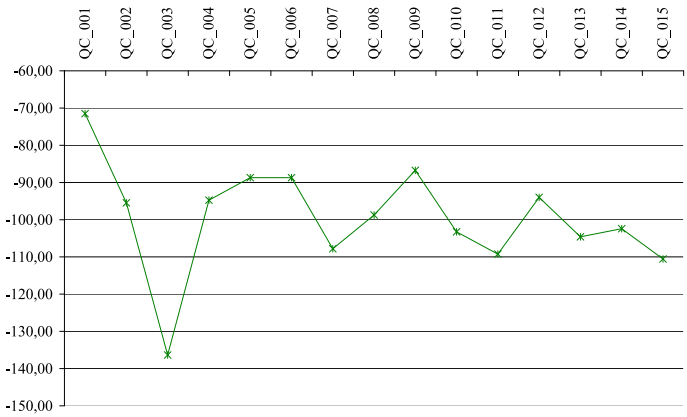

Figure 3.10: Preliminary measurements:horizontal offset (μm)

of the horizontal and the angular offset versus the measured quadrupole. During these measure-

ments, problems were encountered and they are reported in the next part which deals with the bench defects. Both plots are not satisfactory. The sensor defects are quantities which cannot

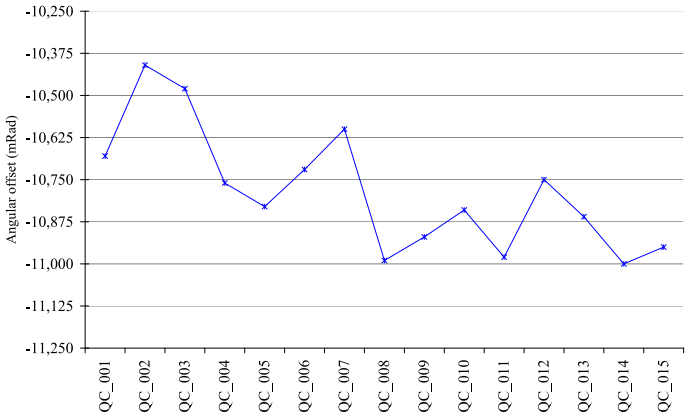

Figure 3.11: Preliminary measurements:angular offset ($mrad$)

vary instantaneously from one quadrupole to another. The variation observed are not acceptable for the objective which have been fixed concerning the magnetic axis. For example, at that moment it is impossible to determine the magnetic angle better than $\pm 0.3\, mrad$ compared to the desired tolerance of $0.1\, mrad$. The $0.1\, mrad$ tolerance represents a $3\mu m$ mechanical stability of the sensor at the 30 mm radius. Despite this very strict tolerance, studies were lead to obtain a sensor which could reach the tolerances.

Causes of the defects

As developed previously, the first attempt to manufacture the magnetic sensor was a failure. The purpose of this paragraph is to describe the problems encountered in order to begin studies which will lead to a more acceptable solution.

General Remarks

First, as the sensor is heavy, there is a big amount of friction and it is not constant during the rotation and not the same for both bearings. Consequently torsional vibration appears which is not good for measurement.

Another source of vibration is the DC motor which cannot start the rotation smoothly. It would be better to resort to an electronic command which could at least drives the motor acceleration.

Then the bronze bearing alignment protocol is too long to apply. Moreover all the clearances needed for the installation of each element of the alignment protocol are accumulated and lead to important final clearance between the bronze bearing and the sensor. Unfortunately these clearances are large enough to enable rolling effect described in part 3.1.2.2. However the clearances were necessary since whenever they have been reduced, the sensor was not able to turn. These are contradictory conclusions which mean that the problem is more complex to solve. That is why deeper studies of the mechanical structure of the sensor are necessary to find an explanation of the effects observed.

Mechanical Calculation

The main problem encountered with the sensor stand might come from its sag. Indeed, it occurred that it was not a simple sag effect which remains constant whatever the sensor angular

position is. The answer is given by a calculation which gives the behaviour of the sag by taking into account the geometrical structure of the sensor. During the design time, it was assumed that even if the sensor stand is half cut, after its assembly, its sag behaviour during rotation was the same as a plain cylinder rotating along its main axis : a constant sag.

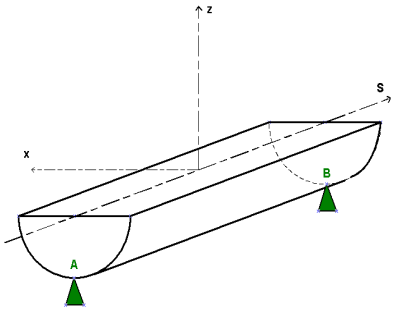

Figure 3.12: Assumptions

The effect of the sag is described by equation (3.1) as a function of the longitudinal position (s), the angular position(θ), the Young modulus(E_y) and the main mechanical moment of inertia ($I_{Gx}(\theta)$).

$$Sag(s,\theta) = \frac{w}{24\,E_y\,I_{Gx}(\theta)}\,L^4\left(\frac{5}{16} - \frac{3}{2}\left(\frac{s}{L}\right)^2 + \left(\frac{s}{L}\right)^4\right) \tag{3.1}$$

MOMENT OF INERTIA
The studied structure is an half cylinder of length L and diameter d.

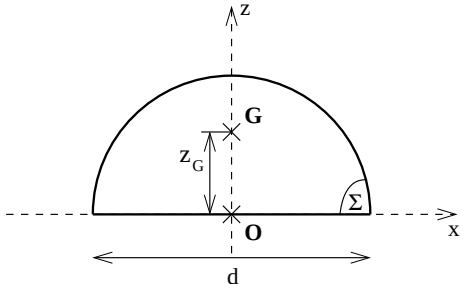

Figure 3.13: Half cylinder

The moment of inertia general expression is given by equation 3.2.

$$I_{Gx} = \int_{\Sigma} z^2\,dS \tag{3.2}$$

The previous integral is calculated with the centre of gravity as the origin but it is more convenient to calculate it from the point O and then to perform a translation of the result from $O(0,0)$ to $G(x_G, z_G)$ by means of Huygens formulas given by the equation 3.3.

$$I_{Ox} = I_{Gx} + S_s\,z_G^2 = \frac{\pi\,R^4}{8}\,[m^4] \tag{3.3}$$

$$I_{Oz} = I_{Gz} + S_s\,x_G^2 = \frac{\pi\,R^4}{8}\,[m^4] \tag{3.4}$$

$$\tag{3.5}$$

Then from Huygens formula 3.3, angular dependence of I_{Gx} can be determined.

$$I_{Gx}(\theta) = I_{Ox} - S_s.z_G(\theta)^2 = I_{Ox} - S_s.z_G(0)^2\ cos(\theta)^2 \tag{3.6}$$

$$I_{Gz}(\theta) = I_{Oz} - S_s.x_G(\theta)^2 = I_{Oz} - S_s.z_G(0)^2\ sin(\theta)^2 \tag{3.7}$$

Guldin's rule gives the means to calculate $z_G(0)$.

If any plane figure revolves about an external axis in its plane, the volume "Vol" of the solid so generated is equal to the product of the area S_s of the figure and the distance traveled by the centre of gravity of the figure.

$$Vol = 2\pi\ z_G\ S_s \tag{3.8}$$

$$\text{Thus for an half disc, } z_G = \frac{2}{3\pi}d \tag{3.9}$$

Then the mechanical moment of inertia along the x-axis is expressed by the following relation (3.10).

$$I_{Ox}(\theta) = I_{Gx}(\theta)cos(\theta)^2 + I_{Gz}(\theta)sin(\theta)^2 \tag{3.10}$$

$$= \frac{\pi\ R^4}{8} + \frac{1 + cos(2\theta)^2}{2}\ S_s\ z_G^2 \tag{3.11}$$

The analytical expression of $Sag(s, \theta)$ is plotted on figure 3.14.

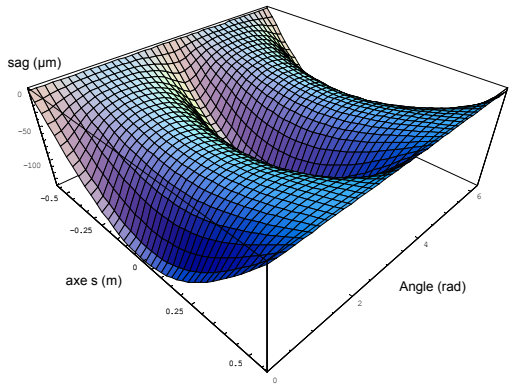

Figure 3.14: Curves

The sensor sag dependence on the angular position has an influence on the measured harmonics. This influence has been analyzed with the theoretical experiments (see part 2.2.1) which showed that this particular type of sag effect was the source of skew sextupole harmonic component we initially measured with the first sensor. Indeed the spurious skew sextupole component is smaller in the case of a simple sag effect of the sensor.

3.2 The SOLEIL Multipolar Magnetic Measurement Bench

As mentioned previously, the SMB has been designed to characterize and to tune magnetic properties of SOLEIL SR multipole magnets. As shown in part 3.1.2, quadrupole electromagnets must be known within low tolerances. Parameters which need to be measured are harmonic content, magnetic axis location and tilt angle orientation. Measuring these parameters is only one

motor → coupling 1 → mech. adapter 1 → mag. sensor → mech. adapter 2 → coupling 2 → rot. encoder

Figure 3.15: Kinetic chain of the bench

step of the work. It is indeed necessary to make the magnets reaching tolerances by tuning them mechanically. Section 3.1.2 shew that the first attempt in magnetic sensor design was a failure. Many specific parts of the bench must be studied again in order to obtain the configuration which fits the machine physicist expectations. To perform these improvements, it may be necessary to review some technical choices in order to obtain new freedom degrees.

3.2.1 Improvements of the mechanics

From the last design, a big work concerning the mechanical design of the bench need to be done. It must provide a sensor with minimized sagitta, torsion and vibration to avoid measurement errors brought out in part 3.1.2. Even if the sensor printed circuit coils weakens its mechanical structure due to the fact that they must skim the magnet poles, it remains an important objective. Easy sensor installation is also another kept objective since there are 160 quadrupole magnets to measure and a high measurement pace must be reached.

All these constraints -some of them are contradictory- make the conception so specific that the sensor has only been developed to measure magnets with a mechanical design close to the SOLEIL multipoles ones. Consequently, it should be reasonable to forget the evolutionary objective.

3.2.1.1 Kinetic chain

First the DC motor is replaced by brushless motor provided with an electronic command which can drive the motor acceleration. Torsional vibrations are reduced since the nominal rotation speed is reached smoothly. After that, it is important to ensure a perfect transmission of the rotation.transmitted at one side of the sensor must be detected and properly measured by the rotary encoder instantaneously. The kinetic chain drawn on figure 3.15 shows the elements mentioned previously. The kinetic chain must be optimized by keeping in mind the torsion constraint during the sensor mechanical structure design but also by choosing adapted mechanical adapters and couplings: they must transmit angular information perfectly ($0.1\,mrad/10 = 0.01\,mrad$).

Then magnetic sensor vibrations due to rolling effect in bronze bearings is cancelled by changing the bearing technology. Ball bearings are used now to reduce the clearance which is typically few tens of micrometers, the internal shaft is tight mounted on the sensor. Clearances and friction are now very small compared to the initial solution. Two problems are solved but the mechanical configuration of the bench has completely changed. The bearings are now part of the sensor, therefore the sensor stand have to be adapted. A perfect positioning of the sensor can be provided by "V/cylinder" interface, cylinders standing for ball bearing external shaft. That is why the stand is transformed into 2 "V" interfaces as shown on the scheme 3.16.

The only constraint of this concept is that external diameter of the ball bearing must be smaller than the 2m-pole magnet aperture ($66\,mm$). Concerning the advantages, the sensor is now very easy to install, no more bearing alignment process is required, the gain in reproducibility would become important.

Moreover, ball bearings are tight mounted to reduce natural clearance between balls and shafts. Consequently the clearance between the sensor and the stand is reduced to few micrometers compared to the many tens of micrometers with the bronze bearing. Reducing clearance in

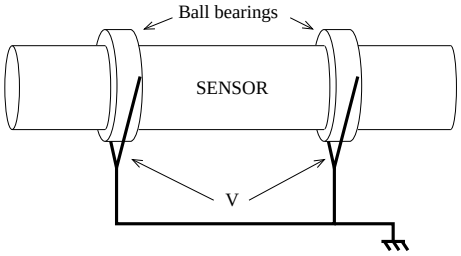

Figure 3.16: "V"/cylinder interface

ball bearing would induce thermic problems but the sensor rotation speed is very small to imply overheating of the mechanical structure and then mechanical deformations.

3.2.1.2 Sag effect minimization

As demonstrated in section 3.1.2.3, sag must be strongly reduced but also its angular dependence which leads to really erroneous magnetic measurements. Indeed, angular position dependence of the sensor sag has to be cancelled since it is the main source of spurious harmonic.

The first parameters which can be used to limit sag are the structure length and weight. But the only one parameter which could limit the sag angular dependence is the moment of inertia (I_{Gz}) that is to say the geometry of the sensor mechanical structure. Thus the main directive way of the study is to get an homogeneous moment of inertia since the length and the weight of the sensor are reduced as far as possible.

As the figure 3.14 shows it, the initial sensor undergoes less sag effect when θ is 90 °. A rectangular parallelepiped has the same behaviour and the idea is to take advantage of the position for which its rigidity is maximum.

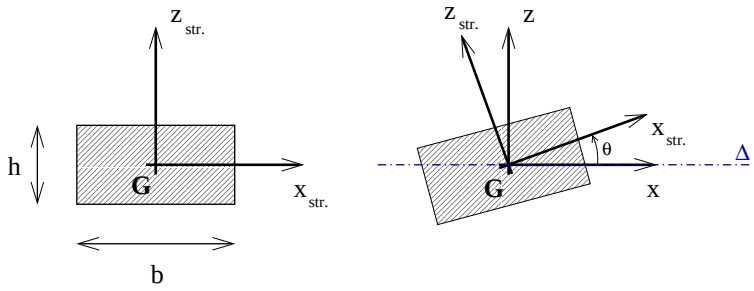

Figure 3.17: Rectangular cross section

Indeed the moment of inertia of this rectangular structure is weaker around the $x_{str.}$ direction than around the $z_{str.}$ one. It is confirmed by comparing the moment of inertia, using the dimension h and b defined in the figure 3.17.

$$I_{G\Delta}(\theta = 0) = I_{Gx|str.} = \frac{b.h^3}{12} < \frac{h.b^3}{12} = I_{Gz|str.} = I_{G\Delta}(\theta = \frac{\pi}{2}) \qquad \forall\, h < b \tag{3.12}$$

Hence the analytic expression of $I_{G\Delta}(\theta)$

$$I_{G\Delta}(\theta) = I_{Gx|str.}\, cos^2(\theta) \; - 2\underbrace{I_{Gxz|str.}}_{=0} sin(\theta)cos(\theta) + \; I_{Gz|str.}\, sin^2(\theta) \tag{3.13}$$

$$= \frac{1}{2}\left[(I_{Gx|str.} + I_{Gz|str.}) + (I_{Gx|str.} - I_{Gz|str.})\, cos(2\theta)\right] \tag{3.14}$$

Studying 3.13, a structure which has $I_{Gx|str.} = I_{Gz|str.}$ and $I_{Gxz|str.} = 0$ only undergoes a sag independent of the angular position. That is why a cross shaped structure is well indicated. The purpose is to take advantage of the rectangular shape on its rigid position. As much less material is used, the sag is also limited by the smaller weight of the structure. Moreover if the dimensions of this cross shaped structure are well chosen, a better rigidity compared to a plain cylinder could be expected. For a cross shaped structure, the mechanical moment of inertia is expressed by the equation 3.15, with e and d its dimensions defined on the figure 3.18

$$I_{Gx|Cross} = \frac{1}{12}(e\, d^3 + d\, e^3 - e^4) \tag{3.15}$$

Concerning the application of the concept, the printed circuit stand needs to be located in the median plane of the sensor and therefore of the cross shaped structure. The printed circuit plate is mechanically reinforced by two fiberglass rectangular plates in order to form a rectangular structure. Then two other rectangular plates are stuck and their dimensions are adapted to obtained a symmetric cross shaped structure as drawn on the figure 3.18.

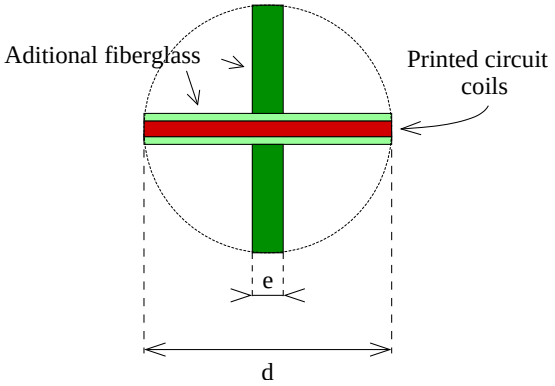

Figure 3.18: Cross shaped structure

However such a structure is not well designed for torsion optimization it must be reinforced to reach the angular stability specification.

3.2.1.3 Torsion minimization

The previous structure can be reinforced to minimize torsion since space has been liberated by designing a structure which use less material. When a torsion momentum is applied to a structure with a Coulomb modulus G and a momentum of inertia around the s direction $I_{Gs|str.}$ is rotated by an angle $\theta_{Tors.}$ as expressed by the equation 3.16.

$$\theta_{Tors.} = \frac{M_t\, L}{G\, I_{Gs|str.}} \tag{3.16}$$

$$\text{With } I_{Gs|str.} = I_{Gx|str.} \; + \; I_{Gz|str.} \tag{3.17}$$

M_t comes from the acceleration of the motor and mainly from the resistance during the rotation due to friction. Acceleration is mastered by the electronic command and the friction has been minimized since ball bearings are used. However since the tolerance concerning the angular stability is very low, the structure needs to be reinforced.

Two parameters can be adjusted: the moment of inertia around s and the Coulomb modulus. Indeed larger values are required for both parameters. That means that mechanical pieces must be added and that another material with a greater G must be used. As the cross shaped structure is not optimized for torsion transmission, it could be helpful to uncouple each constraint. The cross shaped structure is limiting sag and the additional structure has to reduce torsional errors and consequently ensures the movement transmission.

As carbon fiber composite material has an interesting Coulomb modulus, it is used to transmit the motion coming from the motor to the cross shaped structure. However additional pieces are necessary, thin pairs of halve cylinder are ensuring the mechanical interface needed between the cross and the tube to ensure the movement transfer.

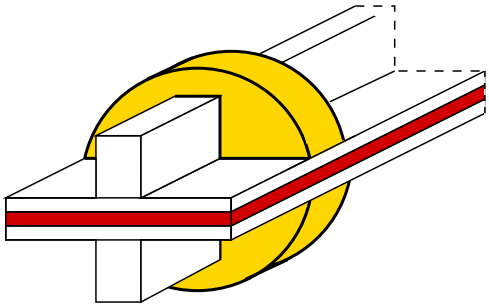

Figure 3.19: Halves cylinders

Halves cylinders transmit the torque from the tube to the cross and at the same time they reinforce the cross for torsion. By means of these halves cylinders, the tube can be stuck to the fiberglass structure (cross + halves cylinders). Using this tube, the kinetic chain is changing. Indeed, the printed circuit does not undergo directly the rotation torque since it is coming from the peripheral tube.

Since the printed circuit plate is 64 mm large, whatever the thickness of the tube is, it is not possible to find a tube which can receive the fiberglass structure and which can be inserted in the aperture of the quadrupole ($\phi = 66\,mm$). That is why the tube must be separated in two parts and both part are stuck on the fiberglass structure. Positioning pins are added to ensure adjustment of these carbon fiber shells.

Figure 3.20 shows all the elements mentioned before. Other important improvements are treated in the next part.

3.2.2 Alignment during the sensor assembly

The purpose of this part is to describe the mechanical parts which play an important role in the printed circuit positioning. First the assembly procedure is depicted. Indeed, an assembly tool has been manufactured to ensure accurate positioning of each part of the fiberglass structure. Then the role of the aluminum tips is emphasized since they link the printed circuit alignment to the bench alignment.

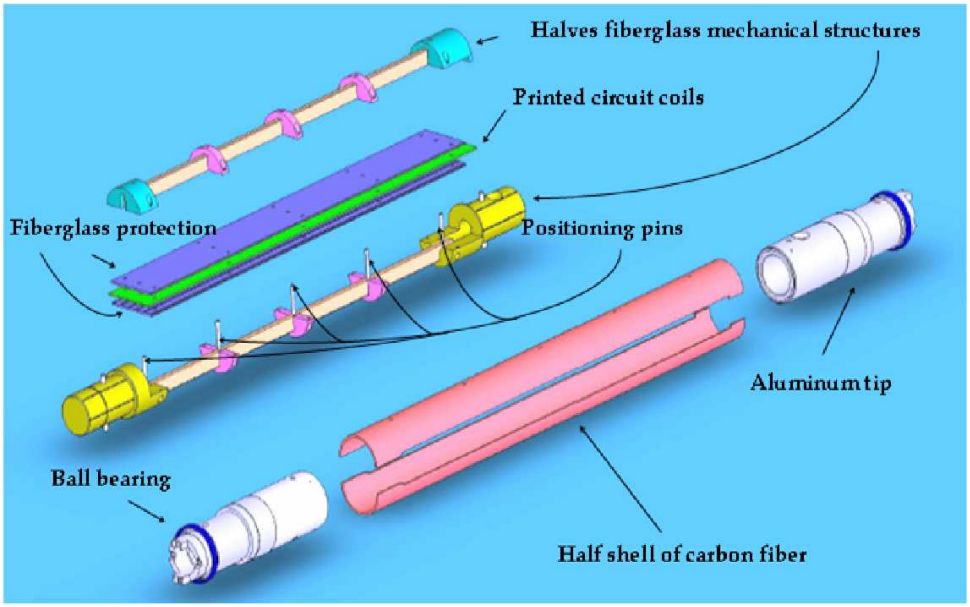

Figure 3.20: Detailed view of the sensor mechanical structure

3.2.2.1 Fiberglass structure assembly

A mounting tool has been manufactured to stuck precisely all parts of the fiberglass structure. As shown on the figure 3.21, the assembly tool has tunable parts in order to enable their alignment with a cylinder (on the right on the figure 3.21). The goal is to align the printed circuit plate

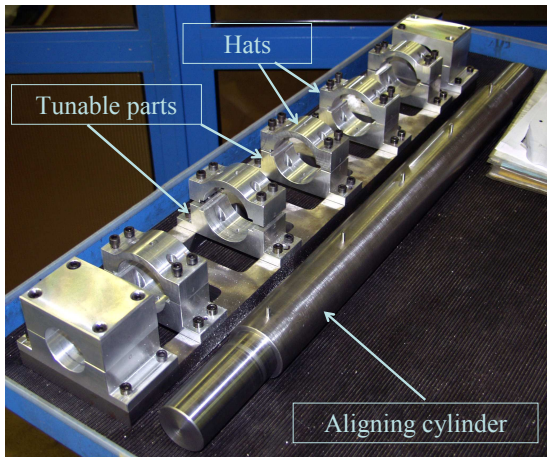

Figure 3.21: Assembling tool

versus the mechanical axis of the fiberglass cylinder located at the ends of the structure (in yellow on the figure 3.20). This alignment is ensured for the x direction by means of the positioning pins and for z direction by the precise machining of the fiberglass cylinders. All parts are positioned by means of positioning pins and are stuck together. The assembly tool tightly keep this structure during the glue drying by means of halves cylinder hats (figure 3.21). All the steps of this assembly are shown in the appendix B.

3.2.2.2 Aluminum Tips

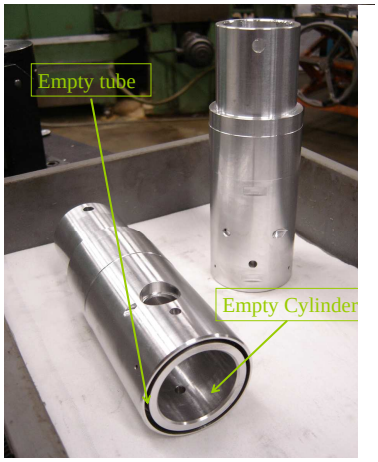

Figure 3.22: Aluminum Tip

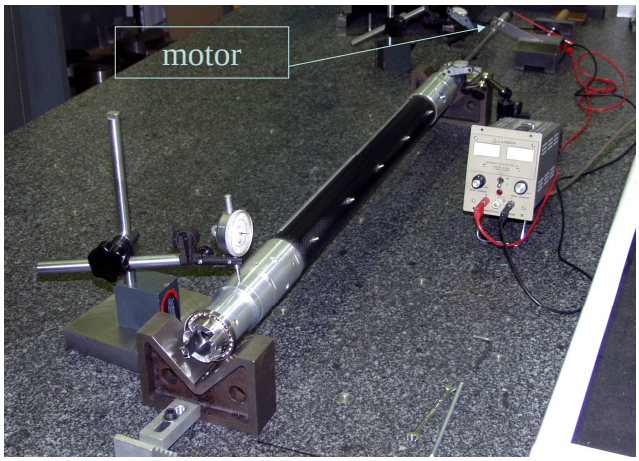

Figure 3.23: Glue Drying Process

Sensor structure centering
Now on one hand there are the fiberglass structure and the carbon fiber shells and on the other hand the motor and the rotary encoder. Both must be mechanically connected but not directly. This mechanical connection is ensured by the aluminum tips (figure 3.20). The alignment interface between the stands and the sensor is performed by the ball bearings which are mounted on the tips. That is why an empty cylinder which has the same mechanical axis as the ball bearings is machined in the tips. Consequently the end cylinders of the fiberglass structure can be adjusted and stuck in the empty cylinders. This adjustment ensures the centering versus the whole bench of the fiberglass structure and therefore of the printed circuits. The centering of the printed circuit versus the ball bearing is ensured.

Rotating motion transmission
Then as mentioned in part 3.2.1.3, the carbon fiber shells are also used to transmit the rotation motion.

An empty tube of dimensions of the carbon fiber shells is machined in the aluminum tip in order to stuck the shells inside. A particular drying process has been set up to obtain a uniform distribution of glue between the tips and the shells. Indeed to avoid the effect of gravity, the sensor was rotating during the glue drying (see figure 3.23).

Once the sensor is totally assembled, the final kinetic chain has changed. Addition of carbon fiber shells enables to distribute the torsion torque. Indeed the torque coming from the motor is no more concentrated in the central stand of the printed circuits. The torque is rigidly transmitted from the tip to the shells and from the shells to the fiberglass structure.

Angular Reference Interface
The absolute horizontal plane is taken as the angular reference for the magnet alignment in the machine and therefore for their magnetic measurements. Bubble level technology has been preferred to accelerometer or electronic level to determine this reference. Indeed the simplest and the more reliable technology has been chosen since it was not possible to take risk with random electronic offset derivation.

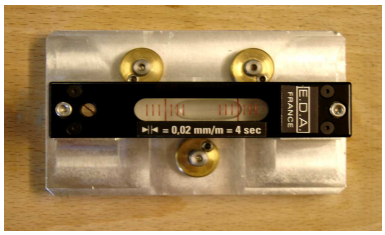

Figure 3.24: Bubble Level

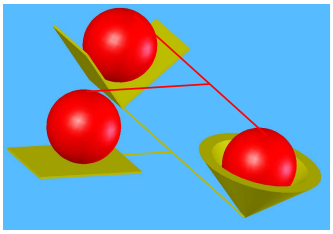

Figure 3.25: Line/Dot/Plane Principle

The determination of this angular reference is a key step in the magnetic angle measurement. Any error during this process is directly transmitted to the measured magnetic tilt angle measurement. To minimize error, the first idea is to get a bubble level with a greater resolution than the tolerance. This is why the bubble level (figure 3.24) chosen has a resolution of 0.02 $mrad$ which is five times smaller than the tolerance and approximatively 10 steps for the rotary encoder.

However such mechanical device needs to be adapted in order to install it on the sensor before each magnetic measurement. The purpose is to create a fixed angular reference between the horizontal plane of the printed circuits and the mechanical interface of the bubble level. That is why a line/dot/plane interface has been machined on one aluminum tip (figure 3.25 and 3.26). The bubble level is rigidly fixed on a plate on which are fixed micrometric screws provided with small spheres at their ends.

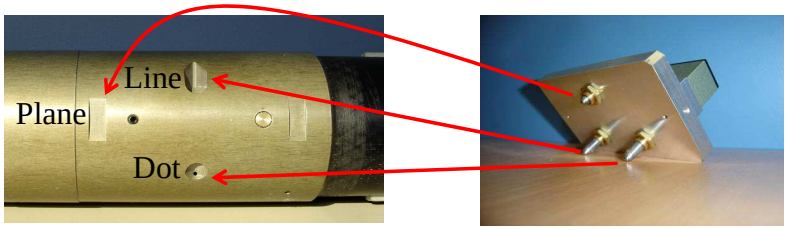

Figure 3.26: Real Line/Dot/Plane interface and its adapted bubble level

Obviously, plane described by the printed circuit plate and the Line/Dot/Plane interface cannot be exactly parallel. There is an unavoidable tilt angular offset which could generate errors. But what is important is whatever the value of this offset is, it must remain constant for a period larger than the time needed for some measurements. Indeed, in part 2.3 a method is proposed to measure this offset so that it can be taken into account.

Magnetic Axis Memorization

Once the magnetic axis is properly tuned, it is important to measure its location versus the mechanical frame of the quadrupole magnet. Such data are important to check the alignment of the magnets in the machine. The mechanical device which performs these measurement was provided by the alignment group and is named the "grasshopper". The principle is to install this device on the quadrupole magnet and to measure the location of the sensor mechanical axis. For this, a small zone on the aluminum tips has been dedicated to enable the measurement of the shape of the precisely machined cylinder.

This measurement is totally automated. The motor positions the sensor at N angular positions with a waiting time between each. It enables the mechanical measurement by the electronic comparators. These measurements are performed in both direction (x and z) and enable to take

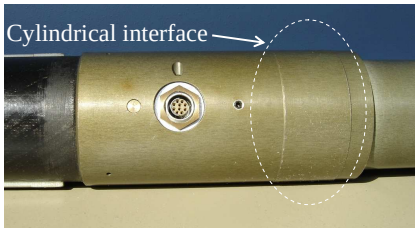

Figure 3.27: Interface

into account any circularity defect of the cylindrical interface. Moreover, the surface of these tips has been treated to become very hard in order avoid scratching the cylindrical interface.

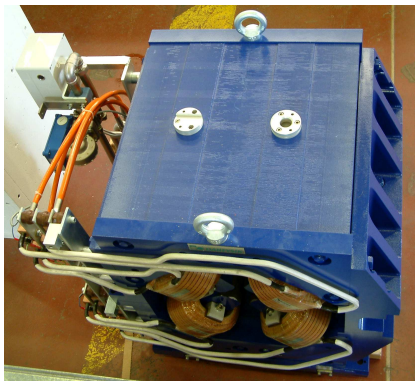

Figure 3.28: Line/Dot/Plane

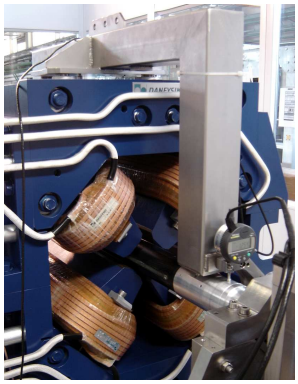

Figure 3.29: The grasshopper

Aluminum tips play a very important role in the alignment quality for the magnetic measurement. As developed in this part the tips enable to center the printed circuit versus the sensor mechanical structure, to center the sensor versus the bench mechanical frame by means of the external shaft of ball bearings, to report the magnetic axis location to the magnet mechanical frame, and to determine precisely (few tens of micro-radians) the angular reference for the measurements.

The figure 3.30 shows the SMB with its "V" and the sensor described previously.

3.3 Commissioning of the SMB

A survey concerning all the error sources of the measurement bench has been carried out in order to quantify the relative and the absolute accuracy of the magnetic measurement. 2m-pole magnet magnetic axis properties, their magnetic field main component and their harmonics are the key points which must be deeply studied. These calculations and experimental tests are mandatory to get reliable measurements or, if errors cannot be corrected, to get a better comprehension of the electron beam behavior during the commissioning.

3.3.1 Measurement Protocol

The objective of this part is to describe the measurement protocol for one quadrupole. As developed in part 2.1, all the magnetic measurement are based on magnetic field harmonic measurements.

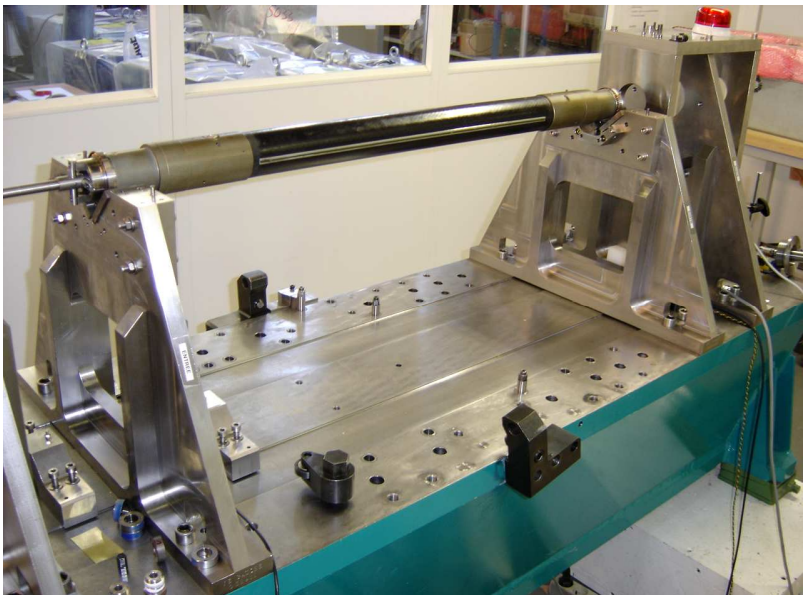

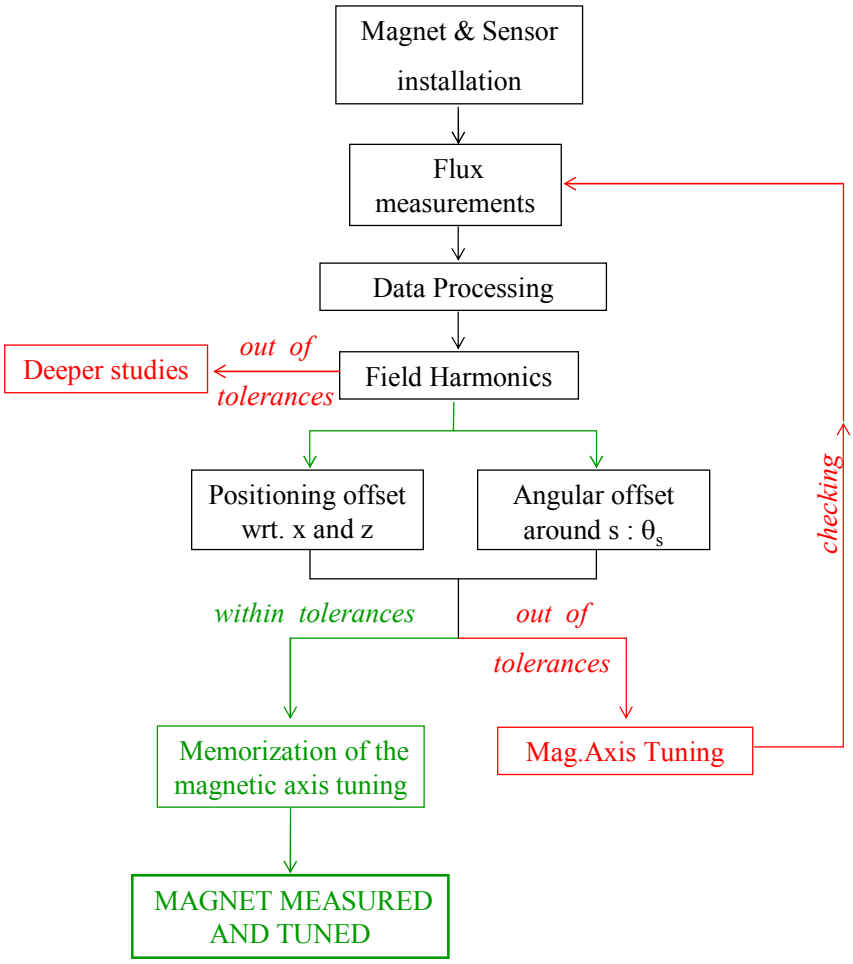

Figure 3.31: Magnetic measurement protocol

Magnet installation

Magnetic measurement of a quadrupole begins by its installation on the bench. It means that the magnet temperature is stabilized at the room temperature. For that, it must installed in the measuring room at least 4 hours before its measurement. Positioning pins fixed on the girder ensure the magnet positioning. These pins are on the picture 3.32 and also in green on the figure 3.33. For each quadrupole installation, its contacts with the pins must be checked. If the magnet is mis-installed particularly along x direction, it can lead to erroneous measurement of the magnetic axis location. Then once it is properly installed on the bench the magnet is connected to fluids (cooling water, power supply). The security system which prevents from classical problems (windings temperature, cooling water flow) is also connected. Then the sensor is positioned by

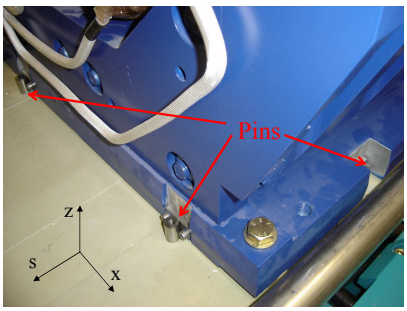

Figure 3.32: Positioning Pins

means of the two "V" in the aperture of the magnet. Once it is mechanically connected to the motor and the rotary encoder, the sensor is ready to rotate.

The next step concerns the horizontal reference characterization. By means of the command and control program, the sensor performs one turn to find and memorize the fixed mechanical reference of the encoder. Afterwards, the bubble level is installed on the line/dot/plane interface of the sensor. Then the horizontal reference is finely searched using the toothed wheel of the motor. Once the bubble is centred in the bubble level, the number of step given by the encoder is noted and must be subtracted to any angular position given by the rotary encoder. It gives the absolute angular position of the horizontal plane versus the encoder fixed reference. It is a very important step in the magnetic tilt angle measurement. That is why a reproducibility campaign has been led to determine the quality of this process. The bench is now ready to perform any magnetic measurement.

All these operations take approximately one hour.

Flux Measurements and Data Processing

When the program is launched, it makes the integrator-voltmeter (Metrolab) measuring 64 integrated voltage between 64 angular positions. The 64 voltage integrations are accurately launched thanks to the angular position information transmitted by the rotary encoder. To eliminate any electronic offset, two sets of measurements are taken. Then from the flux jumps measured between the 64 angular positions, the flux versus the angle is calculated [19]. A Fourier analysis is performed and it led to magnetic field harmonics according to the relation 2.20. Magnetic field harmonics are now available to be treated, particularly to extract magnetic axis information.

Harmonics and Magnetic Axis Properties

The magnetic axis properties are deduced from harmonic values using formulas 2.22 and 2.24

mentioned in part 2.1.2. If these values are out of tolerances, the thickness of the magnet positioning wedges must be changed to modify the magnetic axis transverse position and tilt angle. These wedges are shown on the figure 3.33. One rectangular wedge is used to tune the magnetic

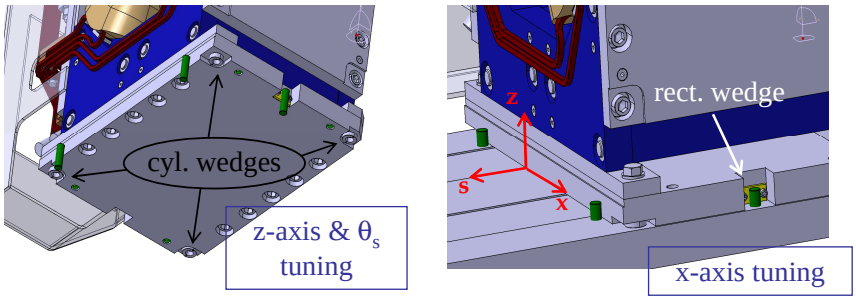

Figure 3.33: Magnetic Axis Tuning

axis in the x direction. Then four cylindrical wedges are necessary to adjust both magnetic axis altitude and tilt angle. Any wedge (one or more) changing takes 15 minutes. Indeed it requires the magnet to be displaced in both direction (x and z) in order to enable any manual operation. Once the wedges are changed, the magnet positioning process must be applied. It is important to note that during this operation, the sensor is never removed. The one millimeter clearance between the sensor and the magnet poles is sufficient despite appearances.

Improvement

However magnetic axis tuning appeared soon to be not so easy to operate. The initial idea was to tune the magnetic axis step by step. That is to say, firstly by removing the x-axis offset from the rectangular wedge thickness, changing the wedge and checking the measurement. Then the same is performed with cylindrical wedges for the z axis offset first and finally for the angular offset. The process seemed to work perfectly after each checking measurement until the last after the angular offset tuning. To tune the magnetic tilt angle, cylindrical wedges are of different thicknesses whether they were located on a different side from the beam axis (x>0 or x<0).

Basic geometry enables to understand what happened and the reasoning is detailed in the appendix C. The figures 3.34 and 3.35 describe the influence of the magnet rotation if the wedges thickness has not been changed. The cause of the error is the arm lever between the theoretical axis (M) and the contact points of the magnet (wedges: points W and C). The main problem is to predict the rectangular wedge thickness despite this arm lever. The cylindrical wedges must also be modified but the effect is very small.

Moreover, the point of contact between the wedge and the pin is different with respect to the sign of the tilt angle. On the figure C.1 and C.2, the point of contact is the red disc for $\theta_s > 0$ and the blue one for the contrary case. The purpose is to calculate the exact thickness needed to the wedges to enable tilt angle correction without changing the magnetic axis position. A numerical example is detailed in the appendix C.4.

3.3.2 Tests

The first parameter to check is the stability of all the peripheral equipments.

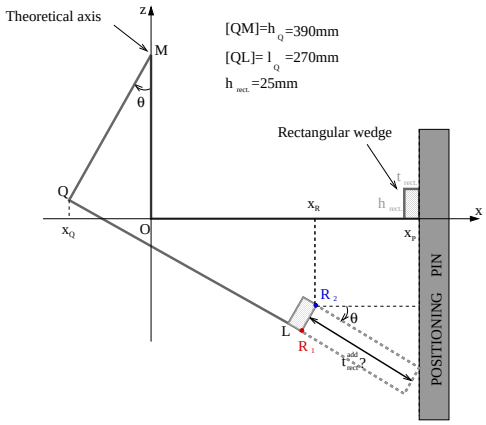

Figure 3.34: Arm Lever: rectangular wedges

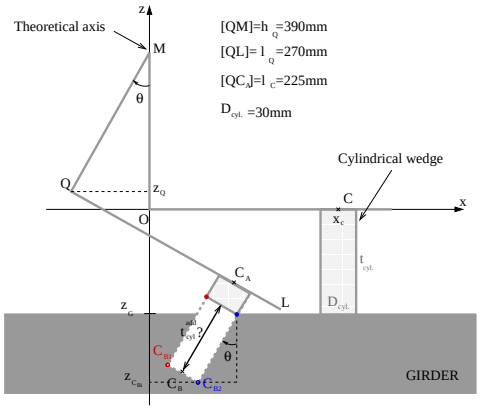

Figure 3.35: Arm Lever: cylindrical wedges

3.3.2.1 Equipments

These equipment tests can be grouped in function of quantity which undergoes the produced error. Consequently magnetic field harmonics, magnetic axis location or orientation are the two main quantities which will be checked.

Magnetic field harmonics
Any variation of the magnet power supply current during the magnetic measurement can introduce spurious magnetic field harmonic component. Consequently the power supply has been isolated from the standard electrical network to avoid that external harmonics disturbs measurements. Moreover any current jitter can lead to bad quality measurements and above all it can be harmful for the electron beam. A curve has been plotted to check the current stability for several hours but in the case of jitter, only 30 minutes is required to achieve the working stability.

Magnetic axis
The 21 ° C air-conditioned has been tested during several days and a temperature variations were small enough to validate the temperature regulation. What is important is that the magnet must have reached a stable temperature which value is the measuring room one. Indeed, if the magnet is installed on the bench with a temperature different from the room one, its equilibrium temperature will change which implies mechanical dilations. If these dilations occur during the magnetic measurements, we are sure to obtain wrong information concerning the magnetic field harmonics. Then the girder stability has been tested by surveying the orientation of the girder with a two axis bubble level (tilt and roll angle). The main objective was to qualify the vibration filtering carpets installed between the floor and the blocks on which the girder is fixed. Even if stability of the girder has been qualified, tilt angle of the girder has been noted after each quadrupole measurement in order to take into account any variations during the alignment of the magnets in the machine.

3.3.2.2 Reproducibility

A complete work has been lead to check the reproducibility of the bench. Each part of the bench have been checked point by point to identify more precisely error sources but also to highlight weak points of the bench which could be improved after additional developments.

Experiment n ° 1
This experiment is dedicated to reproducibility of angular reference determination performed by means of the bubble level and the rotary encoder. Reference of the measurement chain is taken from the physical angular reference of the rotary encoder which remains intrisically fixed in space. As the horizontal plane is the physical quantity which can be measured accurately by the bubble level, it is the absolute angular reference for every θ_s measurements. Consequently, before each 2m-pole magnet measurement, it is mandatory to determine the angular offset between the horizontal plane and the fixed reference of the encoder in order to get a reliable magnetic tilt angle characterization. By noting the offset value for several measurements, a maximum variation of 2 encoder steps is obtained which corresponds to 20 μrad for θ_s determination. The angular transmission and particularly the line/dot/plane interface are adapted to our requirements.

Experiment n ° 2
A quadrupole is installed on the bench, the horizontal reference is taken only once by means of the bubble level and several measurements are performed. This experiment enables to check only the sensor quality after the assembly. The measurements performed are similar for each type of quantities noted. Here are given the largest variations ($\Delta_{p-p}X$) observed during the experiment.

$$\begin{aligned} &\Delta_{p-p}gradient = 1\ \mu T.m \\ &\Delta_{p-p}harm = 0.15.10^{-4} \\ &\Delta_{p-p}x = 1\ \mu m \\ &\Delta_{p-p}z = 0\ \mu m \\ &\Delta_{p-p}\theta_s = 3\ \mu rad \end{aligned} \tag{3.18}$$

Very encouraging harmonic and integrated gradient variations are obtained. It is more interesting to look at magneto-geometrical quantities because they can be interpreted as sensor mechanical instabilities amplitudes. From that point of view, the rotation of the sensor is stable from a measurement to another. Indeed, it is highlighted by the magneto-geometrical quantities low values and particularly by the 3 μrad for $\Delta_{p-p}\theta_s$. Such a value confirms that the sensor mechanical structure does not undergo any dynamic instabilities which could affect its measurement accuracy. These results enable continuing experimental tests.

Experiment n ° 3
To check the quality of the 'V' cylinder interfaces, the protocol applied is similar to the first experiment one but the sensor is taken off and installed again between each measurement. It is the last test before testing the whole measurement protocol which must check the 2m-pole magnet installation. The results obtained are similar to the previous except for the magnetic tilt angle. Indeed, the resolution of the bubble level being 20 μrad and in the best case we can manage to determine the angular position of beginning of the measurements within $\pm 10\ \mu rad$. However concerning the magnetic axis, the result are very encouraging since they are very close to the previous ones. It means that the V/cylinder interface provided by the stand and the ball bearings is an adequate solution to achieve a good installation reproducibility.

Experiment n ° 4
Finally, the last step is to experience the final operation protocol which consists in installing and taking off both quadrupole magnet and sensor several times. A setting up of a strict installation procedure is required to get acceptable reproducibility. The reproducibility of the series measurements process taking into account the previous remarks has been tested. Measurements

were performed for several installations and taking off of quadrupole and sensor. Finally these maximum variations are reached and are within tolerances.

$$\begin{aligned} &\Delta_{p-p} harm = 2.10^{-4} \\ &\Delta_{p-p} x = 15\ \mu m \\ &\Delta_{p-p} z = 10\ \mu m \\ &\Delta_{p-p} \theta_s = 45\ \mu rad \end{aligned} \tag{3.19}$$

3.3.3 Bench defect measurements

From the previous experiments the bench is sensitive enough to perform measurement of any magnetic characteristic of 2m-pole magnet. It provides a very good level of reproducibility which enables to be confident in the magnetic measurements which will be operated. The first task is to confirm that the sensor does not undergo any sag effect. Indeed, from the measurement performed until here, the skew sextupole harmonic component is very small compared to the one measured with the first sensor. Then the final step of the bench defect characterization process is to determine the magnetic offset of the sensor: Δx_{coils}, Δz_{coils}, θ_{coils}.

3.3.3.1 Sag of the sensor

The measurement of the sensor sag is based on the measurement of the vertical position of the reference magnet magnetic axis. If the reference quadrupole can be displaced on a perfect horizontal plane, any vertical variation of the magnetic axis position is due to a sag effect of the sensor. To check that the reference quadrupole is displaced on a plane parallel to the horizontal plane, the alignment group installed devices equipped with a laser which provides an accuracy of few microns ($2\ \mu m$). The experiment is showed on the figure 3.36.

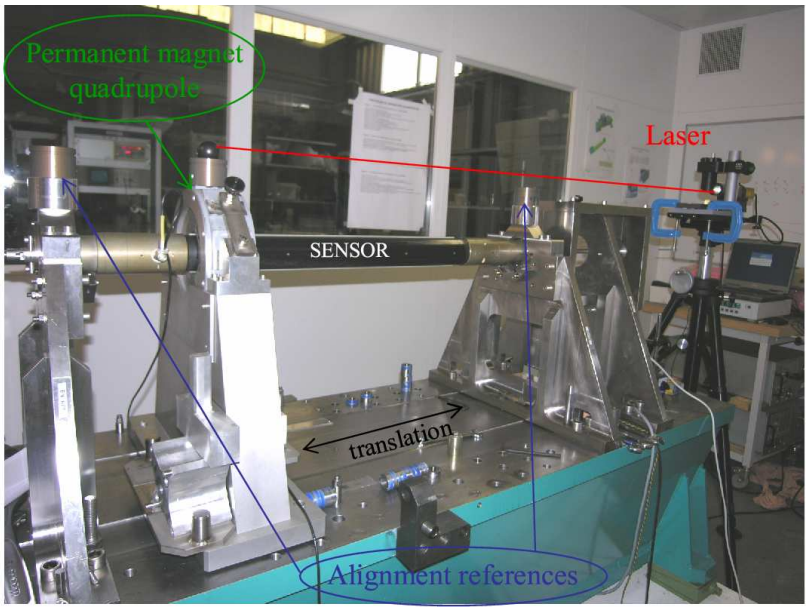

Figure 3.36: Sag determination experiment

These equipments enable to follow any mechanical movements of the reference quadrupole. Indeed, these mechanical errors could lead to erroneous calculations of the sag.

Nine measurement points were taken and the result is plotted on the figure 3.37. The measured points are within the accuracy delivered by the alignment devices. According to the plot 3.37, the sensor does not undergo any measurable sag effect.

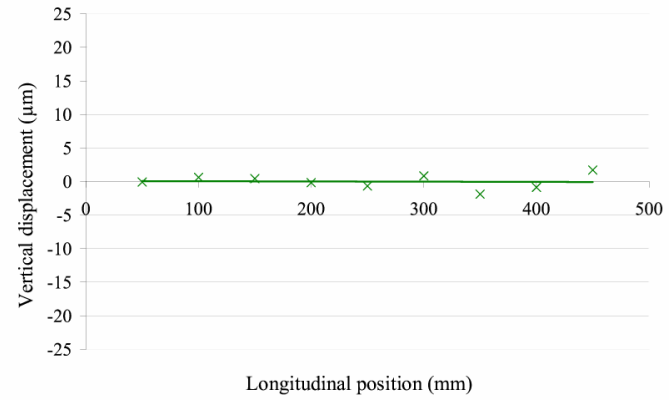

Figure 3.37: Vertical displacements of the sensor

3.3.3.2 Magnetic misalignment

By applying the method developed in 2.3.1, the positioning offset of the printed circuit coil has been measured. Magnetic defects were measured by means of real magnet in order to take into account the real integration length. However, the vertical magnetic offset cannot be determined with real magnet since it is impossible to swing (180 °) them around the horizontal axis.

Vertical Offset

The vertical offset has been measured by means of the octagonal quadrupole with the method of 2.3.1. Since this quadrupole can be rotated by steps of 45 ° , the octagonal way followed by its magnetic axis has been plotted on the figure 2.15.

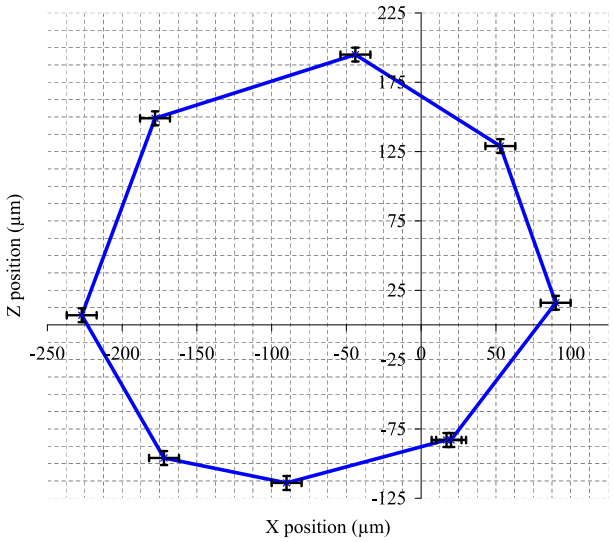

Figure 3.38: Displacements of the reference quadrupole magnetic axis

Even if the octagon on the figure 3.38 has a good general shape, it should be closer to the perfect octagon. As developed in part 2.3.2.2, it is difficult to obtain a good accuracy on its

positioning along the X axis. Contrary to the positioning in the Z-direction which is facilitated by the gravity: the contact between the quadrupole and its stand is better ensured. From these experiments, it appeared that a permanent magnet quadrupole with a cylindrical outer mechanical interface provided with a "V" shaped stand is the best solution. This idea is developed in part 2.3.2.2.

The vertical offset is thus deduced from the previous experiment with the permanent magnet quadrupole.

$$\Delta z_{coils} = +26\,\mu m \tag{3.20}$$

The $+26\,\mu m$ of the vertical offset are constituted of:

- the error in the height of the two "V",
- the error in the ball bearing diameter,
- and all the errors in stacking of each part of the sensor mechanical structure until the median horizontal plane of the printed circuits.

Horizontal and Angular Offset

Two of the three offsets to determine (horizontal and angular) were directly measured with real quadrupole magnets. Swing measurements are performed and magnetic offsets Δx_{coils} and θ_{coils} can be deduced. For these quantities the magnet is swung of 180 ° around the vertical axis.

After standardizing measurements, it occurred that the magnetic measurement device has the following imperfections:

$$\begin{aligned} \Delta x_{coils} &= +56\,\mu m \\ \theta_{coils} &= -8.7\,mrad \end{aligned} \tag{3.21}$$

The horizontal offset is the sum:

- the error in the x axis position of the two "V",
- the mean error of the sensor positioning pins location,
- and the errors of the printed circuits positioning.

Concerning the angular offset, there are many sources of error. Obviously, the erroneous orientation of the printed circuit plane is the first error we think about. But each part between the encoder (its included) and the sensor introduces an error. Moreover, all the parts which intervene in the angular reference determination are also sources of errors.

- the angular error between the plane of the aluminum tip line/dot/plane interface and the printed circuit plane,
- the angular error of the bubble level stand,
- the residual angular offset of the bubble level.

Being aware of all these error sources, the magnetic defects which have been measured can be considered to be very small.

3.4 Magnetic Data Study

The bench is now ready to perform magnetic measurements. Its main defects are measured and are taken into account. The magnetic measurement protocol has been optimized to reduce the time required for the 160 quadrupoles characterization and tuning. Finally after 2 months and a half of hard pace magnetic measurement campaign, statistics can be calculated and studied. Around these series measurements, many special magnetic measurements campaigns were led in order to complete the data obtained.

3.4.1 Special Measurements

Several types of measurements were led on quadrupoles in order to collect a maximum amount of information for the SR commissioning. First, measurements were performed on two prototypes to validate the magnetic design of quadrupoles, especially to optimize the 12-pole harmonic component. Then, some magnetic phenomena such as effect of magnetic forces on poles and hysteresis were characterized. Afterwards, quadrupole and sextupole were both measured at the same time in order to quantify any cross-talk effect. Finally, the magnetic length was measured using a more appropriate bench.

3.4.1.1 Optimization of the 12-pole

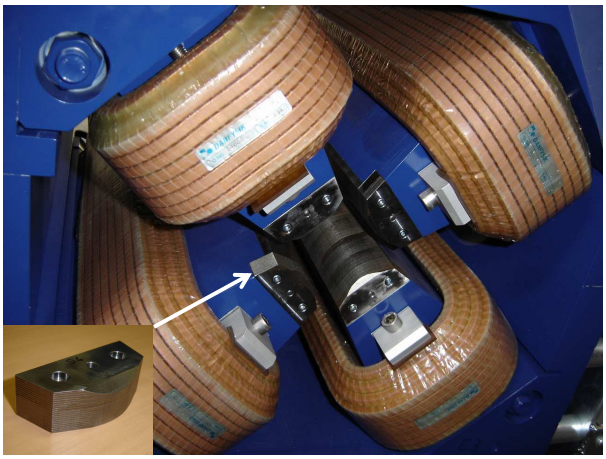

Figure 3.39: Prototype quadrupole and a removable chamfer

Before launching the series manufacturing, two prototype quadrupoles (one of each type) were studied. In order to check the quality provided by the manufacturer. These prototypes were aimed to determine the design of poles in order to minimize the 12-pole harmonic. The 12-pole harmonic is the consequence of the finite length of the magnetic circuit in the longitudinal direction. It is thus necessary to smooth the cut by machining 45° chamfers at ends of poles. To determine the depth of the chamfers to machine, prototypes were provided with games of 8 removable chamfers (4 at the entry + 4 at the exit). Once the chamfers (one for each type, short and long quadrupoles) are experimentally determined by means of magnetic measurements, the series manufacturing is launched.

For both prototypes, 5 games of 8 chamfers were available, the different depth value being anticipated from the numerical simulations.

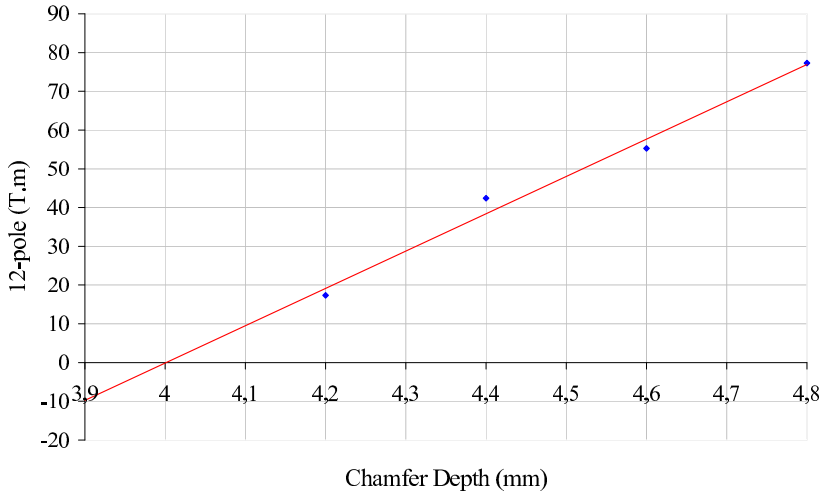

Figure 3.40: Variation of the 12-pole harmonic component versus the chamfer depth at 250A

For the case of the short quadrupoles, figure 3.40 shows the value of the 12-pole versus the depth of the chamfer. By interpolating the measured points with a straight line, the optimized chamfer is 4.0 mm for the short quadrupoles and 3.2 mm for the long ones. Figures 3.41 and 3.42 gives the distribution of the 12-pole harmonics ($\mathcal{B}_6$) among the 160 quadrupoles after the chamfer optimization.

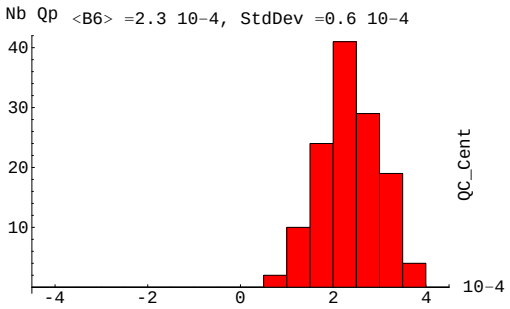

Figure 3.41: $\mathcal{B}_6$ for short quadrupoles

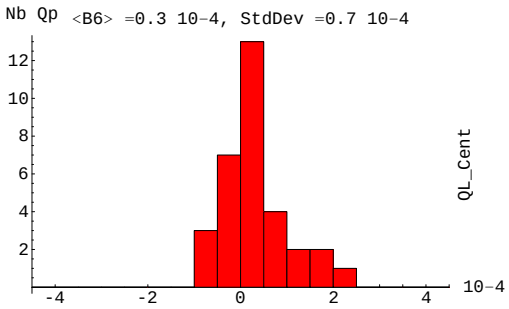

Figure 3.42: $\mathcal{B}_6$ for long quadrupoles

The mean value of $\mathcal{B}_6$ is not close to zero in the case of short quadrupoles. Indeed, both chamfers were determined at maximum current (250A) and this current closer of the long quadrupole nominal current than of the short one. However despite this experimental error, the 12-pole component remains small and within tolerances.

3.4.1.2 Magnetic Forces

The magnetic structure undergoes magnetic forces which could imply some mechanical displacements, especially at high current. That is why it has been tested by means of the grasshopper described in part 3.2.2.2. Under magnetic forces, the top structure would get closer to the bottom one. The sensor is installed in the aperture and the grasshopper on the quadrupole. The mechanical reference is performed by the sensor on which mechanical comparators of the grasshopper are in contact. For each value of the current, the displacement detected by the comparators is noted.

These effects were predicted by numerical calculations. Indeed, it was expected to get a

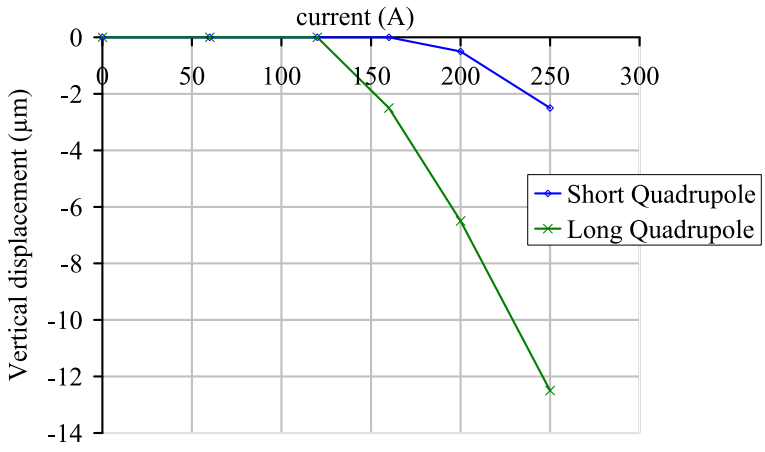

Figure 3.43: Magnetic forces effect versus the current

displacement of 10 μm at 250 A for the long quadrupole. This value can be compared to the 12.5 μm measured. Moreover the experiment confirmed that these displacements were reversible.

3.4.1.3 Hysteresis

Hysteresis effect is an intrinsic characteristic of iron which is used for magnet magnetic circuits. Whenever the magnetic field is varied in the magnetic circuit of a magnet, hysteresis effect appears and must be mastered. Hysteresis effect is the memory of the magnet, it keeps traces of its previous states.

Current cycling

During the commissioning, the current of magnets is often varied. Consequently the final current obtained cannot lead to the real value of the magnetic field since it depends on the hysteresis ways covered in the B(I) plane. The difference between the first field and the end field at the same current can be minimized. That is why the work area of the magnet is prepared by performing current cycling at the beginning of each experiment. We make the assumption that mechanical constraints are uniforms which enables us to affirm that hysteresis phenomenon has the same behaviour in all the magnetic material. To show the need of current cycling, two cycling curves are compared: the "poor" cycling and the "rich" cycling which are depicted on the figures 3.44 and 3.45.

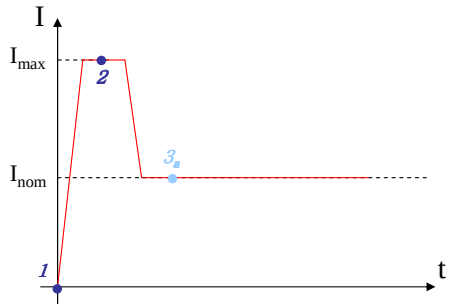

Figure 3.44: "Poor" Current Cycling Schem

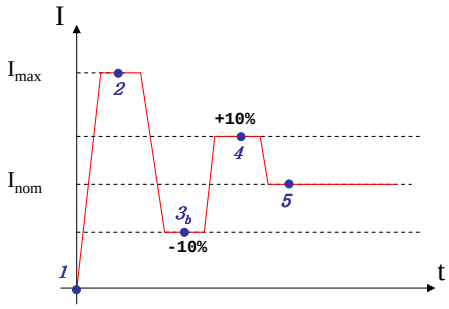

Figure 3.45: "Rich" Current Cycling Scheme

The steps marked by blue circle are reported on the hysteresis curve on the figure 3.46. The

final working point is the point 3_a for the poor cycling and 5 for the rich cycling. The evolution of the working point versus the cycle is reported on the figure 3.46.

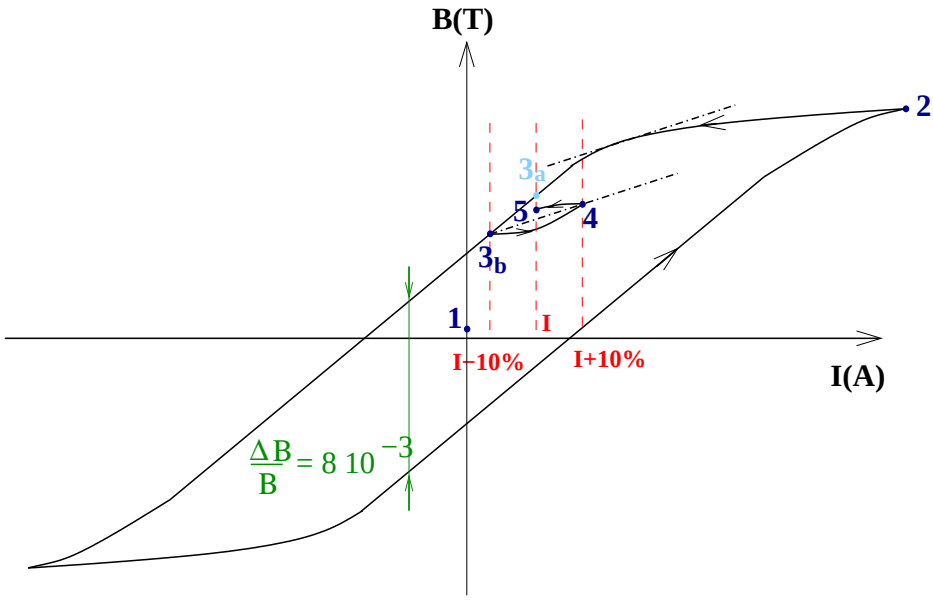

Figure 3.46: Hysteresis Curve

The purpose is to choose the cycling scheme which is the most reproducible. That is to say the one which minimizes the difference between the field measured at the same working current after several current variations.

The reference current is I_0 and the protocol of the experiment is the following:

1- Cycling at $I_{nom} = I_0$,

2- Magnetic measurement of the main component ($\mathcal{B}_2$),

3- Current variation: $I = I_0 + 1\%$, magnetic measurement,

4- Current variation: $I = I_0$, magnetic measurement,

5- Current variation: $I = I_0 - 1\%$, magnetic measurement,

6- $I = I_0$, mag.meas., $I = I_0 + 2\%$, ..., and so on until $I = I_0 + 3\%$.

The result of this experiment is plotted on the figure 3.47.

With the poor cycling, the final magnetic field obtained (WP_A = Working Point A) is 1.5% lower than the initial magnetic field (WP_0). The rich cycling is far much more reproducible since final (WP_B) and initial fields (WP_0) are similar.Before any magnetic measurements and for machine operations, the magnets of the SR are cycled with the rich cycling scheme.

Magnetic drift

Despite the application of the rich cycling scheme, there is a difference between the magnetic field obtained just after the cycling WP_0 and the one at the same current but after some current variations WP_B. This part is aimed at quantifying the difference between WP_B and WP_0. These curves are plotted on the figure 3.48.

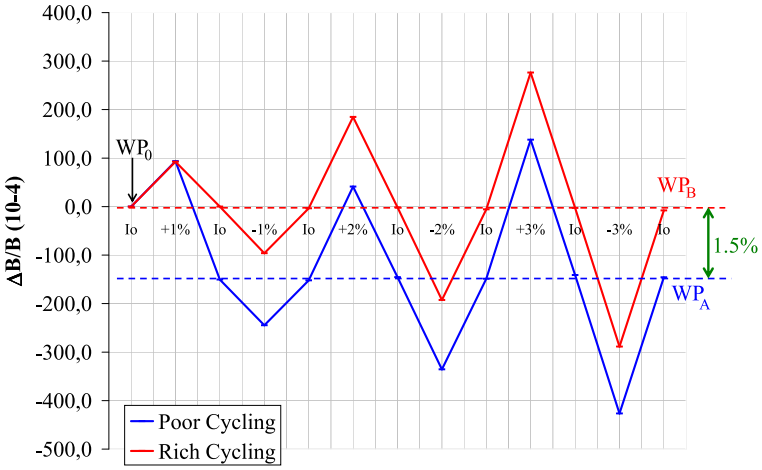

Figure 3.47: Comparison: Poor and Rich cycling schemes

The experiment is based on the measurement of the $\mathcal{B}_2$ component at several working point attained in three different manners. The measuring currents are spaced of 0.5 A between 160 A and 165 A and three curves are noted.

- Curve 1 (red): A rich cycling is performed for all the current,
- Curve 2 (blue): A rich cycling is performed only at $I_0 = 160A$ and the current is varied until 165 A,
- Curve 3 (green): A rich cycling is performed only at $I_0 = 165A$ and the current is varied until 160 A.

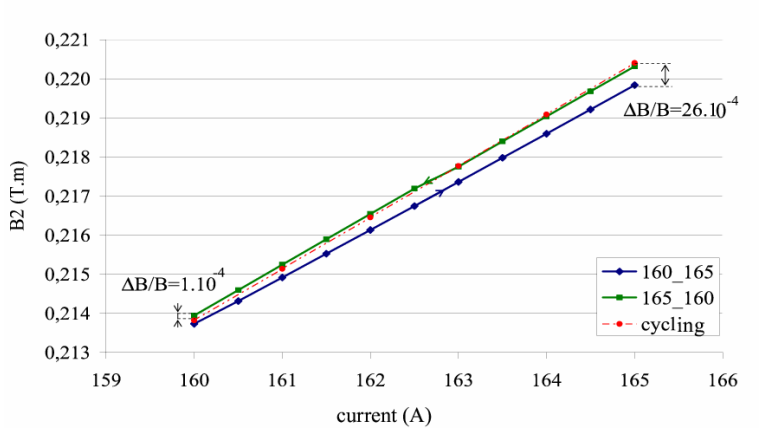

Figure 3.48: Magnetic field drift versus current variations

These experiments show that the working points are more reproducible when they are reached with a decreasing current. Such a result was predictable but what is important is the error performed between the decreasing current protocol and the increasing one. When the current is decreasing, the error in the magnetic field is only 1.10^{-4} whereas it is 25.10^{-4} in the other configuration. However from the machine physics point of view if the worst case occurs for one quadrupole ($I = I_0 - 5A$), it represents a tune shift (see part 1.2.3.1) of few 10^{-2} which is significant. Nevertheless, a cycling process has then to be performed.

3.4.1.4 Cross-Talk

In the SR, it often occurs that a quadrupole and a sextupole are particularly close (120 mm). It is important to determine if this proximity influences or not the magnetic field of both magnets. That is why experiments were led to quantify this effect. The figure 3.49 shows both quadrupole and sextupole installed on the SMB equipped with its initial sensor,which is the longest harmonic coil sensor available at SOLEIL.

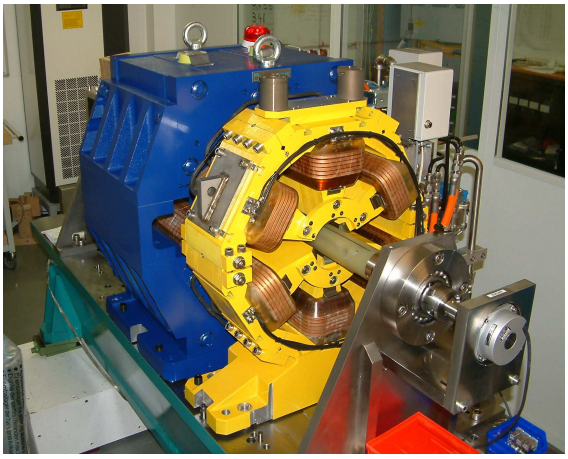

Figure 3.49: Quadrupole and sextupole on the SMB

The principle is to measure first the quadrupole alone on the bench at several currents and then the sextupole alone. These measurements establish references which are compared to the next measurements. Afterwards, both magnets are installed on the bench and measurements are performed for all the current combinations.

The harmonics obtained for both magnet alone are added. The result is compared to the harmonics obtained when both magnet are mounted on the bench. By calculating the difference, the results is of order of magnitude of the bench accuracy. This enables to conclude that there is no cross-talk effect between quadrupole and sextupole when they are close to each other.

3.4.1.5 Magnetic length

The last measurement campaign concerned the quadrupole magnetic length measurement. It has been measured on another bench dedicated to multipole cartographies.

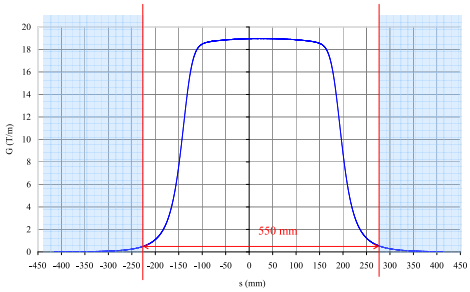

Figure 3.50: Short Quadrupole

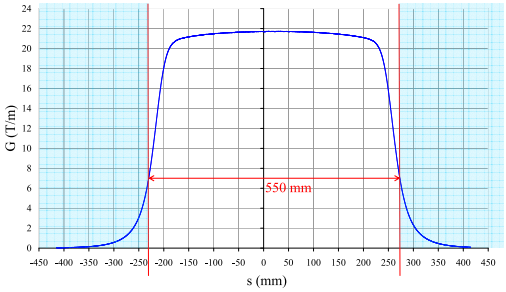

Figure 3.51: Long Quadrupole

The figures 3.50 and 3.51 show the longitudinal on axis gradient variation for both short and long quadrupoles prototypes. In both cases, the length of the SMB sensor is shorter than the

	Calculations	Measurements	Mechanical
Long	481 mm	490mm	460mm
Short	350 mm	350mm	320mm

Table 3.1: Magnetic length values from different sources for long and short quadrupoles

magnetic length of both types of quadrupole but are close to the predicted ones. The different values of magnetic length are reported in the table 3.1.

Consequently, the rate of non measured magnetic field represents an error on the main component ($\mathcal{B}_2$) of 0.3% for the short quadrupoles and of 1.6% for the long ones. These rates must be taken into account in the gradient ($\mathcal{B}_2$) versus the current calibration. These measured length are used in the physics model of the machine.

3.4.2 Series Measurements

The series measurement campaign of the 160 quadrupoles required to set up a two shift organization. Once one magnet was measured, it was validated in real-time by a machine physicist. This step was very important because only machine physicists could decide the future of a mean quality magnet.

The first quantity to be measured was the harmonic content of the quadrupole magnets. Then its magnetic axis properties are calculated and tuned if necessary. The purpose of this part is to analyse the series results campaign by calculating statistic data.

3.4.2.1 Magnetic field harmonics

A perfect quadrupole would only provide a quadrupolar magnetic field, if its length is infinite and its poles shapes are infinite hyperbolae. Such a quadrupole is not achievable in real world. It is indeed necessary to cut infinite geometry to enable the magnet assembly. Consequently, cutting the perfect geometry of the magnetic circuit generates magnetic field harmonics. These harmonics are called the natural harmonics of a 2m-pole magnet, and are unavoidable as it is unavoidable to cut the perfect magnet circuit geometry. However these harmonics can be minimized by means of numerical computation before their manufacturing (pole shape optimization).

There could be unexpected harmonics which come from quadrupole magnet defects. These defects cannot be predicted by any numerical code. This is one of the reasons which makes magnetic measurements so much important. It is the only means to determine the real properties of the magnets or the real magnetic field harmonics which the electron beam will undergo.

Natural harmonics

These harmonics are predictable and well known [22]. Even if it is impossible to cancel them, they can be minimized to attain very low values. Each natural harmonic has a specific tolerance which is related to the minimum acceptable disturbance on the electron beam. Table 3.2 shows these specifications followed by these obtained after numerical computations for short and long quadrupoles. Quadrupole magnets were designed by the Magnetism and Insertion Devices Group of SOLEIL and they were manufactured by the Danfysik company [24].

Harmonics	12-pole	20-pole	28-pole
Tolerances	$5.4\ 10^{-4}$	$2.9\ 10^{-4}$	$1.6\ 10^{-4}$

Table 3.2: Harmonics: Tolerances

The numerical optimization was performed with Tosca, an Opera-3D code distributed by Vector Fields [30]. After harmonic optimization, the code returned the harmonic values which could be expected from the numerical magnetic design. As shows table 3.3, numerical calculations performed with Tosca, from Opera 3D code, can ensure quadrupole magnetic field harmonics below or close to those fixed by machine physicists.

Harmonics	12-pole	20-pole	28-pole
Design (short)	0.2 10^{-4}	1.4 10^{-4}	0.7 10^{-4}
Design (long)	0.8 10^{-4}	1.8 10^{-4}	1.7 10^{-4}

Table 3.3: Harmonics: Design Values

Only the data collected during the series measurement enable to check these predictions. The mean value of the measured natural harmonics are reported in the table 3.4.

Harmonics	12-pole	20-pole	28-pole
Design (short)	2.3 10^{-4}	0.7 10^{-4}	0.9 10^{-4}
Design (long)	0.3 10^{-4}	1.9 10^{-4}	1 10^{-4}

Table 3.4: Harmonics: Measured Values

Then figures 3.52 to 3.57 represent the natural harmonic histograms for the 128 short quadrupole magnets and for the 32 long ones (12-pole, 20-pole and 28-pole). Histograms give the number of measured quadrupole which have an harmonic value expressed in of 10^{-4} of the main component (here it is $\mathcal{B}_2$). All histogram provide the mean value of the measured data noted $< \mathcal{B}_i >= x.10^{-4}$ and their standard deviation noted $StdDev = x.10^{-4}$. They provide the means to qualify the quadrupole machining quality in terms of identity between magnets.

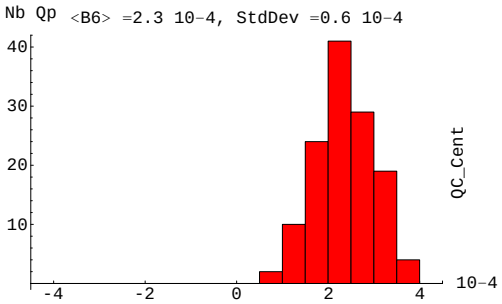

Figure 3.52: 12-pole: Short Quadrupole

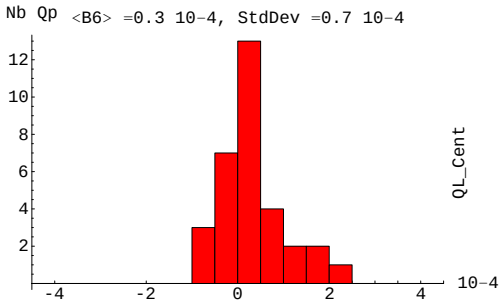

Figure 3.53: 12-pole: Long Quadrupole

From figures 3.52 to 3.57, natural harmonics have a small dispersion. Indeed the standard deviation is close to zero for the 20-pole ($\mathcal{B}_{10}$) and the 28-pole ($\mathcal{B}_{14}$) (both short and long). Concerning the 12-pole, the result obtained are also very small even if they seem to be worse. The 12 pole-component is particular since it is the only one which has been experimentally optimized. The process is depicted in part 3.4.1. Between short and long quadrupole magnet, the 12-pole has a different central value. This difference is also explained in 3.4.1.

The measured natural harmonic values show a small difference between the numerical simulations and the manufacturing. Simulation gives now the mean to design magnets accurately. However it occurred that spurious harmonic components have been measured: it is the purpose of the next part.

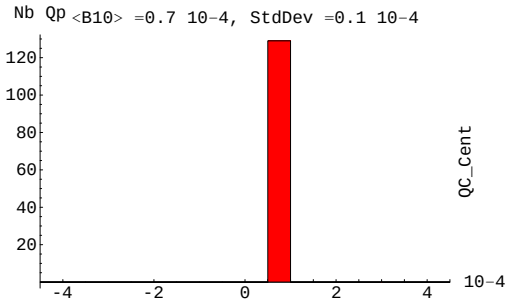

Figure 3.54: 20-pole: Short Quadrupole

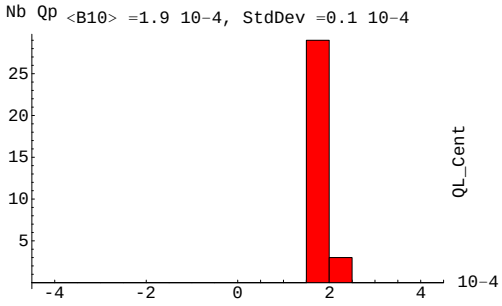

Figure 3.55: 20-pole: Long Quadrupole

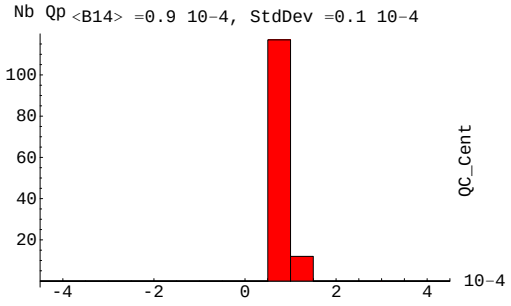

Figure 3.56: 28-pole: Short Quadrupole

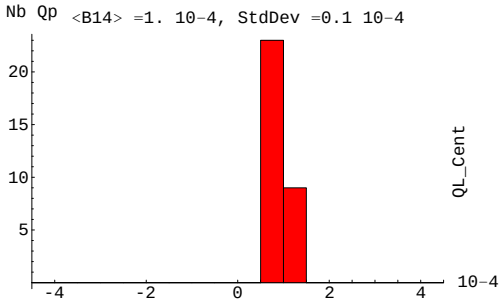

Figure 3.57: 28-pole: Long Quadrupole

Spurious harmonics

Spurious harmonics are the one which are not expected. These harmonics do not exist if the magnet is strictly identical to the design. Any defect in the magnetic circuit geometry occurring during the magnet manufacturing and assembly is a source of spurious harmonics. The sources of these harmonics were studied in the case of a quadrupole magnet by J.Cobb and R.Cole [22]. During series measurements, it occurred that all the measured magnet have a normal 8-pole component ($\mathcal{B}_4$) as showed by the histograms 3.58 and 3.59

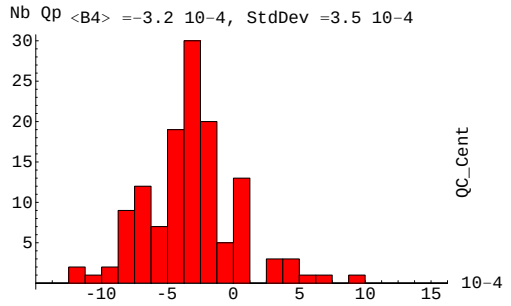

Figure 3.58: 8-pole: Short Quadrupole

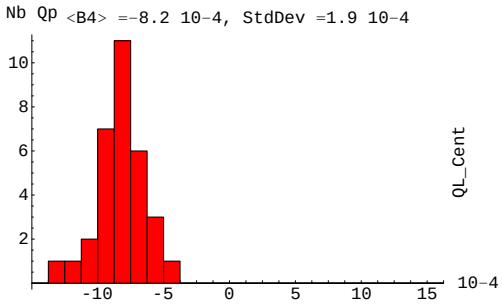

Figure 3.59: 8-pole: Long Quadrupole

The effect observed is stronger for long quadrupole magnets than the short one. From [22], appearance of a 8-pole component has two main sources. These sources depend on the distance between each consecutive poles at the point of truncation (a, b, c, d) and on the distance between opposite poles (A and B). These parameters are drawn on the figure 3.60. Obviously for a perfect real quadrupole, a=b=c=d and A=B.

The $\mathcal{B}_4$ can be explained by:

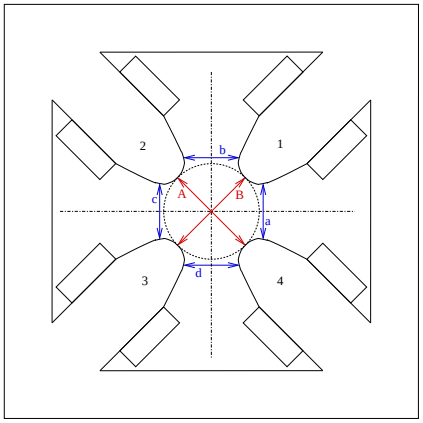

Figure 3.60: Quadrupole Parameters

- A $\neq$ B with a = b = c = d,
- A = B, a = c, b = d but a $\neq$ b.

The SOLEIL quadrupoles are constituted of four independent parts (one for each pole) in order to enable the coil mounting. The assembly of these four parts can generate erroneous distance between poles. Moreover, the effect observed depends on the quadrupole length but not on the magnetic field strength. It means that the $\mathcal{B}_4$ does not have a magnetic cause (fringe field, sensor defect).

It is more probable to have an asymmetry. To find the direction of this asymmetry (a < b or a>b), the theoretical experiment method developed in part 2.2 is used. The purpose is to use the inverse concept: the sensor geometry is perfect and it measures a theoretical quadrupole with some introduced defects.

First the harmonics of a symmetric quadrupole are simulated and memorized. Then an asymmetry (a<b) is introduced and the harmonics obtained are subtracted to the initial one. The same is performed with the other asymmetry (a>b).

Figures 3.61 and 3.62 show the difference between the harmonic of the initial quadrupole (symmetric) and the asymmetric one.

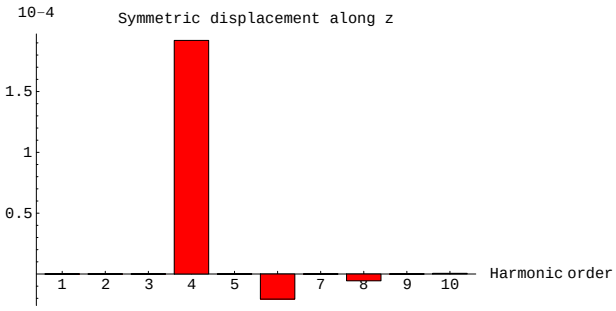

Figure 3.61: a < b



Figure 3.62: a > b

From these figures, it can be concluded that the measured $\mathcal{B}_4$ is due to an asymmetry for which a>b because its mean value obtained for both long and short quadrupoles is negative. Even if it enables to get qualitative information about the error source, this model cannot give any values. Indeed it is not possible to represent the effect of the real quadrupole with only

4 magnetic moments. With a > b, it is not possible to know which of both value is the most erroneous but at least the final magnetic configuration is known.

This 8-pole component has a strong effect on the electron beam dynamics and without the magnetic measurements it would have been impossible to detect this spurious harmonic before the commissioning of the storage ring.

It confirms that despite the quality of the numerical design it is difficult to obtain a final product identical to the design.

Magnetic Flowers

In order to get a global view of the harmonic distribution in the transverse plane (x, z), magnetic flowers were drawn for each magnet. The purpose is to give the gradient homogeneity in the transverse plane versus the gradient at the centre. The value of $\Delta G/G$ is calibrated with colours which has the advantage to give a direct global view of the gradient homogeneity quality.

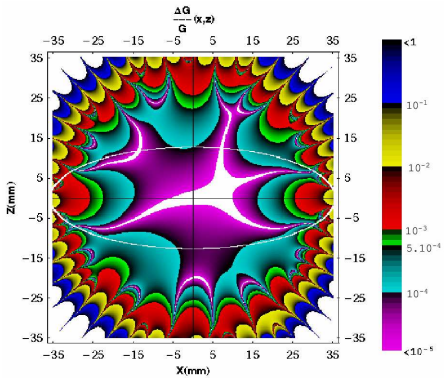

Figure 3.63: Flower for a short quadrupole

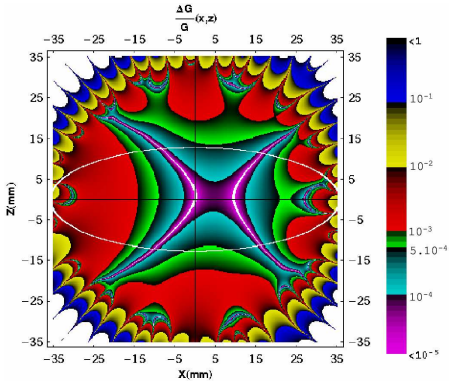

Figure 3.64: Flower for a long quadrupole

The figure 3.63 shows an example of magnetic flower calculated from harmonic measured on a short quadrupole. The homogeneity is plotted in the transverse plane from -35 mm to 35 mm in both x and z directions. The ellipse shows the physical limit imposed by the elliptic vacuum chamber where the electrons are stored.

In order to facilitate the analysis, some theoretical flower are on the figures 3.65 to 3.68. The purpose is to introduce a known quantity of one harmonic and to plot the related magnetic flower.

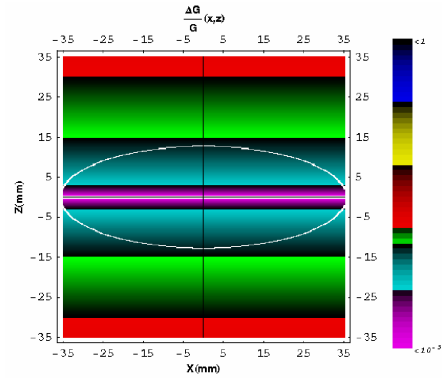

Figure 3.65: Quadrupole + 5.10^{-4} of $\mathcal{A}_3$

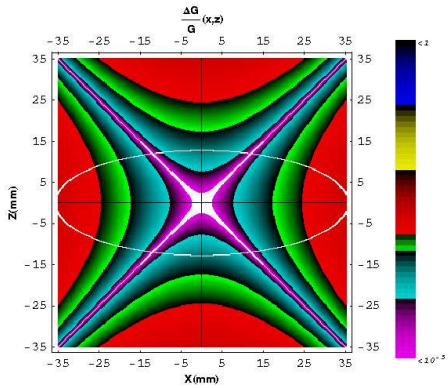

Figure 3.66: Quadrupole + 5.10^{-4} of $\mathcal{B}_4$

The shapes cans be deduced mathematically from the expression of magnetic field harmonics

from equation 2.16. The simplest case is the skew sextupole case ($\mathcal{A}_3$).

$$\Im m\left[\mathbb{B}_3\right] = \Im m\left[\left(\mathcal{B}_3 + i\mathcal{A}_3\right)\left(\frac{x+iz}{r_0}\right)^2\right] = \mathcal{A}_3\left(x^2 - z^2\right), \qquad \text{with } \mathcal{B}_3 = 0 \tag{3.22}$$

If the gradient along the x direction G_x is calculated from the skew sextupole magnetic field, we obtain the following result:

$$G_x(x,z) = \frac{\partial \Im m\left[\mathbb{B}_3\right]}{\partial z} = -2\mathcal{A}_3\, z \tag{3.23}$$

To plot the magnetic flower, the homogeneity versus the gradient at the centre is calculated and leads to the 2D function.

$$f_3^S(x,z) = \frac{G_x(x,z) - G_x(0,0)}{G_x(0,0)} \propto \mathcal{A}_3\, z \tag{3.24}$$

As shows the figure 3.65, the homogeneity depends linearly on the z variable at fixed x and is constant at a fixed z.

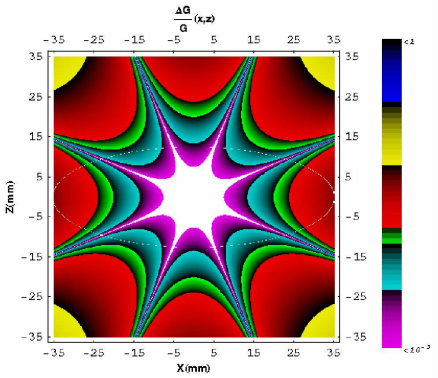

Figure 3.67: Quadrupole + 5.10^{-4} of $\mathcal{B}_6$

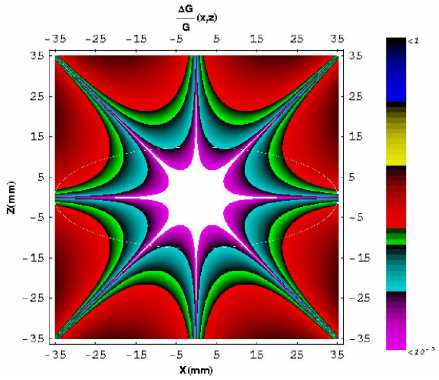

Figure 3.68: Quadrupole + 5.10^{-4} of $\mathcal{A}_6$

From these perfect flowers, some rules can be expressed to facilitate the analysis of any magnetic flower.

- A branch which is merged with the x axis, means that the component observed is skew,
- for a given harmonic order m, the number of branch pairs of the flower is $m-2$

Then the flowers corresponding to the short quadrupole measurements are drawn for all the measuring currents : 60 A, 120 A, 160 A, 200 A, 250 A and nominal current (here it is 180 A). Figure 3.69 shows the variation of harmonics with current. That is why the flower of the measured quadrupole seems to move continuously versus the current.

At 250 A the magnetic circuit saturation appears and puts the flower out of shape compared to its shape for the three previous currents. The magnetic flower gives generally, like any harmonic analysis, the most important component of the quadrupole apart from the $\mathcal{B}_2$. However, in the case of the flowers shown by figures 3.63 and 3.69, there are no known shapes which are distinguishable. That means that the homogeneity of the measured quadrupole is really good. For example, in the case of long quadrupole (figure 3.64), it is reported in part 3.4.2.1 that they have an important 8-pole component. The flowers plotted for all the short quadrupoles at their nominal current are reported in the appendix D.

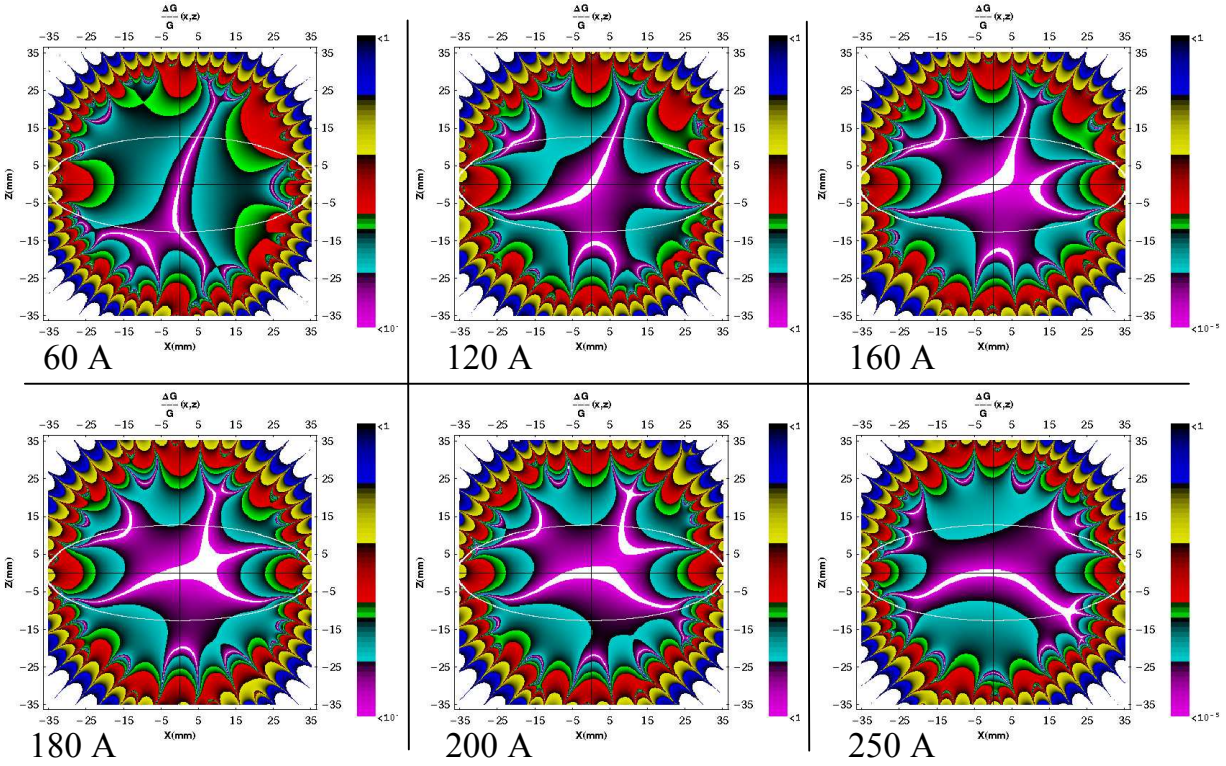

Figure 3.69: Evolution versus the current

3.4.2.2 Centering

Magnetic axis measurements and tuning are the central work of the series measurement. All the quadrupoles were mechanically tuned in order to cancel the magnetic axis offsets. The tuning process is explained in part 3.3.1. Wedges were used to displace and rotate the magnetic axis.



Figure 3.70: Game of rectangular wedges



Figure 3.71: Game of cylindrical wedges

The wedges are distributed in a range of $\pm 0.2\,mm$ with steps of $25\,\mu m$ and $10\,\mu m$.

These games of wedges, showed on the figures 3.70 and 3.71, enable to get a tuning resolution of:

- $5\,\mu m$ for the magnetic axis position,
- $10\,\mu rad$ for the magnetic tilt angle.

After two months and a half of measurements and tuning, statistics about all the quadrupole magnetic axis are available.

Transverse Magnetic Position

The figure 3.72 enables to compare the magnetic axis distribution before and after any tuning. The statistics results obtained for the quadrupoles at their initial state are very small. It highlights the manufacturer mastering of quadrupole machining and assembly. From these statistics, it seems more difficult to master the x-axis positioning of the magnetic axis since the spread is larger than in the z direction.

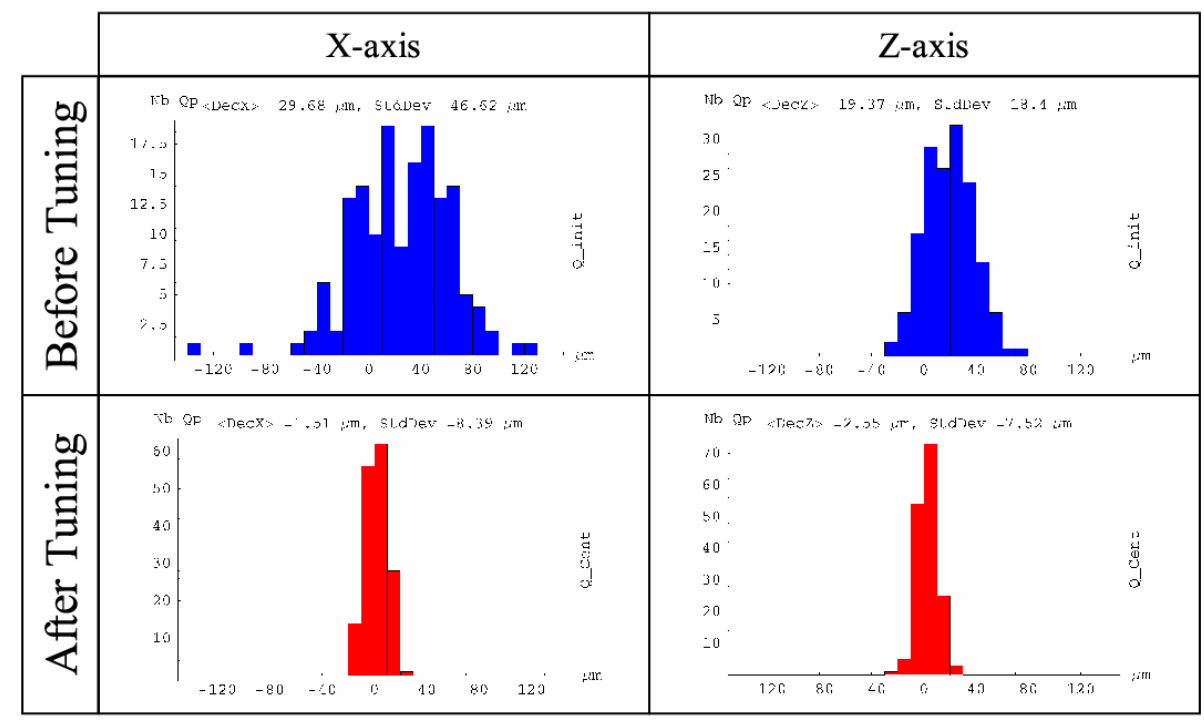

Figure 3.72: Transverse offsets tuning

After the wedges tuning, the spread has been reduced by a factor of

- 5 in the x direction,
- 2 in the z direction.

The mean value of the magnetic axis has been brought back close to zero. The magnetic axis of the 160 quadrupoles are distributed on a longitudinal axis with a standard deviation smaller than 10 μm. The location of this axis in the machine is determined by the errors accumulated from the magnetic measurements to the alignment in the machine.

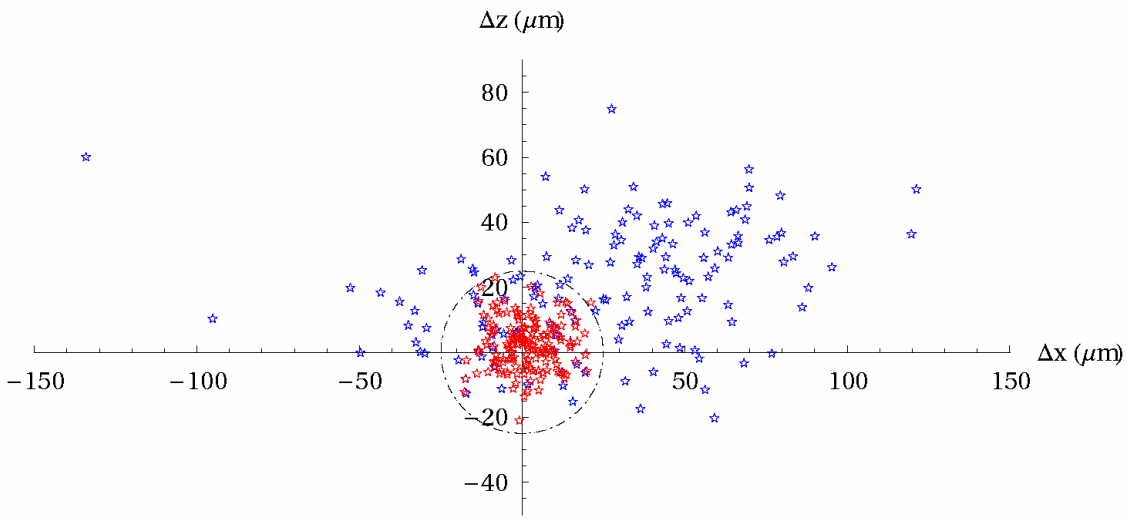

Figure 3.73: Transverse offsets tuning of the 160 quadrupoles

These results are very encouraging for the beginning of the commissioning since it is a performance to obtain a 10 μm dispersion on the magnetic axis location. The identity between the magnetic axis measurement is ensured

Magnetic Tilt Angle

The magnetic tilt angle angle has also been corrected by means of similar method as previously.

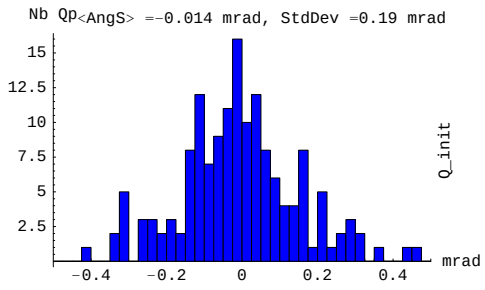

Figure 3.74: Tilt angle: before tuning

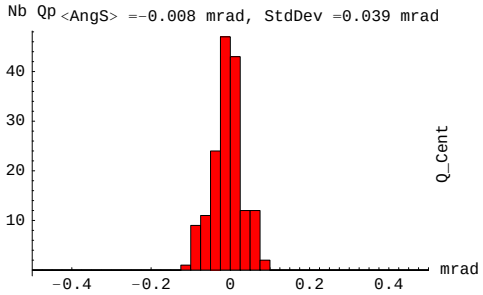

Figure 3.75: Tilt angle: after tuning

It was a real challenge to tune this angle within few tens of μrad. The residual angular offset distribution obtained is 5 times smaller than the initial values. These results would not have been achieved without all the work performed on the measuring system. According too these value, we could expect that the electron beam will undergo a few amount of coupling due to erroneous magnetic tilt angles.

3.4.3 First SR electron beam results

To highlight the quality of the work performed on magnetic axis tuning, we propose to show some results from commissioning for the first turn of the electron beam. The figure 3.76 shows in blue the signal seen by the Fast Current Transformer (FCT). The FCT is located near the end of one turn (2 cells before) and deliver a signal each time its aperture is crossed by the beam. The blue curve shows 3 peaks (the third is smaller) which corresponds to three turns of the electron beam.

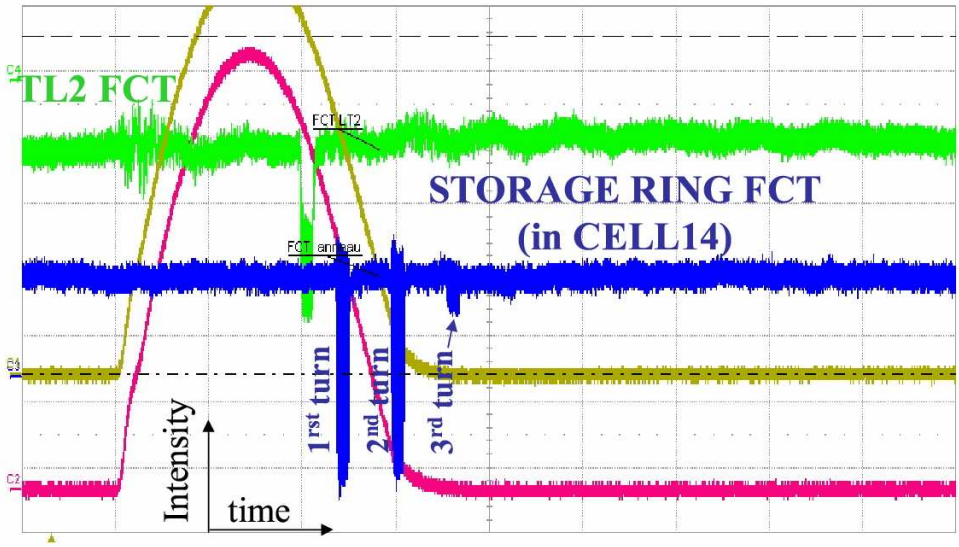

Figure 3.76: The first three turns in the Storage Ring

Once it was possible to store the electron beam in the storage ring, the natural orbit was corrected and the result is shown on the figure 3.77. The orbit is the electron location measured by the Beam Position Monitors.

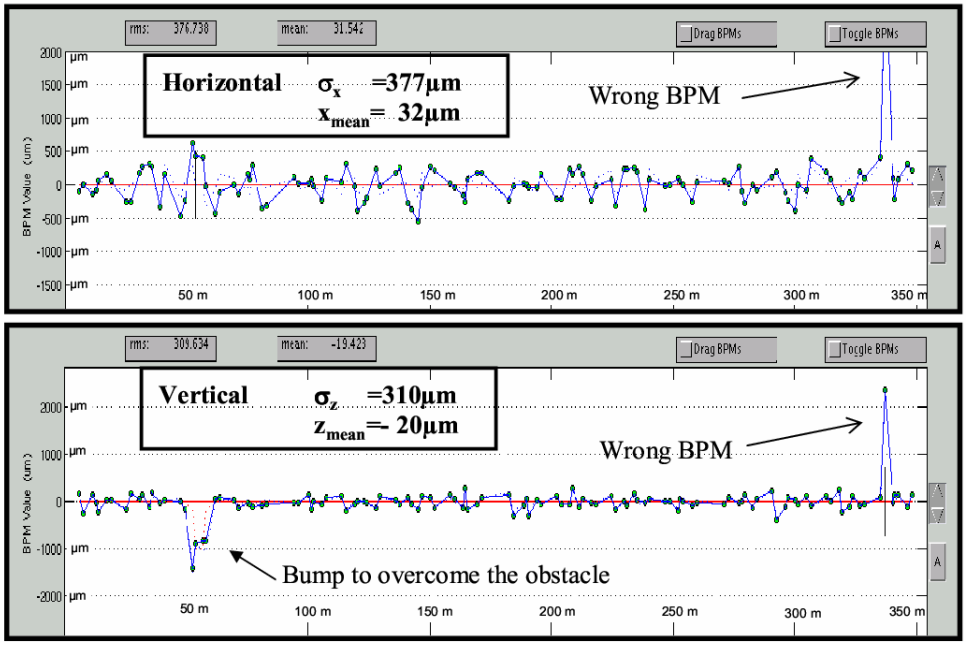

Figure 3.77: Best orbit after correction

From the standard deviation obtained for the orbit in both planes, we can say that the quadrupole are well aligned thanks to the work of the SOLEIL alignment team and to the accurate magnetic axis tuning we provide to each quadrupole.

Résumé du chapitre

Après un état de l'art des technologies mises en oeuvre dans les bancs de mesures à bobines tournantes utilisés dans les différents laboratoires, nous avons présenté dans ce chapitre la configuration initiale du banc de mesures magnétiques de SOLEIL disponible au début de nos travaux de recherche. Le premier objectif de notre travail a consisté à caractériser ce banc de mesures. Des défauts rédhibitoires ont été détectés tels que des problèmes de flêche du capteur et de reproductibilité des mesures liés à la conception mécanique du banc de mesure. Dans ce contexte, nous avons développé un nouveau banc de mesures dont les principales spécifications étaient de réduire la flêche du capteur, de rigidifier sa structure et d'assurer une bonne stabilité mécanique lors de son positionnement. Un protocole de mesure a été développé visant à éprouver le nouveau banc de mesures.

Suite à sa validation, des mesures dites "spéciales" ont été réalisées sur des quadrupôles prototypes. L'objectif de ces mesures étaient de déterminer certains paramètres sur les aimants prototypes de façon à les appliquer ensuite à l'ensemble des quadrupôles de l'anneau de stockage de SOLEIL. C'est par exemple le cas du dimensionnement des chamfreins du circuit magnétique ou encore du choix du cyclage à appliquer aux quadrupôles pour atteindre leur point de fonctionnement nominal. Ces mesures ont également permis de quantifier l'influence de certains phénomènes sur la qualité de champ comme par exemple le couplage entre les sextupôles et les quadrupôles une fois montés dans l'anneau, qui s'est révélé être négligeable. Enfin la mesure de la longueur magnétique des quadrupôles a pu être réalisée.

Ces mesures spéciales ont été suivies des mesures de série des 160 quadrupôles de l'anneau de stockage. Nous avons montré ici les résultats obtenus pour les mesures des harmoniques qui ont permis de déterminer la position de l'axe magnétique de chaque quadrupôle ainsi que leur angle par rapport au plan médian. Par l'utilisation de cales et de plots, la position des axes magnétiques et l'angle de chaque quadrupôle ont été corrigés de façon à respecter les tolérances fixées, à savoir 25 μm r.m.s. par rapport à l'axe théorique des quadrupôles et 0,1 mrad r.m.s. autour de l'axe longitudinal par rapport au plan horizontal.

Enfin, la méthode dite des expériences théoriques développée dans le chapitre 2 a été appliquée dans le but de comprendre la présence d'un harmonique octupolaire dans le contenu harmonique de certains quadrupôles. Elle a ainsi permis de mettre en évidence un dissymétrie haut/bas du circuit magnétique.

Chapter 4

Beam-Based Alignment

Objectifs du chapitre
Après une mesure et une correction très précise de l'axe magnétique des quadrupôles et leur alignement dans l'anneau, l'orbite du faisceau est égale à 2.3 mm dans le plan horizontal et à 0.4 mm dans le plan vertical. Cependant, pour atteindre les performances fixées en terme de brillance notamment, le faisceau d'électrons doit circuler dans une orbite de quelques microns. Lors des premiers tours d'anneau réalisés par le faisceau, sa position était déterminée par rapport à l'axe électrique des BPM. Pour améliorer l'orbite du faisceau, il est capital de connaître sa position par rapport aux axes magnétiques des quadrupôles qui ne sont pas confondus avec les axes électriques des BPM. Il est donc indispensable de connaître avec précision la position relative de l'axe magnétique de chaque quadrupôle et de l'axe électrique du BPM le plus proche. Pour cela, la méthode dite BBA (Beam Based Alignement), c'est-à-dire d'alignement basé sur le faisceau, est utilisée. Elle se décline en plusieurs variantes. De plus, de façon à optimiser l'orbite du faisceau, il est également nécessaire de connaître la position du faisceau par rapport à l'axe magnétique des sextupôles.
Dans ce chapitre, après avoir exposé les différentes méthodes de BBA existantes pour les quadrupôles et les sextupôles, nous détaillerons celle mise en oeuvre pour les quadrupôles de l'anneau de stockage de SOLEIL. Les résultats expérimentaux obtenus à partir d'un programme MATLAB seront commentés et confrontés à ceux obtenus par une autre méthode. Nous présenterons également l'interface graphique développée pour les opérateurs. Enfin, nous proposerons une méthode de BBA innovante pour sextupôles avec pour objectif sa validation par des résultats expérimentaux.

The beam orbit with no correction is 2.3 mm in the horizontal plane and 0.4 mm in the vertical plane. These results were obtained after very accurate tuning of quadrupole magnetic axis and a meticulous alignment. However to attain the targeted performances, the electron beam must circulate within few microns orbit. Until here, the reference orbit is given by the Beam Position Monitor (BPM) electric axis, whereas the reference orbit must be given at first by the quadrupole magnetic axis which can be different from the BPM ones. That is why the offsets between both axis must be measured accurately and taken into account. Several Beam-Based Alignment (BBA) methods exist to perform these measurements on the quadrupoles. They use the electron beam and beam physics phenomena to get accurate measurements. Moreover, it could also be interesting to take the sextupole magnetic axis as reference. In that context, an innovative method for sextupole BBA is proposed.

Concerning the organisation of this chapter, a general study on existing BBA methods for quadrupole and sextupole is described. Then studies for SOLEIL SR quadrupole BBA are lead. Experimental results obtained from the automate algorithm are commented. These results were obtained by means of MATLAB program which has been implemented in a graphical user interface. This interface is very important since it enables non experimented user to perform SR quadrupole BBA. Even if one main method was applied, some results obtained were cross-checked with an other method. Then the last work is about sextupole BBA for which a new method validated with experimental results is described.

4.1 Introduction to tools and methods for BBA

Beam-Based Alignment of any multipole magnet of a machine is the last measurement of its magnetic axis position. This step is extremely necessary since it is the only one which enables to measure the real position of the magnetic axis seen by the beam. One could wonder if all the work performed during magnetic-based alignment is really useful. It is. Indeed, Beam-Based Alignment requires that the machine could store the beam. And it cannot be achieved without a good alignment of the machine element and especially of the quadrupoles. As developed in the part 3.4.3, the natural beam orbit reached small values which highlights the quality of the quadrupole magnetic axis tuning and alignment. As mentioned previously, BBA is the means to reduce the defects which led to an erroneous reading of the BPM measurements. The purpose of the BBA of a multipole is to determine the offset ($\Delta_{Mag_{BPM}}$) between its magnetic axis and the closest BPM electric axis as shown by the figure 4.1.

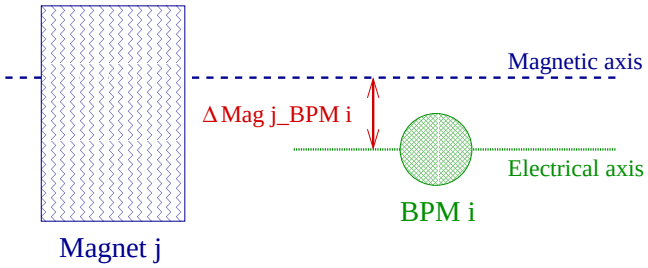

Figure 4.1: Alignment Offset

The objective of this part is to study the existing BBA methods for both quadrupole and sextupole. Then the environment where some of these methods were implemented is described. Indeed, even if the general principle of method are universal, they must be adapted to each machine configuration and control and command concept.

4.1.1 Methods for quadrupole magnets

The purpose of this section is first to calculate the effect of a quadrupole magnet misalignment on the beam position and then to study existing BBA methods for quadrupoles. A beam which go through a quadrupole which magnetic axis is displaced by Δy, is deflected as described by the figure 4.2.

To understand this behaviour, it is important to remind the effect of an error in a dipole field $B_z = B_0 + \Delta B_z$ on the beam excursion (x).

$$\Delta x(s) = -\frac{\Delta B_z(s_0)}{B\rho}\frac{\sqrt{\beta_x(s)\beta_x(s_0)}}{2\,sin(\pi\nu_x)}\,cos(|\varphi(s)-\varphi(s_0)|-\pi\nu_x) \tag{4.1}$$

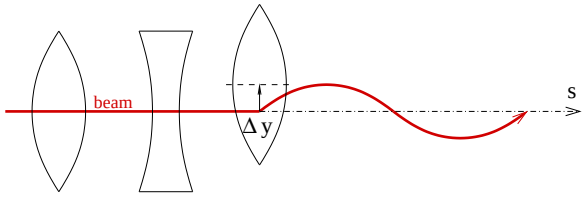

Figure 4.2: Effect of a quadrupole misalignment

For the vertical plane case "$z(s)$",$-\Delta B_z(s_0)$ must be replaced by $\Delta B_x(s_0)$ and x subscripts become z.

Then the dipolar magnetic field created by both an error on a quadrupole gradient (Δg) and its alignment (Δx) is calculated using the series expansion of the magnetic field from equation 2.16.

$$B_z = (g + \Delta g)\,(x + \Delta x) + \mathcal{O}(x^2) \tag{4.2}$$

Developing 4.2 and dividing it by $B\rho$, this leads to

$$\frac{\Delta B_z}{B\rho} = +K \cdot \Delta x + \Delta K \cdot x \qquad where\, K = \frac{g}{B\rho} \tag{4.3}$$

Then the expression of equation 4.3 is introduced in 4.1 for $s = s_0$ in order to eliminate the Δx term.

$$\Delta x(s_0) = (+K \cdot \Delta x + \Delta K \cdot x)\frac{\beta_x(s_0)}{2\,tan(\pi\,\nu_x)} \tag{4.4}$$

$$= \Delta K \cdot x \frac{\frac{\beta_x(s_0)}{2\,tan(\pi\,\nu_x)}}{1 - K\frac{\beta_x(s_0)}{2\,tan(\pi\,\nu_x)}} \tag{4.5}$$

Hence equation 4.3 becomes

$$\frac{\Delta B_z}{B\rho} = +\Delta K \cdot x\,\frac{1}{1 - K\frac{\beta_x(s_0)}{2\,tan(\pi\,\nu_x)}} \tag{4.6}$$

By introducing equation 4.6, the change in the orbit observed at a point s related to a change of a quadrupole strength at s_0 is expressed by the next formula:

$$\Delta x(s) = +\Delta K \cdot x(s_0)\left(\frac{1}{1 - K\,\frac{\beta_x(s_0)}{2\,tan(\pi\,\nu_x)}}\right) * \frac{\sqrt{\beta_x(s)\,\beta_x(s_0)}}{2\,sin(\pi\,\nu_x)}\,cos(|\phi_x(s) - \phi_x(s_0)| - \pi\,\nu_x) \tag{4.7}$$

K is the quadrupole strength, ΔK the change in quadrupole strength, β the beta function, ν the betatron tune and ϕ the betatron phase. In the case of the horizontal plane "$K + \Delta K$" becomes "$-K - \Delta K$". According to the equation (4.7), if the beam goes through the quadrupole magnetic axis ($x(s_0) = 0$), there is no orbit variation ($\Delta x(s) = 0$) for the horizontal plane case.

If the BPM must give the electron beam position versus the quadrupole magnetic axis, there will be misalignment errors. Indeed for several reasons, the BPM electrical axis and the quadrupole magnetic axis cannot be merged as shown on the figure 4.1. Consequently, the beam behaves as expressed by the equation 4.7. Using this relation between the quadrupole strength and the effect of a misalignment, several methods can be determined.

4.1.1.1 Methods using correctors

The principle of these types of method is to displace the beam several times in the studied quadrupole and to deduce the researched offset. Indeed, the closer from the magnetic axis is the beam, the smaller is the orbit distortion read by all the BPMs (see figure 4.3). For BBA, correctors are horizontal and vertical dipole magnets. According to the equation 4.1, the orbit variation depends linearly with the dipole strength.

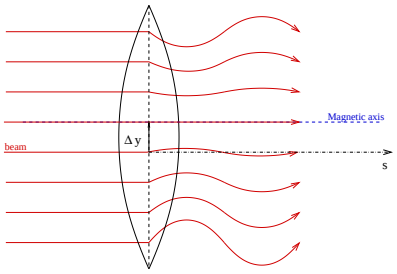

Figure 4.3: Beam orbit displacements

Most Effective Corrector

The corrector which provides the largest orbit variation at the quadrupole "j" is its most effective corrector. The quadrupole most effective corrector is determined by means of correctors response matrices. The purpose of these preliminary choices of corrector is to ensure that the orbit will be sufficiently varied in the studied quadrupole without reaching the non linear limit of the BPMs .

The principle of the method is to apply two symmetrical steps of the quadrupole strength ($\pm\Delta K$) for each position of the beam, i.e. for each corrector current value (I_{cor}). If there is no offset, the orbit distortion seen by the BPM will be the same for both steps of quadrupole. The magnetic axis location is thus determined by calculating the difference of both orbit. The orbit position read by the closest BPM when the orbit difference is zero gives the offset between the BPM and quadrupole.

Obviously, it is a waste of time to search for the corrector current which will make the beam going through the quadrupole magnetic axis. The offset can be deduced since the relations between the orbit location and both corrector and quadrupole variations are well known (equations 4.1 and 4.7). From these equations,

$$\Delta x(s) \propto \Delta B_{cor} \propto I_{cor} \qquad \& \qquad \Delta x(s) \propto \Delta K \propto I_{quad} \tag{4.8}$$

That is why for each step of corrector, the square of the difference of the measured orbits at $\pm\Delta K$ follows a parabolic function of the corrector current (I_{cor})

$$f(I_{cor}) = \left[\sum_{i=1}^{N_{BPM}} (y_i(+\Delta K) - y_i(-\Delta K))^2 \right] \propto (I_{cor})^2 \tag{4.9}$$

It is the merit function to minimize, where N_{BPM} is the number of BPMs and y_i is the position of the beam read by the BPM number i. The minimum of this function gives a corrector current (I_{cor}^{off}) which enables us to deduce the researched offset. Indeed, the orbit read by this BPM depends linearly on the corrector current. a_{BPM} and b_{BPM} are real coefficients of the previous linear equation.

$$y_i(I_{cor}) = a_{BPM}\, I_{cor} + b_{BPM} \tag{4.10}$$

Hence

$$y_i(I_{cor}^{\text{off}}) = \Delta_{Mag-BPM\,i} \tag{4.11}$$

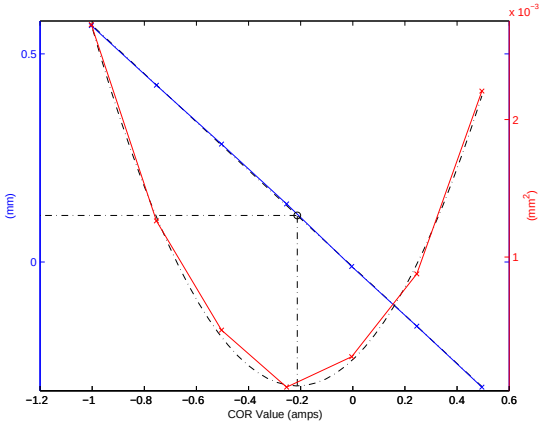

Figure 4.4: Merit function and BPM_i response

The figure 4.4 shows an example of a quadrupole BBA using the method detailed here. the experimental point of the merit function are plotted in red, then the fit used to evaluate numerically the minimum of the parabola is in dashed line, the BPM_i response versus the corrector current is plotted in blue with its fit and the black point shows the offset value. This method is easy to operate and is very reliable. However it does not enable to master the beam as desired. Indeed, when the beam goes through a quadrupole with an angle, it could lead to a small error on the measured offset. The figure 4.5 illustrates with an exaggerated angle this erroneous configuration.

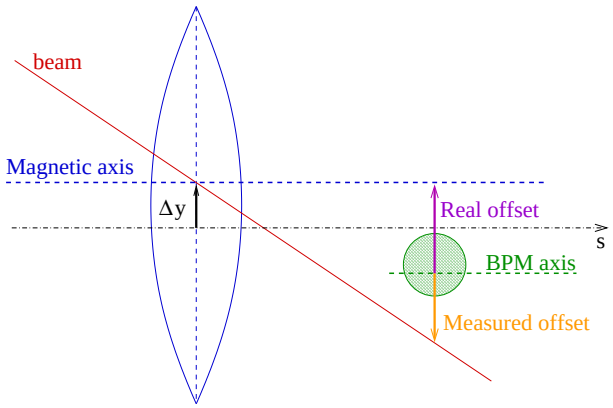

Figure 4.5: Error with an angle on the beam

That is why it is sometimes preferred to work with a beam parallel to the longitudinal axis. This can be achieved with a bump performed with four correctors. An orbit bump is a local displacement of the beam.

Four Corrector Bump

Orbit bumps are used to change locally the beam position or/and angle by means of dipole

magnet correctors. The determination of the current in the correctors is based on transfer matrix calculations. The transfer matrix between two point located at s_1 and s_2 is given by the equation 1.29 and is recalled here.

$$\begin{bmatrix} y \\ y' \end{bmatrix}_{s_2} = M_{s_1/s_2} \cdot \begin{bmatrix} y \\ y' \end{bmatrix}_{s_1} \tag{4.12}$$

with,

$$M_{s_1/s_2} = \begin{pmatrix} \frac{\sqrt{\beta_2}}{\sqrt{\beta_1}}(cos(\Delta\varphi) + \alpha_1 sin(\Delta\varphi)) & \sqrt{\beta_2\,\beta_1}\,sin\,(\Delta\varphi) \\ \frac{1}{\sqrt{\beta_2\,\beta_1}}\left((\alpha_1 - \alpha_2)cos(\Delta\varphi) - (\alpha_2\,\alpha_1 + 1)sin\Delta\varphi\right) & \frac{\sqrt{\beta_1}}{\sqrt{\beta_2}}(cos\Delta\varphi - \alpha_2 sin\Delta\varphi) \end{pmatrix} \tag{4.13}$$

The number of corrector needed depends on the number of parameters which must be mastered. Only the four corrector bump is treated here but in the appendix E, other bumps are detailed (π bump and three corrector bump). Four corrector bump are often used since they enable to master both the beam angle and position at a given longitudinal position s_Q.

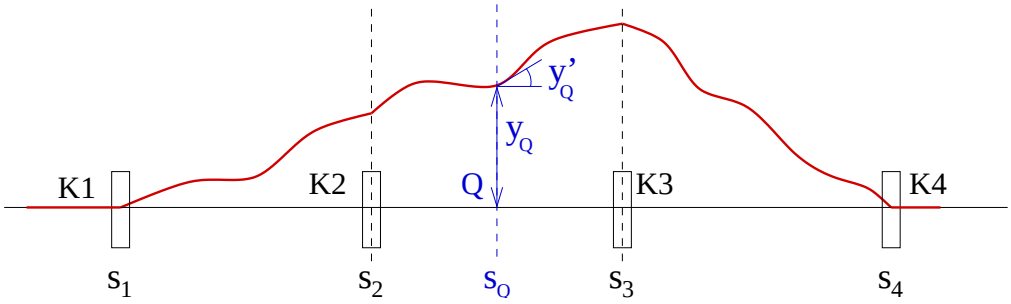

Figure 4.6: Four corrector bump

As previously, the corrector strength can be calculated and lead to

$$y'_1 = \frac{1}{\sqrt{\beta_1\beta_Q}}\frac{cos(\varphi_Q - \varphi_2) - \alpha_Q\,sin(\varphi_Q - \varphi_2)}{sin(\varphi_2 - \varphi_1)}\,y_Q - \sqrt{\frac{\beta_Q}{\beta_1}}\frac{sin(\varphi_Q - \varphi_2)}{sin(\varphi_2 - \varphi_1)}\,y'_Q \tag{4.14}$$

$$y'_2 = -\frac{1}{\sqrt{\beta_2\beta_Q}}\frac{cos(\varphi_Q - \varphi_1) - \alpha_Q\,sin(\varphi_Q - \varphi_1)}{sin(\varphi_2 - \varphi_1)}\,y_Q + \sqrt{\frac{\beta_Q}{\beta_2}}\frac{sin(\varphi_Q - \varphi_1)}{sin(\varphi_2 - \varphi_1)}\,y'_Q \tag{4.15}$$

The strength of the other correctors are obtained by replacing respectively "1" and "2" subscripts by "4" and "3". Then, α_Q and y_Q become $-\alpha_Q$ and $-y_Q$.

In the BBA context, this type of bump is used to perform a pure bump of position ($y'_Q = 0$) in the studied quadrupole. The purpose is to avoid errors on offset measurements due natural angle of the beam as shown by the figure 4.5. It is done by displacing the beam on several axis parallel to the reference one (figure 4.7)

4.1.1.2 K-modulation

The principle is to send a sinusoidal current into the magnet coils and to measure the beam position at the closest BPM. Eddy currents would appear when time varying current is provided to quadrupoles. These currents can lead to erroneous determination of the quadrupole magnetic axis since there are no reasons for the distribution of the eddy currents to be periodically reproducible. After a Fourier analysis of the signal seen by this BPM, the spectrum obtained shows peak at the

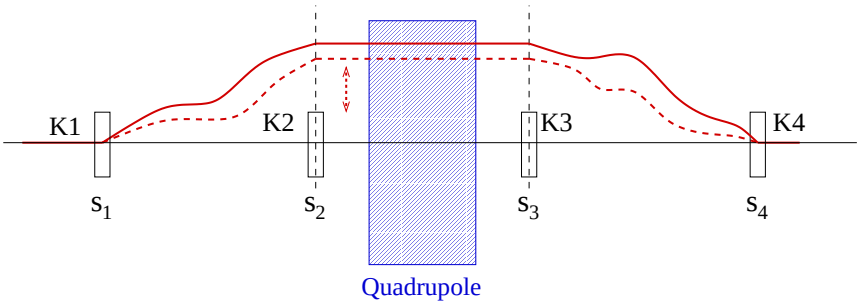

Figure 4.7: Pure four corrector bump

excitation frequency and its amplitude is proportional to the offset. Hence for several position of the beam in the BPM, the amplitude of the peak plotted and the BPM offset can be deduced. The plot obtained has a V shape and its minimum gives the BPM offset.

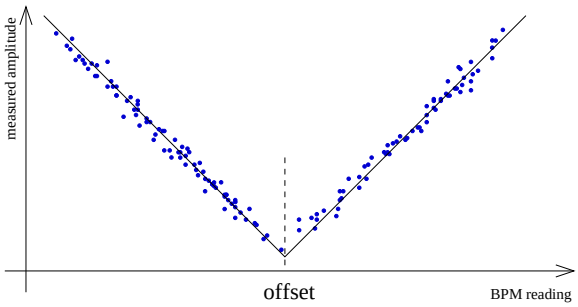

Figure 4.8: K-modulation

This method requires power supplies which could deliver time varying current which is rarely the case for Storage Ring power supplies. Indeed magnetic field produced by multipole is static. However if the problem of power supply is solved, the advantage of this method is that several BBA can be performed at the same time since different excitation frequencies can be used. Indeed after an FFT analysis the each peak correspond to an excitation frequency of a quadrupole.

According to this BBA methods study, the main method which is applied at SOLEIL is the one working with the most effective corrector. Then, there are not enough correctors to perform pure four correctors bump of position for all the SR quadrupoles with the SOLEIL optics. Consequently, this method is only used to cross-check the measurements obtained from the most effective corrector method.

4.1.2 Methods for sextupole magnets

To determine the effect of a misaligned sextupole, the reasoning is the same as the one developed at the beginning of the section 4.1.1.

$$B_z = S(x^2 - z^2) \tag{4.16}$$

$$B_x = 2S(x\,z) \tag{4.17}$$

$$\Delta x(s) = +\Delta S\left(x(s_0)^2 - z(s_0)^2\right)\left(\frac{1}{1-2Sx(s_0)\,\frac{\beta_x(s_0)}{2\,tan(\pi\,\nu_x)}}\right) * \frac{\sqrt{\beta_x(s)\,\beta_x(s_0)}}{2\,sin(\pi\,\nu_x)} cos(|\phi_x(s) - \phi_x(s_0)| - \pi\nu_x) \tag{4.18}$$

And $\Delta z(s)$ is deduced by replacing $(x(s_0)^2 - z(s_0)^2)$ by $2x(s_0)z(s_0)$.

Hence

$$\Delta x(s) \propto \Delta S\left(x(s_0)^2 - z(s_0)^2\right) \qquad \& \qquad \Delta z(s) \propto 2\Delta S(x(s_0)z(s_0)). \tag{4.19}$$

4.1.2.1 Methods with Correctors

The same method as developed previously can be applied. Indeed the merit function is:

$$f(y) = \frac{1}{N_{BPM}}\left[\sum_{i=1}^{N_{BPM}} (y_i(+\Delta S) - y_i(-\Delta S))^2\right] \propto (x\,z)^2 \tag{4.20}$$

Then by displacing the beam in only one plane (y) each time, the merit function depends on the square of the variable related to this plane (y^2). The BBA process is thus the same as for the quadrupole magnets.

However it is much less sensitive in the case of sextupoles. The relation between the change in the sextupole strength and in quadrupole gradient is:

$$\Delta S = \frac{\Delta K}{2x(s)} \tag{4.21}$$

With the examples given in [31], it is possible to quantify the need in change of sextupole strength to obtain the same sensitivity as in the quadrupole case.

At SOLEIL the value of the main component measured for the quadrupole at the 30 mm radius is 2 times greater than the the main component of the sextupole measured at 30mm. This rate is only a mean trend because quadrupole and sextupole are grouped in 10 families with a different working current for each family. If the beam displacement is fixed to 1 mm, the change in the quadrupole field seen by the beam is aK. Then the purpose is to calculate the change in sextupole field ($b\,S$) versus the change in the quadrupole field seen by the beam. Using 4.21 and the rate between the field of both multipole at the 30 mm radius, we are able to calculate the change in the sextupole magnetic field (bS) needed versus the change in the quadrupole magnetic field ($a\,K$).

$$x(s) = \frac{a\,K}{2\,b\,S} = \frac{2\,a\,S}{b\,S} \tag{4.22}$$

$$\Rightarrow b = 1000\,a \tag{4.23}$$

Consequently if a sextupole BBA with a corrector method is performed, the change in the sextupole field seen by the beam is 1000 times smaller than the one seen in a quadrupole ($a\,K$).

4.1.2.2 Method with Movers

This method is based on sextupole mechanical displacements. By moving the sextupole, the purpose is to find the position which will position the magnetic axis at the beam position.

The effect of an horizontal misalignment is the following for both plane:

$$B_z(x+\Delta x) = S(x^2 - z^2) + 2S\Delta x\,x + S(\Delta x)^2 \tag{4.24}$$

$$B_x(x+\Delta x) = 2S(x\,z) + 2S\Delta x\,z \tag{4.25}$$

Hence by displacing the sextupole at several positions Δy^{Mech} in one plane ($y = x$ or z), it changes the value of Δy in the equations above. By calculating ΔB_y and inserting it in the equation 4.1, we can deduce that the displacement of the beam $\Delta y(s)$ is proportional to the mechanical displacement Δy^{Mech}. In that case, the merit function is the difference to the square of the initial orbit and the new one. Its shape is also a parabola. The purpose of this type of beam based alignment is to find the right mover positions which cancel Δx and Δz. The main disadvantage of this method comes from the additional mechanical equipment it requires with movers. Indeed, if it is not automated, the measurement protocol could be long to apply since the beam must be killed to change by hands the sextupole position.

Since the BBA method with correctors seems to be not efficient enough it has not been tested at SOLEIL. Then SOLEIL SR sextupoles are not equipped with the movers method which makes impossible to apply this method. Another method exits, it uses a quadrupolar configuration performed by additional corrector coils located on the sextupole magnetic circuit. Since SOLEIL SR sextupoles are provided with these additional coils, this method is deeper studied in the part 4.3. Before working with BBA method applications, the context where BBA methods are experimented must be detailed. The additional coils of sextupoles belong to this context.

4.1.3 Environment

Even if the BBA principle can be experimented on every types of accelerator, its operation depends a lot on the machine configuration. Application of a BBA algorithm depends on the optic structure which can make the application of some methods impossible. The machine optic structure will be detailed in order to determine the BBA methods context. Then since an automated BBA program has been developed, a part is dedicated to the description of the SOLEIL control and command organisation of the machine.

4.1.3.1 Element description

SOLEIL SR Optics

First, the SR optics design has the main influence on the BBA methods which are applied. Figure 4.9 describes the 16 cells of the SOLEIL SR. These cells are grouped in 4 super-periods in order to keep a good order of symmetry. On this picture are showed the location of the dipoles, the quadrupoles (focusing and defocusing), the sextupoles, the three types of correctors located on the sextupole magnetic circuit and the Beam Position Monitors (BPM). The corrector implementation is developed further.

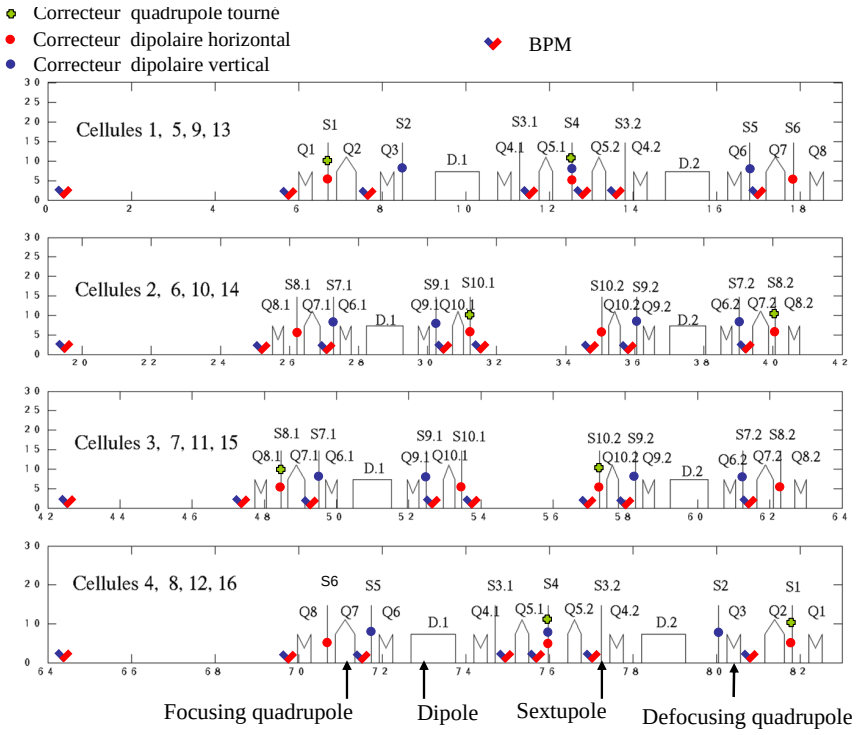

Figure 4.9: Cells description

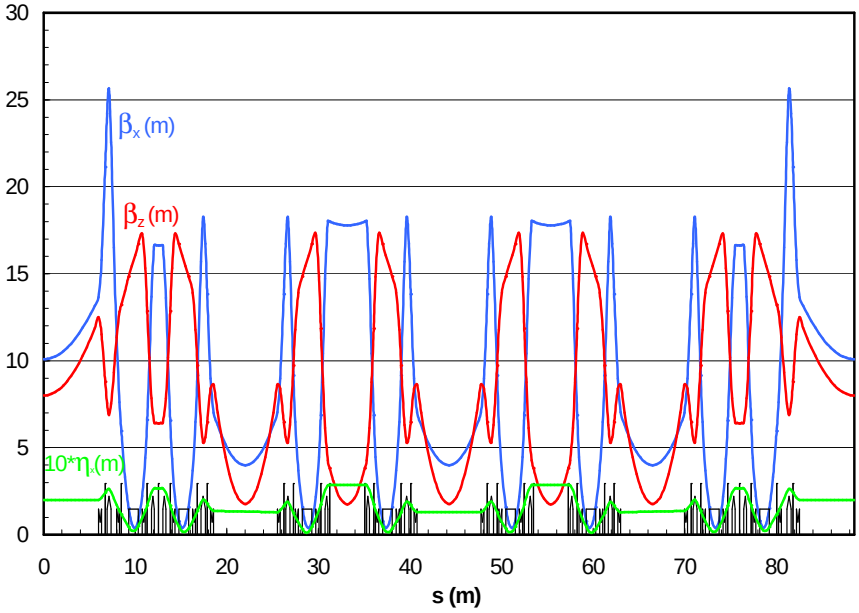

Figure 4.10: SOLEIL Storage Ring beta functions and dispersion function

Concerning the Beam Based Alignment, quadrupoles are all provided with independent power supplies contrary to the sextupole which are grouped in ten families (= ten power supplies for the 120 sextupoles). The fact that the sextupoles are serial connected inside one family makes the method with corrector difficult to apply. It is one more reason which led us to propose a new method using the corrector coils which are provided with independent power supplies. There are

56 dipolar correctors for both planes which values directly depends on the orbit read by the 120 BPMs. Moreover, 32 skew quadrupole correctors are used to cancel the coupling of the machine. when there is a coupling between horizontal and vertical plane, an action in one plane is observed in the other plane and physics problem become more complex.

From the optics design of the figure 4.9, the theoretical beta functions and the dispersions are plotted on the figure 4.10. In the context of BBA, beta functions act on the sensitivity of the measured multipole (quadrupole or sextupole) as showed by the equations 4.7 and 4.18. For the quadrupole BBA, 160 offsets will be obtained, one for each quadrupole, and there are only 120 BPMs which can take these offset into account. Beta functions will help us to choose between these offsets. The algorithm we develop to choose offsets is described in part 4.2.2.

SOLEIL SR Correctors

To get more free spaces for insertion devices, a concept that is often used now is to provide sextupole magnetic circuit with additional coils which are used to play the role of correctors. The figure 4.11 shows the additional coils installed on sextupole to perform the three types of slow correctors needed for SOLEIL.

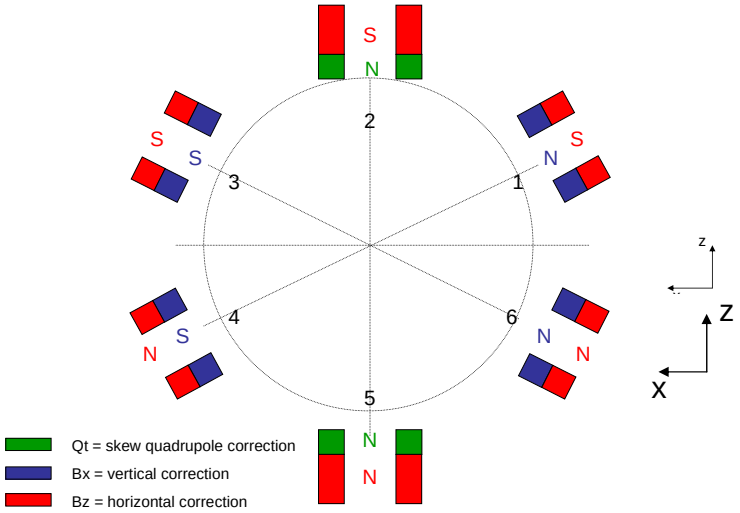

Figure 4.11: Additional corrector coils on the sextupole magnetic circuit

Dipolar corrector are used for BBA to displace the orbit in both planes. However in the part 4.3 which deals with sextupole BBA, the skew quadrupole corrector appears to be useful for the method we propose.

All the element of the SOLEIL optics (see figure 4.9) are remote commanded and controlled. It is the purpose of the next part.

4.1.3.2 Control and command organisation

From our point of view, MATLAB environment is used to develop the high level applications required to study the physics of the machine.

The SOLEIL control and command system is TANGO already used at the ESRF. In the SOLEIL context, TANGO has to manage approximatively 6000 parameters (power supplies, vacuum equipments, diagnostics and others). TANGO makes the link between the equipments and the high level application.

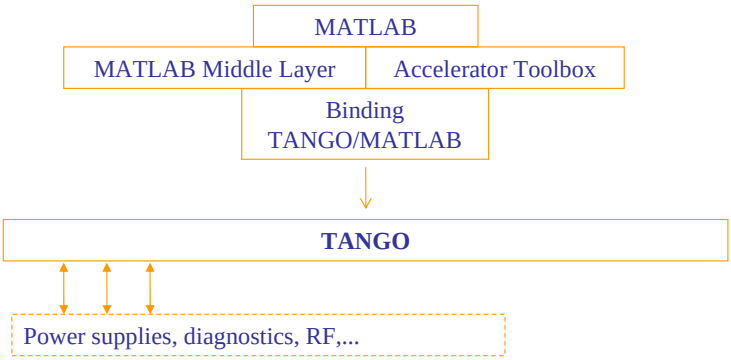

Figure 4.12: Simplified command and control architecture

4.2 Application of the BBA to the SOLEIL SR quadrupoles

4.2.1 Development of a Matlab Graphical User Interface

Beam-Based Alignment is often performed during the life of the machine (every 6 months). In the SOLEIL context, there are 2 times 160 BBA to perform since there are 160 quadrupoles. The need for an automated and reliable program is more than necessary. Moreover, it would be better to provide a graphical interface which enables to follow the BBA measurement progress. This kind of information must be communicated in a way that it facilitates judgement of a non experimented user. According to all these requirements, two BBA methods were implemented:

- Most effective corrector,
- Pure four corrector bump.

The general process of the method is expressed by the figure 4.13. The general purpose is to perform two symmetrical variation a quadrupole strength ($\pm\Delta K$) and for each variation to vary several times the current in the most effective corrector. After each step of the corrector current, the orbit position is measured by means of the BPMs. Once all these measurements are performed, the merit function expressed by the equation 4.9 can be computed in order to find its minimum which leads to the researched offset.

The BBA interface must give us the ability:

→ to choose the quadrupole to measure,

→ to choose the method,

→ to choose the plane,

→ to choose between the manual or the automated operation (choice of the BBA parameters),

→ to judge the quality of the measurement,

→ to obtain enough information for post-data analysis,

→ to know the parameters applied in the equipments (current in the corrector, in the quadrupole).

We implemented all these requirements in the BBA graphical user interface shown by the figure 4.14. It is divided into two parts. The left side is dedicated to the choices related to

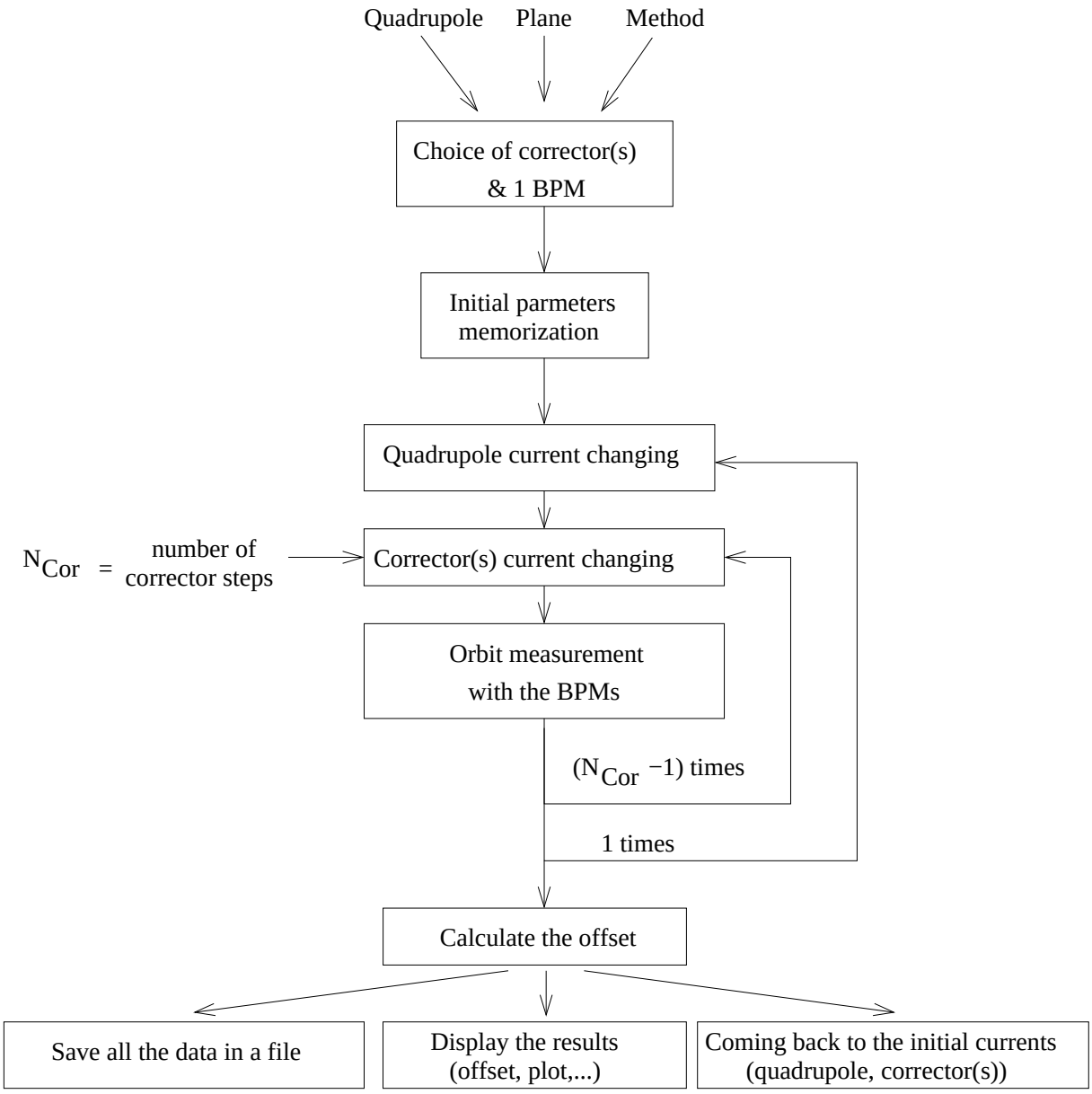

Figure 4.13: BBA process

the quadrupole to measure (quadrupole, plane, method). Then the right side is reserved for the results display and measurements launching. Indeed, the top part of this side display the measured quadrupole, the quality of the parabola fitting and the directory and the name the file in which the results are saved.

Then the most part of right side is dedicated to the curves display which shows the measured merit function (red crosses), the parabola fit of the merit function (dashed parabola), the orbit read by the closest BPM (blue crosses), the related linear fit (dashed line) and finally the minimum of the parabola and the BPM offset. All these data are plotted versus the applied corrector current.

Just under there are more detailed information concerning, the measured quadrupole (family [cell number; element number]), the name of the closest BPM, and the most effective corrector used.

And finally the "Action" button enables to launch the BBA process according to the parameters displayed on right corner. The manual button enables to choose whether the launched BBA is automated or not. The parameters on the right corner define respectively:

- nb Cor: the number of the current step in the chosen corrector,
- Step Cor: the value in amperes of each step of the corrector current variations,
- offs Cor: a corrector current offset which necessary to centre the the measurement in order to obtain a symmetrical parabola,
- Delai: the pause in second between each steps of corrector,
- Step Qp: the value of the quadrupole current variation step.

4.2.2 Beam-Based Measurements

Measurements

After the BBA measurement campaign, we were able to analyse the measured data and to perform some statistics calculations. The first observation is that BBA of quadrupole was necessary since the standard deviation of the measured offset is large for both planes (approximatively 160 μm). Moreover, it occurs that some offsets were of the order of the millimetre.

The offset distribution along the SR are showed by the figures 4.15 and 4.17. These figures are associated with the histograms of the figures 4.16 and 4.18. These results confirm that it is easier to align mechanical devices versus the vertical plane than versus the horizontal one since the mechanical reference is often better determined along the vertical direction. Figure 4.17 shows a continuous peak which reaches the millimetre. It is a defect which has to be soon investigated by the SOLEIL alignment group.

Application of the offsets

Now two games of 160 offsets are available (one game for each plane). As mentioned in the part 4.1.3.1, there 120 BPMs. Consequently, 120 offsets must be extracted without loosing the information given by all the 160 offsets. As the BBA process has always chosen the closest BPM, it occurs that some BPMs were used twice to measure two different quadrupole offsets. Such a case is represented by the figure 4.19.

One way to proceed is to choose one offset between the ones obtained for each quadrupole Q_1 and Q_2. Consequently, this type of choice does not take into account 40 offsets.

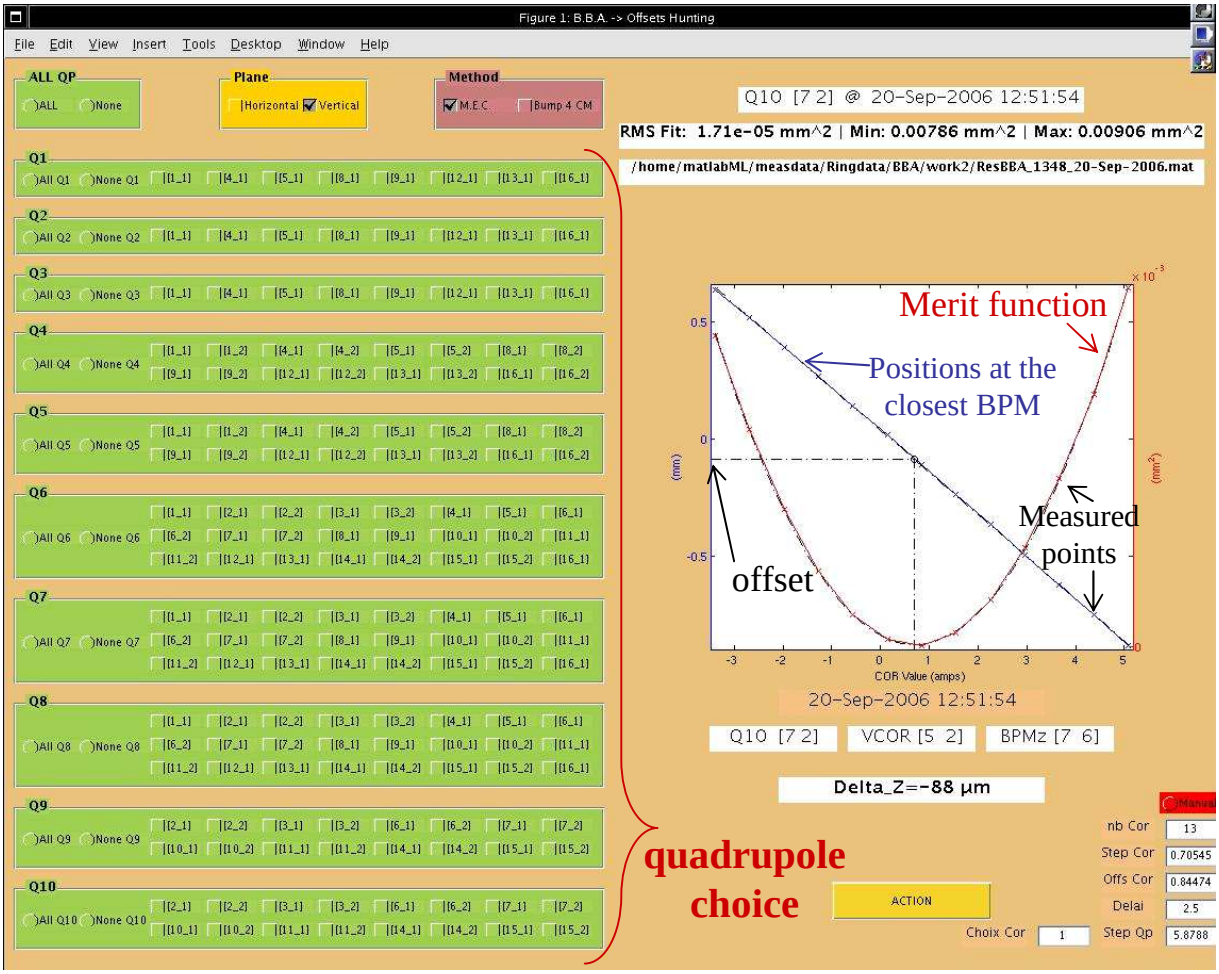

Figure 4.14: Beam Based Alignment graphical user interface

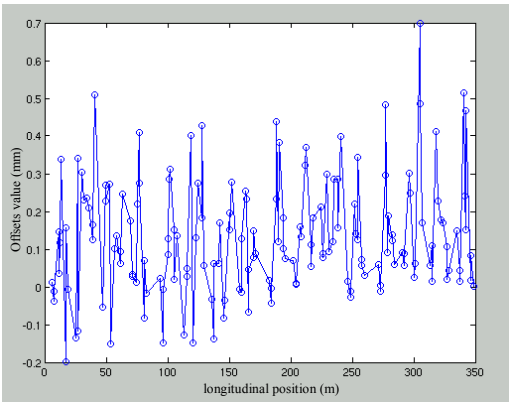

Figure 4.15: Horizontal offsets along the SR

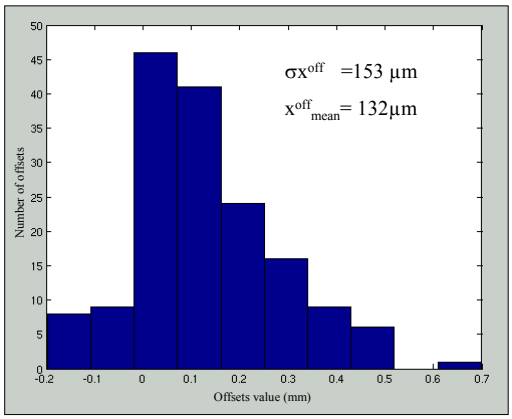

Figure 4.16: Horizontal offsets histogram

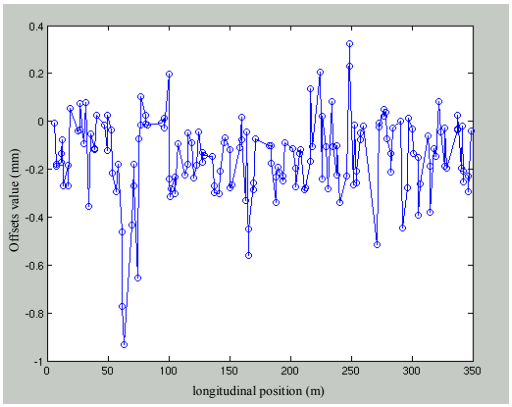

Figure 4.17: Vertical offsets along the SR

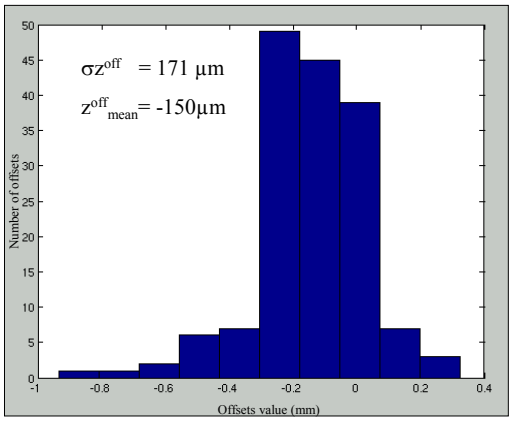

Figure 4.18: Vertical offsets histogram

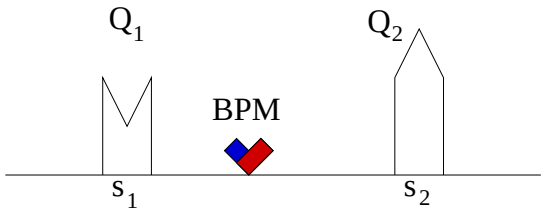

Figure 4.19: One BPM between 2 quadrupoles

The solution we have chosen is to perform a weighted mean of both offset. The equation 4.7 shows that proper weights could be the quadrupole strength and the value of the beta function in these quadrupoles. If two quadrupoles Q_1 and Q_2 have their offsets (off_1 and off_2 respectively) measured with the same BPM, the calculated offset off_{calc} is expressed by the equation 4.26.

$$\text{off}_{calc} = \frac{\text{off}_1 \sqrt{\beta_1}\,|K_1| + \text{off}_2 \sqrt{\beta_2}\,|K_2|}{\sqrt{\beta_1}\,|K_1| + \sqrt{\beta_2}\,|K_2|} \tag{4.26}$$

Using this formula, we were able to determine 120 offsets which take into account all the measured offset. Then, these offsets were applied to the BPMs in both planes and the results are

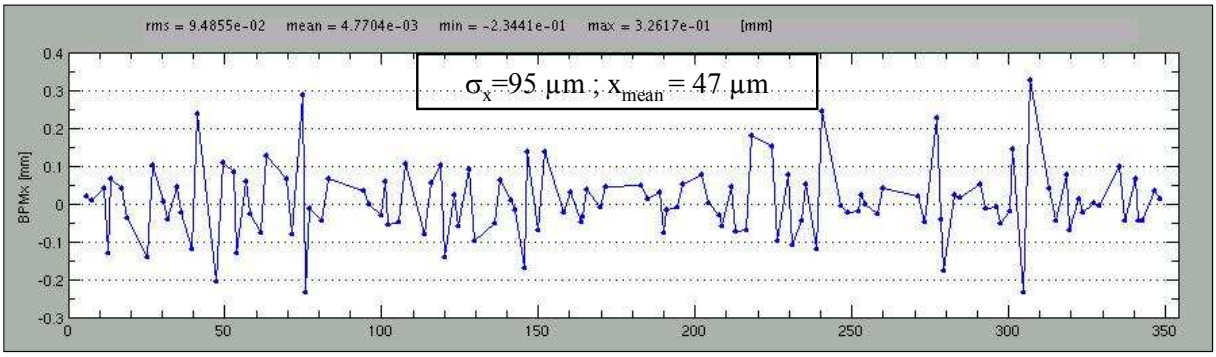

Figure 4.20: Horizontal orbit after the first application of BBA offsets:first correction

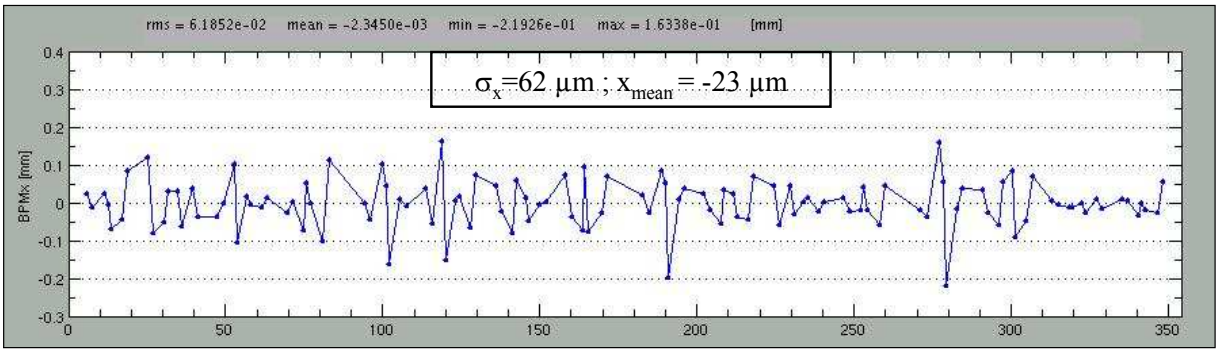

Figure 4.21: Horizontal orbit after application of BBA offsets: best correction

Unfortunately, the horizontal orbit before the BBA offset application has not been stored. However from the run report, we observed that the standard deviation of the read orbit has been divided by a factor of two. The peak values have also been reduced and the corrector standard deviation is close to 1A compared to the 10A available.

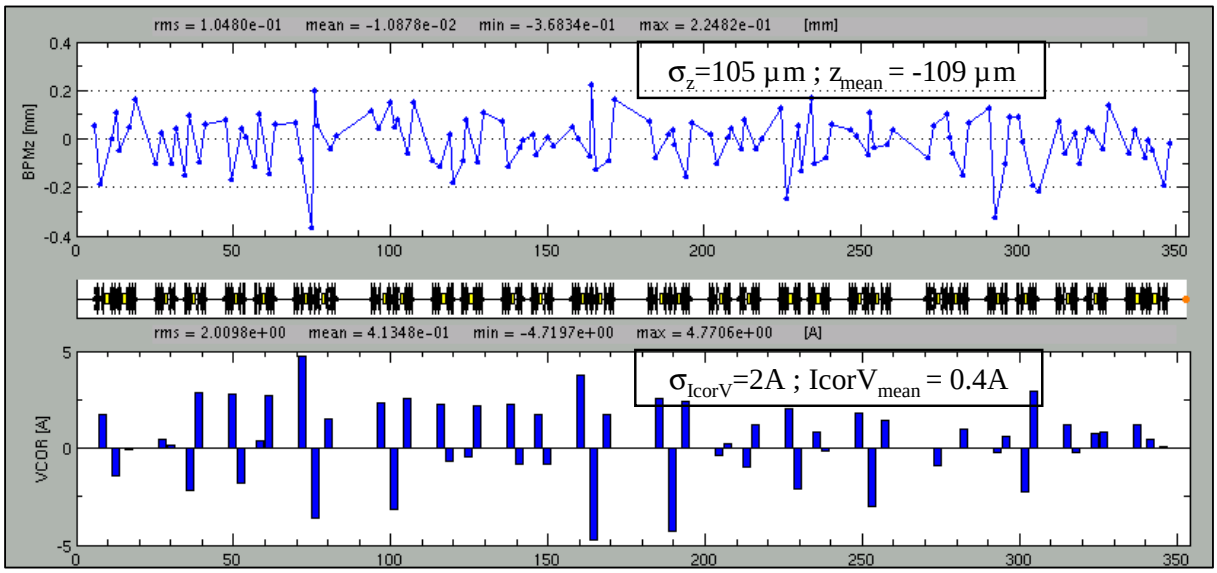

Figure 4.22: Vertical orbit and corrector values before application of BBA offsets

Concerning the vertical plane, the result is less spectacular for the orbit. However, the standard deviation of the corrector current has been divided by 5 to reach 0.4A.

When we performed the correction for both planes after the BBA offsets application, the effects observed where slightly different. Since there are 56 correctors for both planes, the orbit correction program enables us to choose up to 56 eigenvalues. For the horizontal plane case, choice of the 56 eigenvalues leads directly to the best result: the one of the figure 4.21. Then only the use of 32 eigenvalue in the vertical plane leads to best compromise between corrector current distribution and orbit minimization. This effect means that some errors are remaining in the vertical plane. We are not able for the moment to determine if these errors come from bad operation of BBA or from other sources. It is a point to investigate.

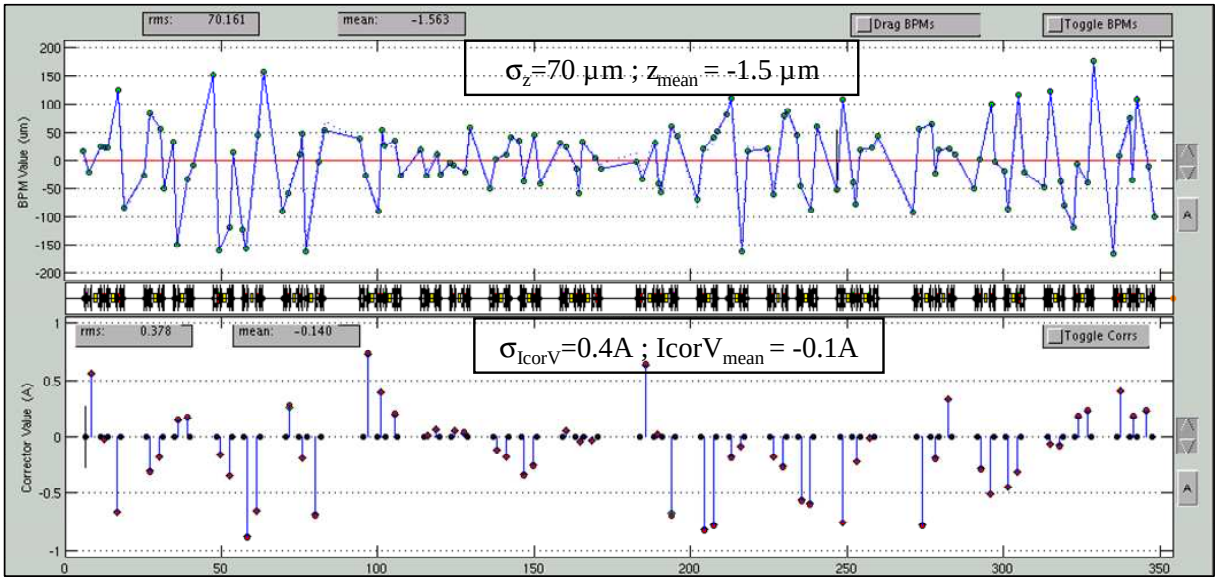

Figure 4.23: Vertical orbit and corrector values after application of BBA offsets

During these BBA measurement, we have verified that BBA applied with the four corrector bump method gives the same result as the one obtained with the most effective corrector method. We only checked it for one quadrupole. The result obtained was different of ten microns which is the current reproducibility of the our main BBA algorithm (most effective corrector method). We observed that 4 corrector bump method is longer to apply since the algorithm must wait that the four correctors have reached the values ordered.

In parallel to the quadrupole BBA, we have experimented a sextupole BBA method. It is the purpose of the next part.

4.3 BBA for sextupole magnets

Beam based alignment of sextupole is more complex since the methods are less sensitive. Indeed, effects of sextupole misalignments imply second order effects like magnetic field gradient apparition. During the study of sextupole beam based alignment methods, one method retain our attention: the one using additional corrector coils located in the sextupole poles to perform a pseudo quadrupole magnet. The main assumption of this method is that the magnetic axis of the sextupole magnet and this pseudo-quadrupole are merged. Then the magnetic axis of this pseudo quadrupole is measured by operating a classical quadrupole beam based alignment. However, the components which define magnetic axis of both type of magnet are not the same and we can wonder if the assumption is reliable. By developing the relation 2.22, the magnetic axis position are obtained for both magnets.

$$\overline{\Delta\zeta}^{Quad} = r_0 \frac{B_1\,B_2 + A_1\,A_2}{B_2^2 + A_2^2} + i\frac{A_1\,B_2 - A_2\,B_1}{B_2^2 + A_2^2} \approx r_0 \left(\frac{B_1}{B_2} + i\frac{A_1}{B_2}\right) \tag{4.27}$$

$$\overline{\Delta\zeta}^{Sext} = \frac{r_0}{2}\frac{B_2\,B_3 + A_2\,A_3}{B_3^2 + A_3^2} + i\frac{A_2\,B_3 - A_3\,B_2}{B_3^2 + A_3^2} \approx \frac{r_0}{2}\left(\frac{B_2}{B_3} + i\frac{A_2}{B_3}\right) \tag{4.28}$$

The approximate results are obtained by making the assumption that the skew components of the main fields, A_2 for the quadrupole and A_3 for the sextupole, are very small. This assumption

is validated by magnetic measurements. In the SOLEIL sextupoles, there are residual dipolar components remaining after their correction.Hence, even if the pseudo quadrupole has the same magnetic axis location as the sextupole, these dipolar components directly displace this magnetic axis and lead to erroneous beam based alignment (see figure 4.24).

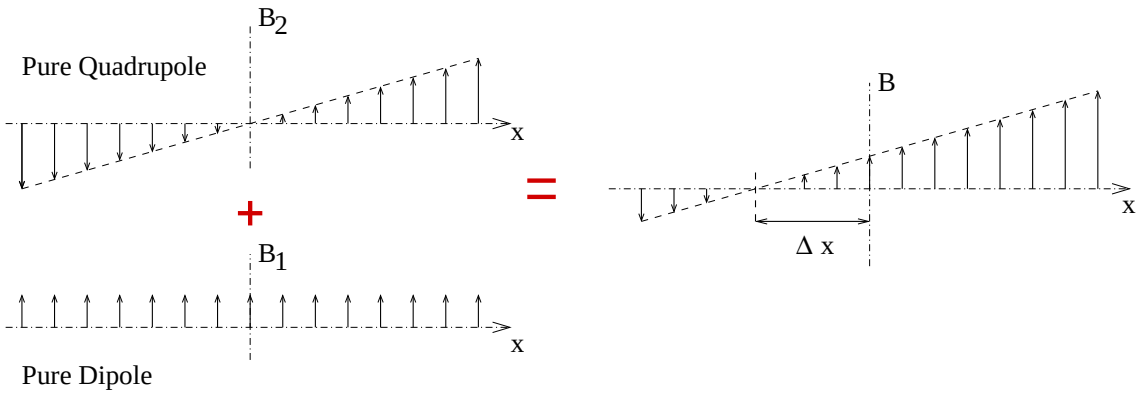

Figure 4.24: Effect of an initial dipolar component on a quadrupole magnetic axis measurement

According to the figure 4.24, the magnetic axis of the pseudo-quadrupole depends on the presence or not of the initial dipolar component and not on the sextupole magnetic axis properties. Whatever the magnetic axis location of the pseudo quadrupole is, the sextupole magnetic axis position depends on the strength of the pseudo quadrupole field as shown by the figure 4.25. Indeed, adding a dipolar component only change the mean value of the sextupole magnetic field but never its magnetic axis location.

Moreover, if both magnetic axis are merged which verifies the assumption another defect can disturb the measurement. Indeed, magnetic axis properties of the sextupole are given by magnetic circuit geometry, that is to say by its six poles. The magnetic axis of the pseudo quadrupole have the properties of the four pole chosen among the six of the sextupole. Hence three combinations are possible which can lead to three magnetic axis positions.

Sextupole beam-based alignment method by measuring magnetic axis properties of a pseudo-quadrupole seems to be compromised. However the use of an additional quadrupolar magnetic field can be advantageous in sextupole BBA if it is used in another way. It is the purpose of the next part.

4.3.1 Proposition of a new method: The Magnetic Axis Moving method

The principle of the method proposed has similar effects than the one that uses movers. Indeed, with movers, the sextupole is displaced mechanically of a given quantity which implies the magnetic axis displacement of the same quantity. The purpose is to find the position of the sextupole which leads to a minimum orbit distortion. That is to say to minimize second order effect by displacing the sextupole magnetic axis.

This method can be improved. Indeed there is no need to displace the magnetic axis mechanically since it is possible to perform it magnetically. It is the idea we propose to develop.

First it is necessary to recall the effect of a sextupole misalignment expressed by the equation 4.24.

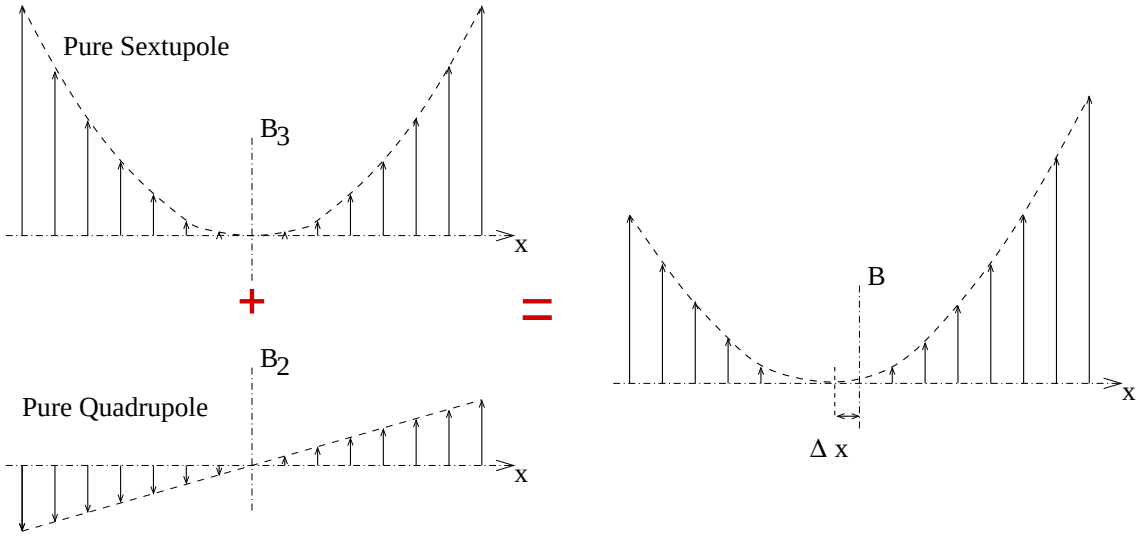

Figure 4.25: Effect of an additional quadrupolar component on a sextupole magnetic axis measurement

$$\Delta B_z(x + \Delta x) = +2S\Delta x\, x + \mathcal{O}(S(\Delta x)^2) \tag{4.29}$$
$$\Delta B_z(z + \Delta z) = -2S\Delta z\, z + \mathcal{O}(S(\Delta z)^2) \tag{4.30}$$

If these expressions are compared to the development of the series expansion of the magnetic field in the case of a pure normal quadrupole and a pure skew quadrupole.

$$\text{Normal quadrupole;} \qquad B_z = \; r_0\, B_2\, x \tag{4.31}$$
$$\text{Skew quadrupole;} \qquad B_z = -r_0\, A_2\, z; \tag{4.32}$$

By identifying the terms versus x and z of both set of equations, the approximate results of the equation 4.28 can be deduced again.

If additional quadrupolar fields are applied (normal and skew), the effect of sextupole misalignment can be cancelled. It can become a mean to measure the magnetic offset seen by the beam. The merit function is then the square of the orbit difference seen by the horizontal or vertical BPMs, since the misalignment defect acts in both planes (B_z and B_x).

The additional skew quadrupole field can be performed with skew quadrupole correctors which are already present on the sextupole magnetic circuit. Then for the normal quadrupole, the purpose is also to use correctors placed on sextupoles. That is why, this normal quadrupole is performed with the vertical correctors coils connected in the quadrupolar mode.

Hence the merit function is a function of the current applied to these quadrupoles.

$$f(y) = \frac{1}{N_{BPM}} \left[\sum_{i=1}^{N_{BPM}} (y_i(I_{Quad}) - y_i(I_{Quad=0}))^2 \right] \propto (I_{Quad})^2 \tag{4.33}$$

And magnetic measurements enable to obtain the relation between the current applied and the strength of the field produced. The optimal values of A_2 and B_2 are deduced with these two optimal currents (horizontal and vertical or normal and skew). Then from magnetic measurements,

the strength of the sextupole can be found (B_3). With the approximate formula 4.28, the offset Δx and Δ_z can be easily calculated.

With hands, we can say that adding quadrupolar field to a sextupole field displace its magnetic axis. Like the movers methods, the Magnetic Axis Moving method (MAM) tries to find the best position of the magnetic axis which minimizes sextupole positioning errors. That is to say, the one which will generates the less defects on the transverse beam dynamics.

4.3.2 First application of the MAM method at SOLEIL

The purpose of the work is to validate the new approach proposed previously. According to the equations 4.29 and 4.31, two parameters can be used to optimize the sensitivity of the method: the pseudo-quadrupole strength (B_2 or A_2) and the orbit of the beam (x or z).

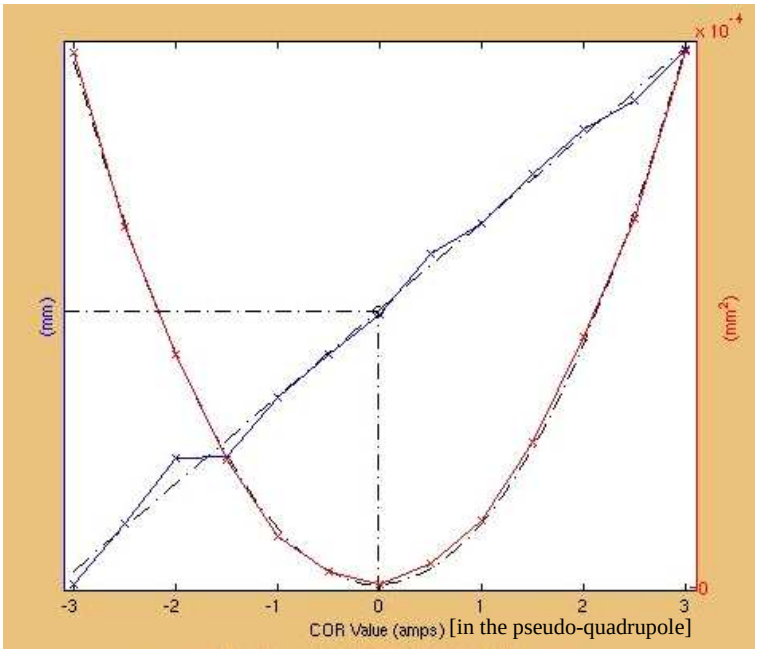

Figure 4.26: First reliable sextupole BBA

The figure 4.26 shows that the merit function of the MAM method generates a parabola as predicted by the theoretical calculations. For the example plotted on the figure reffig:bbasext, the sextupole seems to have a very small offset since the minimum of the parabola occurs for a current close to zero in the pseudo-quadrupole.

After two attempts concerning the normal pseudo-quadrupole configuration, it seems that the horizontal beam position is centred with respect to its magnetic axis horizontal position. Whereas for the skew pseudo quadrupole configuration, it occurred that there were measurable offsets. An offset has been calculated for an experiment with a skew pseudo quadrupole. From the current determined by the minimum of the merit function parabola, we were able to find the added skew quadrupole which cancel the initial residual magnetic axis offset. Indeed, before these sextupole BBA, evolution of the pseudo-quadrupole magnetic field response versus the current has been measured with the SMB (SOLEIL Multipolar Magnetic Measurement Bench). According to these measurements, we were able to estimate the offset at $110\mu m$ in the vertical direction. More MAM sextupole BBA must be performed to increase the statistics on the results obtained.

For the moment, we are not able to quantify the accuracy of this promising method.

We think that this new approach can constitute the beginning of a new era in the field of Storage Ring Beam-Based Alignment. If the MAM method for sextupole BBA can ensure the same sensitivity as the most effective corrector method for the quadrupole BBA, the final step of a Storage Ring BBA would be a mixed Beam-Based Alignment between quadrupole and sextupole offsets. That is to say, in the case of SOLEIL, that the 120 BPMs would have optimized offsets obtained from the 280 measured offsets for one plane (280 = 160 quadrupoles + 120 sextupoles). The merit function of this offsets optimization would be the minimization of orbit distortion due misaligned quadrupoles and sextupoles.

Résumé du chapitre
Après avoir rappelé les différentes méthodes d'alignement basé sur le faisceau (BBA) pour les quadrupôles et les sextupôles, une méthode "du correcteur le plus efficace" a été appliquée avec succès aux quadrupôles de l'anneau de stockage de SOLEIL puisque la dispersion horizontale de l'orbite a été réduite de 95 à 62 μm et la dispersion verticale est passée de 105 à 70 μm. Cette amélioration est particulèrement visible dans le plan vertical s'il on considère la dispersion du courant dans les correcteurs qui passe de 2 A à 0.4 A après application du BBA.
Cette première partie nous a permis de prendre en main ce type de méthode. Nous avons ensuite proposé une méthode innovante d'alignement basé sur le faisceau pour les sextupôles appelée "Méthode de l'axe magnétique Mouvant". Elle met en jeu les bobines de correction montées sur les sextupôles, ce qui a pour avantage majeur de ne pas nécessiter d'équipement supplémentaire. Cette méthode a été testée et s'est montrée tout à fait applicable. Des tests complémentaires, qui n'ont pu être effectués dans le cadre de ce travail, devront être menés notamment quant à sa précision .

Conclusion

As the electron beam size needs to become smaller and smaller to provide a more and more brilliant photon beam, specifications on the Storage Ring accelerator magnets become more and more strict. From the machine physics point of view, the quadrupoles are the most sensitive elements of the SOLEIL Storage Ring (SR).

First, to reduce the electron beam size, the quadrupoles must provide a strong focusing effect. Then, when the beam is going through off a quadrupole magnetic axis, it undergoes an undesired deflection (first order effect) which is proportional to the focusing strength and to the distance from the axis. Consequently the alignment of the magnets versus their magnetic axis is a keypoint for the Storage Ring efficiency. Measurements for magnet alignment are performed in two main steps. The first step occurs before the magnet installation. It enables to determine the magnetic axis characteristics by means of magnetic measurements. Then once the magnet are installed and mechanically aligned according to their magnetic axis properties, a second type of measurements is performed based on electron beam behaviour studies. This last step is called a beam-based alignment. Its aim is to measure the residual misalignments of the Storage Ring quadrupoles in order to obtain a reduced orbit distortion due to first order errors.

In the context of the magnetic measurements, the SOLEIL Synchrotron decided to measure with its own means its Storage Ring magnets and particularly the 160 quadrupoles. The first three chapters of this work are dedicated to the SOLEIL Multipolar Magnetic Measurement Bench (SMB) which was required to measure and tune these magnets within the strict tolerances fixed. That is to say $\pm 25\,\mu m$ for the magnetic axis location in the transverse plane and $0.1\,mrad$ for the magnetic tilt angle.

The third chapter showed the high sensitivity and reproducibility obtained from the bench. Indeed, concerning the magnetic axis characteristics, we managed to ensure an excellent identity between all the magnets. The final standard deviation of the residual magnetic axis location is twice smaller than the specifications, that is to say less than $\pm 10\,\mu m$. The main difficulty we had to cope with was measuring and tuning the magnetic tilt angle. With a tolerance fixed to $\pm 0.1\,mrad$, it represented a challenging mechanical stability of $\pm 3\,\mu m$ on the sensor mechanical structure at a 30 mm radius. Finally we managed to keep the identity between magnets on magnetic tilt angles within $\pm 0.05 mrad$.

The statistical analysis of the results were calculated during the measurements. It was a means to check that there was no drifts during the two months and a half long measurements. This monitoring enables us to early detect the non allowed octupolar component for long quadrupoles. This defect led us to perform studies with the theoretical 3D model developed to simulate sensor geometrical defects. Thanks to these qualitative studies, we could understand the origin of this octupolar component which is due to pairs of poles asymmetry. This octupolar component is also easy to detect with magnetic flowers which correspond to a 2D representation of the effect of harmonics on the gradient homogeneity. Indeed, for all the measured magnets, the gradient homogeneity versus the gradient at the centre was plotted on a transverse coordinates map. The

main advantage of this type of map is that it gives the influence of harmonics on the gradient homogeneity.

With proper alignment during their installation, all the work on the quadrupole magnets provided good conditions to begin the commissioning of the SR. Closing the first turn is known to be difficult. However, for the first try to make the electron beam performing one turn of the SR, it performed three turns. Then with some correctors, 50 turns could be reached. Moreover, SOLEIL is the first machine to start the commissioning with the final vacuum chamber -the smallest ($\pm 5mm$)- in straight sections and with four undulators already installed. For all these reasons the first three turns of the beam in the SR without corrections is considered as a performance.

After several orbit correction attempts, it was not possible to obtain an orbit below $\pm 300\,\mu m$ with a standard deviation of $120\,\mu m$. It is due to residual misalignments between the quadrupole magnetic axis and the Beam Position Monitors (BPM) which provide the beam position versus their electrical axis. Beam-Based Alignment (BBA) is required to cancel these offsets and it is detailed in the chapter 4. The method of the most effective corrector was applied and was firstly implemented in a graphical user interface. The purpose of such an interface is to facilitate BBA operation for non experimented users. Indeed, during machine life, BBA will be applied at least twice a year and requires many hours of operation to measure the 160 offsets related to each quadrupole. After the application of the measured offsets from the first quadrupole BBA campaign, the orbit excursion has a standard deviation of $60\,\mu m$ in the horizontal plane and $70\,\mu m$ in the vertical plane.

Then it would also be better for the photon brilliance to make the beam going through the sextupole magnetic axis. Indeed, an off axis electron beam in a sextupole undergoes a harmful focusing effect (second order) which can lead to a tune shift and a beta beating. Consequently, Beam-Based Alignment methods can also be useful for sextupoles. In the case of SOLEIL SR, there are 120 sextupoles distributed in 10 families. All the sextupoles of one family are connected in series, therefore it is not possible to transpose the quadrupole BBA method to the sextupole case.

The experience acquired during 2m-pole magnet magnetic measurements led us to propose a new approach of sextupole BBA. Indeed, the initial idea was to use additional coils located on sextupole magnetic circuit to generate a quadrupole magnetic field. The purpose was to use the greater sensitivity of quadrupole magnetic field to perform orbit variation. Then it was assumed that magnetic axis of this quadrupole was merged with the sextupole one. From this assumption, if the magnetic axis of this pseudo-quadrupole is determined, it is also the case of the sextupole one. We demonstrated that such a method could not work since the harmonics used to determine their magnetic axis are slightly different. However we kept the idea to create additional quadrupolar magnetic field provided by corrector coils and we developed a new approach.

In that case, the BBA concept becomes different. To sum up the quadrupole BBA, the principle is to displace the beam in order to determine its position which generates the less orbit distortion. At this position, the beam is not deflected, it does not undergo a dipolar magnetic field. We propose to perform the contrary with sextupole BBA. The beam position is fixed and it is the sextupole magnetic axis which is displaced. Indeed, since the sextupole magnetic axis location is proportional to the quadrupolar magnetic field (normal or skew), this type of field is used to cancel the focusing effect seen by an off centred beam.

We established the theory and led the experiments which validated the method. However, the method needs to be more developed in order to get a better idea of its accuracy. This method is advantageous since all correctors in sextupoles are provided with corrector coils with independent power supplies. If this sextupole BBA method proves to be accurate enough, sextupoles will be provided with offset which have to be taken into account. By performing both BBA (quadrupole

and sextupole), two games of offsets (160 quadrupoles + 120 sextupoles) will be available for the same set of BPMs (120). With all these offsets, the final aim of such a work is to find the optimized set of offsets which is the best for the electron beam dynamics.

Current SOLEIL Synchrotron performances relies on the achievement of a lot of innovative research and development projects led by SOLEIL teams. Since May 2006, the beginning of the Storage Ring commissioning, SOLEIL has accumulated many successes. As mentioned previously, the unprecedented results obtained with Storage Ring quadrupole magnetic measurements and tuning contributed a lot to the success of the first day commissioning. These results also enable to perform high quality experiments on the machine accelerator physics during the machine runs. Several tens of machine runs later, the first automated Beam-Based Alignment of the SR quadrupoles has already been finished and allows to obtain a beam orbit sufficiently small to provide to synchrotron light users a golden orbit to prepare their experiments. From its beginning, the quadrupole Beam-Based Alignment has always been operated by means of the graphical user interface which can be used as fairly by experimented physicists as by machine operators. In parallel, during this first phase of the commissioning, the Magnetic Axis Moving innovative method proposed for sextupole Beam-Based Alignment has been experimented and its principle has been validated. If this method becomes as sensitive as expected, mixed Beam-Based Alignment of quadrupoles and sextupoles could be performed, leading to a better management of the magnet misalignment defects. Such method could open a new era concerning the Storage Ring Beam Based Alignment.

Bibliography

[1] W.G. Davies. The theory of the measurement of magnetic multipole fields with rotating coil magnetometer. In *Nuclear Instruments and Method*, A331, page 399, 1991.

[2] J.D. Cockroft and E.T.S. Walton. Artificial production of fast protons. In *Nature, VOL. 129*, page 242, February 13, 1932.

[3] J.D. Cockroft and E.T.S. Walton. Disintegration of lithium by swift protons. In *Nature, VOL. 129*, page 649, April 30, 1932.

[4] R.J. Van De Graaf. A 1,500,000 volt electrostatic generator. In *Physical Review, VOL. 38*, page 1919, 1931.

[5] D.W. Kerst. Acceleration of electrons by magnetic induction. In *Physical Review, VOL. 58*, page 841, 1940.

[6] H.S. Snyder E.D. Courant, M.S. Livingston. The strong focusing-a new high energy accelerator. In *Nuclear Instruments and Method*, 82, page 157, 1970.

[7] D.W. Kerst, F.T. Cole, H.R. Crane, L.W. Jones, L.J. Laslett, T. Ohkawa, A.M. Sessler, K.R. Symon, K.M. Terwilliger, and Nils Vogt Nilsen. Attainment of very high energy by means of intersecting beams of particles. In *Physical Review, VOL. 102*, page 590, 1956.

[8] J. Larmor. On a dynamical theory of the electric and luminiferous medium. In *Philosophical Transactions of the Royal Society*, page 190, 1897.

[9] A.M. Liénard. L'éclairage électrique, 1898.

[10] J. Rossbach P. Schmüser. Basic course on accelerator optics. In *CERN ACCELERATOR SCHOOL: Fifth general acceleralor physics courses*, volume 1, 1994.

[11] K.N. Henrichsen. Classification of magnetic measurement methods. In *CERN ACCELERATOR SCHOOL*, page 70, 1992. Magnetic measurement and alignment.

[12] W. Gilbert Clark. Introduction to magnetic resonance an its application to dipole magnet testing. In *CERN ACCELERATOR SCHOOL*, page 193, 1998. Magnetic measurement and alignment of accelerator and detector magnets.

[13] B. Berkes. Hall generators. In *CERN ACCELERATOR SCHOOL*, page 167, 1992. Magnetic measurement and alignment.

[14] A. Temnykh. Vibrating wire field-measuring technique. In *Proceedings of the Particle Accelerator Conference 1997*, page 3218, 1997.

[15] Gilles QUEMENER. *Cartographie magnétique des quadripôles des spectromètres à haute résolution du Thomas Jefferson National Accelerator Laboratory, Hall A*. PhD thesis, Université Blaise Pascal, 1997.

[16] A.K. Jain. Harmonic coils. In *CERN ACCELERATOR SCHOOL*, page 174, 1998. Magnetic measurement and alignment of accelerator and detector magnets.

[17] G.E. Lee-Whiting. End effects in first-order theory of quadrupole lenses. In *Nuclear Instruments and Method*, 76, page 305, 1969.

[18] G.E. Lee-Whiting. Measurement of quadrupole lens parameters. In *Nuclear Instruments and Method*, 82, page 157, 1970.

[19] L. Bottura. Standard analysis procedures for field quality measurement of the lhc magnets-part**I**:harmonics. In *LHC-MTA-IN-97-007*, july 1997.

[20] Wolfram Research. http://www.wolfram.com/.

[21] E. Durand. *Magnetostatique*. Masson et Cie, 1968.

[22] J. Cobb and R. Cole. Spectroscopy of quadrupole magnets. In *International symposium on Magnet Technology*, page 431, september 1965.

[23] J. Chavanne O. Chubar, P. Elleaume. 3d magnetostatics simulation software. http://www.esrf.fr/Accelerators/Groups/InsertionDevices/Software/Radia.

[24] Danfysik. Accelerator devices manufacturer. http://www.danfysik.dk/.

[25] Sigmaphi. Accelerator magnet manufacturer. http://www.sigmaphi.fr/.

[26] Capital Equipment Corporation. Testpoint: Data acquisition and analysis software. http://www.cec488.com/.

[27] The TANGO framework. http://www.esrf.fr/Infrastructure/Computing/tango.

[28] Metrolab Instruments SA. http://www.metrolab.ch/.

[29] Heidenhain Corporation. http://www.heidenhain.com/.

[30] Vector Fields. Opera: 2d and 3d electromagnetic modelling. http://www.vectorfields.com/.

[31] L. Schachinger D. Robin, G. Portmann. Automated beam based alignment of the als quadrupoles. In *NLC-Note 18*, August 1995.

Notations

$\overrightarrow{A}$	:	Vector potential
$\overrightarrow{A_{Qp}}$	:	Vector potential of the quadrupole
$\overrightarrow{\mathsf{A}}$	:	Integrated vector potential
$\overrightarrow{B}$	:	Magnetic flux density
$\overrightarrow{\mathsf{B}}$	:	Integrated magnetic flux density
$\overline{\mathbb{B}}$	:	Complex integrated Magnetic flux density
$\overline{C_n}$	:	Complex harmonic coefficient
$\overline{\mathbb{C}_n}$	:	Complex integrated harmonic coefficient
$\overline{\mathbb{C}_n^{mag}}$	:	Complex integrated harmonic coefficient in the magnetic frame
$\overline{\mathbb{C}_n^{meas}}$	:	Complex integrated harmonic coefficient in the measurement frame
$\overrightarrow{D}$	:	Electric flux density
$\overrightarrow{E}$	:	Electric field
(E_x, E_z, E_s)	:	Cartesian electric field components
E_y	:	Young modulus of a material
$\overrightarrow{F}$	:	Force
$\overrightarrow{F_l}$	:	Lorentz Force
G	:	Coulomb modulus
$G_x(x,z)$	:	Tranverse function the gradient along x axis
$\overrightarrow{H}$	:	Magnetic field
I_{G_x}	:	Moment of inertia of a mechanical structure around the Gx axis
I_{G_z}	:	Moment of inertia of a mechanical structure around the Gz axis
$I_{G_x\|str.}$	:	Moment of inertia of a mechanical structure around the Gx axis of the structure
$I_{G_z\|str.}$	:	Moment of inertia of a mechanical structure around the Gz axis of the structure
$I_{G_s\|str.}$	:	Moment of inertia of a mechanical structure around the Gs axis of the structure
$I_{G_x\|Cross}$	:	Moment of inertia of a mechanical structure around the Gx axis of the cross structure
I_{O_x}	:	Moment of inertia of a mechanical structure around the Ox axis
I_{O_z}	:	Moment of inertia of a mechanical structure around the Oz axis
I_{G_Δ}	:	Moment of inertia of a mechanical structure around the GΔ axis
I_{Cor}	:	Current in the corrector
I_{Cor}^{off}	:	Particular current of the corrector for which
	:	the electron beam is going through the magnetic axis of the quadrupole
I_{max}	:	Maximum current
I_{nom}	:	Nominal current
I_{Quad}	:	Current in the created pseudo-quadrupole
I_0	:	Reference current
$I_faisceau$	:	Total current of the electron beam
$\overrightarrow{J}$	:	Electric current density

K	:	Focusing function replacing k_x or k_z
$K(s)$	:	Focusing function giving the focusing strength distribution along the machine
$K_n^{N/S}$	:	s-integrated value of $k_{nm}(s)$
$\overrightarrow{M}$	:	Punctual magnetic moment
M_t	:	Torsion momentum
N_a	:	Number of dipole magnet
N_{BPM}	:	Number of BPMs
N_{ph}	:	Number of photons radiated
P_{ray}	:	Radiated power as synchrotron radiation
P_{ray}^e	:	Radiated power as synchrotron radiation by the electron
P_{ray}^p	:	Radiated power as synchrotron radiation by the proton
S	:	Sextupole strength
S_s	:	Section of the studied structure
$\overline{V}$	:	Complex Scalar Potential
Vol	:	Volume
b	:	Structure width
c	:	Speed of the light
d	:	Distance
$d\mathcal{A}$	:	Area unit
$d\Omega$	:	Solid angle unit
e	:	in the chapter 1: Electron charge
e	:	in the chapter 3: Structure width
f	:	Focal length
f_1	:	Focal length of the lens number 1
f_2	:	Focal length of the lens number 2
f_{Tot}	:	Focal length of the equivalent total lens
h	:	Structure height
g	:	Quadrupole gradient
$g_x^i(s), g_z^i(s)$	:	longitudinal functions describing the transverse shape of the measuring coil along the contour $\mathcal{C}_i$
$h_x^i\theta, s, h_z^i(\theta, s)$	:	functions $g_x^i(s)$ and $g_z^i(s)$ rotated by a tilt angle θ
k	:	Focusing strength
k_x	:	Horizontal focusing function
k_z	:	Vertical focusing function
$k_{nm}(s)$	:	Functions giving the longitudinal dependence of the magnetic field
l	:	Length
m_p	:	Mass of a particle
m_{p0}	:	Mass at rest of a particle
m_e	:	Mass at rest of electrons
m_{pr}	:	Mass at rest of protons
m_s	:	Mass of the sensor
off_{calc}	:	Calculated offset of BPMs
p	:	Particle momentum
p_0	:	Nominal particle momentum
q	:	Charge of the particle
r_0	:	Reference radius for the magnetic field harmonic calculation
s	:	s curvilinear coordinate

t	:	Time Variable
v	:	Particle velocity
x	:	Horizontal position of a particle
x'	:	First order curvilinear derivative of x
x''	:	Second order curvilinear derivative of x
$x_\beta(s)$	:	Solution of the Hill's equation
$x_\eta(s)$	:	Particular solution of the trajectory equation when $\Delta p/p_0 \neq 0$
y	:	Variable replacing x or z
z	:	Vertical position of a particle
z'	:	First order curvilinear derivative of z
z''	:	Second order curvilinear derivative of z
$\mathcal{A}_n$	:	Skew components of integrated magnetic flux density
$\mathcal{B}_n$	:	Normal components of integrated magnetic flux density
$\mathcal{B}$	:	Brilliance of a photon beam
$\mathcal{C}$	:	Contour of the measuring coil
$\mathcal{C}_i$	:	Contour i of the measuring coil
$\mathcal{E}$	:	Total Energy of a particle
$\mathcal{E}_0$	:	Energy at rest of a particle
$\mathcal{E}_{cm}$	:	Energy at the mass center
$\mathcal{E}_{cm}^{fixe}$	:	Energy at the mass center for a particle/fixed wall collision
$\mathcal{E}_{cm}^{coll.}$	:	Energy at the mass center for a particle/particle collision
$\mathcal{E}_k$	:	kinetic Energy of a particle
∇	:	Nabla operator
∇^2	:	Laplacian operator
β	:	Beta function
β_x	:	Horizontal Beta function
β_y	:	Beta function replacing β_x or β_z
β_z	:	Vertical Beta function
β_r	:	Reduced Velocity
γ_r	:	Reduced Energy
Δg	:	Constant quadrupole gradient variation
ΔB_{Cor}	:	Constant variation of the corrector magnetic flux
$\Delta_{Mag\,Bpm}$	:	Offset between the quadrupole magnetic axis and the BPM electrical axis
ΔS	:	Variation of the sextupole strength
Δy^{Mech}	:	Mechanical displacement of sextupole
$\Delta\overline{\zeta}^{Quad}$	:	Magnetic offset of the quadrupole axis
$\Delta\overline{\zeta}^{Sext}$	:	Magnetic offset of the sextupole axis
$\Delta_{p-p}gradient$	:	Peak-peak difference of the quadrupole gradient
$\Delta_{p-p}harm$	:	Peak-peak difference of harmonics
$\Delta_{p-p}x$	:	Peak-peak difference of magnetic axis location along the x axis
$\Delta_{p-p}z$	:	Peak-peak difference of magnetic axis location along the z axis
$\Delta_{p-p}\theta_s$	:	Peak-peak difference of magnetic field orientation around the s axis
Δx_{coils}	:	Magnetic axis offset along the x axis due to the measuring coil defects
Δz_{coils}	:	Magnetic axis offset along the z axis due to the measuring coil defects
$\overline{\Delta\zeta_{Meas}}$	:	Measured complex magnetic offset of the multipole magnetic axis
$\overline{\Delta\zeta_{Meas-kx}}$	:	Measured complex magnetic offset of the multipole tool magnetic axis on the position k and on the face X

$\Delta Mech_j, \Delta Mech_l$	:	Displacement of the tool magnetic axis due to a defect on the contact faces, respectevely j and l
$\overline{\Delta\zeta_{Mp}}$	:	Exact complex magnetic offset of the multipole magnetic axis
$\overline{\Delta\zeta_{Tool}}$	:	Complex magnetic offset on the multipole magnetic axis measurement due to the tool defects
$\overline{\Delta\zeta_{Tool\,k}}$	:	Complex magnetic offset on the multipole magnetic axis measurement due to the tool defects on the position k
ϵ	:	Emittance
ϵ_x	:	Horizontal Emittance
ϵ_z	:	Vertical Emittance
$\overline{\zeta}$	:	Complex variable
$\overline{\zeta^{\mathsf{off}}}$	:	Complex location of the magnetic axis
η	:	Dispersion function
η'	:	First order curvilinear derivative of the dispersion function
θ	:	geometrical angle
θ_coils	:	Magnetic field tilt angle offset around the s axis due to the measuring coil defects
θ_m	:	Tilt angle of the n harmonic
θ_{Meas}	:	Measured tilt angle of the main harmonic component
θ_{Mp}	:	Exact tilt angle of the multipole main harmonic component
θ_{Sensor}	:	Error on tilt angle of the main harmonic component due to sensor defects
$\theta Tors.$	:	Torsion angle
μ_0	:	Vacuum permeability
μ_H	:	Hall mobility
ν	:	Tune Number
ν_x	:	Horizontal Tune Number
ν_y	:	Tune Number replacing ν_x or ν_z
ν_z	:	Vertical Tune Number
φ	:	Phase of a particle
φ'	:	First curvilear derivative of the particle phase
ϕ	:	Scalar Potential
Φ	:	Integrated scalar Potential
$\overline{\chi_n}$	:	Complex integrated harmonic coefficient
ψ	:	Magnetic Flux
$\overline{Psi}$	:	Complex magnetic flux harmonics
ρ	:	Curvature Radius
(x, z, s)	:	Cartesian coordinates
(r, θ, s)	:	Cylindrical coordinates
$\mathcal{R}e\ [\,]$	:	Real part of
$\Im m\ [\,]$	:	Imaginary part of

List of Figures

1.1 Générateur Van de Graaf . . . 15
1.2 Structure accélératrice de Wideröe . . . 15
1.3 structure d'Alvarez . . . 16
1.4 Principe du cyclotron . . . 17
1.5 Dipôle en C . . . 19
1.6 Dipôle en E . . . 19
1.7 Quadrupôle . . . 19
1.8 Lignes de lumières de SOLEIL . . . 22
1.9 Espace libre . . . 23
1.10 Dipôle : vue de face . . . 23
1.11 Dipôle : vue de dessus . . . 23
1.12 Quadrupôle focalisant dans le plan horizontal pour un faisceau d'électrons . . . 24
1.13 Lentille mince . . . 25
1.14 Coordonnées cylindriques . . . 26
1.15 Emittance . . . 27
1.16 Décomposition de l'anneau de stockage . . . 29
1.17 Rôle de la métrologie . . . 30
1.18 Plage d'utilisation des capteurs ($1\,Gauss = 1 \cdot 10^{-4}\,T$) [11] . . . 31
1.19 Effet Hall . . . 32
1.20 Boîtier 15 sondes de Hall . . . 34
1.21 Exemple de cartographie . . . 34
1.22 Radiale . . . 37
1.23 Tangentielle . . . 37
1.24 Multipolaire . . . 37

2.1 Frame . . . 40
2.2 Rectangular coil filament location . . . 43
2.3 Magnetic tilt angle . . . 45
2.4 View of an out of shape coil and the four projected segments . . . 47
2.5 Mechanical torsion of coil . . . 49
2.6 Mechanical sag of coil . . . 50
2.7 Punctual magnetic Dipole . . . 51
2.8 Mathematica code process . . . 52
2.9 Coil rotation . . . 52
2.10 Measured flux . . . 52
2.11 Natural Harmonics of the 3D model . . . 53
2.12 Vectorial representation of offset axis: Ideal case . . . 55
2.13 Vectorial representation of offset axis: sensor default . . . 56

2.14 Vectorial representation of offset axis: Tool default . . . 57
2.15 Octagonal mechanical interface . . . 58
2.16 Stand of the reference tools . . . 59
2.17 Influence of θ_{Sensor} value . . . 61
2.18 Machining defects . . . 62
2.19 Angular defects . . . 62
2.20 Machining defects . . . 63
2.21 Angular defects . . . 63
2.22 Offsets determination with the new method . . . 64

3.1 General kinematic scheme . . . 66
3.2 Initial Bench Design . . . 70
3.3 The TestPoint user interface for the SMB . . . 71
3.4 SMB synoptic scheme . . . 72
3.5 Bronze bearing alignment . . . 72
3.6 Rolling phenomenon . . . 73
3.7 Sensitive coils . . . 74
3.8 Cut view of printed circuit . . . 74
3.9 Skew sextupole component (10^{-4} of $\mathcal{B}_2$) . . . 75
3.10 Preliminary measurements:horizontal offset (μm) . . . 75
3.11 Preliminary measurements:angular offset ($mrad$) . . . 76
3.12 Assumptions . . . 77
3.13 Half cylinder . . . 77
3.14 Curves . . . 78
3.15 Kinetic chain of the bench . . . 79
3.16 “V”/cylinder interface . . . 80
3.17 Rectangular cross section . . . 80
3.18 Cross shaped structure . . . 81
3.19 Halves cylinders . . . 82
3.20 Detailed view of the sensor mechanical structure . . . 83
3.21 Assembling tool . . . 83
3.22 Aluminum Tips . . . 84
3.23 Glue Drying Process . . . 84
3.24 Bubble Level . . . 85
3.25 Line/Dot/Plane Principle . . . 85
3.26 Real Line/Dot/Plane interface and its adapted bubble level . . . 85
3.27 Interface . . . 86
3.28 Line/Dot/Plane . . . 86
3.29 The grasshopper . . . 86
3.30 The SOLEIL Multipolar Magnetic Measurement Bench . . . 87
3.31 Magnetic measurement protocol . . . 87
3.32 Positioning Pins . . . 88
3.33 Magnetic Axis Tuning . . . 89
3.34 Arm Lever: rectangular wedges . . . 90
3.35 Arm Lever: cylindrical wedges . . . 90
3.36 Sag determination experiment . . . 92
3.37 Vertical displacements of the sensor . . . 93
3.38 Displacements of the reference quadrupole magnetic axis . . . 93

3.39 Prototype quadrupole and a removable chamfer . . . 95
3.40 Variation of the 12-pole harmonic component versus the chamfer depth at 250A . 96
3.41 $\mathcal{B}_6$ for short quadrupoles . . . 96
3.42 $\mathcal{B}_6$ for long quadrupoles . . . 96
3.43 Magnetic forces effect versus the current . . . 97
3.44 "Poor" Current Cycling Scheme . . . 97
3.45 "Rich" Current Cycling Scheme . . . 97
3.46 Hysteresis Curve . . . 98
3.47 Comparison: Poor and Rich cycling schemes . . . 99
3.48 Magnetic field drift versus current variations . . . 99
3.49 Quadrupole and sextupole on the SMB . . . 100
3.50 Short Quadrupole . . . 100
3.51 Long Quadrupole . . . 100
3.52 12-pole:Short Quadrupole . . . 102
3.53 12-pole:Long Quadrupole . . . 102
3.54 20-pole:Short Quadrupole . . . 103
3.55 20-pole:Long Quadrupole . . . 103
3.56 28-pole:Short Quadrupole . . . 103
3.57 28-pole:Long Quadrupole . . . 103
3.58 8-pole: Short Quadrupole . . . 103
3.59 8-pole: Long Quadrupole . . . 103
3.60 Quadrupole Parameters . . . 104
3.61 a < b . . . 104
3.62 a > b . . . 104
3.63 Flower for a short quadrupole . . . 105
3.64 Flower for a long quadrupole . . . 105
3.65 Quadrupole + 5.10^{-4} of $\mathcal{A}_3$ . . . 105
3.66 Quadrupole + 5.10^{-4} of $\mathcal{B}_4$ . . . 105
3.67 Quadrupole + 5.10^{-4} of $\mathcal{B}_6$ . . . 106
3.68 Quadrupole + 5.10^{-4} of $\mathcal{A}_6$ . . . 106
3.69 Evolution versus the current . . . 107
3.70 Game of rectangular wedges . . . 107
3.71 Game of cylindrical wedges . . . 107
3.72 Transverse offsets tuning . . . 108
3.73 Transverse offsets tuning of the 160 quadrupoles . . . 109
3.74 Tilt angle: before tuning . . . 109
3.75 Tilt angle: after tuning . . . 109
3.76 The first three turns in the Storage Ring . . . 110
3.77 Best orbit after correction . . . 110

4.1 Alignment Offset . . . 114
4.2 Effect of a quadrupole misalignment . . . 115
4.3 Beam orbit displacements . . . 116
4.4 Merit function and BPM_i response . . . 117
4.5 Error with an angle on the beam . . . 117
4.6 Four corrector bump . . . 118
4.7 Pure four corrector bump . . . 119
4.8 K-modulation . . . 119

4.9 Cells description . . . 122
4.10 SOLEIL Storage Ring beta functions and dispersion function . . . 122
4.11 Additional corrector coils on the sextupole magnetic circuit . . . 123
4.12 Simplified command and control architecture . . . 124
4.13 BBA process . . . 125
4.14 Beam Based Alignment graphical user interface . . . 127
4.15 Horizontal offsets along the SR . . . 127
4.16 Horizontal offsets histogram . . . 127
4.17 Vertical offsets along the SR . . . 128
4.18 Vertical offsets histogram . . . 128
4.19 One BPM between 2 quadrupoles . . . 128
4.20 Horizontal orbit after the first application of BBA offsets:first correction . . . 128
4.21 Horizontal orbit after application of BBA offsets: best correction . . . 129
4.22 Vertical orbit and corrector values before application of BBA offsets . . . 129
4.23 Vertical orbit and corrector values after application of BBA offsets . . . 130
4.24 Effect of an initial dipolar component on a quadrupole magnetic axis measurement 131
4.25 Effect of an additional quadrupolar component on a sextupole magnetic axis measurement . . . 132
4.26 First reliable sextupole BBA . . . 133

B.1 Assembling steps . . . 160

C.1 Arm Lever . . . 161
C.2 Arm Lever . . . 163
C.3 SMB graphical user interface before magnetic axis tuning . . . 165
C.4 SMB graphical user interface after magnetic axis tuning . . . 165

D.1 128 Magnetic flowers . . . 168

E.1 π bump . . . 169

Appendix A

Reference measurement

A.1 Measurements relations

⋆ "A" face case:

$$\begin{cases} \overline{\Delta\zeta_{Meas-1A}} = \overline{\Delta\zeta_{Qp}} + \overline{\Delta\zeta_{coils}} = \Delta x_{Qp} + i\Delta z_{Qp} + \overline{\Delta\zeta_{coils}} \\ \overline{\Delta\zeta_{Meas-2A}} = \overline{\Delta\zeta_{Qp}\, e^{i\frac{\pi}{4}}} + \overline{\Delta\zeta_{coils}} \\ \overline{\Delta\zeta_{Meas-3A}} = \overline{i\Delta\zeta_{Qp}} + \overline{\Delta\zeta_{coils}} = -\Delta z_{Qp} + i\Delta x_{Qp} + \overline{\Delta\zeta_{coils}} \\ \overline{\Delta\zeta_{Meas-4A}} = \overline{\Delta\zeta_{Qp}\, e^{i\frac{3\pi}{4}}} + \overline{\Delta\zeta_{coils}} \\ \overline{\Delta\zeta_{Meas-5A}} = \overline{-\Delta\zeta_{Qp}} + \overline{\Delta\zeta_{coils}} = -\Delta x_{Qp} - i\Delta z_{Qp} + \overline{\Delta\zeta_{coils}} \\ \overline{\Delta\zeta_{Meas-6A}} = \overline{\Delta\zeta_{Qp}\, e^{i\frac{5\pi}{4}}} + \overline{\Delta\zeta_{coils}} \\ \overline{\Delta\zeta_{Meas-7A}} = \overline{-i\Delta\zeta_{Qp}} + \overline{\Delta\zeta_{coils}} = \Delta z_{Qp} - i\Delta x_{Qp} + \overline{\Delta\zeta_{coils}} \\ \overline{\Delta\zeta_{Meas-8A}} = \overline{\Delta\zeta_{Qp}\, e^{i\frac{7\pi}{4}}} + \overline{\Delta\zeta_{coils}} \end{cases} \tag{A.1}$$

⋆ "B" face case:

$$\begin{cases} \overline{\Delta\zeta_{Meas-1B}} = \overline{-\Delta\zeta_{Qp}^{*}} + \overline{\Delta\zeta_{coils}} \\ \overline{\Delta\zeta_{Meas-2B}} = \overline{\Delta\zeta_{Qp}^{*}\, e^{i\frac{-\pi}{4}}} + \overline{\Delta\zeta_{coils}} \\ \overline{\Delta\zeta_{Meas-3B}} = \overline{i\Delta\zeta_{Qp}^{*}} + \overline{\Delta\zeta_{coils}} \\ \overline{\Delta\zeta_{Meas-4B}} = \overline{\Delta\zeta_{Qp}^{*}\, e^{i\frac{-3\pi}{4}}} + \overline{\Delta\zeta_{coils}} \\ \overline{\Delta\zeta_{Meas-5B}} = \overline{-\Delta\zeta_{Qp}^{*}} + \overline{\Delta\zeta_{coils}} \\ \overline{\Delta\zeta_{Meas-6B}} = \overline{\Delta\zeta_{Qp}^{*}\, e^{i\frac{-5\pi}{4}}} + \overline{\Delta\zeta_{coils}} \\ \overline{\Delta\zeta_{Meas-7B}} = \overline{-i\Delta\zeta_{Qp}^{*}} + \overline{\Delta\zeta_{coils}} \\ \overline{\Delta\zeta_{Meas-8B}} = \overline{\Delta\zeta_{Qp}^{*}\, e^{i\frac{-7\pi}{4}}} + \overline{\Delta\zeta_{coils}} \end{cases} \tag{A.2}$$

A.2 Mechanical defects relations

face measured: "A"	
facet	mechanical default
1	$\overline{\Delta\zeta_{Mech-35}}$
2	$\overline{\Delta\zeta_{Mech-46}}$
3	$\overline{\Delta\zeta_{Mech-57}}$
4	$\overline{\Delta\zeta_{Mech-68}}$
5	$\overline{\Delta\zeta_{Mech-71}}$
6	$\overline{\Delta\zeta_{Mech-82}}$
7	$\overline{\Delta\zeta_{Mech-13}}$
8	$\overline{\Delta\zeta_{Mech-24}}$

face measured: "B"	
facet	mechanical default
1	$\overline{\Delta\zeta_{Mech-75}} = -\imath\overline{\Delta\zeta_{Mech-35}}^{*}$
2	$\overline{\Delta\zeta_{Mech-86}} = -\imath\overline{\Delta\zeta_{Mech-46}}^{*}$
3	$\overline{\Delta\zeta_{Mech-17}} = -\imath\overline{\Delta\zeta_{Mech-57}}^{*}$
4	$\overline{\Delta\zeta_{Mech-28}} = -\imath\overline{\Delta\zeta_{Mech-68}}^{*}$
5	$\overline{\Delta\zeta_{Mech-31}} = -\imath\overline{\Delta\zeta_{Mech-71}}^{*}$
6	$\overline{\Delta\zeta_{Mech-42}} = -\imath\overline{\Delta\zeta_{Mech-82}}^{*}$
7	$\overline{\Delta\zeta_{Mech-53}} = -\imath\overline{\Delta\zeta_{Mech-13}}^{*}$
8	$\overline{\Delta\zeta_{Mech-64}} = -\imath\overline{\Delta\zeta_{Mech-24}}^{*}$

Table A.1: Reference tool mechanical defaults

A.3 Integrated Magnetic flux density components

Hence the integrated magnetic flux density components are:

$$\mathsf{B}_r(r,\theta) = \frac{1}{r_0}\sum_{n=0}^{\infty}(n)\left(\frac{r}{r_0}\right)^{n-1}\left(-K_n^S cos(n\theta) + K_n^N sin(n\theta)\right) \tag{A.3a}$$

$$\mathsf{B}_\theta(r,\theta) = \frac{1}{r_0}\sum_{n=0}^{\infty}(n)\left(\frac{r}{r_0}\right)^{n-1}\left(K_n^N cos(n\theta) + K_n^S sin(n\theta)\right) \tag{A.3b}$$

$$\mathsf{B}_z(r,\theta) = 0 \tag{A.3c}$$

The study of the magnetic flux density reduces to two dimensions problem. Consequently, it would be advantageous to use complex formalism to pursue the calculations. In cartesian coordinates, magnetic flux density is similar as in equation A.3

$$\mathsf{B}_x(r,\theta) = \frac{1}{r_0}\sum_{n=0}^{\infty}(n)\left(\frac{r}{r_0}\right)^{n-1}\left(-K_n^S cos(n\theta) + K_n^N sin(n\theta)\right) \tag{A.4a}$$

$$\mathsf{B}_s(r,\theta) = \frac{1}{r_0}\sum_{n=0}^{\infty}(n)\left(\frac{r}{r_0}\right)^{n-1}\left(K_n^N cos(n\theta) + K_n^S sin(n\theta)\right) \tag{A.4b}$$

$$\mathsf{B}_z(r,\theta) = 0 \tag{A.4c}$$

A.4 Feed-down formula demonstration

R_M is the sensor mechanical frame

R_A is the quadrupole magnet magnetic frame

The magnetic axis measured by the sensor can be define as following:

$\overline{\zeta}_A = \overline{\zeta}_M - \overline{\zeta}_d$, ζ_d is the measured offset.

Here is the complex integrated magnetic flux density:

$$\overline{\mathbb{B}} = i\overline{\mathsf{B}}^* = \mathsf{B}_z + i\mathsf{B}_x = \sum_{n=1}^{\infty} \overline{\mathbb{C}}_n^M \left(\frac{\overline{\zeta_M}}{r_0}\right)^{n-1} \tag{A.5}$$

$$= \mathsf{B}_z + i\mathsf{B}_x = \sum_{n=1}^{\infty} \frac{\overline{\mathbb{C}}_n^M}{r_0^{n-1}} \left(\overline{\zeta_A} + \overline{\zeta_d}\right)^{n-1} \tag{A.6}$$

Then following formula is used:

$$(a+b)^n = \sum_{k=0}^{n} \mathcal{C}_n^k \, a^k \, b^{n-k} \qquad \text{with } \mathcal{C}_n^k = \frac{n!}{k!(n-k)!} \tag{A.7}$$

$$= \sum_{n=1}^{\infty} \frac{\overline{\mathbb{C}}_n^M}{r_0^{n-1}} \sum_{k=0}^{n-1} \mathcal{C}_{n-1}^k \, \overline{\zeta_A}^{n-1-k} \, \overline{\zeta_d}^{k} \tag{A.8}$$

we set $p = n - k$ with $n \in [1, \infty[$ et $k \in [0, n-1]$ thus

$p = n - k \in [1, n]$ hence

$$= \sum_{n=1}^{\infty} \frac{\overline{\mathbb{C}}_n^M}{r_0^{n-1}} \sum_{p=1}^{n} \mathcal{C}_{n-1}^{n-p} \, \overline{\zeta_A}^{p-1} \, \overline{\zeta_d}^{n-p} \tag{A.9}$$

Now, the following property of binomial cefficients must be taken into account: $\mathcal{C}_n^k = 0$ si $k < 0$. It enables us to sum "p" from 1 to infinity.

$$= \sum_{n=1}^{\infty} \frac{\overline{\mathbb{C}}_n^M}{r_0^{n-1}} \sum_{p=1}^{\infty} \mathcal{C}_{n-1}^{n-p} \, \overline{\zeta_A}^{p-1} \, \overline{\zeta_d}^{n-p} \tag{A.10}$$

Then, using the same property, n-p must be positive thus n must be superior to p. We can deduce that the smaller bound of the n sum is limited to p:

$$= \sum_{p=1}^{\infty} \sum_{n=p}^{\infty} \frac{\overline{\mathbb{C}}_n^M}{r_0^{n-1}} \, \mathcal{C}_{n-1}^{n-p} \, \overline{\zeta_A}^{p-1} \, \overline{\zeta_d}^{n-p} \tag{A.11}$$

Indices variable are changed to obtain the same as in this thesis:

n -> k

p -> n

$$= \sum_{n=1}^{\infty} \sum_{k=n}^{\infty} \frac{\overline{\mathbb{C}}_k^M}{r_0^{k-1}} \, \mathcal{C}_{k-1}^{k-n} \, \overline{\zeta_A}^{n-1} \, \overline{\zeta_d}^{k-n}$$

We recall the known form of the complex flux density: $\overline{B_M}(\overline{\zeta_A}) = \sum_{n=1}^{\infty} \overline{\mathbb{C}}_n^A \left(\frac{\overline{\zeta_A}}{r_0}\right)^{n-1}$

$$= \sum_{n=1}^{\infty} \left(\frac{\overline{\zeta_A}}{r_0}\right)^{n-1} \sum_{k=n}^{\infty} \frac{\overline{\mathbb{C}}_k^M}{r_0}^{k-1-(n-1)} \mathcal{C}_{k-1}^{k-n}\, \overline{\zeta_d}^{k-n} \tag{A.12}$$

$$= \sum_{n=1}^{\infty} \left(\frac{\overline{\zeta_A}}{r_0}\right)^{n-1} \sum_{k=n}^{\infty} \overline{\mathbb{C}}_k^M\, \mathcal{C}_{k-1}^{k-n} \left(\frac{\overline{\zeta_d}}{r_0}\right)^{k-n} \tag{A.13}$$

And finally, the harmonic coefficient in the quadrupole magnetic frame are:

$$\overline{\mathbb{C}}_n^A = \sum_{k=n}^{\infty} \overline{\mathbb{C}}_k^M\, \mathcal{C}_{k-1}^{k-n} \left(\frac{\overline{\zeta_d}}{r_0}\right)^{k-n} \tag{A.14}$$

$$= \sum_{k=n}^{\infty} \overline{\mathbb{C}}_k^M\, \frac{(k-1)!}{(k-n)!(k-1-k+n)!} \left(\frac{\overline{\zeta_d}}{r_0}\right)^{k-n} \tag{A.15}$$

$$= \sum_{k=n}^{\infty} \overline{\mathbb{C}}_k^M\, \frac{(k-1)!}{(k-n)!(n-1)!} \left(\frac{\overline{\zeta_d}}{r_0}\right)^{k-n} \tag{A.16}$$

A.5 Some Machine Physics formulas

μ is the phase advance per cell.

$$\mu = \frac{Tr(M)}{2} \tag{A.17}$$

$$\beta = \frac{b}{sin\,\mu} > 0 \tag{A.18}$$

$$\alpha = \frac{a-d}{2\,sin\,\mu} \tag{A.19}$$

$$\gamma = -\frac{c}{sin\,\mu} \tag{A.20}$$

$$M_F = \begin{pmatrix} cos(l\sqrt{k}) & (1/\sqrt{k})\, sin(l\sqrt{k}) \\ -\sqrt{k}\, sin(l\sqrt{k}) & cos(l\sqrt{k}) \end{pmatrix} \tag{A.21}$$

$$M_D = \begin{pmatrix} cosh(l\sqrt{k}) & (1/\sqrt{k})\, sinh(l\sqrt{k}) \\ \sqrt{k}\, sinh(l\sqrt{k}) & cosh(l\sqrt{k}) \end{pmatrix} \tag{A.22}$$

$$\begin{cases} \overrightarrow{OP_\alpha^1} = x_2\, cos\alpha\, \overrightarrow{e_x} + (0 + x_2\, sin\alpha)\overrightarrow{e_z} + s\, \overrightarrow{e_s} \\ \overrightarrow{OP_\alpha^2} = x\, cos\alpha\, \overrightarrow{e_x} + (0 + x\, sin\alpha)\overrightarrow{e_z} + s_2\, \overrightarrow{e_s} \\ \overrightarrow{OP_\alpha^3} = x_1\, cos\alpha\, \overrightarrow{e_x} + (0 + x_1\, sin\alpha)\overrightarrow{e_z} + s\, \overrightarrow{e_s} \\ \overrightarrow{OP_\alpha^4} = x\, cos\alpha\, \overrightarrow{e_x} + (0 + x\, sin\alpha)\overrightarrow{e_z} + s_1\, \overrightarrow{e_s} \end{cases} \quad \begin{cases} \overrightarrow{dl_{\alpha_0}^1} = ds\, \overrightarrow{e_s} \\ \overrightarrow{dl_{\alpha_0}^2} = -dx\, \overrightarrow{e_x} \\ \overrightarrow{dl_{\alpha_0}^3} = -ds\, \overrightarrow{e_s} \\ \overrightarrow{dl_{\alpha_0}^4} = dx\, \overrightarrow{e_x} \end{cases} \tag{A.23}$$

Appendix B

Sensor Assembly

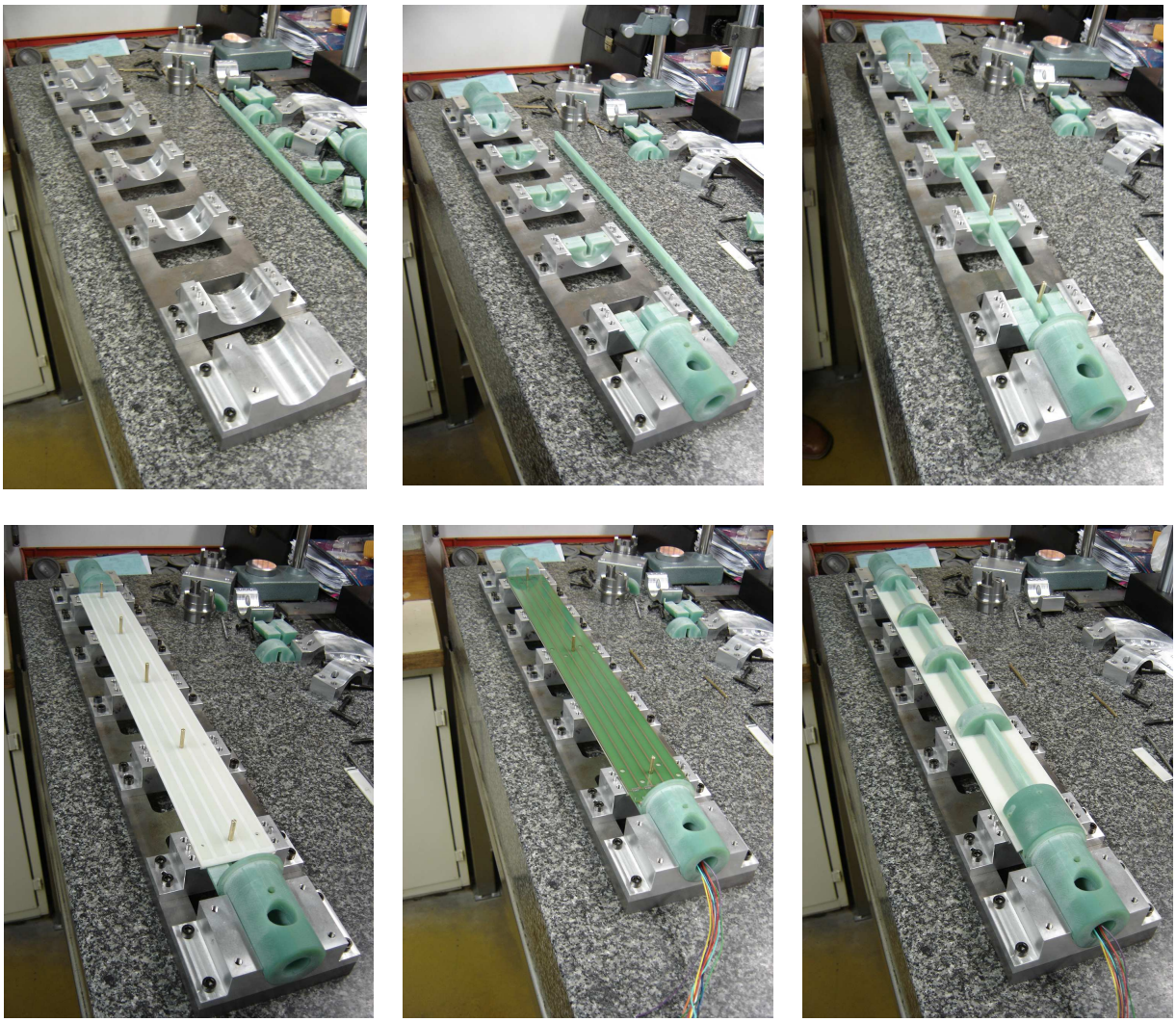



Figure B.1: Assembling steps

Appendix C

Wedges Calculation

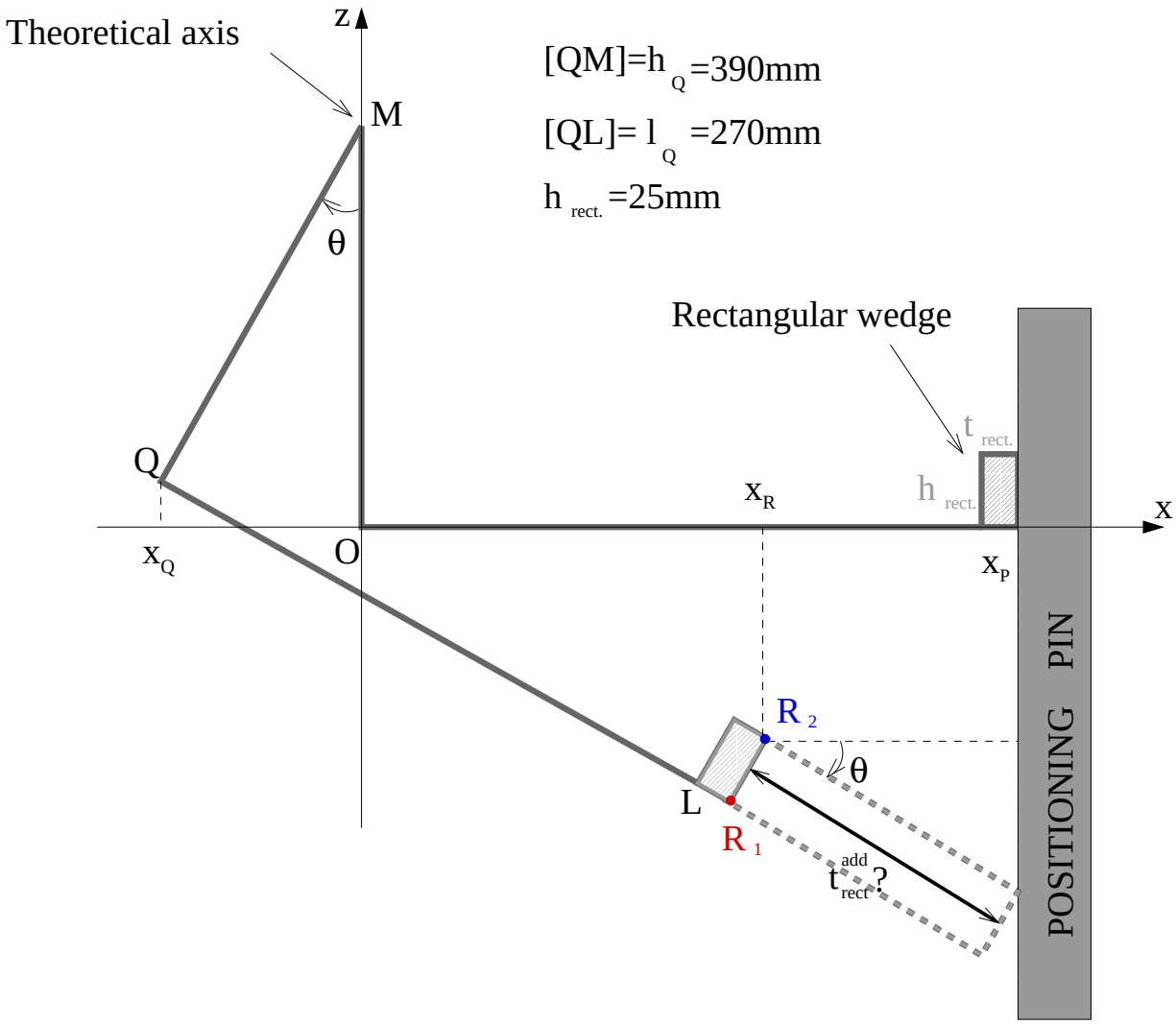

Figure C.1: Arm Lever

$$x_Q = h_Q \, sin\theta \tag{C.1}$$
$$z_Q = h_Q(1 - cos\theta) \tag{C.2}$$

$$x_L = x_Q + l_Q cos\theta \tag{C.3}$$
$$z_L = z_Q + l_Q sin\theta \tag{C.4}$$

C.1 Effect on the rectangular wedge

Coordinates of R_i are obtained by replacing l_Q by $l_Q + t_{rect.}$. Then if θ is negative, h_Q must be replaced by $h_Q - h_{rect.}$.

$$x_{Ri} = \left(h_Q + h_{rect}\frac{sign(\theta) - 1}{2}\right) sin\theta + (l_Q + t_{rect})cos\theta \tag{C.5}$$
$$z_{Ri} = \left(h_Q + h_{rect}\frac{sign(\theta) - 1}{2}\right) (1 - cos\theta) + (l_Q + t_{rect})sin\theta \tag{C.6}$$

with the function $sign\theta$ returning 1 when $\theta > 0$ and -1 for $\theta < 0$.
Hence the thickness to add to the rectangular wedge.

$$t^{add}_{rect.} \, cos\theta = x_P - x_{Ri} \tag{C.7}$$
$$= x_P - \left(\left(h_Q + h_{rect}\frac{sign(\theta) - 1}{2}\right) sin\theta + (l_Q + t_{rect})cos\theta\right) \tag{C.8}$$
$$\tag{C.9}$$

since θ is very small (few 1/10 of mrad), $cos\theta \approx 1$ and $sin\theta \approx \theta$ Hence

$$t^{add}_{rect.} = x_P - \left(\left(h_Q + h_{rect}\frac{sign(\theta) - 1}{2}\right)\theta + l_Q + t_{rect}\right) \tag{C.10}$$

Then the new thickness of the rectangular wedge that takes into account positioning and angular offsets of the magnetic axis is:

$$t^{new}_{rect} = t^{init}_{rect} - x_{\mathsf{off}} + t^{add}_{rect} \tag{C.11}$$

With t^{init}_{rect} the initial wedge thickness of the measured magnet, x_{off} the value of the magnetic axis position along the x direction.

C.2 Effect on cylindrical wedges

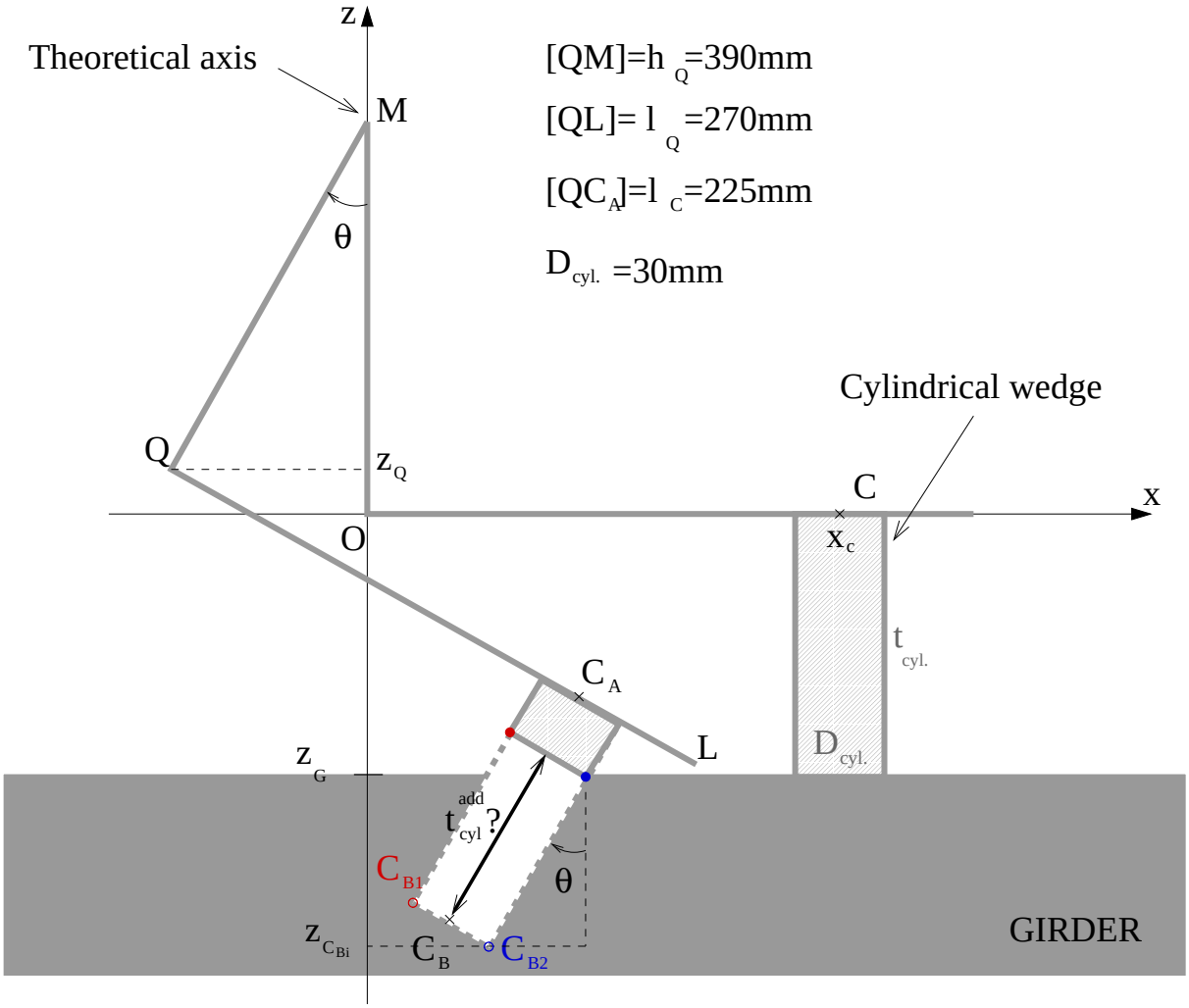

Figure C.2: Arm Lever

$$x_{CB} = x_Q + l_C\, cos\theta \approx h_Q\, \theta + x_C \tag{C.12}$$
$$z_{CB} = -t_{cyl} + z_Q + l_C\, sin\theta \approx -t_{cyl} + x_C\, \theta \tag{C.13}$$

Coordinates of C_{B1} and C_{B2} are obtained by replacing x_C respectively by $x_C - D_{cyl.}/2$ and $x_C + D_{cyl.}/2$ and by replacing h_Q by $h_Q + t_{cyl.}$.

Using all these relations it is now possible to determine the thickness of the wedges necessary to correct both positionning and angular offset of the magnetic axis.

$$t^{add}_{cyl.}\, cos\theta = z_{CBi} - z_G \tag{C.14}$$
$$t^{add}_{cyl.} = -t_{cyl} + (x_C - sign(\theta) D_{cyl.}/2)\, \theta - z_G \tag{C.15}$$
$$= (x_C - sign(\theta) D_{cyl.}/2)\, \theta \tag{C.16}$$

C.3 Example of wedges calculation

The measured defects are:

$$x_{\text{off}} = 15\,\mu m \tag{C.17}$$
$$z_{\text{off}} = 32\,\mu m \tag{C.18}$$
$$\theta_{\text{off}} = -0.24\,mrad \tag{C.19}$$

The initial wedges are:

$$t_{rect\,0} = 5.025mm \tag{C.20}$$
$$t_{cyl\,0}^{right} = 10.03\,mm \qquad \text{located at x>0} \tag{C.21}$$
$$t_{cyl\,0}^{left} = 9.98\,mm \qquad \text{located at x<0} \tag{C.22}$$

The initial wedges must be mechanically measured before any magnetic axis tuning. If the wedges are not well measured, the calculation developed previously lead to erroneous thickness and tuning becomes difficult and long.

First the transverse offset are taken into account.

$$t_{rect\,1} = t^{rect\,0} - x_{\text{off}} = 5.01\,mm \tag{C.23}$$
$$t_{cyl\,1}^{right} = t_{right}^{cyl\,0} + z_{\text{off}} = 10.062\,mm \tag{C.24}$$
$$t_{cyl\,1}^{left} = t_{left}^{cyl\,0} + z_{\text{off}} = 10.03\,mm \tag{C.25}$$

Then the magnetic tilt angle θ_{off} is corrected.

$$t_{cyl.}^{right\,add} = (x_C^{right} + D_{cyl.}/2)\,\theta = (225 + 15) * (-0.24) = -57.6\,\mu m \tag{C.26}$$
$$t_{cyl.}^{left\,add} = (x_C^{left} + D_{cyl.}/2)\,\theta = (-225 + 15) * (-0.24) = 50.4\,\mu m \tag{C.27}$$

The values obtained for the cylindrical wedges show that it is important to take into account the point of contact of wedges ($\pm D_{cyl.}/2$). Indeed if $D_{cyl.}/2$ is not used, symmetrical values are obtained and a residual error remains.

Hence,

$$t_{cyl\,2}^{right} = t_{cyl\,1}^{right} + t_{cyl.}^{right\,add} = 10.062 - 0.058 = 10.004\,mm \tag{C.28}$$
$$t_{cyl\,2}^{left} = t_{cyl\,1}^{left} + t_{cyl.}^{left\,add} = 10.03 + 0.050 = 10.08\,mm \tag{C.29}$$

Correcting the tilt angle has displaced the magnetic center horizontally. That is why the rectangular wedge must also take it into account.

$$t_{rect.}^{add} = x_P - ((h_Q - h_{rect})\,\theta + l_Q + t_{rect\,0}) \tag{C.30}$$
$$= 275 - ((390 - 25) * (-0.24) + 270 + 5.025) = 87.6\,\mu m \tag{C.31}$$

Hence

$$t_{rect\,2} = t_{rect\,2} - t_{rect.}^{add} = 5.01 + 0.088 = 5.098\,mm \tag{C.32}$$

If the height of the rectangular wedge was not in the formula, it would have introduced an error of 5 μm.

C.4 Wedges calculation in the SMB measuring program

The magnetic axis characteristics are given by the yellow values at right corner of the interface. From these values, the thickness of wedges is proposed the three red red box on the left. When these boxes are red, it means that the magnetic axis does not fit the specifications (see figure C.3).

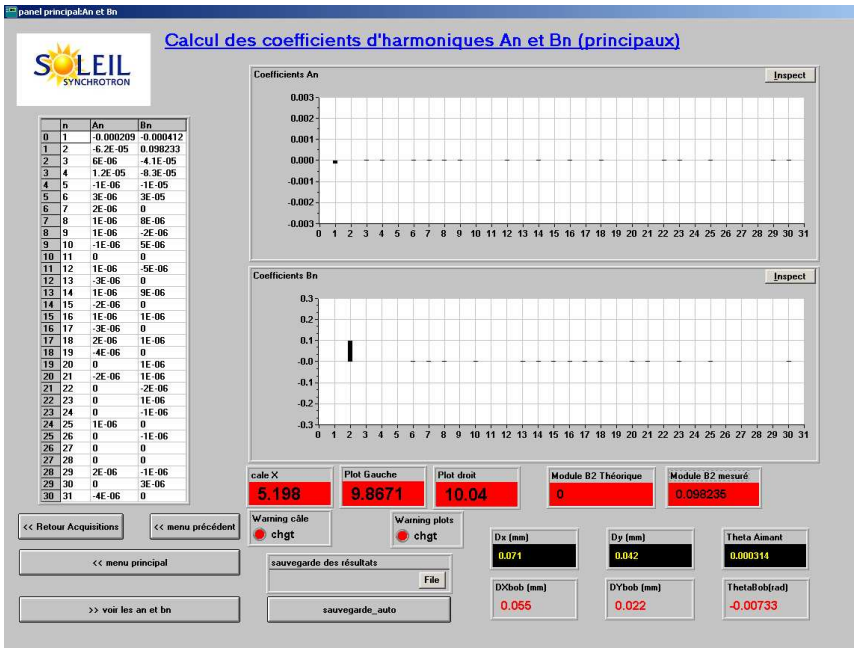

Figure C.3: SMB graphical user interface before magnetic axis tuning

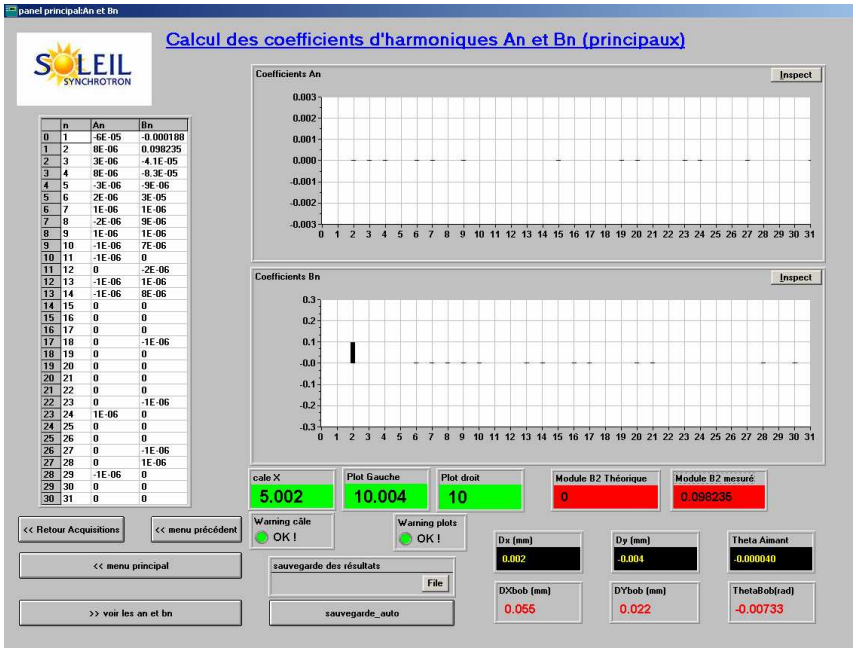

Figure C.4: SMB graphical user interface after magnetic axis tuning

Then after the wedges changing, the figure shows that the quadrupole has its magnetic axis properly tuned. Indeed, the three red boxes became green and the values of the magnetic axis properties are very small.

Appendix D

160 Magnetic Flowers

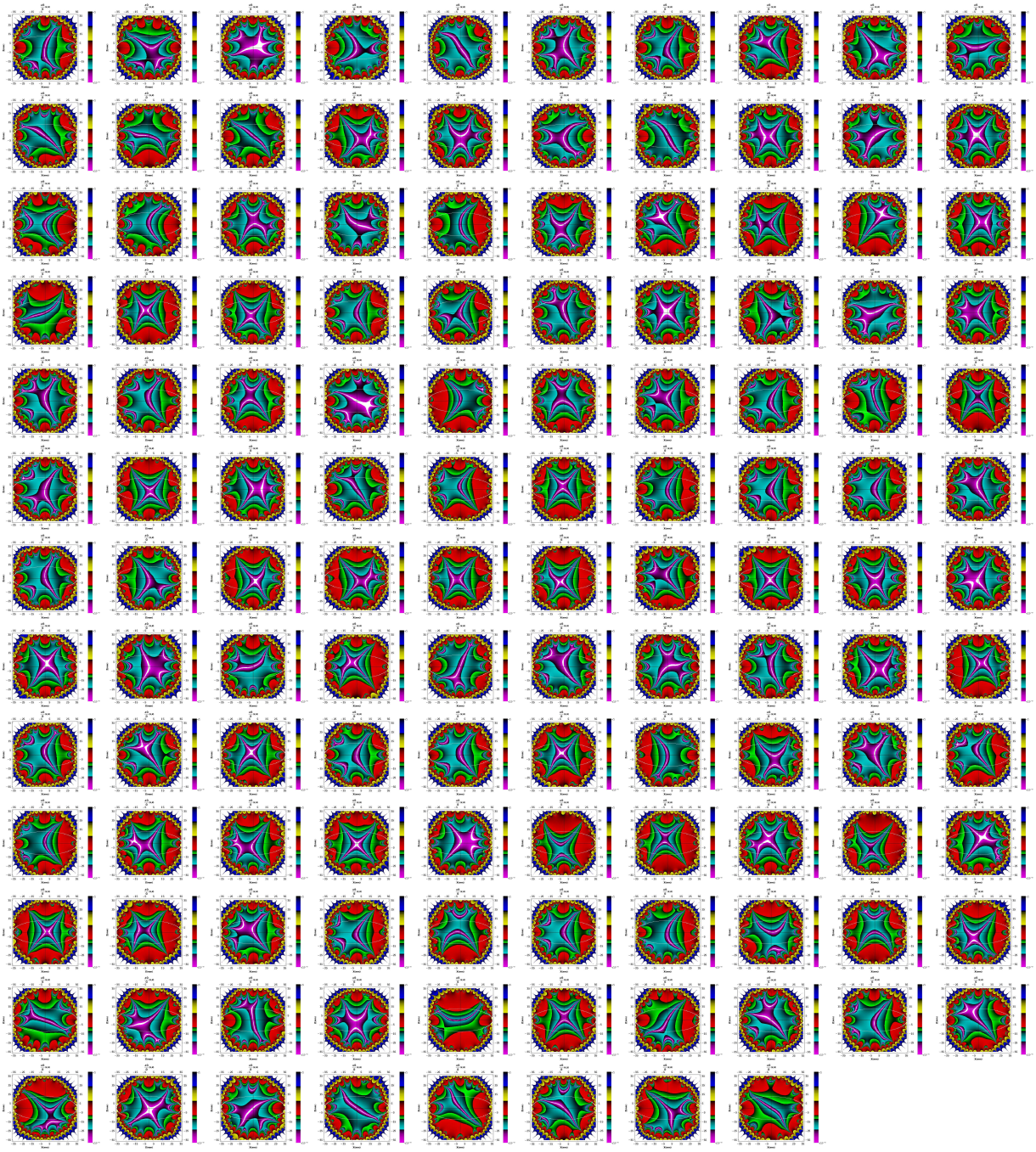

Figure D.1: 128 Magnetic flowers

Appendix E

Corrector bumps

E.1 π bump

π bump only need two correctors. It is the simplest configuration to perform a local orbit bump as shown by the figure E.1. The first corrector K1 deflects the beam of an angle y'_1. The strength

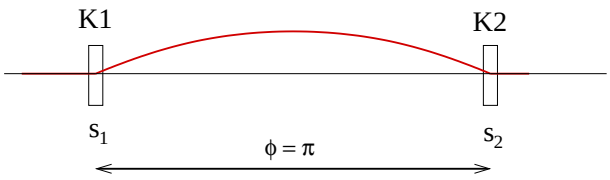

Figure E.1: π bump

of the second corrector (K2) at a phase difference of $\Delta\varphi = \pi$ must be calculated to cancel the effect of the first corrector. Hence the equations to solve:

$$\begin{bmatrix} 0 \\ y'_2 \end{bmatrix}_{s_2} = M_{s_1/s_2} \cdot \begin{bmatrix} 0 \\ y'_1 \end{bmatrix}_{s_1} ; \qquad \text{with } \Delta\varphi = \pi \tag{E.1}$$

This leads to a relation between the correctors strength since they are proportional to the created angle.

$$y'_2 = \sqrt{\frac{\beta_1}{\beta_2}}\, y'_1 \tag{E.2}$$

However this type of bump is not often used since it is very difficult to get two correctors spaced of a phase π.

E.2 Three corrector bump

A third corrector is added to prevent from the phase condition on corrector of the π bump. This makes the local orbit bump easier to operate. By calculating the strength of the correctors needed

to cancel the effect of the first one, these relations are obtained.

$$y'_2 = \sqrt{\frac{\beta_1}{\beta_2}} \frac{sin(\varphi_3 - \varphi_1)}{sin(\varphi_3 - \varphi_2)} \, y'_1 \tag{E.3}$$

$$y'_3 = \sqrt{\frac{\beta_1}{\beta_3}} \left(\frac{sin(\varphi_3 - \varphi_1)}{sin(\varphi_3 - \varphi_2)} - cos(\varphi_3 - \varphi_1) \right) \, y'_1 \tag{E.4}$$

The bump quality only relies on the accuracy on the determination of the phases φ_i and the beta functions β_i.

Appendix F

INSTITUT NATIONAL
POLYTECHNIQUE
DE LORRAINE

AUTORISATION DE SOUTENANCE DE THESE
DU DOCTORAT DE L'INSTITUT NATIONAL
POLYTECHNIQUE DE LORRAINE

o0o

VU LES RAPPORTS ETABLIS PAR :
Monsieur Louis WALCKIERS, Directeur Scientifique, CERN, Genève, Suisse

Monsieur Laurent FARVACQUE, Physicien, ESRF, Grenoble

Monsieur Patrick PUZO, Maître de Conférences, Laboratoire d'Accélérateur Linéaire, Orsay

Le Président de l'Institut National Polytechnique de Lorraine, autorise :

Monsieur MADUR Arnaud

NANCY BRABOIS
2, AVENUE DE LA
FORET-DE-HAYE
BOITE POSTALE 3
F - 54501
VANDŒUVRE CEDEX

à soutenir devant un jury de l'INSTITUT NATIONAL POLYTECHNIQUE DE LORRAINE, une thèse intitulée :

"Contribution à la métrologie des multipôles d'accélérateurs : les quadrupôles du Synchrotron SOLEIL"

en vue de l'obtention du titre de :

DOCTEUR DE L'INSTITUT NATIONAL POLYTECHNIQUE DE LORRAINE

Spécialité : **« Génie électrique »**

Fait à Vandoeuvre, le 16 octobre 2006
Le Président de l'I.N.P.L.,
L. SCHUFFENECKER

TEL 33/03 83 59 59 59

Résumé

Dans les accélérateurs de particules de type synchrotron tels que SOLEIL, le faisceau de particules doit répondre à des critères toujours plus exigeants afin d'améliorer les propriétés du rayonnement synchrotron émis. Le comportement du faisceau d'électrons dépend notamment des aimants multipolaires de l'anneau de stockage du synchrotron. Parmi eux, les quadrupôles, qui produisent une induction magnétique quadrupolaire, ont un rôle capital dans la focalisation des particules du faisceau. Certains défauts de fabrication peuvent introduire des décalages dans la position de leur axe magnétique et dans l'orientation transverse de l'induction magnétique, ce qui détériore la qualité de champ. Il est donc nécessaire de quantifier ces défauts et de les corriger. Pour cela, des mesures magnétiques sont mises en oeuvre. Le premier chapitre de ce mémoire s'attache principalement à expliciter les tolérances imposées aux quadrupôles de l'anneau de stockage du synchrotron SOLEIL. Dans le second chapitre, les outils théoriques permettant de mettre en oeuvre la méthode des bobines tournantes sont présentés. Une modélisation est proposée afin de prévoir les conséquences des défauts des bobines tournantes sur les harmoniques de l'induction magnétique. Une méthode de détection des défauts du banc de mesures est également présentée. Le troisième chapitre est dévolu aux résultats expérimentaux obtenus lors de la mesure des aimants multipolaires (quadrupôles) de l'anneau de stockage de SOLEIL. Dans un dernier chapitre, l'alignement basé sur le faisceau (BBA) des quadrupôles et des sextupôles dans l'anneau de stockage est abordé. Cette étape est indispensable car elle permet de connaître la position du faisceau par rapport à son orbite théorique qui peut être définie comme étant l'axe magnétique des quadrupôles ou l'axe magnétique des sextupôles. Une méthode de BBA est ici validée dans le cas des quadrupôles et une autre est proposée dans le cas des sextupôles.

Mots clés : Métrologie magnétique, bobines tournantes, quadrupôles d'accélérateur, méthode d'alignement sur le faisceau

Summary

In particle accelerators, more particularly in synchrotrons like SOLEIL, the particle beam is submitted to very strict constraints in order to improve the synchrotron radiation properties. The behaviour of the electron beam depends on the magnetic field distribution along the machine, mainly produced by the multipolar magnets of the storage ring (SR). Among them, the SOLEIL quadrupoles make the electron beam very sensitive to their magnetic field errors due to some manufacturing defects. In that context, two main parameters are very important concerning the quadrupoles : the magnetic axis location and the magnetic field orientation in the transverse plane. These quantities are to be quantified and corrected by means of magnetic measurements. The first part of this thesis is mainly devoted to the presentation of the quadrupole constraint origin. In that context, the accelerator history and a brief review of the existing magnetic measurement method are presented. In the second chapter, theoretical tools regarding rotating coils are detailed. A model is proposed to simulate the effects of rotating coil defects on the magnetic measurements. Then, to quantify these defects, a method is detailed in order to take them into account during the measurements. A third chapter is devoted to the magnetic measurement bench set up and to the experimental results of the SR multipolar magnet measurements. Finally, the last chapter deals with the beam-based alignment (BBA) of the SR multipoles. A method is validated for quadrupoles and an innovative BBA method is proposed in the case of sextupoles.

Key words : Magnetic metrology, rotating coils, accelerator quadrupoles, beam-based alignment method